The search for diffuse interstellar bands in quasar absorption line systems

by

Brian A. York
BSc, Mount Allison University, 2004

A Dissertation Submitted in Partial Fulfillment of the
Requirements for the Degree of

Master of Science

in the Department of Physics and Astronomy

University of Victoria

The search for diffuse interstellar bands in quasar absorption line systems

by

Brian A. York
BSc, Mount Allison University, 2004

Supervisory Committee

Dr. S. Ellison, Supervisor (Department of Physics and Astronomy)

Dr. C. Pritchet, Member (Department of Physics and Astronomy)

Dr. K. Venn, Member (Department of Physics and Astronomy)

Dr. C. Bohne, Outside Member (Department of Chemistry)

Supervisory Committee

Dr. S. Ellison, Supervisor (Department of Physics and Astronomy)

Dr. C. Pritchet, Member (Department of Physics and Astronomy)

Dr. K. Venn, Member (Department of Physics and Astronomy)

Dr. C. Bohne, Outside Member (Department of Chemistry)

Abstract

The diffuse interstellar bands (DIBs) probably arise from complex organic molecules whose strength in local galaxies correlates with neutral hydrogen column density, N(H I), and dust reddening, $E(B-V)$. Because Damped Lyman-α systems are known to have high N(H I), and Ca II absorbers in quasar (QSO) spectra are posited to have high N(H I) and reddening, both represent promising sites for the detection of DIBs at cosmological distances. I present the results of a search for diffuse bands in seven DLAs and nine Ca II absorbers. I announce the detection of the first narrow DIBs at $z > 0$ towards one DLA and one Ca II system. I further investigate the relative strengths of the DIBs as well as their correlations with N(H I) and $E(B-V)$. Finally, I discuss the prospects for using DIBs to better understand the properties of quasar absorption systems, and for using DIB searches in absorption systems to better understand the properties of DIBs.

Table of Contents

List of Tables

List of Figures

Acknowledgements

This thesis involved a large amount of research and observing. Thanks go to my supervisor, Sara Ellison, and to the group of fearsomely intelligent and capable people involved in the research. Brandon Lawton, Chris Churchill, Berkeley Zych, Michael Murphy, Peter Sarre and Arfon smith were involved at all satges, while Ted Snow, provided incredible expertise and assistance.

UVic's astro grads were also essential to the completion of the thesis (and my continued sanity, such as it is), in particular Jeff, Melissa, Wes, Lisa, Kaushi, Niko, Sarah, and Alex for making Room 408 an interesting place to sit and work, or just to visit. As for the rest of you, including Chris, Crystal, Ashley, Rachel, Eric, Anudeep, Helen, Ryan, Aaron, Rahul, Karun, Lanlan, and Sheona, you're all the best, even if you don't live in the perfect office.

Equally important in keeping me on track (and sane) were my friends, both in local and not. In particular, Karen for conversations both profound and trivial, Jael for board games and hospitality, and Morgan and Sam for both their hospitality and a stress-free weekend when I needed it the most. Elizabeth for abductions and summer snowballs. Farther afield, Bronwyn and Jason for conversation and support, all the way from Ottawa. Closer to home, Mary, for keeping Victoria fun and interesting.

Finally, without my family, I wouldn't even have arrived here to start work. My parents, Lyanne, Morgan, and DR. Thank you all.

Chapter 1

Introduction

1.1 Overview

I will begin by describing the diffuse interstellar bands (the terms diffuse interstellar bands and diffuse bands, and the acronym DIBs are used interchangeably in this thesis) in §1.2, discussing their discovery, a selection of carriers which have been suggested, the current leading candidates for DIB carriers, the known characteristics of the DIBs, and the detection of DIBs in other galaxies. Next I will introduce quasar absorption line systems (QSOALS) in §1.3, including in particular damped Lyman-α (DLA) and calcium II (Ca II) systems. Finally I will discuss the motivation for searching for DIBs in QSOALS (§1.4).

1.2 The Diffuse Interstellar Bands

The diffuse interstellar bands (DIBs) are a set of several hundred interstellar absorption features found in the optical and near infrared between 4000 Å and 1.3 μm (Herbig 1995). Figure 1.1 shows the diffuse interstellar bands between 4000 and 7000 Å, as seen in the spectrum of the reddened star BD+63^{o}1964. First detected by Heger (1922), and first studied in detail by Merrill (1934), the DIBs have remained an astronomical mystery for more than 80 years (Sarre 2006). In the past 15 years, advances both in observing techniques and in laboratory spectroscopy have brought

an understanding of the diffuse bands much closer (Schmidt & Sharp 2005). The DIBs are currently thought to be complex organic molecules in the gas phase, with polycyclic aromatic hydrocarbons (PAHs), long carbon chains, and fullerenes the current leading candidates for the DIB carrier (Snow 1995a).

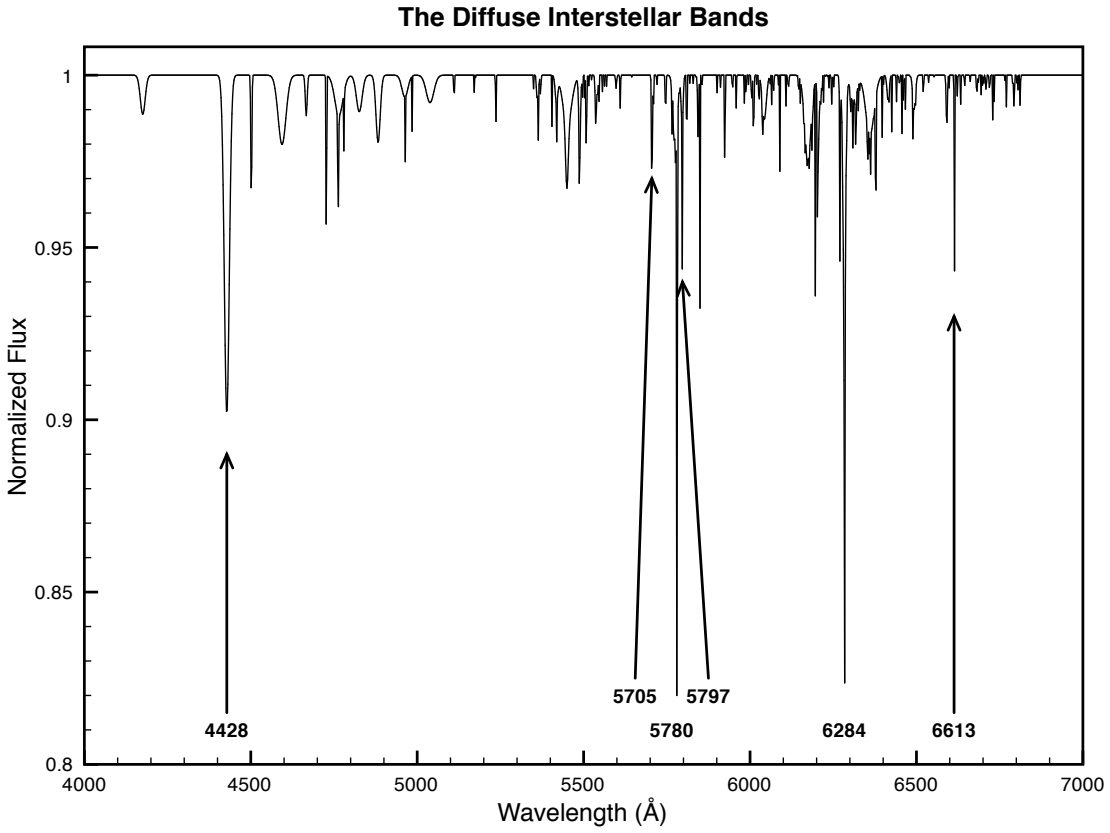

Figure 1.1: A spectrum of the Diffuse Interstellar Bands, with strengths as measured towards BD+63^{o}1964 (Ehrenfreund et al. 1997). The marked DIBs are the strong bands which will be discussed repeatedly in the thesis.

1.2.1 Discovery and History

One of the first discoveries made possible by the new telescopes and spectrographs which came into use at the beginning of the twentieth century was the detection of so-called "stationary" lines in the spectra of "oscillating stars" (e.g. Hartmann 1904). Oscillating stars, now known as spectroscopic binaries, are close binaries which appear

as a single star when imaged, but which show two sets of spectral lines which are alternately blue- and redshifted as the stars orbit around one another. Hartmann (1904), examining the oscillating star δ Orionis, discovered that its spectrum also contained a stationary (non-shifting) absorption line of Ca II at 3934 Å (the "K" line observed in the Sun's spectrum). Hartmann speculated that this stationary line might arise as a result of a cloud of gas located in interstellar space between the solar system and the star. As more stationary lines, including both the Ca II H & K doublet at 3934 and 3969 Å, and the Na I D_1 and D_2 doublet at 5891 and 5897 Å were discovered, almost exclusively towards stars with spectral type B0–B2, Young (1920) suggested that the stationary lines might instead be the result of an extended, calcium-containing atmosphere peculiar to early B stars. Henroteau (1921), on the other hand, argued that stationary lines were seen only towards early B stars because this was the only common type which lacked intrinsic Ca II and Na I atmospheric lines, thus allowing interstellar absorption to be detected. Henroteau (1921) also argued that the existence of emission nebulae and dark clouds implied that other interstellar clouds too faint to be directly observed might also exist.

Shortly thereafter, Heger (1922), in examining another star with stationary lines, noted the presence of unidentified absorption lines at 5780 and 5797 Å. Although Heger (1922) was the first to report these lines, there was no serious investigation of these unidentified absorption lines until Merrill (1934) added two new lines (at 6283.9 and 6613.9 Å), and suggested that the unidentified lines might be the result of absorption from molecules in interstellar space. Merrill (1934) also noted that the lines, rather than being sharp transitions, were widened and had diffuse edges. Since then many more such "diffuse bands" have been detected, and many possible origins have been suggested for the DIBs. Snow (1995a) mentions such diverse proposed carriers as solid oxygen, metastable states in H_2, negative ions of hydrogen and oxygen, two-photon absorption by vibrationally excited H_2, lattice defects (or impu-

rities) embedded in dust grains, and interstellar porphyrins. More recently, several complex organic molecules have been suggested as DIB candidates, including long carbon chains, fullerenes, and polycyclic aromatic hydrocarbons (Snow 1995a).

1.2.2 Observational characteristics of the diffuse bands

Number and shape of the diffuse bands in Galactic sightlines

Since the original two DIBs discovered by Heger (1922), new diffuse bands have been discovered at the average rate of four to five per year. More than 380 DIBs are now known to exist (e.g. Hobbs et al. 2008), suggesting that no single carrier is responsible for all of the diffuse bands. Although the strongest of the DIBs (at 4428 Å) is wide [its full width at half of its maximum intensity (FWHM = 22.5 Å)], most of the known diffuse bands are narrow (FWHM $<$ 1 Å) (Snow 1995a). In addition, as Snow (1995a) notes, the diffuse bands also appear to be invariant in both central wavelength and spectral profile, and to lack any sign of emission wings. Finally Cox et al. (2007) examined the DIBs along five sightlines, searching for evidence of either linear or circular polarization. Neither linear nor circular polarization are detected, with 2-σ detection limits ranging from 0.01–0.14% for linear polarization, and from 0.06–2.5% for circular polarization (Cox et al. 2007).

Reddening and extinction

The diffuse bands are also known to correlate weakly with other characteristics of the ISM. Herbig (1995) noted that, in general, the diffuse bands correlate well with reddening [$E(B-V)$], which measures the difference between extinction in the visual (V band) and the blue (B band), with a positive $E(B-V)$ indicating that more blue light is lost along a sightline than red light. Herbig (1993) shows that the 5780 Å DIB has the tightest such relationship amongst the known diffuse bands (see Figure 1.2 for the Galactic correlation). In an examination of 22 sightlines towards Orion and GMC214−13, however, Jenniskens et al. (1994) found that strength of the 6284 Å

DIB was suppressed *relative to an extrapolation of the DIB–$E(B-V)$ relationship* along sightlines with very low reddening [$E(B-V) < 0.08$ in the sightlines studied by Jenniskens et al. (1994)] and along sightlines passing through the Orion Giant Molecular Cloud (a possible explanation is that the DIBs are sensitive to the level of background UV radiation, as discussed in further detail below in "Radiation Intensity"). The correlation between the 5780 Å DIB and $E(B-V)$ thus appears to hold only for sightlines which pass through the diffuse interstellar medium.

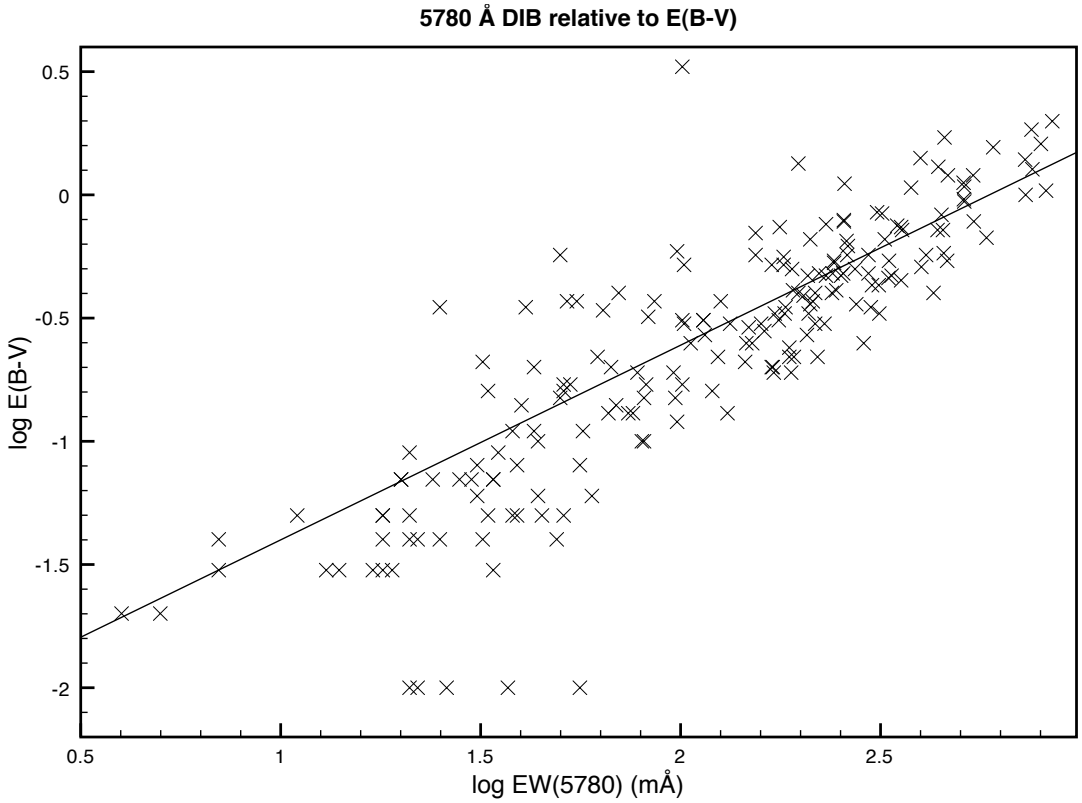

Figure 1.2: Correlation between $E(B-V)$ and the 5780 Å DIB on Galactic sightlines. Data from Table B.2.

Megier et al. (2005) compared the equivalent widths (EWs) of 11 DIBs (at 5780, 5797, 5850, 6196, 6203, 6270, 6284, 6376, 6379, 6613, and 6660 Å) with the dust extinction curves along 49 sightlines, and found that the DIB strength correlated both

with the strength of the 2175 Å bump and with the slope of the extinction curve between the far UV and any other part (not including the 2175 Å bump). The correlation with the 2175 Å bump was always positive, with the 5780 Å DIB having the strongest correlation. The 5780 and 6284 Å DIBs were negatively correlated with the far-UV slope, whilst the 5797, 5850, and 6376 Å DIBs were positively correlated with the slope. Megier et al. (2005) interpret the correlation between the 2175 Å bump and the DIBs as resulting from both being composed of similar materials (carbon-based dust grains for the bump and molecules for the DIBs), while the correlations and anti-correlations with the slope are interpreted as resulting from shielding. Megier et al. (2005) propose that those DIBs correlated with the slope of the far-UV extinction curve might require environments protected from background ultraviolet, whilst the DIBs which are anticorrelated with the slope might instead require environments with a minimum level of UV flux (see also "Radiation Intensity" below).

ISM environment

The diffuse bands are known to exist in a great variety of ISM conditions, including dark clouds, H II regions, and reflection nebulae (Sonnentrucker et al. 1997). Nevertheless, the diffuse bands are weak relative to $E(B-V)$ on sightlines towards H II regions and dark clouds [e.g. Jenniskens et al. (1994), who examined the DIBs at 6177, 6196, 6269, and 6284 Å along sightlines in Orion and towards GMC214−13]. The diffuse bands are also known to be weak or absent in circumstellar environments (e.g. Snow & Wallerstein 1973; García-Lario et al. 2005; Luna et al. 2008), and in reflection nebulae (Josafatsson & Snow 1987).

An intriguing development is the detection of emission features in the Red Rectangle nebula, which displays many unusual unassigned spectroscopic features including strong optical emission bands (Sarre 1991) with wavelengths extremely close (90–250 km s^{-1}) to some of the diffuse bands seen in absorption (Scarrott et al. 1992). Furthermore, as the spatial offset from the centre of the Red Rectangle increases, the

wavelengths of the emission lines converge closer to those of the diffuse bands (Sarre 2006). Although the emission lines are not coincident with the diffuse bands even at the highest offsets examined so far, it is possible that the internal temperature of the carrier becomes 'locked', as occurs for C_2 (which is detected in its excited state out to at least 13.″0 from the nebula) (Sarre 2006).

Atomic column densities

Another trend noted by Herbig (1993) was the relationship between the 5780 Å DIB and the neutral hydrogen column density, N(H I), along the same sight-line (see Figure 1.3). This correlation is extremely tight, with coefficient of 0.953 (T. Snow, private communication). The 5780 Å DIB also correlates with N(Na I), but this is likely because neutral sodium itself correlates with neutral hydrogen (Herbig 1993). Jenniskens et al. (1994) noted that, even on sightlines where the strength of the 6284 Å diffuse band was suppressed relative to $E(B-V)$, their strength was normal with respect to H I. Herbig (1993) also finds correlations between the 5780 Å DIB and the neutral atoms N(K I) and N(C I), although these correlations are weaker than the correlations with N(H I) and N(Na I). In comparing DIB strengths to other atomic transitions, Galazutdinov et al. (2004) found that some diffuse bands (notably at 5797 and 5850 Å) correlate very well with N(K I), whilst the DIB 6613 Å correlates much more weakly, and the DIB at 5780 Å is poorly correlated. None of the DIBs are especially strongly correlated with Ca II, although the 6613 Å DIB is at least weakly correlated with the Ca II K line. Galazutdinov et al. (2004) interprets these results as suggesting that these diffuse bands (5797, 5850, and 6613 Å) are found preferentially in the same areas where K I forms, but that Ca II is more evenly distributed along the sightline.

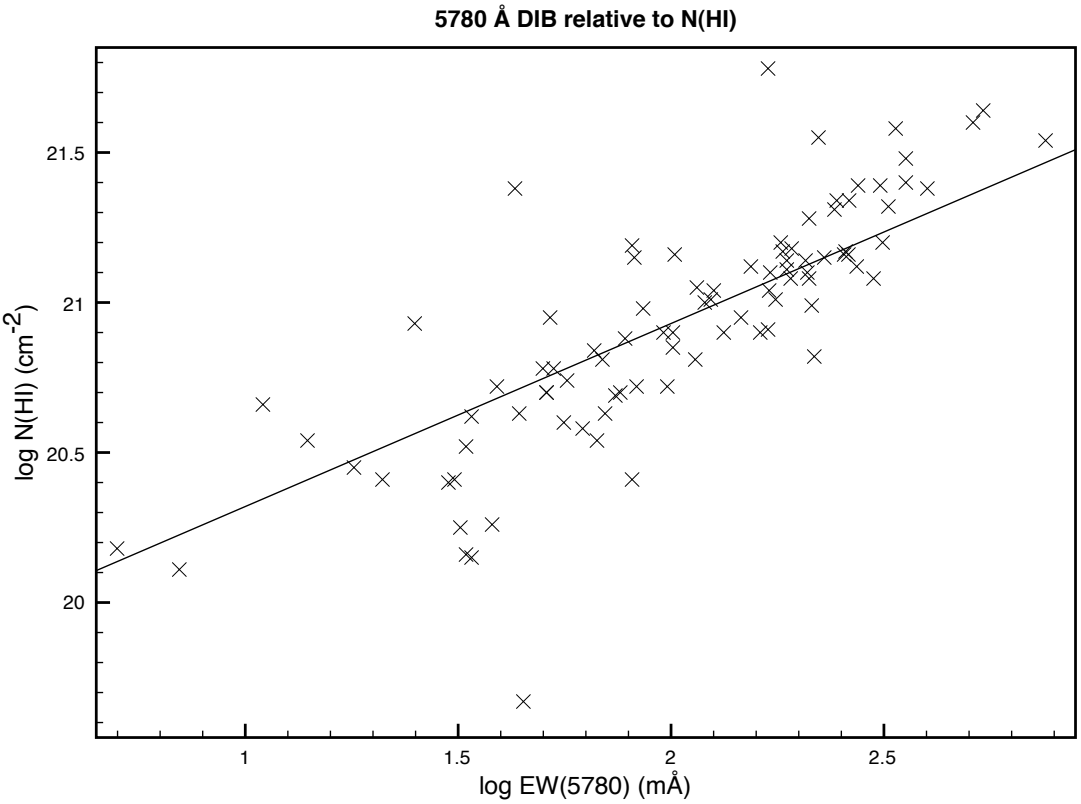

Figure 1.3: Correlation between N(H I) and the 5780 Å DIB on Galactic sightlines. Data from Table B.2.

Molecular column densities

Because molecules have long been suggested as a possible source of the diffuse bands, the relationship between the DIBs and other interstellar molecules, especially H_2, has attracted considerable attention. Herbig (1993) found that the 5780 Å DIB correlated with H_2 but that, when the relationships between N(H_2) and N(H I) and EW_{5780} and N(H I) were accounted for, the correlation disappeared. Figure 1.4 shows the corrected relationship. This lack of a relationship also excludes the possibility that the carrier of the 5780 Å DIB is created by the same process that creates interstellar carbon diatomics, since this formation process requires molecular hydrogen, and would thus create a relationship. Thorburn et al. (2003), however, detect a total of 18 weak

DIBs which do appear to correlate with N(C_2), N(CN), and N(CH), although they note that the DIBs at 5780 and 6284 Å do not correlate with these molecules, and are in fact strongest on sightlines where C_2 is undetectable. These DIBs, at 4364, 4726, 4735, 4964, 4969, 4780, 4985, 5004, 5170, 5176, 5419, 5513, 5542, 5546, 5763, 5769, 5793, and 6279 Å, likely have a carrier related in some way to these molecules, either through method of formation or environmental survival.

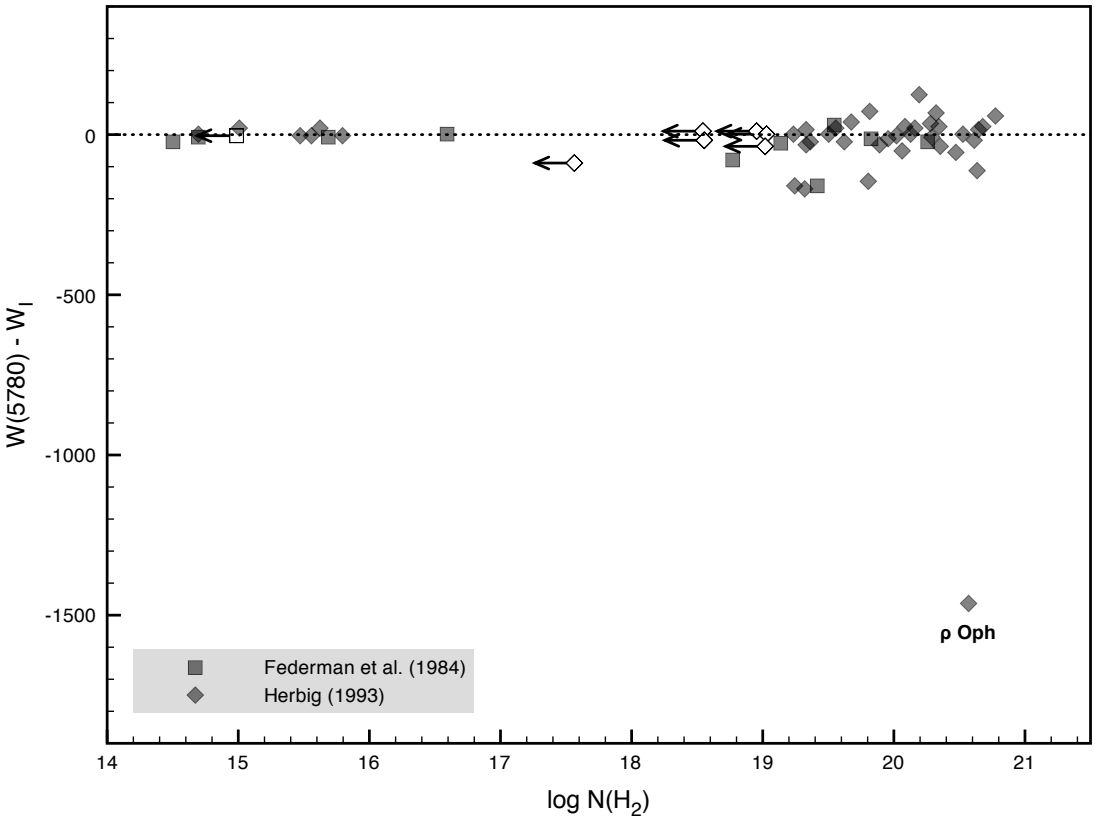

Figure 1.4: Relationship of EW_{5780} to N(H_2) after the dependence of EW_{5780} on N(H I) is removed (see Herbig 1993). The squares are data points from Federman et al. (1984), and the diamonds from Herbig (1993). Solid points represent detections of H_2, and open points upper limits.

Radiation intensity

The discovery by Jenniskens et al. (1994) that the strengths of the 6284 and 5785 Å diffuse bands were depleted relative to reddening (which they interpret as repre-

senting all matter along the sightline), but not relative to H I + H_2 (which they interpret as representing all neutral matter) along sightlines with low reddening ($E(B-V) < 0.08$), which they interpret as sightlines with a considerable amount of ionized hydrogen (H II). Further, they find that the strength of these bands was depleted relative to reddening along sightlines where a significant part of the hydrogen was in molecular form, including sightlines through giant molecular clouds. To explain these results, Jenniskens et al. (1994) suggest that the DIBs may be sensitive to the UV background along their line of sight. In particular, they suggest that DIBs are weak in H II regions, and in regions dominated by self-shielding molecular hydrogen. One possible explanation for this is that the DIBs may be ionized molecules, and thus undetectable when neutral (in giant molecular clouds), or when multiply ionized or dissociated by the UV background (in H II regions) or regions of low reddening. Jenniskens et al. (1994) found that the 6284 Å DIB was significantly weaker relative to the 6196 Å DIB along sightlines towards the Orion Nebula, whilst the reverse relationship holds for the low-reddening sightlines, suggesting that, if DIBs are ionized molecules, the carrier of the 6284 Å DIB has a higher ionization potential than the carrier of the 6196 Å DIB.

Cami et al. (1997) studied the relative strengths of the diffuse bands along sightlines with single clouds, and classified these clouds into four types based on the relative strengths of the 5780 and 5797 Å DIBs, the far-UV extinction, the 2175 Å bump, the presence of simple molecules, the reddening, and the UV background. ζ-type[1] clouds represented sightlines travelling through the innermost regions of the cloud, with significant self-shielding against UV. In these clouds, the 5780 and 5797 Å DIBs had approximately the same strength, and simple molecules such as CH and CN were detectable. σ-type sightlines instead passed through the outer layers of the

[1]The terms ζ-type refers to clouds with the same DIB ratios as the sightline towards ζ Oph, whilst σ-type refers to clouds with the same DIB ratios as the sightline towards σ Sco. These terms originate from Krełowski & Sneden (1995).

cloud, and featured a strong 5780 Å DIB and weak 5797 Å DIB, weak or undetectable CH or CN lines, and a stronger UV background. Orion-type clouds had a still higher UV background, high enough that a significant fraction of gaseous hydrogen was in the form of H II, with weak 5780 and absent 5797 Å DIB strengths. Finally, almost no DIBs were visible towards circumstellar clouds. Cami et al. (1997), in comparing the relative strengths of the 5780 and 5797 Å DIBs to the UV background, found that the behaviour was what would be expected if both DIBs were ionized molecules, but the 5797 Å DIB had a lower ionization potential.

Sonnentrucker et al. (1997) provided further evidence of the DIB dependence on UV background by examining the 5797, 6379, and 6613 Å DIBs along 35 sightlines including H II regions, dark clouds, molecular clouds, and reflection nebulae. They measured the slope of the relationship $EW_{DIB}/E(B-V)$ vs. $E(B-V)$ [deriving the UV background from $E(B-V)$ and A_V] and using the slope to estimate the ionization potential of these diffuse bands. From their observations, Sonnentrucker et al. (1997) determined that the DIBs were weakened by a factor of 2.5 relative to the relationship with $E(B-V)$ in H II regions, correlated well with $E(B-V)$ in thin clouds, and decreased with increasing $E(B-V)$ in dense clouds. Assuming that the DIB carriers are PAHs with 40 to 50 C atoms, Sonnentrucker et al. (1997) derived ionization potentials of 13 eV for the 5797 Å DIB, 7–9 eV for the 6379 Å DIB, and 11 eV for the 6613 Å DIB. Comparing these ionization potentials to the ionization potentials of the modelled PAH cations, Sonnentrucker et al. (1997) found that the 5797 and 6613 Å DIBs had ionization potentials consistent with PAH cations, whilst the 6379 Å DIB had an ionization potential consistent with neutral PAHs. Finally, Megier et al. (2005) found that the 5780 and 6284 Å DIBs were anticorrelated with the slope of the extinction curve, whilst the 5797, 5850, and 6376 Å DIBs were positively correlated. They show that this result may be interpreted as resulting from shielding, with the formation of the 5780 and 6284 Å DIBs requiring UV photons, potentially because

the carriers are ions, whilst the 5797, 5850, and 6376 Å DIBs may be destroyed by an excess of UV photons, possibly as a result of a lower ionization potential.

Correlations between diffuse bands

It has been known for some time that the strengths of diffuse bands are often related to one another (e.g. Krelowski & Walker 1987), and many of the diffuse bands are now known to be correlated with one another to some extent (e.g. Cami et al. 1997), but strong correlations have proved difficult to find (e.g. Wszołek & Wszołek 2003). Krelowski & Walker (1987) were the first to propose "families" of diffuse bands (and see Herbig 1995 for several possible sets of families), but so far no consensus has been reached as to how many families of DIBs exist, or which DIBs fall into which families. A distinction must also be made between "spectroscopic families", i.e. DIBs that correlate because they are both caused by the same carrier, and "environmental families" whose correlation indicates separate carriers which are likely to be found in the same environment, and respond to that environment in the same way. The environmental families may be further divided into local (correlations which hold only within the Galaxy) and universal (correlations which hold for any sightline in which diffuse bands can be detected).

Moutou et al. (1999) divide the possible types of correlation between DIBs into three categories based on the correlation strength. Weak correlations, such as that between the 5780 and 5850 Å DIBs, indicate only that both DIBs are weakly correlated with the same underlying factor, such as $E(B-V)$. Moutou et al. (1999) noted that almost all diffuse bands are at least weakly correlated with one another, and that the strong DIBs never more than weakly correlated, implying that no single carrier is responsible for multiple strong DIBs. Another level of correlation exists between pairs such as the 5780 and 6284 Å DIBs, where a definite trend exists, but it is obvious that there are fairly frequent exceptions to the correlation (note that this is the level of correlation noted in the families described by Herbig 1995). The pres-

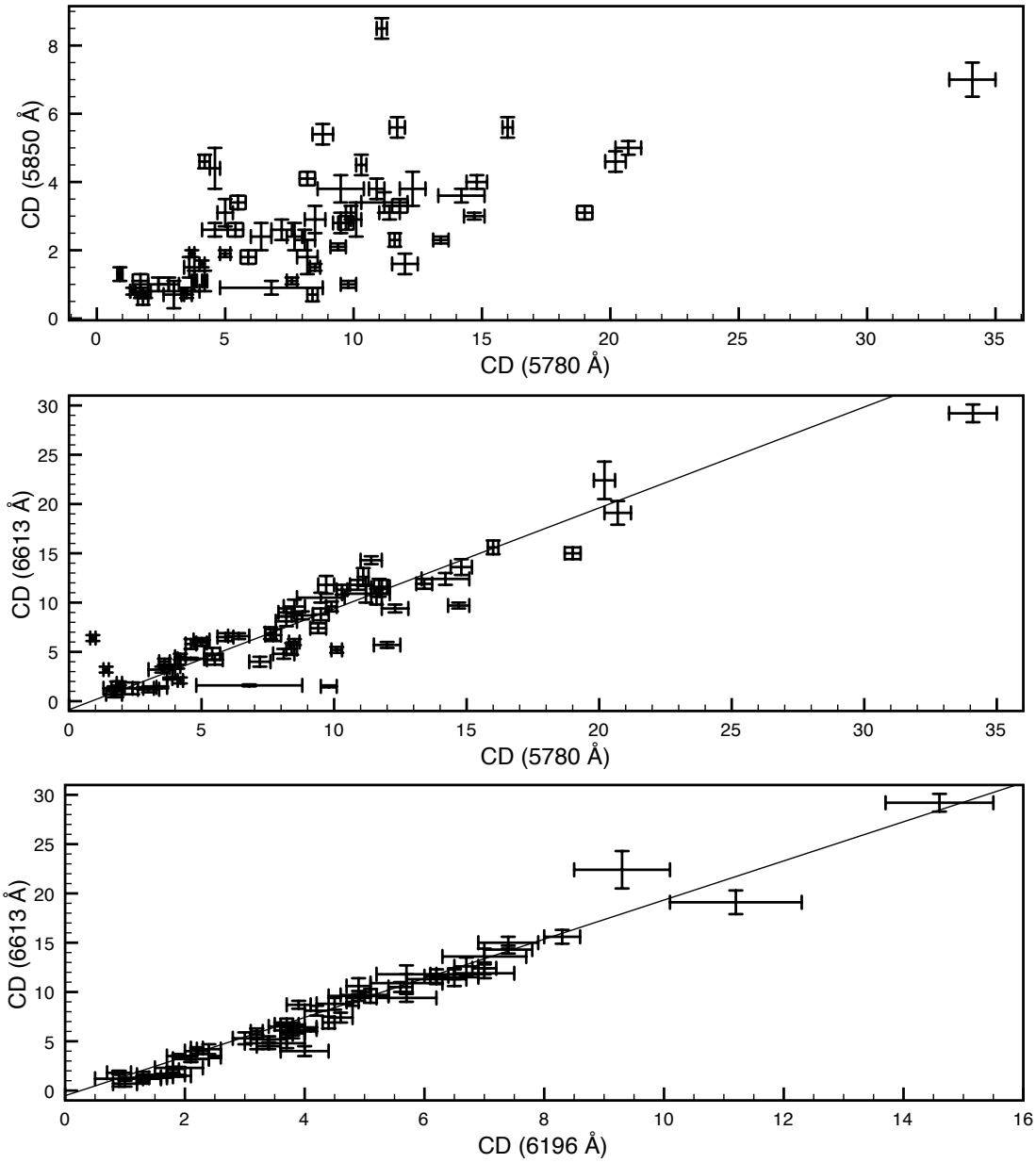

Figure 1.5: Categories of correlations between diffuse interstellar bands. The top panel shows a weak correlation, the middle panel a moderate correlation, and the bottom panel a tight correlation. In all panels, "CD" refers to the central depth of the DIB absorption. Data and best fit lines from Moutou et al. (1999).

ence of exceptions suggests that, rather than showing spectroscopic families, these correlations instead correspond to close species but different carriers, or may indicate

that the bands arise from the same general type of carrier (e.g. both carbon chains or both PAHs). Finally, they note an extremely tight correlation between the 6613 and 6196 Å DIBs, which implies that these DIBs may share the same carrier. Figure 1.5 shows examples of these types of correlation.

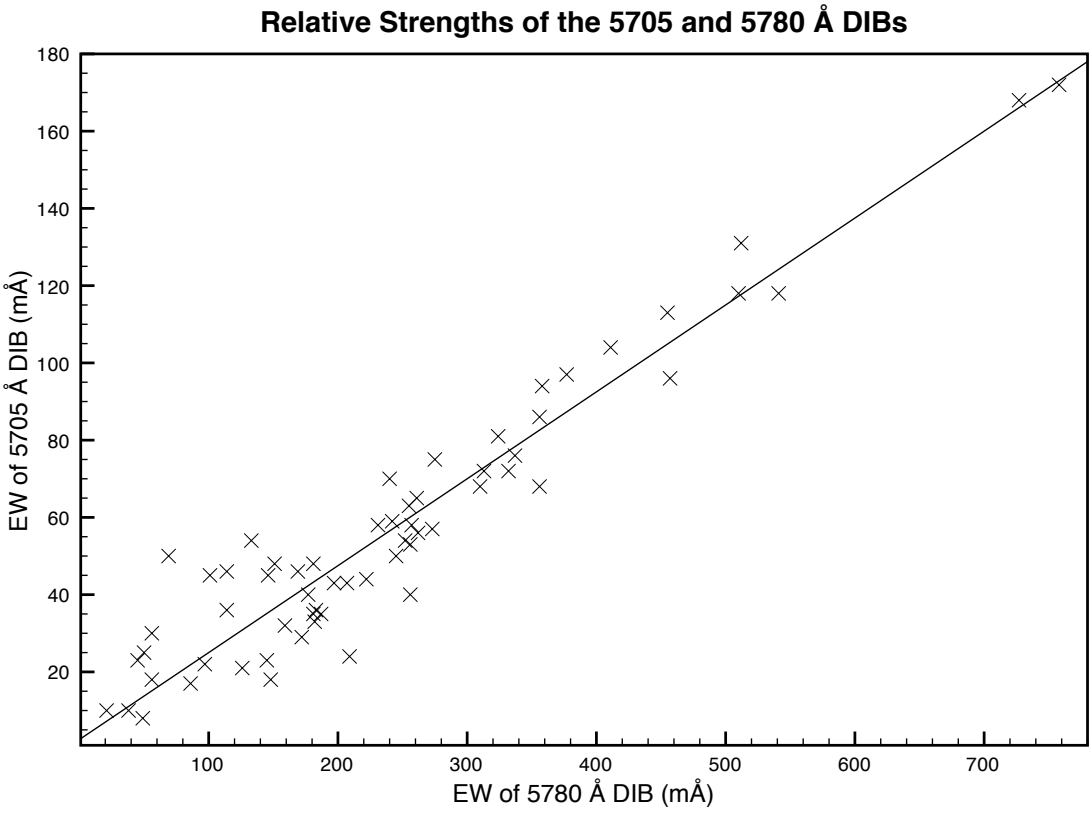

Figure 1.6: Correlation between the 5705 and 5780 Å DIBs. Data from Table B.2.

Wszołek & Wszołek (2003) also describe weak correlations between DIBs under the name "noisy correlation", and note that noisy correlations can be deceptive in that they can suggest the existence of a relationship which is not in fact present. Because all of the diffuse bands tend to correlate at least weakly with neutral atomic lines or reddening (Wszołek & Wszołek 2003), even bands which are not related to one another may appear to be correlated, especially in a small sample. Their suggested recourse is to deliberately search for sightlines with approximately the same ISM

conditions, but where one of the DIBs of interest varies widely in strength, and then to measure the other DIB on those sightlines. Any correlation which persists may indicate a spectroscopic family. Wszołek & Godłowski (2003), using the technique suggested, were able to detect two apparent spectroscopic families, each involving a single strong diffuse band and several weak DIBs. The first family consists of the 5780, 5776, and 5795 Å bands (of which only the 5780 Å band is strong), while the second includes the diffuse bands at 5793, 5797, 5819, 5829, and 5850 Å (here the 5797 Å band is the strongest, but the 5850 Å band is almost as strong). Thorburn et al. (2003), in studying the behaviour of diffuse bands whose strength was apparently related to the abundance of C_2 along the same sightline, also determined that the 5705 and 5780 Å DIBs are well-correlated. This relationship, shown in Figure 1.6, provides an interesting candidate for further research since both of the DIBs involved are relatively strong.

1.2.3 Proposed Galactic carriers

In the time since Merrill (1934) proposed that the diffuse bands resulted from absorption by (unspecified) molecules, many carriers have been proposed (see e.g. Snow 1995a for a recent overview). Solid-state carriers were the most popular hypothesis during much of that time, but more recently complex organic molecules in the gas phase have become the favoured candidates (Snow 1995a). I will first discuss solid-state carriers, followed by the three leading gas-phase carriers: polycyclic aromatic hydrocarbons (PAHs), Fullerenes, and long carbon chains. Finally I will discuss several more exotic carriers which have recently been proposed. During this discussion, it is important to remember that, with more than 380 known diffuse band (Hobbs et al. 2008), it is unlikely that any single carrier can account for every band. With several carriers (or even several groups of related carriers) likely responsible for the DIBs, the final solution to the DIB mystery is likely to be a rehash of the plot in *Murder on the Orient Express* (Tielens 1995).

Solid-state Carriers

The first proposed solid-state carrier was solid oxygen (McKellar et al. 1955), based on the observation that the spectrum of solid oxygen below 55 K had absorption features which appeared close to the wavelengths of several strong DIBs. This proposal has since been abandoned based on the lack of solid oxygen detections in the interstellar medium. Herbig (1963) was the next to propose a solid-state carrier, in this case metastable H_2 embedded in dust grains, which he proposed as a source for the 4428 Å DIB. This proposed carrier required a matrix shift[2] from the dust grain to coincide with the 4428 Å DIB absorption, and was later debunked by Malville (1964) because sufficient column densities of metastable H_2 could not be produced under interstellar conditions. More recently, solid state models have been proposed based either on lattice defects in the crystal structures of dust grains caused by cosmic rays and energetic photons in circumstellar environments (Wickramasinghe et al. 1968), and on impurity centres within interstellar dust grains, including both simple and complex molecules (e.g. Duley & Graham 1969; Shapiro & Holcomb 1986; Duley 1995).

A major argument against the proposed solid-state carriers has been their prediction that the diffuse bands should show emission wings, variable absorption wavelengths, and variable absorption profiles, none of which have been found (see §1.2.2 for more detail and references). Embedded solid-state DIB models also have difficulty reproducing the large number of narrow diffuse bands which are known to exist (Snow 1995a). The models based on lattice defects in grains proposed by Wickramasinghe et al. (1968) also hypothesized that diffuse bands should be abundant in circumstellar material, because the proposed formation mechanism involved Lyα photons

[2]The absorption spectrum of a gas-phase atom is shifted unpredictably when the atom is embedded in a solid matrix. Matrix shifts are most frequently encountered now because obtaining spectra of DIB candidates under gas-phase conditions approximating the ISM is difficult, whilst obtaining spectra of candidate absorbers in a matrix (usually made up of solid neon) is generally easier. In the case of Herbig (1963), the gas-phase spectrum of metastable H_2 was known, and failed to match the 4428 Å DIB, so he hypothesized the existence of a matrix shift that might solve the problem.

emitted from O and B stars. Observations of circumstellar material, however, has revealed that the diffuse bands are instead extremely weak in these environments (García-Lario et al. 2005).

Johnson (1995) proposed another form of solid-state embedded DIBs, involving interstellar porphyrin molecules [specifically tetrabenzoporphyrin (TBP) in the form of H_2TBP and MgTBP, see Figure 1.7 for the structure of these molecules] embedded in paraffin matrices (models suggested that porphyrins would not survive in the ISM without embedding Snow 1995b). While the evidence already amassed against solid-state carriers might be expected to apply to this model as well, Johnson (1995) proposes a solution, that the porphyrins are embedded in Shpol'skii sites within the paraffin matrices. A Shpol'skii matrix results when a substance embedded in a crystalline matrix neatly replaces one or more molecules of the host matrix, resulting in narrow and consistent emission and absorption profiles without emission wings. Johnson (1995) proposes that MgTBP and H_2TBP collectively account for all of the more than 200 DIBs known in 1995, claiming further that porphyrin absorption features had been detected within a few Å of every known DIB. He further proposed the existence of several new diffuse bands which had not yet been observed based on the absorption spectra of the porphyrins.

The proposal of Johnson (1995) has been attacked, primarily on the grounds that there is no compelling reason why only two species of porphyrin should exist in the ISM. The lack of tight correlations between most diffuse bands is also evidence against the porphyrin model, since it would require diffuse bands arising from the same carrier not to be correlated with one another. Finally, the new diffuse bands proposed by Johnson (1995) (and critiqued in Snow 1995b) have not been observed. The model of Johnson (1995) has thus been rejected along with the other solid state models, although the idea of organic molecules as DIB carriers has been gaining in popularity for some time.

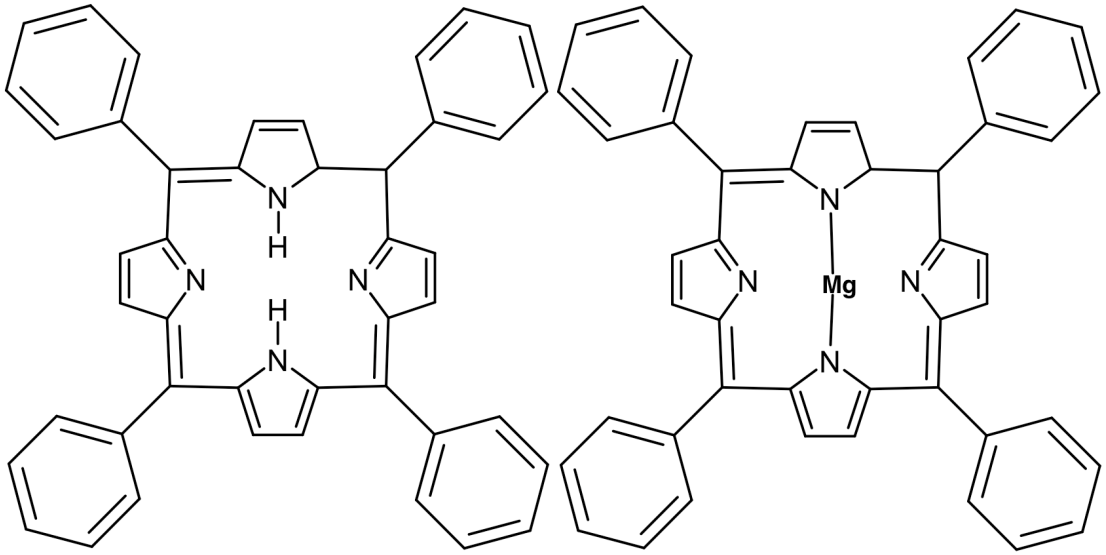

Figure 1.7: Molecular structure of H_2TBP (left) and MgTBP (right). Note that carbon atoms are not explicitly labelled, nor are external hydrogen atoms.

PAHs/PANHs

Polycyclic aromatic hydrocarbons are organic compounds formed from fused aromatic (benzene) rings, ranging widely in size from the small (e.g. anthracene, $C_{14}H_{10}$) to the large (e.g. circum-circumcoronene, $C_{96}H_{24}$). Figure 1.8 shows a number of example PAHs. One key point in the favour of the PAH hypothesis is that PAHs are known to exist in the interstellar medium, and have been detected through infrared emission, both in the Milky Way (e.g. Leger & Puget 1984) and in other galaxies, both locally (e.g. Tielens et al. 1999) and at high redshift (e.g. Teplitz et al. 2007). First proposed as the DIB carrier in 1985 (e.g. Crawford et al. 1985; Leger & d'Hendecourt 1985; van der Zwet & Allamandola 1985), PAHs have remained a leading candidate for the diffuse bands. While neutral PAHs have electronic transitions in the ultraviolet, PAH cations have rich spectra in the optical (e.g. Crawford et al. 1985). In addition, PAHs are able to survive the conditions in the ISM, including the presence of UV photons.

A related carrier model was proposed by Hudgins et al. (2005), who argue that the 6.2 μm feature attributed to PAHs should instead be attributed to polycyclic aromatic nitrogen heterocycles (PANHs), formed by substituting a nitrogen atom for a carbon atom in a PAH. In particular, they find that the emission feature centres at 6.3 μm even in large PAHs, but that the substitution of a nitrogen atom shortens the wavelength sufficiently to reproduce the observed emission feature. Hudgins et al. (2005) further suggest that neutral PANHs with internal nitrogen substitutions should display complex optical spectra with similar line widths to those observed in the diffuse bands. These two carriers are sufficiently similar to one another to be treated as a single hypothesis.

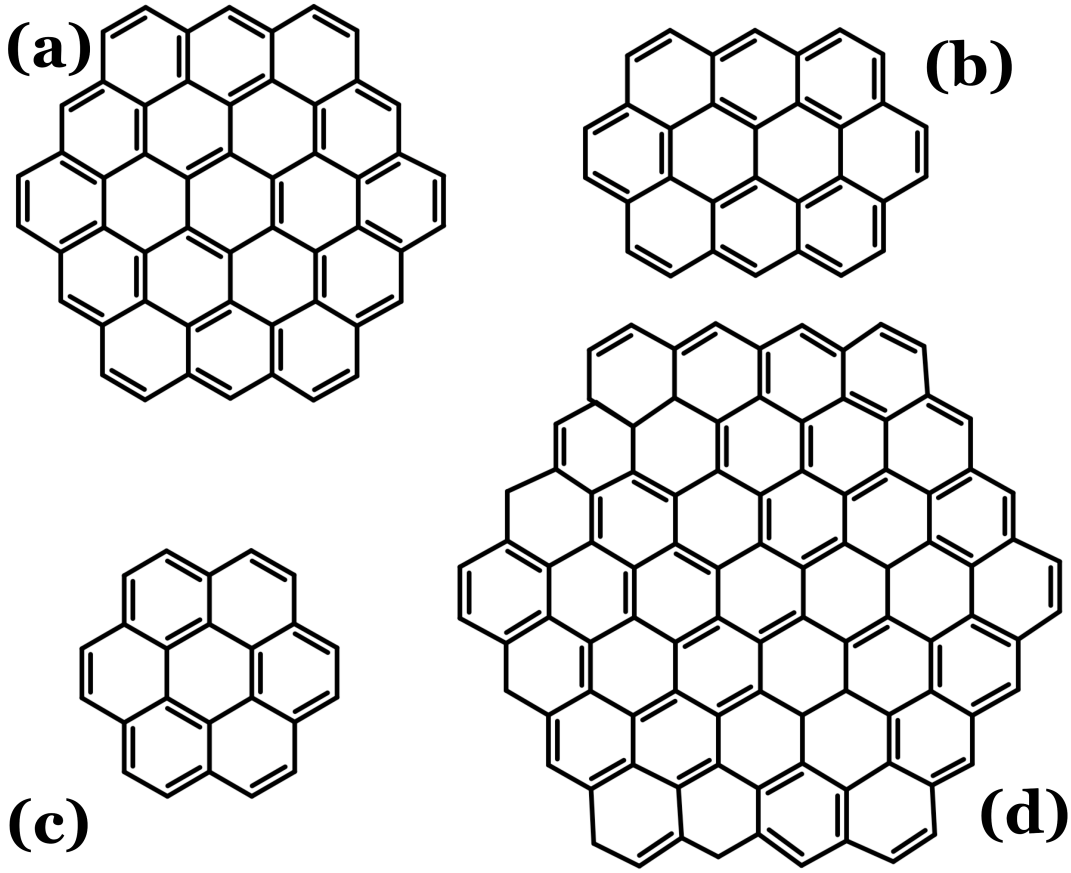

Figure 1.8: Sample polycyclic aromatic hydrocarbons, including circumcoronene (a), ovalene (b), coronene (c), and circum-circumcoronene (d).

PAH cations might also explain at least some of the environmental dependence of the diffuse bands. DIBs are known to be weak in dark clouds and reflection nebulae, and absent in circumstellar environments (Snow 1995a). If PAH^+ ions are indeed the DIB carrier, the weakness in dark clouds would be expected since PAHs would be expected to be neutral in this environment (Le Page et al. 2001, 2003). One weakness of the PAH hypothesis is also related to environmental dependence, in that although infrared emission associated with PAHs has been detected in circumstellar environments, DIBs are known to be weak or absent in those environments (Snow 1995b). Geers et al. (2007), however, argue that PAHs are uncommon in circumstellar disks, indicating that the weakness of DIBs in circumstellar environments may not prove to be a weakness in the PAH hypothesis. (Snow et al. 1995) examined sightlines passing through two reflection nebulae in which PAHs were detected in the infrared, but DIBs were weak compared to reddening, despite a strong UV background. They concluded that the density of these nebulae was great enough to allow the PAHs to remain neutral in these reflection nebulae, indicating that the weakness of the diffuse bands in this environment is not an argument against PAH cations as DIB carriers.

Le Page et al. (2001) produced a model of hydrogenation and charge states of PAHs in diffuse clouds. Their model was tested against laboratory data for small PAHs, and found to produce results consistent with experiment. Le Page et al. (2003), using the model introduced by Le Page et al. (2001), found that PAHs with 15–20 carbon atoms were destroyed in interstellar environments, that PAHs with 20–30 carbon atoms were stripped of their peripheral hydrogen, and that larger PAHs survived with normal hydrogen content. Le Page et al. (2003) also found that PAHs were more likely to be cations than either neutral or anions, and further that larger PAHs (90–100 carbon atoms) were predominantly cations under interstellar conditions.

Cox & Spaans (2006) modelled the charge state distribution of PAHs with 20–100

carbon atoms in single diffuse clouds with metallicities and background UV intensities corresponding to the Milky Way (MW) and Magellanic Clouds. They found that the fraction of PAH cations in the various model clouds were consistent with the relative abundances of the diffuse bands in the Milky Way and Magellanic Clouds. Further, Cox & Spaans (2006) found that the lack of diffuse band detections in the Small Magellanic Cloud (SMC) bar compared to the SMC wing can be explained by the fraction of PAH cations in both environments. Ruiterkamp et al. (2005) modelled the PAH charge distribution and potential DIB absorption for the sightline towards HD 147889, which combines strong DIBs with a single-cloud sightline. They found that, while a combination of PAHs might be able to reproduce the weak and intermediate diffuse bands, it would require the presence of very specific PAH molecules to reproduce the strong DIBs, in particular PAHs with > 100 carbon atoms. The main weaknesses of these studies, as well as Hudgins et al. (2005), is the lack of experimentally derived spectra for large PAHs and PANHs due to their lack of stability under terrestrial conditions (Snow 2001b). Thus, while the PAHs are likely the strongest current candidate for the majority of the diffuse bands, there are still significant challenges to be overcome before the hypothesis can be considered proven.

Fullerenes and Fulleranes

Fullerenes are closed cages of carbon atoms, including C_{50}, C_{60}, and C_{70} (Herbig 1995). While neutral fullerenes do not have strong spectral features in the optical, C_{60}^{+} was found to have a double transition in the 9510–9650 Å range, which might correspond to interstellar features at 9577 and 9632 Å (Herbig 1995). It has also been suggested (Snow 1995b) that fullerane molecules ($C_{60}H_m$) could act as the DIB carrier, and that the degree of hydrogenation of C_{60} would depend on ISM environment, and might explain the absence of DIBs in dark clouds and circumstellar environments. The wide variety of possible neutral and ionized fulleranes makes an exhaustive laboratory search for candidates difficult without more knowledge as to

which fulleranes are able to survive the conditions in the ISM.

One weakness of the fullerane model is the low oscillator strength for broad transitions. Snow (1995b) reports that very nearly a fourth of interstellar carbon (or nearly all the carbon depleted from interstellar gas) would need to be in the form of fulleranes to reproduce known DIB profiles. Another difficulty is the sparsity of optical transitions observed in C_{60}^+ and $C_{60}H_2$, especially given the large number of diffuse bands. Finally, Snow & Seab (1989) report the discovery in the laboratory of an absorption line at 3860 Å associated with C_{60}^+, but which has not been found in the spectra of stars where DIBs are detected. The detection limits established by Snow & Seab (1989), however, are not sufficient to eliminate C_{60}^+ as a viable hypothesis. Thus, although the interstellar nature of the 9577 and 9632 Å features has been confirmed by Galazutdinov et al. (2000), and the two features have been shown to correlate extremely well, no other diffuse bands have yet been identified with fullerenes, nor have other predicted transitions been observed (although the presence of strong telluric absorption close to the predicted features makes any identification difficult). Thus, while C_{60}^+ may be the carrier for a small number of diffuse bands, it appears that other possible carriers are favoured for the majority of features.

Long-chain Carbon Molecules

These proposed carriers are linear carbon chains (possibly with attached side groups), usually of the form C_nH_m with very small m (Snow 1995b). Carbon chains are known to exist in the interstellar medium, and radio observations have shown large abundances of small carbon chains (e.g. C_4H, C_3N, HC_5N, and HC_7N) in environments similar to those in which the diffuse bands are found (Snow 1995b). In addition to carbon chains, this proposed carrier has also expanded to include cyclic molecules such as C_{18} (e.g. Maier et al. 2006).

One of the first long-chain carbon molecules proposed was C_7^-, due to strong similarities between laboratory spectra and known DIBs (Tulej et al. 1998), even to

the point of C_7^- being declared as the first definite discovery of a DIB carrier (e.g. Snow 2001b). Unfortunately C_7^- has a low electron affinity (~ 3 eV), and is unlikely to be able to survive in the ISM in its ionized state. Further, as shown by McCall et al. (2001), the DIB at 5748 Å, thought to arise from C_7^-, was instead a stellar line, whilst the two strongest transitions, at 6270 and 4964 Å, were not correlated in strength with one another (and thus cannot share the same carrier). Maier et al. (2004) also failed to detect absorption at 3789 and 5109 Å, found to be associated with C_4 and C_5 respectively in laboratory measurements, in the diffuse cloud towards ζ Oph. Based on their results, Maier et al. (2004) were able to show that carbon chains and their simple derivatives containing up to 10 atoms can be excluded as carriers of the strong diffuse bands.

Recent work by Maier et al. (2006) has derived an upper limit to the abundance of cyclic C_{18} based on the non-detection of the laboratory-identified transition at 5928.5 Å, but work on long chains of the form C_{2n+1}, in particular C_{17}, C_{19}, ..., C_{31} continue,. These molecules are expected to show electronic transitions in the 4000–8000 Å range. Although cyclic C_{18} is not detected in the ISM, the similarity in line profile between its transition at 5928.5 Å and the line profiles of many DIBs (Maier et al. 2006) suggest that large bare carbon chains are still a viable hypothesis.

Unified Theory

Zhou et al. (2006) recently proposed a potential carrier which may be seen as a unified view of potential DIB carriers. They show that nanometer-sized Fe particles can catalyse the formation single-walled carbon nanotubes (essentially tubular extensions of the C_{60} atom, e.g. Figure 1.9) with H-terminated stubs in environments similar to those found around late-type carbon-rich stars. Note that, despite their size, these nanotubes act as gaseous carriers rather than solid-state carriers. Zhou et al. (2006) performed electronic structure calculations on a family of tubular PAH molecules derived from elongated C_{60}, and found that these molecules should produce strong

optical spectra without additional UV absorption (this is important as no such strong UV transitions have been found in the ISM). While these results are promising, selecting the circumstellar atmospheres of carbon-rich stars as a primary formation site is likely to prove a challenge to this hypothesis, since the diffuse bands are known to be weak or absent in circumstellar environments (García-Lario et al. 2005).

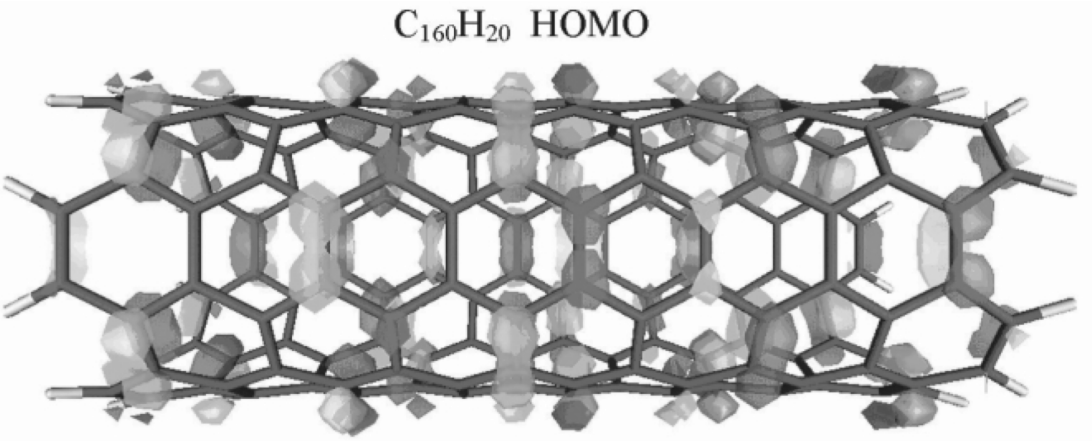

Figure 1.9: Sample $C_{160}H_{20}$ nanotube. Figure appears as Figure 1 of Zhou et al. (2006), and was provided by Dr. M. Hybertsen.

Proposed exotic carriers

Another recent proposed carrier is two-photon absorption by vibrationally excited H_2^+, proposed by Glownia & Sorokin (1994). This hypothesis involves a two-step process wherein the absorption of a Lyα photon leaves an H_2^+ ion in an electronically excited state from which it may then absorb at optical wavelengths. This model predicts that diffuse bands should be found predominantly near bright stars (O and B type stars were examined by Glownia & Sorokin 1994), and that circumstellar DIBs should be common. The weakness of DIBs in circumstellar environments (García-Lario et al. 2005) and the evidence provided by Destree et al. (2007) that diffuse band strength does not depend on the spectral type of the background star, have proven fatal to this model.

A final proposed carrier (Holmlid 2008) is the model that many DIBs (> 60) are caused by transitions in doubly-excited atoms embedded in Rydberg matter (RM). RM is a low-density solid- or liquid-like metastable state of highly excited atoms, which has almost metallic properties and a very long radiative lifetime (Holmlid 2008). Holmlid (2008) claims to have identified the 25 strongest DIBs (and 38 weaker DIBs) with different transitions in Rydberg matter (with errors < 2 Å), with each DIB arising from a separate transition. (Holmlid 2008) thus also predicts that no two diffuse bands will arise from the same individual carrier.

1.2.4 Extra-Galactic DIBs

While most DIB surveys have involved stars within the Galaxy [if only to take advantage of the high signal to noise (SNR) ratios which can be obtained along sightlines towards bright stars], diffuse bands were first detected in other galaxies more than 40 years ago, when Hutchings (1966) detected the 4428 Å DIB in the Large and Small Magellanic Clouds (LMC and SMC). Whilst Hutchings (1966) reported a strong 4428 Å feature, Blades & Madore (1979) found that the strengths reported by Hutchings (1966) (from photographic spectra) were overestimated due to blends with stellar photospheric lines. After several additional detections of the 4428 Å DIB in the Magellanic Clouds (see Snow 2001a for a review), Pettini & Dodorico (1986) made the first detection of narrow DIBs in the LMC, detecting the 6376 and 6379 Å features in two lines of sight in the 30 Doradus region.

Vidal-Madjar et al. (1987) and Vladilo et al. (1987) were the first to detect the 5780, 5797, and 6284 Å DIBs in the the LMC, along the sightline towards the supernova SN 1987A in the LMC. Ehrenfreund et al. (2002) also detected diffuse bands in both the Large and Small Magellanic Clouds, noting that some diffuse bands (in particular the 6284 Å DIB) appeared weaker compared to reddening in the Magellanic Clouds than in the Galaxy. Cox et al. (2006) noted that the 6284 Å DIB was weaker in the LMC than in the MW relative to $E(B-V)$, whilst the 6613 Å DIB

appeared to behave similarly in the LMC and the Galaxy. Cox et al. (2006) conclude that the weakness of the 6284 Å DIB in their sightlines is due to a softer UV field. Welty et al. (2006) find that diffuse bands in the Magellanic Clouds are weaker by factors of 7–9 in the LMC and ~ 20 in the SMC than in the Milky Way, which they attribute to lower metallicity and a higher intensity UV field. Snow (2001a) provides a review of the early extra-galactic DIB detections.

Cordiner et al. (2008) have detected several DIBs in M31, including the 5780, 5797, 6284, and 6613 Å DIBs. These observations targeted two stars in M31, and found that the DIB equivalent widths were higher [with respect to $E(B-V)$] in M31 than in the Milky Way, although still within the scatter of the relation. D'Odorico et al. (1989) used the supernova 1986G to detect diffuse interstellar bands in NGC 5128. Similarly, Sollerman et al. (2005) detected diffuse bands in NGC 1448 through spectroscopy of supernovae, finding that the diffuse bands behaved similarly [with respect to $E(B-V)$], that the ratio of the 5780 and 5797 Å bands implied a relatively strong radiation field, and that the relationship between the 5780 Å DIB and the Na I column density in NGC 1448 was consistent with the Galactic relationship. Heckman & Lehnert (2000) detected DIBs towards seven starburst galaxies, finding that they had similar relative strengths and dependence on $E(B-V)$ and Na I as Galactic DIBs. Finally, Junkkarinen et al. (2004) detected the 4428 Å DIB in a quasar absorption line system towards the quasar AO 0235+164, the first (and before this thesis the only) detection of a diffuse band at cosmological distances.

1.2.5 Summary

Although the carrier(s) of the diffuse interstellar bands have not yet been definitively identified, there has been considerable progress towards a solution. The DIB carriers appear to be gas-phase molecules (Sarre 2006), likely ionized (Cami et al. 1997), and almost certainly organic (Snow 2001b), with PAHs, fullerenes, and carbon chains as the current primary candidates. One possible method of determining the DIB

carrier is the examination of the diffuse bands in a variety of ISM environments, both inside and outside the Milky Way. The DIBs have already been detected in a variety of other galaxies, and in one quasar absorption line system (QSOALS) with a redshift $z = 0.524$ in the sightline towards AO 0235+164. If more diffuse bands are to be detected at cosmological distances, QSOALS are an obvious target for future searches.

1.3 Quasar Absorption Line Systems

Quasars (originally called quasi-stellar objects, and now often abbreviated as QSOs) are point source (star-like) emitters known for their extreme luminosity, high redshift, and broad emission lines. First detected in the 1950s as radio sources, the optical counterpart to the quasar 3C273 was discovered in 1963 (Hazard et al. 1963). In the same year, Schmidt (1963) found that the spectrum of 3C273 was highly redshifted ($z = 0.158$), and Oke (1963) found that the spectral energy distribution was a power law rather than a thermal blackbody. A few years later, Bahcall et al. (1966) found a pair of absorption lines in the spectrum of the quasar 1116+12. The quasar had a redshift of 2.118, while these lines, which appeared to correspond to the Lyα transition of neutral hydrogen and to C IV, had a redshift of 1.949, suggesting that the lines might be due to intervening intergalactic clouds, or to material ejected from the quasar. Young et al. (1982), by examining a sample of 33 quasars, were able to argue that the absorption lines were a result of intervening systems because all of the quasars showed the same line density and equivalent width (EW) distribution and the line density and equivalent width were not functions of relative velocity from the QSO. Since that time, the study of quasar absorption systems has grown to become an exciting part of astronomy. Low H I column density systems are one of the only methods of examining the intergalactic medium, whilst high H I column density systems offer the chance to observe galaxy-like systems in absorption, and without the

luminosity bias that plagues emission-based surveys (Wolfe et al. 2005).

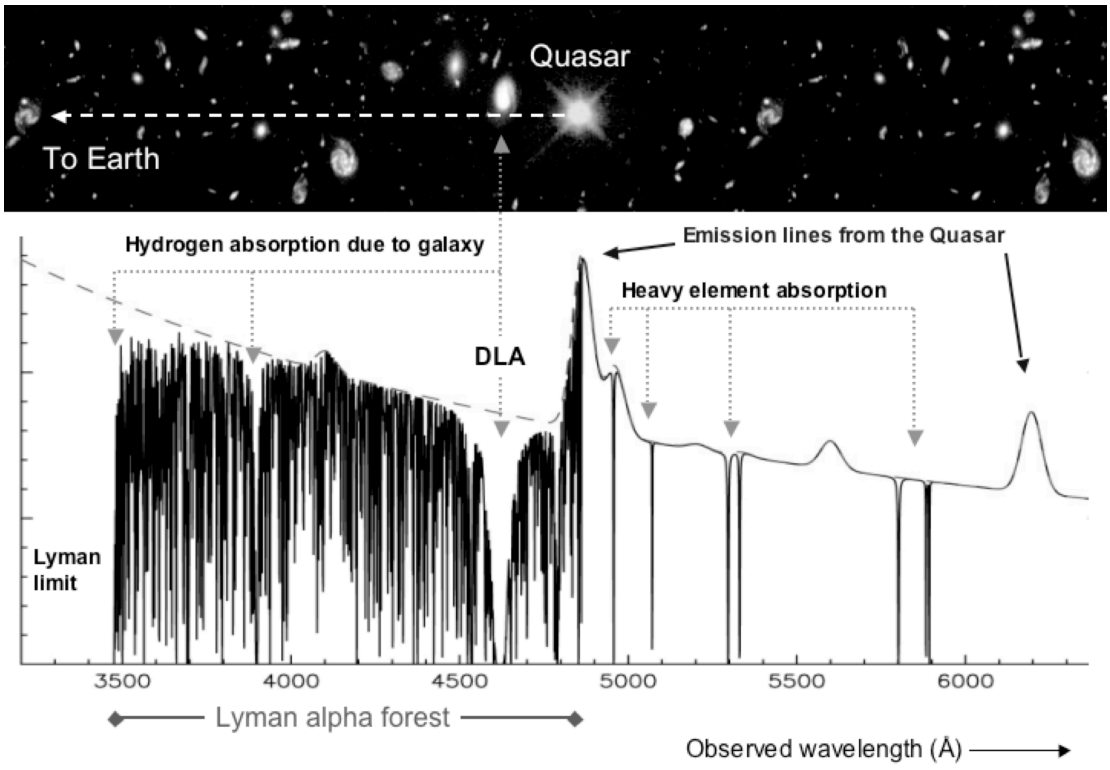

Figure 1.10: The spectrum of a quasar with an intervening DLA. Image courtesy of Dr. J. Webb.

QSOAL systems may be categorized in two ways. The first method involves determining the neutral hydrogen column density from the Lyα transition. Systems with N(H I) $< 10^{17}$ cm^{-2} are known as Lyman-α forest systems because their distribution is dense enough to appear forestlike in a spectrum (see Figure 1.10). Lyman limit systems have $10^{17} <$ N(H I) $< 10^{19}$ cm^{-2}. These systems have a high enough neutral hydrogen density that they may have a significant neutral fraction, but still have N(H II) $\gg$ N(H I). Sub-DLAs are a recent addition to the list of categories, with $10^{19} <$ N(H I) $< 2.0 \times 10^{20}$ cm^{-2} (e.g. Dessauges-Zavadsky et al. 2003). Finally, damped Lyman-α systems (DLAs), named for the visible damping wings in the voigt profile (see Figure 1.10), have N(H I) $> 2 \times 10^{20}$ cm^{-2}. Of these systems, DLAs have

a sufficient H I column density that their ISM is predominantly neutral (Wolfe et al. 2005), whilst sub-DLAs also have a significant neutral fraction (Dessauges-Zavadsky et al. 2003).

At low redshift, the detection of QSO absorption line systems through the Lyα line is considerably more difficult. At $z < 1.5$, the Lyα line is bluewards of 3000 Å, and thus effectively inaccessible to ground-based telescopes. Amongst the current generation of space telescopes, only the Far Ultraviolet Spectral Explorer (FUSE) has a working UV spectrometer, and FUSE will shortly be shut down.[3] The only UV spectrometers which might enter service in the near future are the Cosmic Origins Spectrograph (COS) and the Space Telescope Imaging Spectrometer (STIS), both instruments on the Hubble Space Telescope (HST). COS has yet to be installed (although the final HST servicing mission will attempt installation), and STIS is currently not functional (although, again, the final HST servicing mission will attempt to fix STIS if possible).

Table 1.1: Summary of absorption line systems

Type	log N(H I) (cm^{-2})	Redshift	Spectral Signature	Common Metals
Lyα Forest	< 17.5	$1.5 \leq z \leq 7.2$	Lyα	C IV
LLS	17.5—19	$1.5 \leq z \leq 7.2$	Lyman limit at 912 Å	C IV,Mg II
Sub-DLAs	19–20.3	$1.5 \leq z \leq 7.2$	Lyα damping wings	C IV,Mg II,Zn II,Fe II
DLAs	≥ 20.3	$1.5 \leq z \leq 7.2$	Lyα damping wings	C IV,Mg II,Zn II,Fe II
C IV	> 11	$0.95 \leq z \leq 5.4$	C IV	C IV
Weak Mg II	> 17	$0.07 \leq z \leq 2.6$	$EW_{Mg\ II,2796} \leq 0.3$ Å	C IV,Mg II
Strong Mg II	> 17	$0.07 \leq z \leq 2.6$	$EW_{Mg\ II,2796} > 0.3$ Å	C IV,Mg II,Zn II,Fe II
Ca II	$\gtrsim 20$	$0 \leq z \leq 1.5$	$EW_{Ca\ II,3934} > 0.2$ Å	C IV,Mg II,Zn II,Fe II,Ca II

NOTE Redshift indicates the redshift range over which the system can be detected in the optical (here $3000 - 10000$ Å). Spectral Signature indicates the key spectral feature marking such systems. N(H I) values allocated to metal line systems are approximate.

Given the current difficulties with detecting the Lyα line at low redshift, QSOAL systems may be detected through metal absorption lines found at longer wavelengths, forming the second naming convention for QSOALS. Metal lines used to identify

[3]Even were FUSE to continue in operation, its UV spectrograph covers a wavelength range of 905–1187 Å, unable to detect the Lyα line at any redshift.

absorbers include the C IV doublet at $\lambda\lambda$ 1548.1,1550.7 Å (Sargent et al. 1988), which is detected in all varieties of absorbers, from Lyα forest systems to DLAs. The Mg II doublet at $\lambda\lambda$ 2796.3,2803.5 Å (e.g. Steidel & Sargent 1992, Prochter et al. 2006, Narayanan et al. 2007) is detected only in Lyman limit systems, sub-DLAs, and DLAs. The Ca II doublet at $\lambda\lambda$ 3934.8,3969.6 Å (e.g. Boksenberg & Sargent 1978, Blades et al. 1981 Bowen 1991, Wild & Hewett 2005) has also been detected in quasar absorption systems, albeit much less frequently. In general, for low-redshift detections by metal lines, the absorber is named after the metal line detected, so absorbers might be referred to as C IV systems, Mg II systems, or Ca II systems. The diffuse band searches which form the core of this thesis were conducted towards DLAs and Ca II systems, so I will describe both types of absorber in greater detail in the remainder of this section.

1.3.1 Damped Lyman-α Systems

DLAs are unique amongst quasar absorption systems in that their hydrogen content is *predominantly* neutral (Wolfe et al. 2005), although sub-DLAs also seem to be mostly neutral (Dessauges-Zavadsky et al. 2003). The existence of a predominantly neutral medium is required in order for molecular hydrogen to form, and H_2, in turn, is required for star formation. Thus, because DLAs dominate the neutral gas content of the universe for $z < 5$, the neutral hydrogen in DLAs is likely the primary reservoir for star formation (Storrie-Lombardi & Wolfe 2000). I will begin by describing metal and dust content in DLAs, followed by the abundance of molecules, galaxies associated with DLA absorbers, and the prospects for detecting DIBs in DLAs.

Metals in DLAs

The critical source of information about the physical characteristics of DLAs is the metal lines which can be detected. Measuring the strength of these lines allows not only the chemical abundances to be determined, but also the dust to gas ratio,

inferences on the star formation history, and possibly even the star formation rate. Amongst the metals commonly observed are Fe, Si, S, O, Zn, and Cr. In determining chemical abundances, the elements most commonly used are Si, S, and Zn, although O is used when possible. S, O, and Zn have the advantage of being nonrefractory (i.e. they do not deplete significantly onto dust grains) (Prochaska et al. 2007). The O transitions, however, are frequently saturated, whilst the transitions of S are often lost within the Lyα forest. Prochaska et al. (2007) avoids the use of Zn where possible, due to its low abundance and to concerns about how closely it traces Fe, whilst other observers, including Pettini (2004), prefer the use of Zn as it is known to have a very low dust depletion (e.g. Pettini et al. 1990). The transitions of Si are also frequently used in order to determine metallicity, especially by observers who prefer to avoid the use of Zn (Prochaska et al. 2007).

Kulkarni et al. (2005) found a weak evolution of [Zn/H] with decreasing redshift, rising from [Zn/H] ~ -2 at $z \sim 3$ to [Zn/H] ~ -1 in their lowest redshift bin.[4] Meiring et al. (2006) found a similar result, also measuring [Zn/H], with metallicity falling short of solar by a factor of > 4 even at $z = 0$. Prochaska et al. (2003), using metallicities from S, Si, and Zn, found a slow evolution of metallicity with redshift, and a large scatter of metallicities at any given redshift, with the column-density weighted mean metallicity rising to [X/H] ~ -0.6 in the lowest redshift bin. Although the DLA population remains on average poor in metals, Khare et al. (2007) find that sub-DLAs are often more metal-rich than DLAs, finding a trend of decreasing metallicity with increasing N(H I) for N(H I) $> 10^{19}$ cm^{-2}. Overall, the average metallicity of DLAs remains sub-solar at all redshifts, as shown in Figure 1.11.

The relative abundance of various metals can also provide useful information on DLA characteristics. For example, the ratio of α-capture elements[5] to iron-peak

[4] [X/H] is the logarithmic metallicity relative to solar. So [Zn/H] = log(Zn/H) - log(Zn/H)$_\odot$

[5] α-capture elements include Si, S, C, O, Mg, Ca and Ti, and are synthesized through fusion

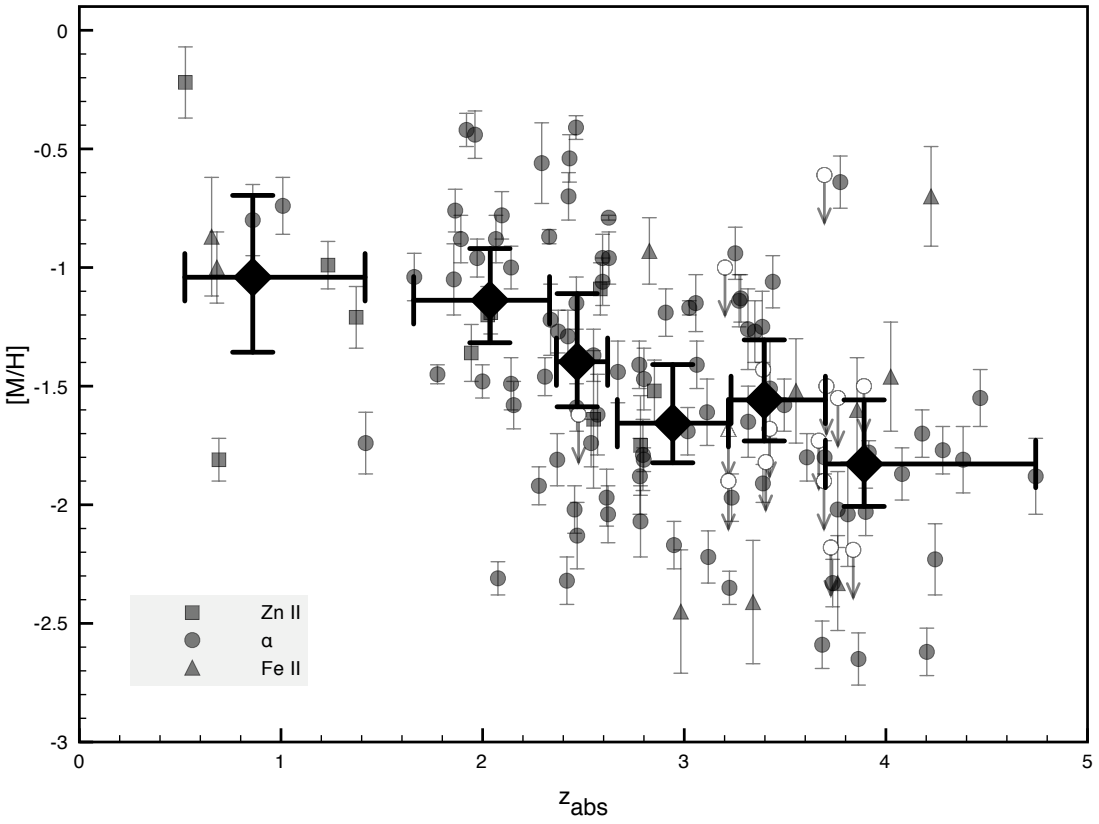

Figure 1.11: DLA metallicity vs. redshift. The large points represent unweighted mean metallicity, divided into six redshift bins (horizontal error bars indicate the bin sizes). The small points represent individual DLAs, with solid symbols showing detections and outlines upper limits. Data from Prochaska et al. (2003). Metallicities derived from Fe II, including upper limits, have been increased by +0.4 dex in order to compensate for dust depletion.

elements may be used as a tracer of star formation history. In the Milky Way, metal-poor stars are enhanced in α-capture elements relative to iron peak elements, with a systematic trend of decreasing [α/Fe] with increasing [Fe/H] (Edvardsson et al. 1993). In DLAs, measurements of [S/Zn][6] by Nissen et al. (2004) found that, while some DLAs had enhanced [S/Zn] ratios, others had solar, or even sub-solar ratios. Dessauges-Zavadsky et al. (2006) studied 11 DLAs at $1.8 < z < 2.5$, and found [α/Fe,Zn] enhancement in systems with low dust depletion, particularly in the

reactions involving the capture of an α particle (helium nucleus). For example, ${}^{12}_{6}\mathrm{C}+{}^{4}_{2}\mathrm{He}\rightarrow{}^{16}_{8}\mathrm{O}+\gamma$.

[6]Zn is used here instead of Fe because Fe is depleted onto dust, whilst [Zn/Fe] ~ 0 in Galactic stars (Nissen et al. 2004)

[Si/Fe] ratio. The [α/Fe] ratio provides information about the star-formation history (SFH) of the DLA, and in particular about time elapsed time since the last major burst of star formation. Most α-capture elements are produced in Type II supernovae (which occur a few Myr after star formation), while a significant fraction of Fe and other Fe-peak elements are produced in Type Ia supernovae, several Gyr after star formation (Edvardsson et al. 1993). Figure 1.12 shows α enhancement both in the Milky Way and in DLAs.

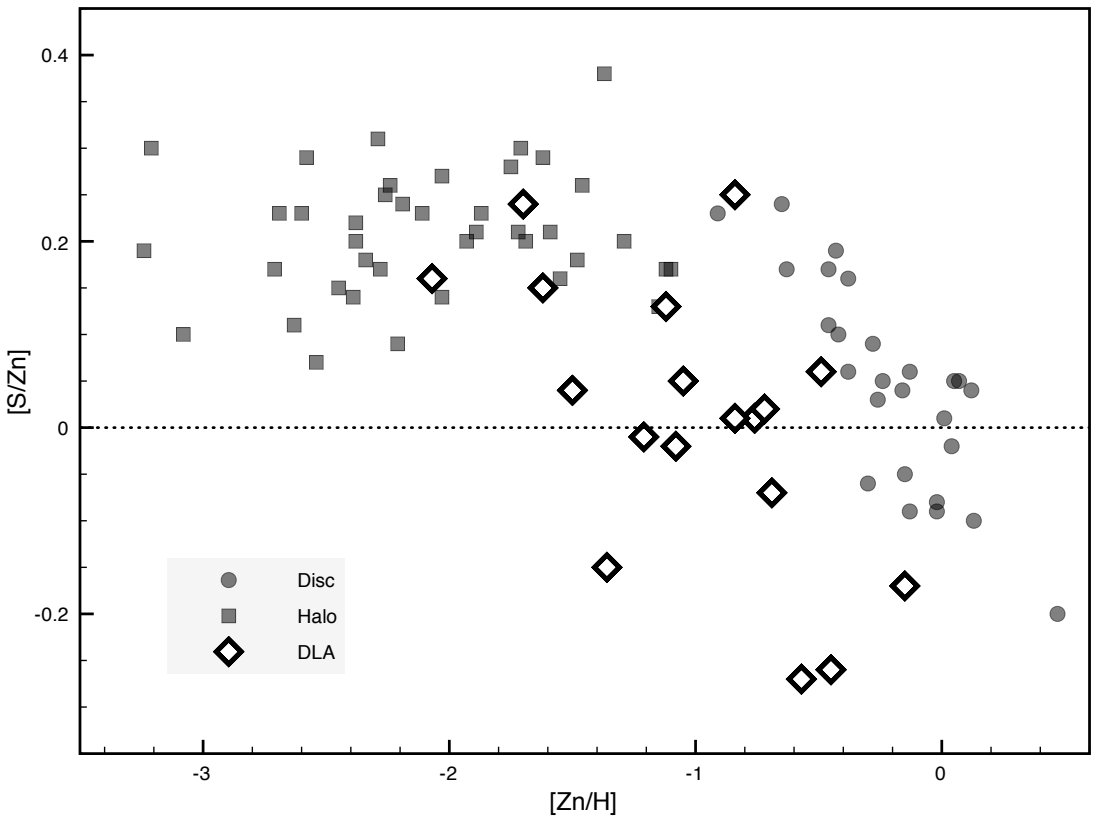

Figure 1.12: α enhancement in DLAs and the Milky Way. DLAs are taken from Nissen et al. (2004) and Nissen et al. (2007), disk stars from Chen et al. (2002), and halo stars from Nissen et al. (2007).

Other relative abundances may also provide information on the star formation history of a DLA. Henry et al. (2000) argue that nitrogen is formed primarily in intermediate-mass stars (between 4 and 8 $M_{\odot}$), with a characteristic delay of 0.25 Gyr

between the production of α elements and the primary production of nitrogen. Pettini et al. (2002) found evidence that 40% of DLAs had low [N/O] ratios, a much larger fraction than would be expected based on the time delay hypothesis. Dessauges-Zavadsky et al. (2006) found [N/Si] values ranging from [N/Si] $= -0.8$ to [N/Si] $= -1.5$, which is consistent with Centurión et al. (2003), who found a bimodal distribution of [N/α], with 75% of the 32 DLAs they examined having [N/α] $= -0.87$, and the remaining 25% having [N/α] $\simeq -1.5$ (compared to 40% in Pettini et al. 2002 above). Dessauges-Zavadsky et al. (2007), using the same DLA sample as Dessauges-Zavadsky et al. (2006), find that no single star formation history fits all of the DLAs in their sample. Instead, a combination of quiescent spiral galaxies, dwarf irregular starbursts, and dwarf irregular galaxies with continuous star formation are required for the systems they examined. Henry & Prochaska (2007), however, using published abundances of N, Si, S, and Fe for 30 DLAs, found that a continuous star formation model with only two parameters (star formation efficiency and the period of time over which evolution occurs) was able to reproduce the relative elemental abundances of these systems.

Another reason for non-solar relative abundances is the depletion of metals on to dust grains. Whilst S, O, and Zn are non-refractory, other metals including Fe and Cr are significantly depleted on to dust grains. Meiring et al. (2006) found that [Cr/Zn] and [Fe/Zn] decreased with increasing [Zn/H], implying that the dust to gas ratio (κ) increases with increasing metallicity.[7] Khare et al. (2007) find that DLAs in general have a low dust fraction, with sub-DLAs having not only a higher metallicity, but also a higher κ. Although metal lines are the most straightforward way of determining the dust fraction in DLAs, determining κ is dependent on knowing the intrinsic abundance ratios of the metals used, which in turn is dependent on the star formation history of the DLA (Wolfe et al. 2005).

[7] $\kappa = 10^{[\mathrm{Y/H}]_{\mathrm{intrinsic}}}(10^{[\mathrm{X/Y}]_{\mathrm{intrinsic}}} - 10^{[\mathrm{X/Y}]_{\mathrm{gas}}})$.

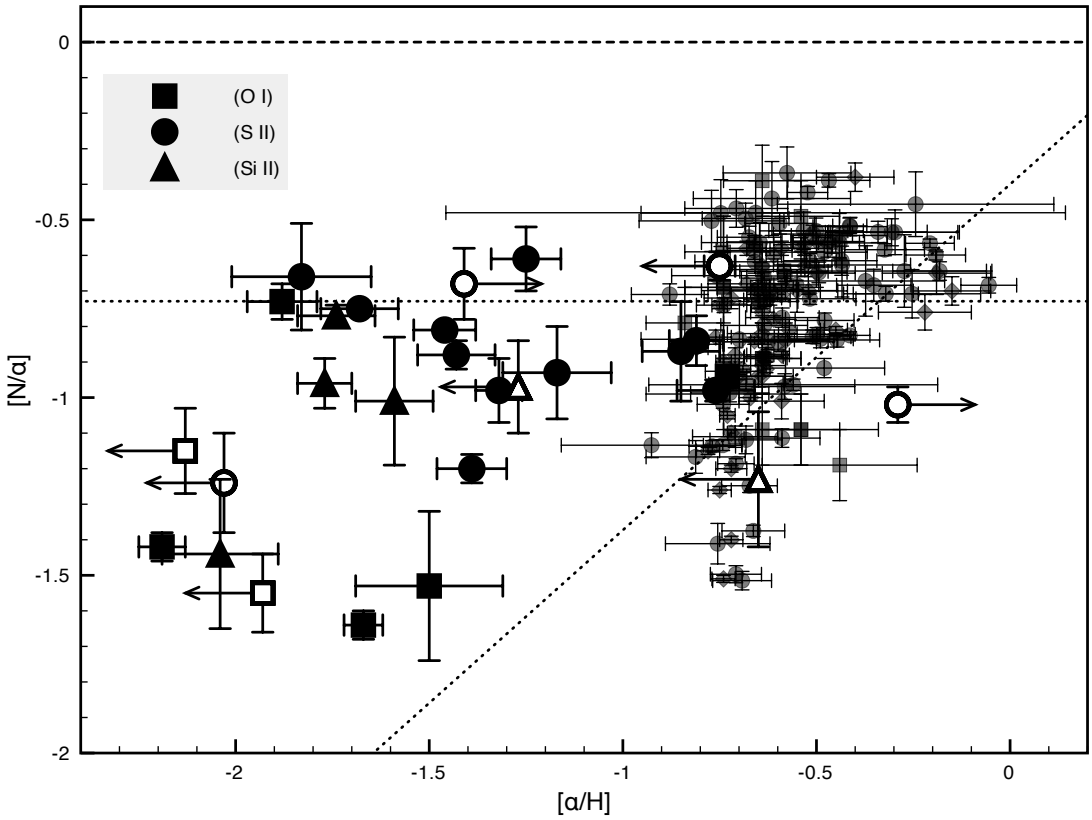

Figure 1.13: N/α Ratios in DLAs. Small symbols are from blue compact dwarf (BCD) galaxies, with diamonds from Izotov & Thuan (1999), circles from Kobulnicky & Skillman (1996), and squares from van Zee et al. (1996) and van Zee et al. (1997). Large symbols show DLAs collected in Centurión et al. (2003). The dashed line shows the solar [N/α] ratio, whilst dotted lines show the mean BCD value for primary production (horizontal) and the the secondary production (sloped) (Centurión et al. 2003).

Dust in DLAs

In addition to measuring the dust fraction via depletion of metals, other methods exist for measuring the dust content in DLAs. Cardelli et al. (1989) parameterized the extinction curve of the Milky Way based on the parameter $\zeta(\lambda) = A_\lambda/A_V$, which allows (Galactic) extinction to be computed along sightlines where the ratio of the absolute extinction at any wavelength (A_λ) to the absolute extinction in the Visible

(A_V) is known.[8] Pei (1992) also parameterized the Galactic extinction curve, as well as providing extinction curves for the LMC and SMC (see Figure 1.14). Because these three extinction curves are the only ones which have been well-characterized, the extinction curves of DLAs are modelled after one of these three (Ellison et al. 2005a). If the underlying shape of the extinction curve is known (i.e. if it is known whether an LMC-type curve, an SMC-type curve, or an MW-type curve is appropriate), and the intrinsic QSO spectral energy distribution (SED) is known, then measuring the relative colours of a QSO can determine the amount of reddening of its associated absorber. For DLAs, Khare et al. (2005) find no evidence of the 2175 Å absorption feature, and a generally SMC-like extinction curve in QSO absorbers found in the SDSS. Because different quasar spectra may vary considerably from one another, measuring the extinction curve directly is a difficult process. For both direct and colour-based measurements, combining multiple spectra to measure the average colour difference is a more straightforward process.

Determining the dust content of DLAs has two primary motivations. The first is that DLAs have been described as the reservoirs for star formation (Wolfe et al. 2005), but star formation requires not only neutral hydrogen, but molecular hydrogen (H_2). Because H_2 is thought to form primarily on the surface of dust grains (e.g. Hollenbach & Salpeter 1971; Perets et al. 2005), the dust content of DLAs may serve to limit their $N(H_2)$. The other motivation is that DLAs with significant dust may both redden and extinguish their background QSOs such that the QSOs are not included in optically-selected surveys (e.g. Heisler & Ostriker 1988). Pei et al. (1991) found that quasars with foreground absorbers were significantly redder than those without, concluding that up to 70% of bright QSOs will be missed by flux-limited surveys (Fall & Pei 1993). If such a large fraction of DLAs were missed, including the systems

[8] In measuring dust extinction, several parameters are used. These include reddening [$E(B-V) = A_B - A_V$], two-colour normalization [$E(\lambda - V)/E(B-V)$], and total-to-selective extinction $R_V = A_V/E(B-V)$]. If the underlying extinction curve is known, then any of these may be derived from the others.

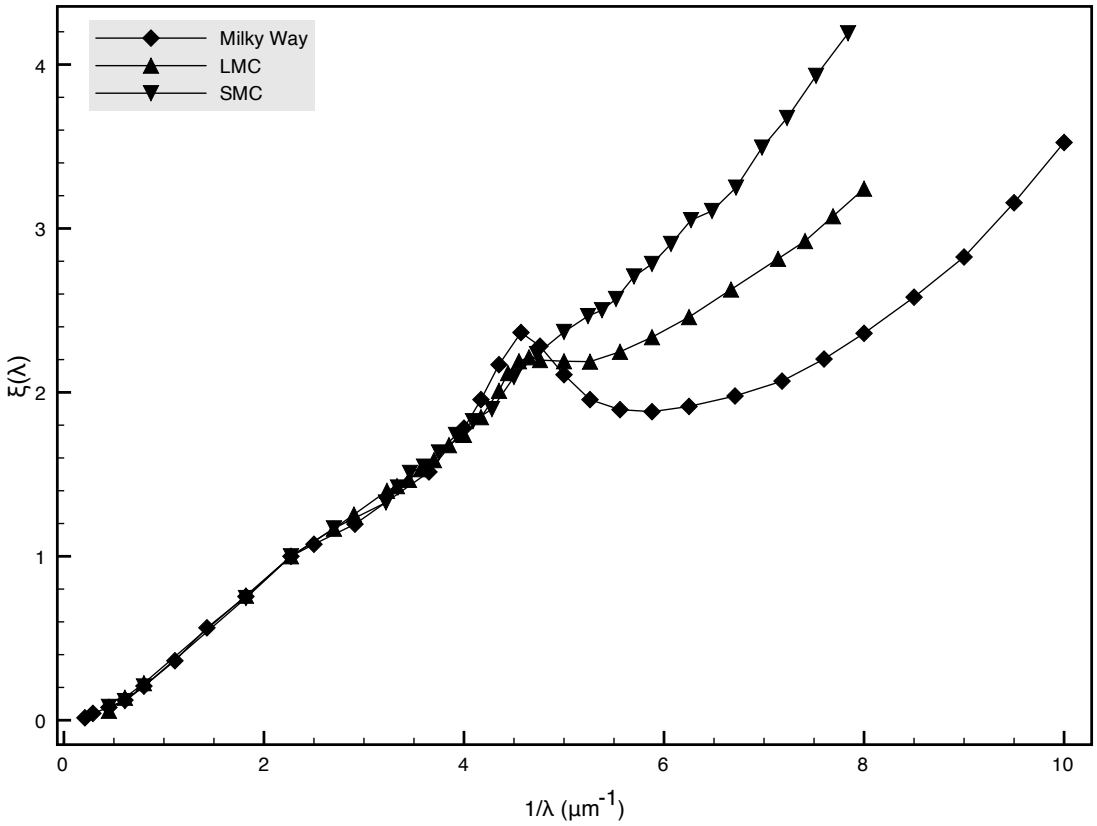

Figure 1.14: Galactic, LMC, and SMC extinction curves, derived from the empirical curves presented in Pei (1992). $\xi(\lambda) = [E(\lambda - V)/E(B - V) + R_V]/(1 + R_V)$.

with the highest dust content, the use of DLAs to determine the characteristics of the ISM at high redshift would be significantly biased.

Ellison et al. (2001) conducted the Complete Optical and Radio Absorption Line System (CORALS) survey in order to test this possibility by studying a group of quasars selected through their radio emission rather than optically.[9] Ellison et al. (2001) selected 66 QSOs from radio emission, found the optical counterpart to each quasar, and obtained spectra which resulted in the detection of DLAs at $1.8 < z_{abs} < 3.5$ towards 14 of the quasars surveyed. They found that both the number density per unit redshift, $n_{DLA}(z)$ and the neutral gas mass, Ω_{DLA} of the systems

[9]Because the effects of dust increase at short wavelengths, even extremely dusty systems would not be noticeably extinguished at radio wavelengths

they detected were consistent with those found from optical surveys. Ellison et al. (2005a) then obtained B and K-band images of the QSOs, and determined that the QSOs with foreground absorbers were not significantly different in colour from those with no DLAs, and finding that the DLAs in their sample had $E(B-V) < 0.04$ assuming an SMC-like extinction curve. Akerman et al. (2005) found that the Zn II abundances in the CORALS DLAs ($\langle[\mathrm{Zn/H}]\rangle = -0.88 \pm 0.21$) were not significantly higher than the abundances of a control sample ($\langle[\mathrm{Zn/H}]\rangle = -1.09 \pm 0.10$). These results are consistent with the results for optically-selected QSOs, including Murphy & Liske (2004), who found $E(B-V) < 0.02$ at $z \sim 3$ for 70 DLAs selected from the SDSS, and Vladilo et al. (2008), who found $E(r-z) = 0.0027 \pm 0.0009$ and $E(g-z) = 0.0054 \pm 0.0012$ from a sample of 248 DLAs with $2.2 < z_{abs} < 3.5$ selected from the SDSS. DLAs, then appear to be genuinely dust-poor systems in general.

Despite the general lack of dust in DLAs, at least one absorber has been detected with significant dust content. Junkkarinen et al. (2004) were able to determine that the $z = 0.524$ DLA towards AO 0235+164 has $E(B-V) = 0.23$ through extracting its extinction curve from the underlying QSO spectrum. Junkkarinen et al. (2004) found that the DLA had a pronounced 2175 Å bump in its extinction curve, making the Milky Way extinction curve the best fit for the absorber. Kulkarni et al. (2007) also detected a 9.7 μm absorption feature characteristic of silicate dust in this DLA, indicating that it is indeed a dust-rich system. Such systems, however, must form only a small fraction of the total DLA population.

Molecules in DLAs

DLAs are lacking not only in metals and dust, but also in molecules. H_2 is the most common molecule in the universe, and a prerequisite for star formation. Noterdaeme et al. (2008), for example, detect H_2 in less than 20% of DLAs (13 of 77) at $1.8 < z < 4.2$, significantly lower than the Milky Way detection rate ($\sim$ 85% Savage et al. 1977), but comparable to detection rates in the Magellanic Clouds ($\sim$ 50% for the

LMC Tumlinson et al. 2002). Noterdaeme et al. (2008) further found that DLAs with high metallicity or κ values were considerably more likely to have detectable H_2, and to have larger f_{H_2}.[10]. Systems with [X/H] ≥ -1.3 had a 35% chance to have $\log f_{H_2} > -4.5$ (compared to 4% of the systems with [X/H] < -1.3), and all H_2 detections were in systems where the column density of Fe depleted onto dust grains was larger than 5×10^{14} cm^{-2} (and 40% of those systems had detectable H_2). The f_{H_2} values detected were also consistent with LMC and SMC sightlines. Srianand et al. (2008), however, report finding a DLA at $z_{abs} = 2.41837$ with $f_{H_2} = 0.27^{+0.10}_{-0.08}$, the first DLA with such a high molecular fraction. Figure 1.15 shows the comparison between DLAs and Galactic, LMC, and SMC searches for H_2.

In addition to H_2, DLAs have been searched for other molecules. Curran et al. (2004), for example, searched 25 DLAs for CO and HCO^+ with no detections. They established that N(CO) $\lesssim 10^{-7}$N(H I), and N(HCO^+) $\lesssim 10^{-9}$N(H I). Curran et al. (2006) searched for OH in 16 targets, achieving a single tentative detection. Although the systems investigated by Curran et al. (2006) are QSOs and radio galaxies (rather than DLAs), it does provide an indication of the difficulty involved. Srianand et al. (2008), however, were able to detect both HD and CO in the same DLA where they found $f_{H_2} = 0.27$ (discussed above), making this the first DLA with known CO absorption.

Summary

DLAs, as described thus far, are metal-poor, dust-poor systems with low molecular abundance. In terms of local galaxies, this matches the LMC and SMC far better than the Milky Way. DLAs have sub-solar metallicities (e.g. Prochaska et al. 2003), which compare with metallicities of 1/3–1/2 and 1/10–1/5 solar in the LMC and SMC respectively (Welty et al. 2006). DLA extinction curves on average resemble the SMC extinction curve (Khare et al. 2005), whilst their molecular fractions also

[10] $f_{H_2} = 2N(H_2)/(2N(H_2) + N(HI))$

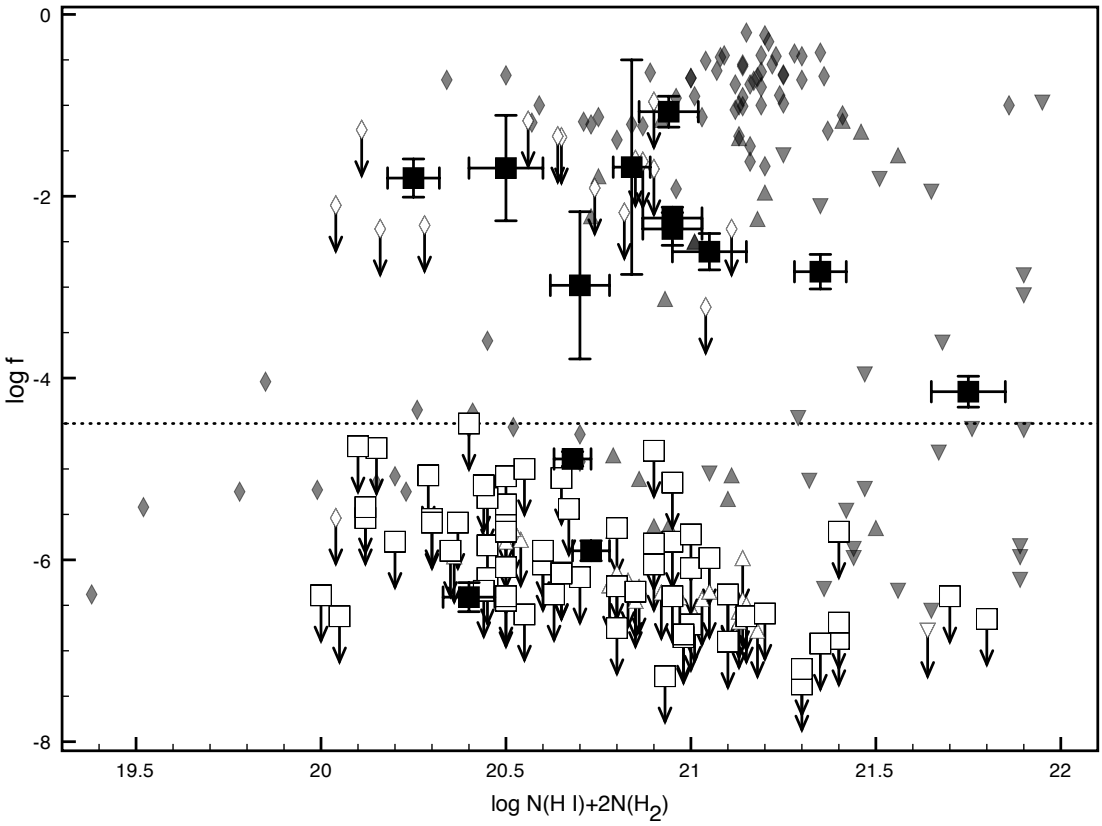

Figure 1.15: f_{H_2} for DLAs vs. the Milky Way, LMC, and SMC. Squares represent DLAs (Noterdaeme et al. 2008), diamonds MW sightlines (Savage et al. 1977), upwards pointing triangles LMC sightlines (Tumlinson et al. 2002), and downwards pointing triangles SMC sightlines (Tumlinson et al. 2002). Filled symbols show detections and open symbols upper limits.

resemble the Magellanic Clouds (Noterdaeme et al. 2008). At low redshift, it is possible to identify the galaxies associated with DLA absorbers, and several surveys have done just that (e.g. Chen et al. 2005, Rao et al. 2003, Chen & Lanzetta 2003, Le Brun et al. 1997). The results include a mix of spiral galaxies, dwarf galaxies, and low surface brightness (LSB) galaxies. Le Brun et al. (1997) found three spiral galaxies, three compact objects, and two LSB galaxies, including three sightlines with apparent galaxy groups associated with the DLA. Chen & Lanzetta (2003) found six disks, one lenticular, one LSB, five compact, and two irregular galaxies, with overall galaxy statistics of 45% disk-dominated, 22% bulge-dominated, 11%

irregular, and 22% galaxy groups. Rao et al. (2003) found their sample dominated by low-luminosity dwarfs close to the QSO sightlines. At $z_{abs} > 1.6$, Møller et al. (2002) found that three galaxies corresponding to high-redshift DLAs fell within the range of parameters of Lyman Break Galaxies (LBGs). More recently, Christensen et al. (2007) used integral field spectroscopy to search for Lyα emission at the redshift of known DLAs, finding six candidates and confirming two previous detections. They found that the characteristics of their candidates were also consistent with LBGs.

1.3.2 Ca II Systems

Although C IV is frequently detected towards QSOAL systems, and Mg II is effectively always detected towards Lyman limit systems, sub-DLAs, and DLAs, Ca II is detected in only a small fraction of QSO absorbers (Bowen 1991). Wild & Hewett (2005) note that Ca II is heavily depleted onto dust, and that the presence of significant Ca II in the gas phase thus implies either a high abundance of Ca II (so that it can be detected despite heavy depletion), or a lack of dust. Wild & Hewett (2005) further find that the Ca II systems in their sample have an average $E(B-V) = 0.06$, whilst a subset of their sample with $EW_{Ca\ II,K} > 0.7$ Å has average $E(B-V) = 0.099$. This increase of $E(B-V)$ with increasing $EW_{Ca\ II}$, and generally larger $E(B-V)$ than inferred for DLAs, implies that the Ca II systems are more likely to be a calcium-rich population with relatively high dust depletion than a population of dust-poor systems with little depletion. The strength of the metal lines detected in Ca II systems also implies that they are metal-rich.

Because the Lyα transition of the Ca II systems found in Wild & Hewett (2005) is not within the spectral range of the SDSS spectra, other methods must be used to estimate N(H I) for these systems. In addition to the Ca II lines, other absorption lines were also detected, including Mg II, Mg I, and Fe II. Rao et al. (2006) found that 42% of absorbers in which $EW_{Mg\ II,\lambda2796}/EW_{Fe\ II,\lambda2600} < 2$ and $EW_{Mg\ I,\lambda2853} > 0.1$ Å were DLAs, whilst $\sim 80\%$ of systems which instead have $EW_{Mg\ I,\lambda2853} > 0.8$ Å are

DLAs. Of the 31 Ca II systems in Wild & Hewett (2005), 30 meet the first set of criteria, and 20 of those also meet the second set. It is thus likely that a majority of these systems are DLAs. Because the Ca II systems appear to have high metallicity, as well as greater reddening than most DLAs (Vladilo et al. 2008), and because they appear to be DLAs, it is likely that they form a metal- and dust-rich subset of the DLA population. Ca II systems also have a number density only 20–30% as high as the number density of DLAs, even taking into account potential DLAs missed by the SDSS due to their high dust extinction (see §1.3.1).

Early detections of Ca II absorption in QSO spectra involved absorbing galaxies such as NGC 3067 (Boksenberg & Sargent 1978), a luminous starburst galaxy with star formation rate 1.4 $M_\odot$ yr^{-1}. Bowen (1991) found Ca II absorption along six sightlines, which were identified with both bright foreground galaxies and material disturbed from foreground galaxies though interactions with other galaxies. More recently, Zych et al. (2007) used SDSS images of quasars with known Ca II absorbers to identify the galaxies associated with the Ca II systems. For those systems where the galaxies could be identified, they selected absorbers whose SDSS spectra showed $EW_{Ca\ II,3934} \geq 0.2$ Å, along with confirmed Mg II absorption (if in the spectral range) or Na I absorption (if the Mg II lines were not observable). The sample was further restricted to $z_{abs} < 0.5$ to ensure that the Hα emission line remained in the optical, and to simplify the process of detecting the host galaxy from SDSS imaging. The candidate spectra were then inspected visually and unconvincing spectra discarded. Then, because most of the identified galaxies did not have SDSS spectra, the VLT was used to obtain spectra of four of the associated galaxies. One other Ca II system had an SDSS spectrum of its associated galaxy, and this galaxy spectrum was also studied. Four out of five of these galaxies proved to be bright ($L \simeq L^*$), massive ($\sigma_v \simeq 100$ km s^{-1}), metal-rich ($Z \simeq Z_\odot$) spiral galaxies, with star formation rates in the range $0.3 < \mathrm{SFR} < 30$ $M_\odot$ yr^{-1} (Zych et al. 2007), which is large compared to the

median star formation rate for local galaxies from the Nearby Field Galaxy Survey (NFGS), $\mathrm{SFR}_{median} = 0.5$ $\mathrm{M}_{\odot}$ yr^{-1} (Kewley et al. 2002). Three of the systems have measured $E(B-V) = 0.211$, 0.55 and 0.49, with $E(B-V)$ estimated from the Balmer decrement. In all cases, the low impact parameters mean that the Ca II systems are extremely likely to be DLAs. While this small sample of bright associated galaxies may not be typical of Ca II systems in general, it certainly implies that Ca II-selected systems can be dusty and metal-rich.

1.3.3 Summary

Quasar absorption systems offer the chance to inspect the interstellar medium of distant galaxies directly, even at high redshift. As such, QSO absorbers are the most promising systems for the detection of diffuse bands at cosmological redshifts. With respect to DLAs, the low average $E(B-V)$ and metallicity suggest that diffuse bands may be difficult to find, but the relationship between N(H I) and the 5780 Å DIB suggests otherwise. The low H_2 abundances should not affect the DIB strength, because the DIBs do not appear to correlate with H_2. While DLAs include a wide variety of host galaxies, DIBs have been detected in many different galaxies including dwarf, irregular, and starburst. The 5780 and 6284 Å DIBs, in particular, are thought to be associated with the outer regions of interstellar gas clouds (and thus the warm neutral medium), which again should be common in DLAs (see e.g. Kanekar & Chengalur 2003 or §3.2 for a description of the neutral medium in our sample). In order to quantitatively assess the feasibility of detecting DIBs in DLAs, we have calculated the expected equivalent width of the 5780 Å DIB as a function of N(H I) based on the Galactic relation. Figure 1.16 shows this relation, as well as the detection limits for a variety of exposure times with a typical 8-m telescope. I have assumed a QSO with $M_V = 18$, and $z_{em} = 1$, with a $z_{abs} = 0.25$ foreground DLA. At this redshift, the observed $FWHM_{5780} = 2.64$ Å (based on the DIB towards stellar target HD 204827 Hobbs et al. 2008), and the detection limits were calculated based on the Very Large

Telescope (VLT) FOcal Reducer and low dispersion Spectrograph 2 (FORS2) 600RI grism, with a resolution of $\lambda/\Delta\lambda = 1000$ at 6780 Å assuming a 1.″0 slit. The detection of the 4428 Å DIB towards AO 0235+164 by Junkkarinen et al. (2004) also serves as a proof of concept.

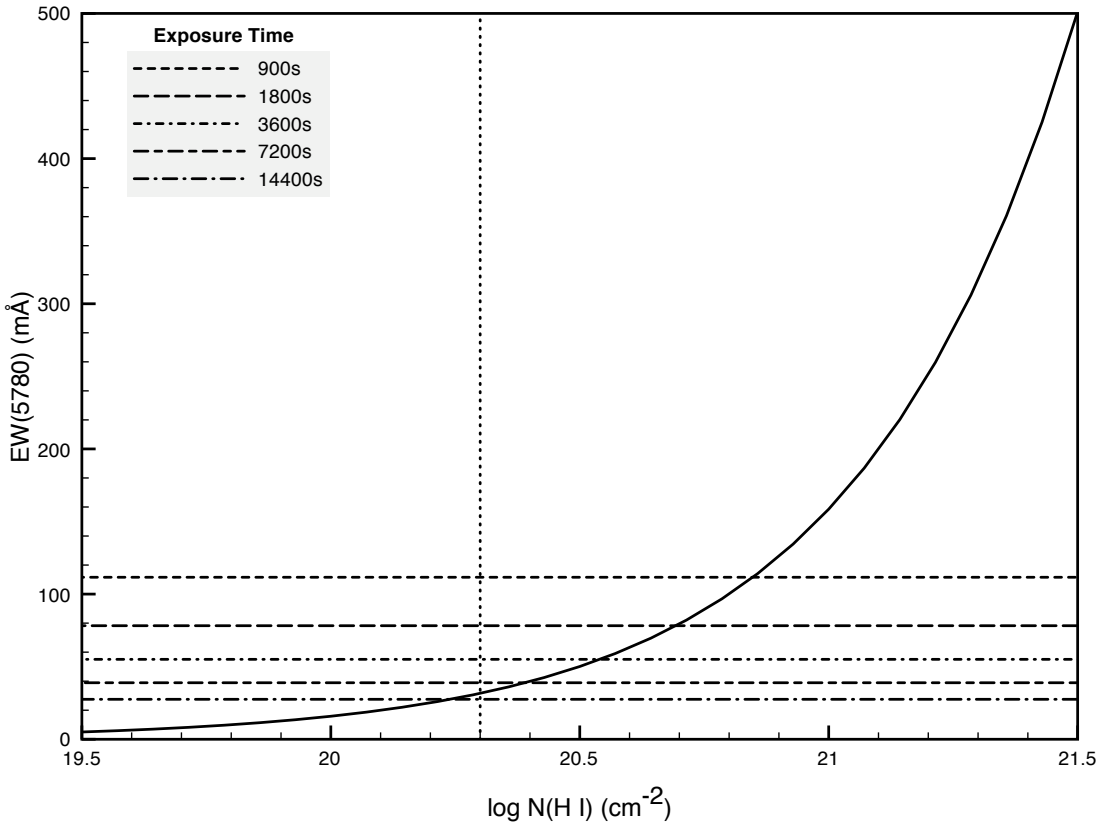

Figure 1.16: Expected equivalent widths and detection limits for the 5780 Ådiffuse band in DLAs. The horizontal lines represent detection limits for the given observing times, assuming an $M_V = 18$, $z_{em} = 1$ QSO with a $z = 0.25$ absorber, and assuming the use of the VLT, with FORS2 and the 600RI grism and a 1.″0 slit. The vertical dotted line shows N(H I) $= 2.0 \times 10^{20}$ cm^{-2}, the dividing line beyond which systems are considered DLAs. The solid curved line shows EW_{5780} as a function of log N(H I).

The prospects for detecting diffuse bands in Ca II systems appear even better than for DLAs, especially given the high $E(B-V)$ detected in Ca II systems thus far. Because the reddening appears to increase with $EW_{Ca\ II,K}$, the selection of Ca II systems with strong Ca II absorption will likely be the most important characteristic to

select. Figure 1.17 shows the estimated exposure times required to detect the 5780 Å DIB towards a Ca II system based on its $E(B-V)$, using the same assumptions as Figure 1.16. As shown in Figure 1.17, detecting DIBs towards a Ca II system should take approximately the same exposure time as detecting DIBs towards a DLA. These quick tests show that diffuse interstellar bands could be detected with integrations of a few thousands of seconds.

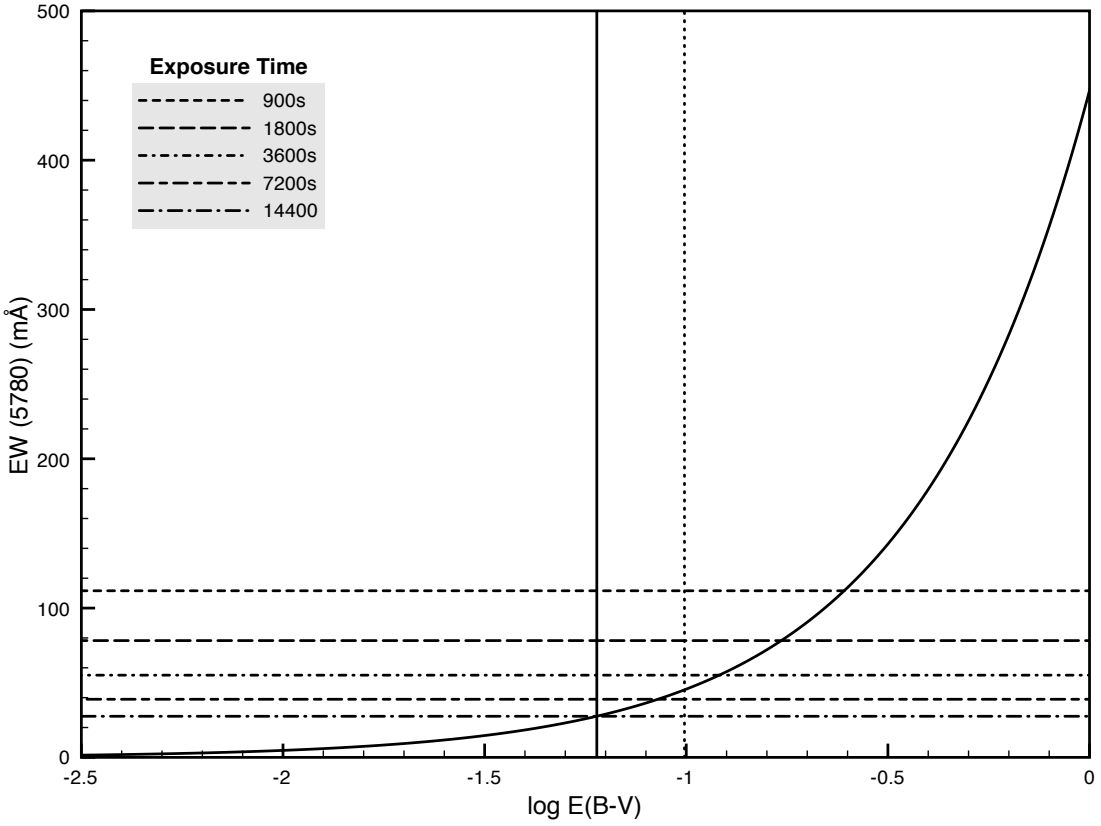

Figure 1.17: Expected equivalent widths and detection limits for the 5780 Ådiffuse band in Ca II systems. The horizontal lines represent detection limits for the given observing times, assuming an $M_V = 18$, $z_{em} = 1$ QSO with a $z = 0.25$ absorber, and assuming the use of the VLT, with FORS2 and the 600RI grism and a $1\farcs0$ slit. The solid vertical line shows $E(B-V) = 0.06$, the average value for Ca II systems in Wild & Hewett (2005), whilst the dotted vertical line shows $E(B-V) = 0.099$, the average value for Ca II systems with $EW_{Ca\ II,K} > 0.7$ Å. The solid curved line shows EW_{5780} as a function of log $E(B-V)$.

1.4 Motivations of the search for DIBs in QSO Absorption Systems

The search for diffuse bands has a variety of motivations. I will begin by discussing the prospect for learning more about the diffuse bands by observing them in QSO absorption systems, followed by the potential to learn more about the absorption systems themselves, and conclude with a discussion of the prospects for using diffuse interstellar bands to estimate the N(H I) of low-redshift quasar absorbers.

1.4.1 The potential to learn about DIBs

Identifying correlations amongst the DIBs, and especially spectral families, has proved to be a difficult task, especially due to the need to separate out correlations due to carrier from correlations due to environment (Wszołek & Wszołek 2003). Quasar absorbers, because they offer an entirely different environment (at an entirely different stage of evolution) from the Local Group of galaxies, offer a chance to test the correlations which have been observed locally. Correlations which are not observed in quasar absorbers are likely to occur as a result of local environment, whilst any correlations which hold even in quasar absorbers may indicate actual spectroscopic families, and should thus be examined more closely. In addition, if the DIBs are indeed large ionized molecules (Cami et al. 1997), the relative strengths of the DIBs in DLAs may allow a further determination of the ionization potential of some diffuse bands. Finally, the relative chemical abundances in DLAs may constrain the DIB carrier, especially those carrier models which include elements (e.g. nitrogen Hudgins et al. 2005) which are often underabundant in DLAs (Dessauges-Zavadsky et al. 2006).

1.4.2 The potential to learn about QSO absorbers

Molecules of any sort have rarely been detected in QSOs (see §1.3.1). Since the leading DIB carrier candidates are all organic molecules, the presence of DIBs in quasar absorbers would strongly suggest the presence of organic molecules even at cosmological redshifts. Furthermore, PAHs (in particular) are considered an important early constituent of organic compounds on Earth (Bada & Lazcano 2002), so the presence of PAHs in quasar absorbers (assuming of course that at least some DIBs are caused by PAHs) could have implications for astrobiology. Given the existing detections of PAHs at cosmological redshifts (Teplitz et al. 2007) quasar absorbers may be likely to also have PAHs in their ISM. Finally, given the already noted environmental dependence of the diffuse bands, if the relative strengths of the DIBs in an absorber matched the relative strengths in a Galactic sight-line, it would imply that the environmental conditions in that absorber resembled those found on the local sight-line, providing an important clue to the physical conditions inside quasar absorbers. Finally, $E(B-V)$ can be difficult to determine directly for QSO absorbers (see §1.3.1), so the detection of diffuse bands known to correlate with $E(B-V)$ may provide a method to more easily derive reddening for individual absorbers.

1.4.3 The potential to identify low-redshift DLAs

At low redshift, determining the N(H I) of a quasar absorber would require either UV spectroscopy on large ($>$ 2m) space telescopes (currently unavailable), or the identification of some other substance whose correlation with N(H I) is strong enough to allow the neutral hydrogen column to be derived indirectly. Given the relationship found by Herbig (1993), the 5780 Å DIB might be able to serve that purpose, should the relationship be shown to hold in known DLAs. Even if the relationship does not hold completely, the presence of the 5780 Å DIB may still be useful in deriving a limit to N(H I), or an approximate value. Finally, the presence of diffuse bands may prove

to be much like the presence of Ca II absorption – able to select a subset of DLAs which are particularly rich in dust and metals, and which in turn may represent the progenitors of galaxies like the Milky Way.

1.5 Thesis Plan

In Chapter 2, I will describe the target selection, observations, and data reduction methods used. Next, in Chapter 3, I describe a search for diffuse bands in DLAs, and present the first detection of narrow DIBs at $z > 0$. In Chapter 4, I describe a search for DIBs in Ca II systems, including the detection of the 5780 Å DIB in one system. Finally, in Chapter 5 I will summarize my results and suggest some future directions in the search for diffuse bands at $z > 0$.

Chapter 2

Methods of Data Acquisition and Reduction

2.1 Introduction

All observations made during the DIB search involved longslit spectroscopy of single targets. Data reductions were carried out using standard IRAF routines[1] except as otherwise noted. For a brief description of a standard IRAF data reduction procedure, including examples, see "A Beginner's Guide to Using IRAF", "A User's Guide to CCD Reductions with *IRAF*", and "A User's Guide to Reducing Slit Spectra with *IRAF*", all available from `http://iraf.noao.edu/docs/spectra.html`.

This chapter will begin with a description of the observations (§2.2), describing the general strategy followed by the details for each individual telescope. Data reduction and analysis methods are described in §2.3.

2.2 Observing Strategy

The first project described here is an attempt to detect diffuse interstellar bands in damped lyman-α systems (see Chapter 3 for science results), while the second

[1]IRAF is distributed by the National Optical Astronomy Observatories, which are operated by the Association of Universities for Research in Astronomy, Inc., under cooperative agreement with the National Science Foundation.

Table 2.1: Diffuse bands of interest

DIB Name	λ_{air} (Å)	λ_{vac} (Å)	FWHM (Å)	EW (mÅ)
4428	4428.19	4429.43	22.5	1221 ± 40
5705	5705.08	5706.66	2.58	42 ± 4
5780	5780.48	5782.08	2.11	257 ± 3
5797	5797.06	5798.67	0.77	199 ± 1
6284	6283.84	6285.78	4.77	460 ± 7
6613	6613.62	6615.45	0.93	165 ± 1

NOTE DIB characteristics from Hobbs et al. (2008), as measured towards HD 204827.

involved a similar search in quasar absorption systems selected for strong Ca II absorption (see Chapter 4 for science results). In order to cover as many strong DIBs as possible, the observations were designed to ensure that the DIBs of interest were not redshifted into areas of the spectrum not suited for observation. Figure 2.1 shows the wavelength at which the various DIBs of interest appear as a function of redshift, and also shows those regions of the spectrum suitable for ground-based observations (i.e. the parts of the spectrum not containing strong sky lines or telluric absorption). Table 2.1 lists the characteristics of these DIBs.

The DLA targets were selected from the literature primarily on the basis of N(H I), with high column densities preferred. Brighter QSOs were preferred over faint QSOs in order to achieve high SNRs with modest exposure times. Finally, potential candidates where the candidate DIBs could not be observed due to absorber redshift were removed from the target list (see Figure 2.1). Table 2.2 lists our trial sample of DLAs.

In the DLA search, where the N(H I) of the absorbers are known, the observations were intended to detect the DIBs at a strength of 1/3 of the strength that would be expected given the Galactic relationship between the EW of the 5780 Å DIB and the N(H I) of the sight-line (or 1/3 of the value shown in Figure 1.16). The expected

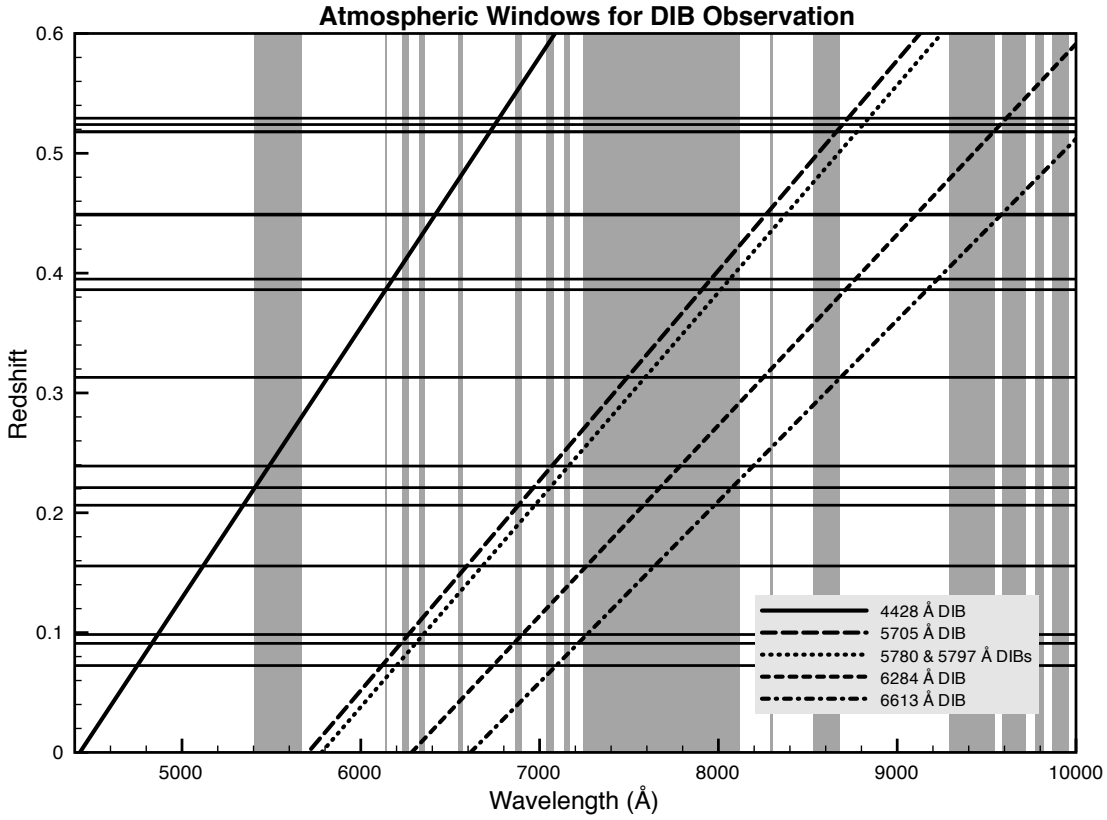

Figure 2.1: This plot shows DIB wavelengths as a function of redshift. The dark vertical bands show parts of the night sky where strong features would make the detection of any DIBs either difficult or impossible. The horizontal lines show the redshifts of the target systems (note that some systems were close enough in redshift to overlap in this diagram). See Table 2.2 and Table 2.3 for target information.

equivalent width of the DIB was calculated from the relation

$$\log(EW(\text{mÅ})) = \log(N(\text{H I})) - 18.8 \tag{2.1}$$

based on the data in Herbig (1993).[2] The weakest EW which can be detected in an

[2]Note that, in the remainder of this thesis, the relationship will be given as $\log(EW(\text{mÅ})) = 1.64\log(N(\text{H I})) - 32.31$ (Welty et al. 2006). While this value provides an improved fit, it was not yet available when these observations were being planned.

observation is given by

$$EW(\text{Å}) = \frac{N \times D(\text{Å}) \times \sqrt{\text{npix}}}{SNR \times (1+z)} \tag{2.2}$$

where EW is the smallest rest equivalent width which can be detected, N the desired detection threshold in units of the standard deviation (the default for this thesis is 5-σ, so $N = 5$), D the dispersion of the instrument (Å pix^{-1}), npix the number of pixels over which the DIB feature is spread (because the DIBs are broad absorption lines, npix will depend not only on the instrumental resolution, but also on whether the chosen instrument was capable of resolving the DIB in question), SNR the signal-to-noise ratio per pixel of the observations, and z the redshift of the DLA. Table 2.2 shows these values for the DLAs sample presented here.

Table 2.2: Predicted EW for DLAs

System	z_{abs}	log(N(H I)) log(cm^{-2})	$EW_{5780,1/3\ Galactic}$ (mÅ)	Target $SNR_{5\sigma}$ (pix^{-1})	Refs
AO 0235+164	0.524	21.70	265	32	1
Q 0738+313[1]	0.091	21.18	80	149	2
	0.221	20.90	42	253	2
B2 0827+243[2]	0.525	20.30	11	774	3
PKS 0952+179	0.239	21.32	110	95	3
PKS 1127−145[3]	0.313	21.71	271	37	4
Q 1229−020	0.395	20.75	30	310	5

NOTE Target SNR assumes a dispersion of 1.5 Å pix^{-1}, and a resolution $\lambda/\Delta\lambda \sim 1500$.
REFERENCES 1. Junkkarinen et al. (2004); 2. Rao & Turnshek (1998); 3. Rao & Turnshek (2000); 4. Turnshek et al. (2003); 5. Boissé et al. (1998).

The Ca II system sample was compiled by Dr. M. Murphy, who searched for Ca II systems with $z_{abs} < 1.25$ and $EW_{Ca\ II,K} \geq 0.2$ Å using the Sloan Digital Sky Survey (SDSS). The list was first cut based on absorber redshift, and then Ca II systems were selected on the basis of $EW_{Ca\ II}$ and QSO brightness. The final result was nine systems with average $EW_{Ca\ II,3934} = 0.7$ Å. Table 2.3 shows these systems and their characteristics.

Because no N(H I) values are available for the Ca II systems, another method

for setting the EW detection limit was required, specifically the relationship between EW_{5780} and $E(B-V)$ described in §1.2.2. An average value of $E(B-V) = 0.06$ had been derived from Wild & Hewett (2005) for all Ca II absorbers in their sample[3], and $E(B-V)$ was related to EW_{5780} through the relationship

$$\log(EW(\text{mÅ})) = 0.99 \times \log(E(B-V)) + 2.65 \tag{2.3}$$

as obtained by Welty et al. (2006) (and see Figure 1.2). The Galactic relationship was used here instead of 1/3 the Galactic relationship because the latter yielded highly demanding exposure times for these relative faint objects (on average these Ca II systems are 1.5 magnitudes fainter than the DLAs in Table 2.2). In order to determine the target SNR, the relationship between $E(B-V)$ and the 5780 Å DIB was first used to derive EW_{5780} (assuming that $E(B-V)$ was uniformly equal to 0.06). EW_{4428} was then derived by assuming that $EW_{4428}/EW_{5780} \simeq 4.2$ (this value was derived from Herbig 1995), and the exposure time was calculated based on assuring a 3-σ detection of the 4428 Å DIB (if present). Based on the method described above, the 5780 Å DIB had a predicted $EW_{5780} = 27.6$ mÅ, whilst the 4428 Å DIB had a predicted $EW_{4428} = 116$ mÅ. Table 2.3 shows the target signal-to-noise ratios for the Ca II systems in the sample.

The contents of this thesis may be divided into an initial pilot project to determine if DIB searches with a 4-m telescope were feasible [conducted with the William Herschel Telescope (WHT)], followed by an in-depth search for diffuse bands in DLAs, which was in turn followed by a search for diffuse bands in Ca II systems. The European Southern Observatory's Very Large Telescope (ESO-VLT) formed the backbone of the search, with VLT spectra taken for three of the DLAs and all of the Ca II sys-

[3]In a later paper, published after the observing strategy was chosen, Wild et al. (2006) found that Ca II systems with $EW_{Ca\ II,3934} > 0.5$ Å (including seven of the nine systems here) have average $E(B-V) = 0.1$ instead of $E(B-V) = 0.06$ as assumed here.

Table 2.3: Characteristics of the observed Ca II systems

System	z_{abs}	EW_{3934} (Å)	EW_{3969} (Å)	Target $SNR_{5\sigma}$ (pix^{-1})
J0013−0024	0.1556	1.208 ± 0.149	1.264 ± 0.150	131
J1009+0529	0.3862	0.506 ± 0.048	0.185 ± 0.053	119
J1040+0705	0.2063	0.607 ± 0.122	0.246 ± 0.115	128
J1137+0136	0.4492	0.540 ± 0.117	0.466 ± 0.127	117
J1219−0043	0.4485	0.565 ± 0.079	0.215 ± 0.069	117
J1226−0006	0.5179	0.455 ± 0.107	0.748 ± 0.143	114
J1437−0104	0.0725	1.065 ± 0.203	0.978 ± 0.302	136
J2135+1038	0.0984	0.897 ± 0.192	0.429 ± 0.275	134
J2259−0844	0.5293	0.453 ± 0.087	0.609 ± 0.118	114

NOTE – Ca II EW values and redshifts were provided by Dr. M. Murphy. Target SNR assumes a dispersion of 1.5 Å pix^{-1}, and a resolution $\lambda/\Delta\lambda \sim 1500$.

tems. The spectrum of PKS 1127−145 was taken with Gemini South, whilst the spectrum of Q0738+313 was taken at the Apache Point Observatory (APO). Finally, additional spectra of B2 0827+243 and PKS 1127−145 were provided from previously-completed observations.

2.2.1 The William Herschel Telescope Pilot Program Observations

The initial WHT observations were intended to test the feasibility of searching for DIBs using a 4-m class telescope. These observations were conducted in service mode, and employed the red arm of the Intermediate dispersion Spectrograph and Imaging System (ISIS) spectrograph. ISIS is mounted at the Cassegrain focus of the WHT, and uses a dichroic to split the signal into separate blue and red arms (only the red arm was used in these observations). The ISIS red arm detector is a 4096×2048-pixel CCD which features extremely low fringing. Approximately 500 pixels on each edge of the CCD (in the spectral direction) have significant vignetting. The R600R grism was selected because of its high spectral coverage ($\sim$ 1800 Å), and high dispersion ($\sim$ 0.45 Å/pix). Table 2.4 shows the journal of observations. Both observations were conducted the same night, with seeing varying from $1\farcs0$ to $1\farcs5$, and cirrus clouds which became heavier as the night went on. Only half of the planned observations

of Q 1229−020 were taken due to the weather conditions worsening. The moon was dark for these observations (see Table A.1).

Table 2.4: WHT Journal of Observations

System	Instrument	Slit	Date [UT]	Exposure (s)	Wavelength (Å)	DIBs Covered
PKS 0952+179	ISIS R600R	1.″0	2004 May 20	4500	6312–8114	5780,5797,6284
Q 1229−020	ISIS R600R	1.″0	2004 May 20	3600	7212–9018	5780,5797,6284

2.2.2 Gemini South Observations

The Gemini South (GS) observations were conducted during the same observing period as the WHT observations, and employed the R400 grating on the Gemini Multi-Object Spectrometer South (GMOS-S) spectrometer. GMOS-S features three 2048×4608-pixel CCD arrays arranged to form a 6144×4608-pixel array (with the spectrum along the longer dimension). The CCD has minimal vignetting, but there are gaps of ∼20 Å between the detectors, and the detectors experience moderate to severe fringing effects in the red. The R400 grating, with a dispersion of 2.88 Å/pix binned by 2 in the spectral dimension, allowed all of the DIBs of interest to be covered with a single setting, and without any DIB falling on the gap between detectors. Table 2.5 shows the journal of observations. Observing conditions were acceptable during these observations, with adequate (albeit unspecified) seeing, light cloud, light wind and a new moon (see Table A.1).

Table 2.5: Gemini South Journal of Observations

System	Instrument	Slit	Date [UT]	Exposure (s)	Wavelength (Å)	DIBs Covered
PKS 1127−145	GMOS-S R400	1.″0	2004 Jun 19	3600	5962–9998	5780,5797, 6284,6613

2.2.3 The Very Large Telescope Observations

The Very Large Telescope (VLT) at the European Southern Observatory (ESO) was selected for the majority of the DIB search, in both DLA and Ca II systems, due

to its high optical efficiency, lack of fringing in the red, and excellent service mode completion rate. All observations employed the FOcal Reducer and low dispersion Spectrograph 2 (FORS2) spectrometer. FORS2 is mounted at the Cassegrain focus of UT1, and is optimized for the red with a mosaic of 2 2000×4000 pixel MIT CCDs (the CCDs are arranged along the spacial dimension, so no detector gaps are encountered in longslit observations of point sources). Several grisms were used, including the 600B, 600I, 600RI, 600z, 1200R, and 1028z, all binned 2X2. The central wavelength of the observation is fixed by grism choice. Table 2.6 shows the planned observations for both the DLA and Ca II system observations. Observing conditions involved clear skies or light clouds, winds up to ~ 10 m s^{-1}, and seeing from $0\farcs5$–$1\farcs2$. The phase of the moon varied from dark to grey (see Table A.1).

Table 2.6: VLT Observing Plan

System	Instrument	Slit	Date [UT]	Exposure (s)	Wavelength (Å)	DIBs Covered
AO 0235+164	FORS2 600z	$1\farcs0$	2005 Jul 20	2800	7318–10744	5780,5797,
			2005 Sep 06	2800		6284,6613
			2005 Oct 01	2800		
PKS 0952+179	FORS2 600RI	$1\farcs0$	2005 Apr 04	6000	5298–8622	5780,5797,
			2005 Apr 07	3000		6284,6613
Q 1229−020	FORS2 600z	$1\farcs0$	2005 Apr 09	5600	7464–10000	5780,5797,
			2005 Apr 13	4200		6284,6613
J0013−0024	FORS2 1200R	$1\farcs0$	2006 Aug 06	2640	5960–7370	5780,5797,
			2006 Sep 02	2640		6284
J1009+0529	FORS2 600RI	$1\farcs0$	2006 Apr 02	3960	5495–8620	4428
	FORS2 1028z	$1\farcs0$	2006 Apr 03	2640	7930–9575	5780,5797,
						6284,6613
J1040+0705	FORS2 600I	$1\farcs0$	2006 May 22	2640	6925–9470	5780,5797,
						6284,6613
J1137+0136	FORS2 600RI	$1\farcs0$	2006 Apr 04	2640	5495–8620	4428,5780,
			2006 Apr 06	2640		5797
J1219−0043	FORS2 600RI	$1\farcs0$	2006 Apr 02	2640	5495–8620	4428,5780,
						5797
J1226−0006	FORS2 600RI	$1\farcs0$	2006 Apr 06	2640	5495–8620	4428
			2006 May 17	2640		
J1437−0104	FORS2 1200R	$1\farcs0$	2006 Apr 02	10560	5960–7370	5780,5797,
						6284,6613
J2135+1038	FORS2 600B	$1\farcs0$	2006 May 28	5280	3490–6360	4428,5780
			2006 Jun 22	7920		
J2259−0844	FORS2 600RI	$1\farcs0$	2006 Jul 10	5280	5495–8620	4428

For the DLA observations, the VLT Observing Blocks (OBs) were designed in

order to ensure two exposures within each OB, with a 20.″0 offset along the slit between the observations. For PKS 0952+179, a total of six 1500-second observations were executed, divided into three OBs. For AO 0235+164, six 1400-s observations were executed, again divided into three OBs. Finally, for Q 1229−020, seven 1400-s observations were completed, divided into three OBs of two observations each (with offset), and the single remaining observation in its own separate OB. For the Ca II systems, OBs contained either one or two 1320-second observations, and each system had between two and ten 1320-second observations completed.

2.3 Data Reduction and Analysis

The general data reduction procedure will be summarized in §2.3.1, with special attention to the cosmic ray removal procedure, which differs from standard IRAF routines. The actual data reduction will then be described, with §2.3.2 discussing the data obtained from the William Herschel Telescope, §2.3.3 discussing the data obtained from Gemini South, and §2.3.4 discussing the data obtained from the Very Large Telescope.

2.3.1 General Procedure

Image Preparation

The first step involved in reducing a raw image is to prepare the image for the later stages of reduction. The image axes must first be set properly, since in any longslit spectrum, one dimension will be spatial (position on the sky) and one spectral (wavelength), but telescopes vary as to whether the spectral dimension is horizontal or vertical (see Figure 2.2 for an example). Next, IRAF must be set to recognize the various types of images (including bias frame, dark exposure, flatfield, wavelength calibration, and science exposure), through defining which header parameters represent which image type. The images must also be examined in order to determine the location of the overscan region, as well as which part of the science images contain

"good" pixels (the overscan region and the trim section are described in more detail in §2.3.1).

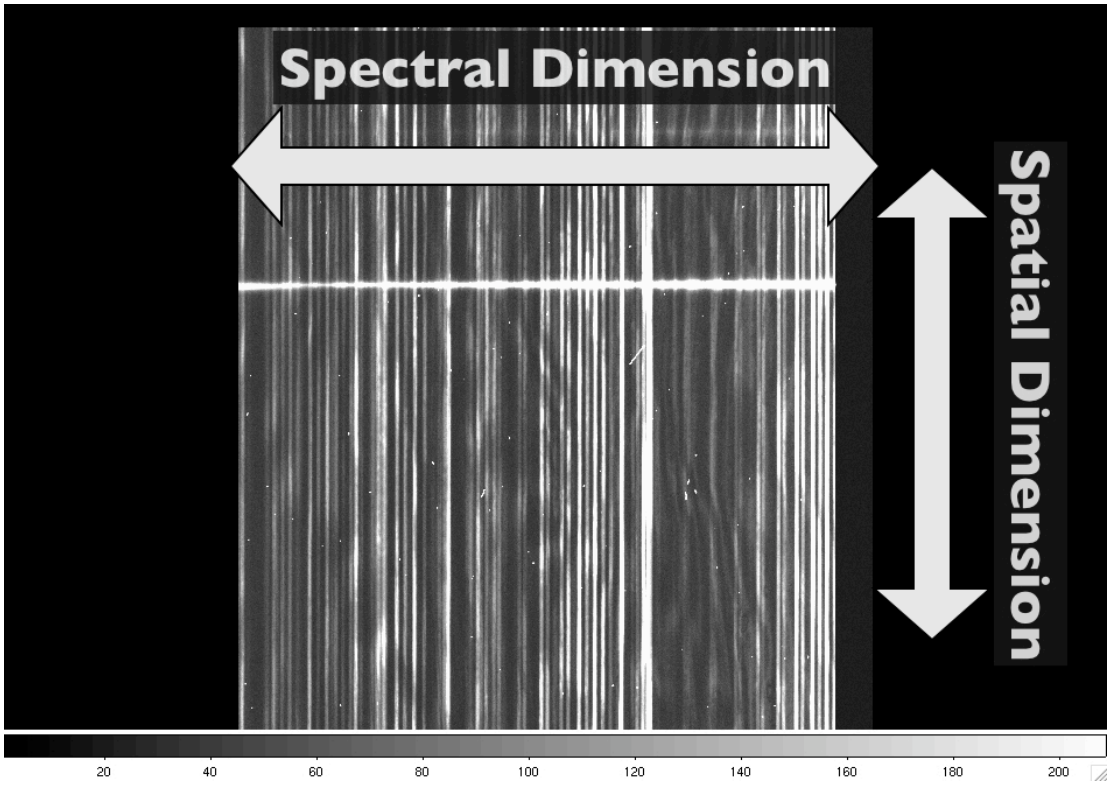

Figure 2.2: A raw longslit spectrum, with the spatial and spectral dimensions marked, and the blue and red ends of the spectrum indicated. The small point-like objects are in fact cosmic rays, which must be removed from the frame as described in §2.3.1. The vertical lines are sky lines (emission lines caused by water vapour and OH^- in the Earth's atmosphere), described in §2.3.1 and the brightness variations are caused by fringing, described in §2.3.3.

Bias Subtraction

Astronomical images and spectra are intrinsically dark in that they contain large areas with little or no signal, and only isolated points or lines of high signal. In order to prevent problems with readout errors in dark regions, CCDs are given a positive "bias voltage" which produces a positive signal level even in areas which received no light. Because the bias value changes not only from telescope to telescope (and from CCD to CCD), but also with position on the CCD, and even with time, a set of bias

frames are taken as part of the observation in order to determine the bias voltage so that it can then be removed. Bias frames are zero-second exposures taken with the shutter closed, and they should thus provide an accurate record of the chip-wide bias value as they are taken. Bias frames are usually taken in groups of 5 to 10, and may be taken weekly, daily, or even more often depending on the stability of the bias voltage.

A group of bias frames is averaged together to provide a master bias frame by the IRAF task `zerocombine`. The task is usually set to reject the highest value for each pixel before averaging the rest, and to reject any pixels more than three standard deviations (3-σ) above the mean value. This ensures that inaccurate readouts, cosmic rays, or other problems which might result in an inaccurately high value for a few pixels on a bias frame are not incorporated into the master frame. CCDs also often contain an overscan region, generally a number of rows or columns which are not exposed even when data is being collected. This overscan provides a way of tracking any changes in the bias voltage with time, and the overscan region on each frame is usually fit with a function (usually a first- or second-order polynomial) and then any residual flux in the overscan region (after the master bias frame has been subtracted) is itself removed from the image.

Flatfield Correction

In an ideal CCD, every pixel would respond in exactly the same way to incident light. However, in a real CCD each pixel has its own response characteristics. While most pixels are very close in response to the average pixel in the CCD, some will produce noticeably different charges if exposed to the same amount of incident light. Flatfield images are intended to allow this variation to be removed.

Flatfield images may be exposures of the inside of the telescope dome or a flat screen (illuminated with a white light), or of the twilight sky, both of which provide almost the same illumination to every pixel. Many modern instruments may also

incorporate a set of internal lamps which may be activated and reflected directly into the CCD by means of an adjustable mirror. These lamps also provide an even illumination to all of the pixels, so that any variation in pixel sensitivity may be divided out of the science images. In the case of spectroscopy, the flatfields must be normalized as well, since otherwise the intrinsic spectral shape of the lamp would influence the resulting image. In addition, some CCDs experience fringing (especially when observing in the red) as a result of thin-film interference effects in the detectors. Since the flatfield is taken with the same grism/grating and slit setting as the image, it should have the same pattern of fringes as the exposure. Dividing the image by the flatfield will thus remove the fringes as well as any other variations.

As with bias frames, multiple flatfields are combined together, generally by averaging, although median combination may also be used. The highest and lowest pixel values are often rejected before the remaining pixel values are averaged together, and extremely high values (e.g. cosmic ray impacts) may also be rejected before flatfield combination. Generally in the reductions of the data presented here all possible flatfield combination methods were tested, and the normalized flatfield with its mean closest to 1, and the lowest standard deviation was selected as the master flatfield.

Cosmic Ray Removal

There are a variety of algorithms designed to remove cosmic rays from spectra, but all centre around removing the known features of the exposure (the sky lines, as well as the spectra of the observed objects), and then finding any remaining bright points and masking them out of the final image, usually by interpolating from adjacent pixels which are unaffected. That data collected here had cosmic rays removed via two procedures: a cosmic ray removal script (herein called "`mkdecos`") designed by Dr. G. Mallen-Ornelas and Dr. S. Ellison in 2002, and another script, entitled "LA-Cosmic", designed by Dr. P. G. van Dokkum (van Dokkum 2001).

`mkdecos` works by subtracting the background (both sky lines and object spec-

tra) from the exposure, followed by a two-pass search for cosmic rays. The first pass works by searching for any pixels over a certain threshold value (with a default threshold of 150), and marking both those pixels, and any pixels within an adjustable radius of those pixels (with a default radius of 1.3) as cosmic rays. The second pass marks any pixel with a value greater than 20 as a cosmic ray (but does not include a radius around those pixels). The two passes are then multiplied together, ensuring both that only pixels near detected cosmic rays are selected, and that low-valued pixels near cosmic rays are not affected. The script then marks any remaining selected pixels as "bad" pixels (as if the CCD had faulty pixels in those locations), and calls on existing IRAF routines to remove those pixels and find their values based on interpolating the values of the surrounding pixels. As an example of the `mkdecos` procedure, Figure 2.3 shows the process of cosmic ray removal on a sample spectrum. In order to determine the best threshold values to use for `mkdecos`, the final image was subtracted from the initial image in order to test whether the object spectrum has been affected, and the final image was also examined for any remaining cosmic rays in order to ensure that the removal was complete.

LA-Cosmic, in contrast, uses Laplacian edge detection to detect cosmic rays. While it uses a similar method to detect and remove sky lines and object spectra before searching for cosmic rays, it then convolves the resulting image with a Laplacian kernel in order to highlight the edges in the image (regions where the pixel value jumps sharply, such as the edges of cosmic rays, sky lines, or object spectra, although the latter two have ideally already been removed). Cosmic rays are distinguished from other point sources by their lack of symmetry. In the case of spectroscopic data, LA-Cosmic also allows the effects of fringing to be removed, or at least be reduced, since they display a similar pattern of sharp edges and a lack of symmetry. LA-Cosmic then replaces the cosmic ray pixels by the median value of the surrounding good pixels. If necessary, LA-Cosmic may be iterated multiple times, with each iteration

finding a number of cosmic rays which were not detected by the previous iteration.

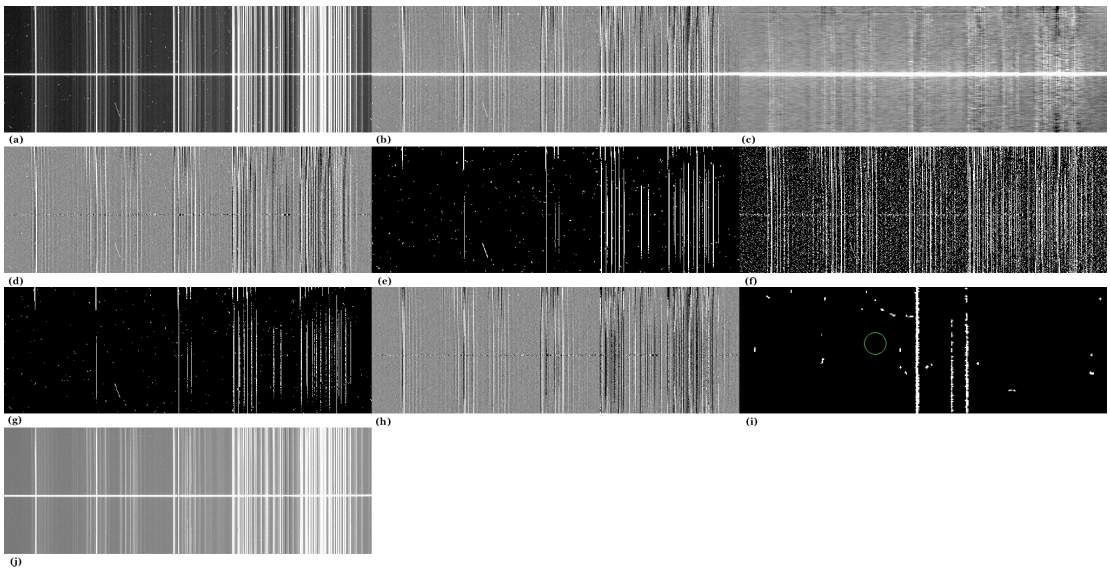

Figure 2.3: The `mkdecos` cosmic ray removal routine. The initial image (a) is first background subtracted to remove the sky lines (b), and a median filter is then applied in the spectral direction to average out the QSO spectrum (c). This filtered image is then subtracted from image (b) to yield image (d). Note that image (d) shows that the sky line removal has been ineffective near the top and bottom of the image due to the curvature in the spatial dimension. Pixels with values above a specified threshold (default 150), and points within a radius of them (default 1.3 pixels) are then selected and set to a value of 10000 with all other pixels set to 0, forming image (e). Independently, another copy of image (d) has all pixels with a value <20 set to zero to form image (f). Images (e) and (f) are then multiplied together to form the final cosmic ray map (g). A copy of image (d) then has the pixels selected in image (g) removed, and their values interpolated from the surrounding pixels to form image (h). Image (h) is then subtracted from image (d) to form the cosmic ray mask, this time incorporating the actual values of the cosmic ray pixels (image i). Finally, image (i) is subtracted from image (a) to produce the output image (j).

`mkdecos` was used for the majority of the data reduction described here, primarily since it functions quite well, accurately removing the cosmic rays while leaving the spectral features intact. LA-cosmic was employed for the majority of the Ca II system reductions, generally alongside `mkdecos` in order to provide a comparison. The comparison was performed by subtracting one final image from another and examining the image for missed cosmic rays (or any subtraction of the object spectrum). In general, the two systems produced comparable results, with `mkdecos` requiring

more adjustment of its parameters, but completing more quickly.

Spectral Extraction

In IRAF, spectral extraction is conducted using the task `apall`, a large and complex task which conducts several operations sequentially, including:

- aperture detection (apertures are objects in the slit, such as the horizontal line shown in Figure 2.2). It is possible to mark apertures manually, or to allow `apall` to search for apertures automatically.
- tracing apertures. While the ideal spectrum would have a perfectly horizontal (or vertical) spectral dimension, the track of a spectrum is generally both at an angle and curved. `apall` traces the aperture by fitting a function to this shape, either interactively or through user-provided parameters
- sky subtraction (explained in more detail in §2.3.1)

Multiple apertures may be extracted from a single spectrum, each with different settings. `apall` also allows for a spectrum to be extracted according to the trace provided by a previous spectrum. This allows wavelength calibration spectra, for example, to be extracted in the same shape and location as the objects in the science spectra (see §2.3.1 for more details). Note that the IRAF packages used for the Gemini telescopes split `apall` into several different tasks, and conduct wavelength calibration and sky subtraction before the spectra are extracted (see §2.3.3) for details.

Sky lines

While the night sky appears dark, there are certain wavelengths at which it is bright enough to interfere with observations. There are two main ways in which the sky causes difficulties in observing – in emission and absorption. Sky emission lines (the vertical lines in Figure 2.2) are mostly caused by OH^- ions in the atmosphere,

while telluric absorption lines (see §2.3.3 for examples and information) are caused mostly by H_2O absorption. Both sky lines and telluric lines can cause difficulties in attempting to detect spectral features, and both require very different methods of removal. Both sky lines and telluric lines are more prevalent in the red and infrared than in the blue, making them important features in the search for DIBs (since the most easily detected DIBs are themselves concentrated towards the red end of the spectrum even at their rest wavelengths).

The sky emission lines are easily visible in the two dimensional spectrum even in areas with no object in the slit. As such, their intensity can be measured in these locations, and then a function can be fit across the object spectrum and then subtracted. Care must be taken in producing the fit due to the inherent curvature of the spectral and spatial dimensions, but provided the sampling region is sufficiently close to (but *not* overlapping with) the object spectrum, sky lines can be efficiently removed. The chief strategy for dealing with sky lines is to attempt to ensure that none of them overlap with any features of interest (the positions of sky lines are well known and effectively unchanging, although their strength can vary considerably with the weather conditions). This selection was performed at the target selection phase (see Figure 2.1).

Another method of removing sky lines involves subtracting the science spectra from one another. If the position of the target is iterated along the slit (so that, for example, it falls at row 100 for one exposure, row 200 for the next, row 300 for the next, and so on), then when one exposure is subtracted from another, the sky in the second will be subtracted from the target+sky in the first (and, if the procedure is reversed, vice-versa). This technique requires the images to be scaled prior to subtraction (to compensate for differences in the overall image levels), and will provide good results only if the images were taken sufficiently close together than the sky has not had time to change significantly from one image to the next. In order

to prevent problems caused by the sky conditions changing, this technique was only used with spectra observed in direct sequence, and then only when the initial sky subtraction techniques proved inadequate.

Wavelength Calibration

In order to determine the actual wavelength corresponding to each pixel of the reduced spectrum, wavelength calibration images (often abbreviated as "arcs" for the arc lamps which were originally photographed to produce the comparison spectra) are taken at the same time as the original observation. Each arc is an exposure of a gas discharge tube containing known elements (e.g. Copper-Argon or Helium-Neon-Argon). Because the extraction path of the arc is matched to the path of the exposure, the two will have essentially the same wavelength scale. In turn, the wavelengths of the emission lines on the arc image are already known, so by identifying these emission lines the wavelength scale of the arc can be calibrated (by using the identified lines as fixed points, and then fitting a function to describe the wavelength scale), and this same calibration can in turn be applied to the exposure. The result at the end of the process is a one-dimensional spectrum with the bias voltage removed, flatfield irregularities divided out, cosmic rays eliminated, sky lines subtracted, and an accurate wavelength scale applied.

There remain several more minor tasks necessary to produce an exact wavelength calibration. The first is the air-vacuum correction, required because absorption and emission lines have different wavelengths in vacuum than they do in air. If the arc spectra were originally calibrated to vacuum wavelengths, this is not a necessary step, but it is conventional to convert air-calibrated arcs to vacuum wavelengths for QSOALS observations. The corrective factor depends on the wavelength and the air temperature and pressure at the observatory. Finally a heliocentric correction may be applied, to remove the redshift or blueshift resulting from the relative motion of the Earth's surface (where the observatory is located) with respect to the Sun.

Observations taken at the same time and from the same location do not in principle require this correction, but observations taken at different times, even from the same location, will have different relative velocities. Although present, heliocentric corrections are often not essential for low-resolution spectra because the effect may be significantly smaller than the dispersion of the spectra, but there is certainly no disadvantage to applying them, apart from needing to re-bin the spectra as part of the correction process.

Final Processing

After wavelength calibration the various exposures can be combined together into a single frame. This will assist in removing any remaining problems (e.g. if an incomplete cosmic ray subtraction still exists in one exposure, it is unlikely that the other exposures will have a cosmic ray in exactly the same place, so by giving more weight to the clean exposures in that region the remaining effects of the cosmic ray can be removed). Spectral combination is commonly done either by using the median value for each pixel, or by taking the mean of all exposures. Using the median value is more likely to remove spurious high or low values from poorly subtracted cosmic rays or sky lines (so long as those values are present in fewer than half of the exposures), but in parts of the spectrum that are already clean, the mean value is the best approximation of the true value (assuming that all sources of error are both independent and random).

Once the exposures have been combined, they must generally be normalized. Normalization removes the underlying shape of the continuum, making emission and absorption lines easier to discern, especially in highly sloped regions of the spectrum. The spectrum is normalized by fitting a function to the continuum, taking care to avoid fitting absorption lines or noisy sections of the spectrum as part of the continuum. Normalization is a complex process, so the individual continuum fits will be described in greater detail during the descriptions of the telescope-by-telescope data

reduction. In the following sections, I now describe how these general procedures were applied or fine-tuned to the data obtained at individual telescopes.

2.3.2 WHT Data Reduction

The observations were processed through standard IRAF routines. A total of 33 bias frames were combined with `zerocombine`, followed by using `ccdproc` to subtract the master bias frame from all other exposures. A total of four lamp flatfields were taken with the same wavelength settings as the observations of PKS 0952+179, and three with the same settings as Q 1229−020 (an additional two flatfields of PKS 0952+179 and four of Q 1229−020 were present but saturated). The flatfield images were examined for any signs of cosmic rays (there were none), and then combined with `flatcombine`. The `response` task was used to normalize both combined flatfields (referred to hereafter as NormF09 and NormF12). On inspection, the NormF09 flat had a high standard deviation (0.6137), which through visual inspection proved to be a result of poor normalization in the vignetted region of the flatfield. Examining the central pixels of the flatfield proved that the overall standard deviation was much lower. Final flatfield statistics for the central region only are shown in Table 2.7.

Table 2.7: Flatfield statistics for the WHT

Target	Mean	Median	Mode	σ
PKS 0952+179	1.000	1.005	1.031	0.0456
Q 1229−020	1.002	1.004	1.012	0.0723

Cosmic rays were removed with `mkdecos` and the spectra were extracted with `apall` in interactive mode. Apertures were located manually, as were background subtraction regions. The background (including sky lines) was fit with a second-order chebyshev polynomial. The `apall` extraction was variance-weighted, and optimal extraction was used for all spectra. Arc spectra were also extracted by `apall` in non-interactive mode, with each arc extracted once following the trace of an asso-

ciated science spectrum. Two arcs were taken for each science target, so each arc was used as a reference by each associated science exposure with equal weight. Arc spectra were fitted with the `identify` task, with 20 spectral lines identified from the Isaac Newton Group (ING) spectral atlas followed by fitting the spectral curve with a fifth-order chebyshev polynomial. Representative RMS values (at least one for each arc) are shown in Table 2.8. Science spectra were wavelength calibrated using the task `dispcor`, weighting each arc equally and applying a linear wavelength scale (with interpolation). `dispcor` was set to preserve flux during these operations. During calibration, offsets between the arcs were discovered making accurate wavelength calibration difficult. However, both systems were later re-observed with the VLT, so the impact on the final DIB search is negligible. Spectra were combined with `scombine` set to median mode (although, given that Q 1229−020 had only two exposures, the final `scomb` result for that spectrum was the mean of the two spectrum).

Table 2.8: Accuracy of wavelength calibration for the WHT targets

Target	Grism	λ_c (Å)	RMS (Å)
PKS 0952+179	R600R	7155	0.0533
			0.0525
Q 1229−020	R600R	8061	0.0554
			0.0543

After the spectra had been combined, both were normalized with the `continuum` task employing a 10^{th}-order cubic spline function, and focussing on normalizing the main part of the spectrum rather than the vignetted regions to the far red and blue. The final spectral characteristics for the WHT spectra are shown in Table 2.9. The WHT observations were intended as a test run, and the final spectra had SNR values (20–22 for PKS 0952+179 and 5–13 for Q 1229−020) considerably below the target values (95 and 310 respectively), indicating that an 8-m telescope would be required

for any remaining targets. The systems observed with the WHT were thus also observed with the VLT, and the VLT observations will form the basis for the data analysis. The VLT data reductions are described in §2.3.4, and the final spectra are described in Table 2.12.

Table 2.9: Final Reduced spectra for the WHT

Target	Dispersion (Å pix^{-1})	R ($\lambda/\Delta\lambda$)	SNR pix^{-1}
PKS 0952+179	0.4448	3780	20–22
Q 1229−020	0.4460	4980	5–13

2.3.3 Gemini South Data Reduction

Gemini South was used for only one target, PKS 1127−145, due to the much poorer quality (both in terms of sensitivity and CCD fringing) compared to FORS. In addition, the observations of PKS 1127−145 were made more difficult due to the lack of a standard star taken with the same settings as specified during Phase 2 preparation (while standard star observations were provided, they were taken with a different central wavelength). As such, all remaining targets were observed with the VLT.

The Gemini observations were taken on the night of June 19^{th} 2004 with a central wavelength of 810 nm, as were the standard star observations of Feige 67, with a central wavelength of 755 nm. Gemini has developed a set of extensions to IRAF intended specifically for reducing data taken with the Gemini telescopes. Gemini provides its data in the form of a multi-extension FITS (MEF) file with the CCD images in separate extensions. The Gemini IRAF packages are intended to reduce the data in that format, including combining the CCD images and handling the gaps between adjacent CCDs. The Gemini images were thus reduced with a completely different procedure than the rest of the data, although the overall essentials remained the same.

The Gemini data was first prepared using the `gprepare` task. `gprepare` at-

taches a Mask Definition File (MDF) to each observation depending on the instrument and slit settings (the MDF also includes some information on bad pixels). `gprepare` also serves to update the FITS headers as needed. As the necessary MDF is found based on existing header parameters, no changes needed to be made to `gprepare` before use.

The five prepared bias frames were then processed with `gbias`, a bias combination task equivalent to IRAF's `zerocombine`. As recommended by Gemini's procedures, the overscan level was not subtracted during the bias combination, nor were the image borders trimmed. Unlike standard IRAF procedures, the bias level was not immediately subtracted from the image frames, as the Gemini packages conduct bias subtraction and flatfielding at the same time with `gsreduce`. The bias frames were combined with a median combine.

While standard IRAF routines employ two separate tasks for the creation of a master flatfield, first combining with `flatcombine` and then normalizing with `response`, the Gemini `gsflat` routine performs both operations at once. Only two usable flatfields were taken as part of the Gemini calibration plan.

All the flatfields showed fringing at the 25% level, sufficient to make normalization extremely difficult. Because `gsflat` fits a normalization function to each row of the flatfield independently, the normalization process ended up distorting the fringe patterns which otherwise could have been removed through flatfield division. To remove the fringes, a spectral shape image was created by taking the median value in each column of the unnormalized flatfield, and copying the resultant one-dimensional image until it had the same overall size as the original flatfields. This image was then normalized, and the function employed was in turn divided into the unnormalized master flatfield to create a normalized flatfield. The final flatfield had mean, median, and mode values of 1.0, and a standard deviation $\sigma = 0.2834$. The high standard deviation is entirely due to the fringing. When the unnormalized flat was divided by

this flatfield, the fringing was eliminated completely.

Once master bias and flatfield images had been produced, all science, arc, and standard star images were processed with `gsreduce`, which subtracted the bias image, trimmed out the overscan regions (although again, as suggested by Gemini, the overscan regions were neither fit nor subtracted), applied the flatfield correction and combined the three CCD images into a single image (using the hidden task `gmosaic`). Although `gmosaic` offers the option of interpolating across the chip gaps, this option was not chosen. Instead, the chip gaps were left at zero flux in order to ensure that their locations remained obvious (because all object spectra were taken with the same central wavelength, the chip gaps were in the same location for all images, so not even combining the final spectra eliminated the chip gaps. The same procedure discussed above was also used to reduce the standard star images, including building a (separate) spectral shape image for normalization.

Once `gsreduce` had been successfully run on the object, standard star, and arc frames, with the appropriate master bias and flatfield images in each case, the next step in the Gemini reduction process was to fit the arc spectra with `gswavelength`. Instead of the one-dimensional wavelength fit produced after extraction (described above in §2.3.1), `gswavelength` fits the two-dimensional arc by fitting along the spectral dimension every ten rows, and deriving a full two-dimensional fit by, in turn, fitting a function to describe how the initial fit changes. The RMS error in the wavelength calibration of the arc was 0.0859 Å. Both the standard star and object spectra were then run through `gstransform` in order to provide a wavelength fit, each with the appropriate arc selected as the reference spectrum. Cosmic rays were removed with `mkdecos`.

Sky subtraction was performed by a combination of `gsskysub` and by subtracting the object images from one another (made possible because the position of PKS 1127−145 on the slit differed by more than seven resolution elements between

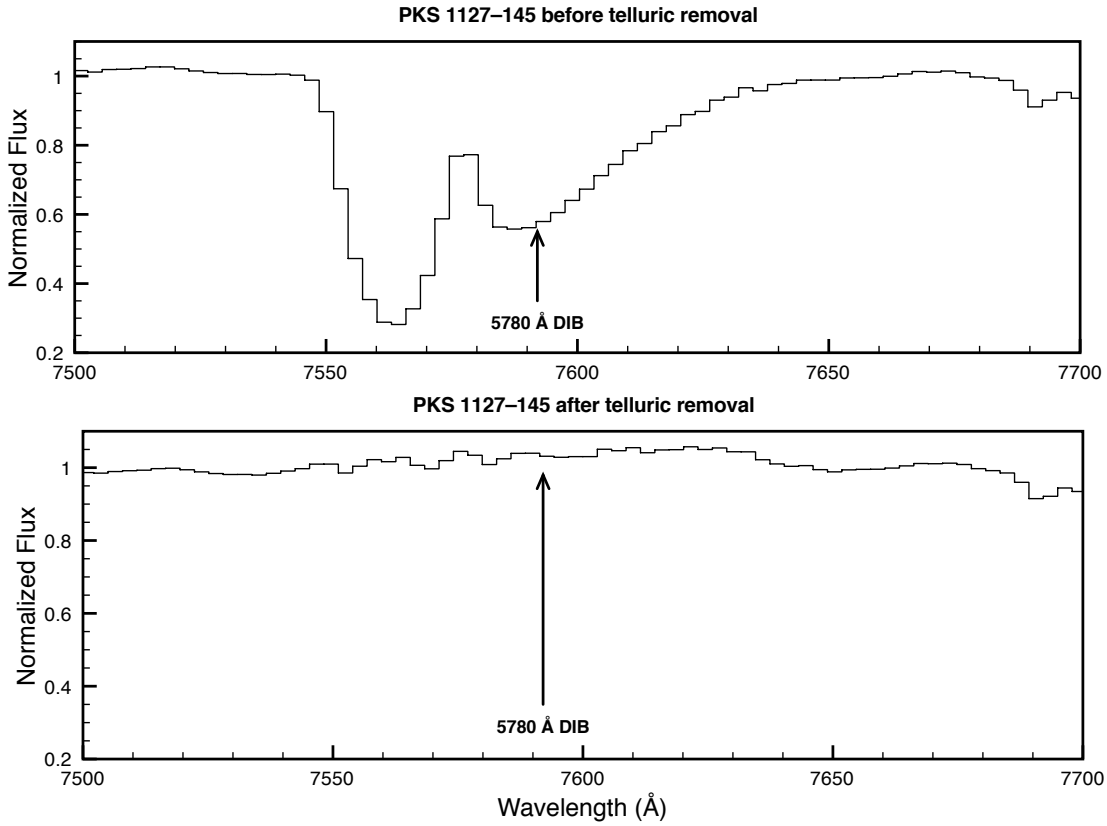

Figure 2.4: This is the spectrum of PKS 1127−145 both before (top panel) and after (bottom panel) telluric removal. The location of the 5780 Å DIB has been marked.

exposures). The images were scaled to the same mode and then subtracted from each other. Each of the sky subtraction techniques was tested separately, as was the combination of both (with the image subtraction performed first and `gsskysub` second to remove any remaining residuals), with the combination providing the best results. With sky subtraction complete, the spectra were passed through `gsextract` for extraction into one-dimensional spectra. Apertures were located manually, sky subtraction was not performed, and the spectral trace was fit interactively with a fifth-order chebyshev polynomial.

With `gsextract` completed, the spectra were copied out of their MEF shells and standard IRAF routines (`scomb` and `continuum`) were employed to combine

and normalize the spectra. The `scomb` routine was run with median combination and equal weighting for all spectra. No pixels were rejected before the median was taken because only three object spectra were available. `continuum` was run with a ninth-order cubic spline to normalize the combined spectrum, again with the focus on correctly normalizing the central regions of the spectrum where the DIBs (if any) would be located. The final spectrum had dispersion 2.75 Å pix^{-1}, $R = 1060$, and $SNR = 29$–62 pix^{-1}.

In the case of PKS 1127−145, the 5780 and 5797 Å DIBs were redshifted into a major telluric absorption band between 5750 and 5820 Å (see Figure 2.4). As a result, the standard star observations were used to remove the telluric absorption. This was accomplished through IRAF's `telluric` package. In order to prepare the standard star spectrum for this use, it was first normalized, and then set uniformly to a value of 1 everywhere except for the telluric absorption bands (this step is necessary to prevent small fluctuations in the continuum value from affecting the object spectrum when the two are divided). `telluric` then divides the two spectra, after scaling the standard star spectrum and shifting it by however many pixels are required to line up the absorption bands in both spectra. See Figure 2.4 for before and after spectra.

2.3.4 VLT Data Reduction

The majority of the observations taken were made with the VLT. Observations of three DLAs were conducted during Period 75, while observations of nine Ca II systems were conducted during Period 77. Although formatted as standard FITS files, the VLT data required a certain amount of preparatory work before beginning the IRAF reduction. The VLT header files store gain and readout noise information in a set of hierarchical headers which are not easily read by IRAF, and further store gain in units of ADU/e^- rather than the more usual e^-/ADU. In addition, while the VLT uses a horizontal spectral axis, this information is not coded into the header files in a format readable to IRAF. All VLT files are thus passed through a short script which

determines the gain and readout noise, storing them in the standard header format as GAIN and READNOIS, while adding the header parameter DISPAXIS=1 so that IRAF will check the correct dispersion axis.

For all systems observed, sets of either five or 10 bias frames were included for each night when that system was observed. Bias frames were combined with `zerocombine`, followed by bias subtraction with `ccdproc`, with the overscan strip was fit with a second-order chebyshev polynomial. The flatfields were combined next, split by day and by type (longslit flatfields for the science spectra, and multi-object spectrometer flatfields for the standard star spectra). Flatfields were combined with `flatcombine` and normalized with `response`, and the results are shown in Table 2.10.

Table 2.10: Flatfield statistics for the VLT

Target	Date	Grism	Mean	Median	Mode	σ
AO 0235+164	2005 Jul 20	600z	1.000	1.009	1.040	0.0654
	2005 Sep 06		1.000	1.008	1.038	0.0648
	2005 Oct 01		1.000	1.000	1.036	0.0651
PKS 0952+179	2005 Apr 04	600RI	1.000	0.995	0.960	0.0687
	2005 Apr 08		1.000	0.995	0.961	0.0686
Q 1229−020	2005 Apr 09	600z	1.000	1.008	1.037	0.0650
	2005 Apr 13		1.000	1.009	1.035	0.0651
J0013−0024	2006 Aug 06	1200R	1.000	1.006	1.035	0.0508
	2006 Sep 02		1.000	1.004	1.033	0.0513
J1009+0529	2006 Apr 02	600RI	1.000	0.994	0.961	0.0583
	2006 Apr 03	1028z	1.000	1.006	1.038	0.0531
J1040+0705	2006 May 22	600I	1.000	1.008	1.042	0.0527
J1137+0136	2006 Apr 04	600RI	1.000	0.993	0.959	0.0587
J1219−0043	2006 Apr 02	600RI	1.000	0.994	0.961	0.0583
J1226−0006	2006 May 17	600RI	1.000	0.991	0.959	0.0580
J1437−0104	2006 Apr 02	1200R	1.000	1.004	1.033	0.0514
J2135+1038	2006 May 28	600B	1.000	1.002	1.036	0.0632
	2006 Jun 22		1.000	1.000	1.036	0.0665
J2259−0844	2006 Jul 10	600RI	1.00	0.992	0.960	0.0582

After flatfielding, all science and standard star exposures were processed through cosmic ray removal. Initially `mkdecos` was used to remove the cosmic rays, but at a later date LA-Cosmic was also tested, in order to determine the best method

for use with data from the VLT. Overall, for the DLAs LA-Cosmic preserved the skylines more completely, but `mkdecos` caught a higher percentage of the cosmic rays, so `mkdecos` was ultimately used for cosmic ray removals. For the Ca II systems, however, LA-Cosmic was able to remove a higher percentage of the cosmic rays, so it was used for cosmic ray removal in the final spectra.

Table 2.11: Accuracy of wavelength calibrations for the VLT targets

Target	Date	Grism	RMS (Å)
AO 0235+164	2005 Jul 20	600z	0.0791
	2005 Sep 06		0.0967
	2005 Oct 01		0.0851
PKS 0952+179	2005 Apr 04	600RI	0.0755
	2005 Apr 08		0.0631
Q 1229−020	2005 Apr 09	600z	0.0987
	2005 Apr 13		0.0969
J0013−0024	2006 Aug 06	1200R	0.0624
	2006 Sep 02		0.0624
J1009+0529	2006 Apr 02	600RI	0.0847
	2006 Apr 03	1028z	0.0930
J1040+0705	2006 May 22	600I	0.0910
J1137+0136	2006 Apr 04	600RI	0.0935
J1219−0043	2006 Apr 02	600RI	0.0847
J1226−0006	2006 May 17	600RI	0.0935
J1437−0104	2006 Apr 02	1200R	0.0666
J2135+1038	2006 May 28	600B	0.0838
	2006 Jun 22		0.0838
J2259−0844	2006 Jul 10	600RI	0.0976

After cosmic ray removal, spectra were extracted with `apall` in interactive mode, including background (sky) subtraction. Apertures were located manually, and background subtraction regions on either side of the aperture were manually selected and fit with a first-order legendre polynomial. The spectral trace was fit with a fourth-order chebyshev polynomial, with RMS values less than 0.03 pix for all apertures. The extraction was variance-weighted, and the optimal extraction was used for all spectra. A single arc was taken each night. The arcs were fit with `identify` using

the line list provided by ESO in their FORS2 reference manual. RMS values for the wavelength fit are found in Table 2.11. After wavelength calibration, heliocentric corrections were applied.

Table 2.12: Final Reduced spectra for the VLT

Target	Grism	Dispersion (Å pix^{-1})	R ($\lambda/\Delta\lambda$)	SNR pix^{-1}
AO 0235+164	600z	1.59	1880	44–155
PKS 0952+179	600RI	1.63	1650	65–400
Q 1229−020	600z	1.59	1860	69–150
J0013−0024	1200R	0.74	2800	60–80
J1009+0529	600RI	1.63	1350	130–180
	1028z	0.86	3240	70–130
J1040+0705	600I	1.33	2050	40–55
J1137+0136	600RI	1.63	1350	55–75
J1219−0043	600RI	1.63	1350	90–115
J1226−0006	600RI	1.63	1350	100–120
J1437−0104	1200R	0.74	2800	70–85
J2135+1038	600B	1.50	1025	70–85
J2259−0844	600RI	1.63	1350	75–100

Normalization of all spectra was done via the `continuum` task. A 200-Å range around each DIB was selected for normalization, and a fourth-order cubic spline was fit to the continuum in that area, taking care to exclude any visible emission or absorption features from the sample region, as well as the region where the DIB would be located (if present). Even with the central region of the spectrum not included in the fit, the fits were examined to ensure that the apparent continuum level was well-fit. The final spectral characteristics are shown in Table 2.12

2.3.5 Data Analysis

The main tool involved in line searches is visual inspection, although Lawton et al. (2008) also employed an automated search technique to these data. In searching by eye for absorption features, it is often helpful to start with a normalized spectrum. If a feature is found, its equivalent width may be determined either through a pixel-by-pixel count, or through a fitting function (tasks are available in IRAF, as part of

`splot`, to assist in both of these methods). The per-pixel equivalent width is defined as follows:

$$EW(\text{Å}) = \sum_{i=0}^{n} \frac{f_c - f_i}{f_c} \times D \tag{2.4}$$

where D is the dispersion of the spectrum in Å, f_c the continuum flux level, f_i the flux level of pixel i, and n the number of pixels over which the absorption line is spread. Fitted equivalent width instead fits a gaussian profile to each component of the absorption, and determines the total EW from the profiles. If no lines are detected, the task is then to derive an appropriate upper limit to any absorption that may be present (but undetectable). The equivalent width limit for undetected features in a spectrum is provided in §2.2.

2.4 Third-party Observations, Reduction, and Analysis

In addition to the observations described above, several DIB searches in DLAs were undertaken by our collaborators, and the resultant data is important in providing a complete picture of the presence of DIBs in DLAs. Table 2.13 shows this additional data, involving spectra taken of Q 0728+313 (2 DLAs) and B2 0827+243 (1 DLA), and an additional spectrum taken of PKS 1127−145. The spectrum of Q 0728+313 was acquired and reduced by B. Lawton, from observations at the 3.5 m Apache Point Observatory, using the Double Imaging Spectrometer (DIS), which uses a dichroic (beam-splitter) to produce separate blue and red spectra. The HIGH grating was used in both cases, giving the blue chip a dispersion of 0.62 Å pix^{-1} and the red chip a dispersion of 0.84 Å pix^{-1}. The resolution of both spectra is $R = 2040$, and the SNR 57–84 pix^{-1}. Further details of the reduction may be found in Lawton et al. (2008).

The spectrum of B2 0827+243 was initially observed by Dr. W. L. W. Sargent, who provided it to B. Lawton for the DIB search. The observations were taken with the HIRES echelle spectrometer on the Keck telescope, and feature a dispersion of

Table 2.13: Journal of Third-party Observations

System	Instrument	Slit	Date [UT]	Exposure (s)	Wavelength (Å)
Q 0738+313	APO/DIS HIGH	1.″5	2004 Dec 15/19 2005 Feb 04	40600	4367–7817
B2 0827+243	Keck/HIRES	0.″861	1998 Dec 22	22500	5185–9234
PKS 1127−145	VLT/UVES #1 & #3 dichroic	1.″0	2002 Jul 17/18	24900	3041–6809

0.04 Å pix^{-1}, a resolution $R = 43,000$, and SNR values ranging from 27 pix^{-1} in the red to 114 pix^{-1} in the blue. Finally, the additional spectrum of PKS 1127−145 was observed by Dr. M. Murphy, who again allowed B. Lawton to use it in a DIB search. The dispersion of the spectrum is 0.05 Å pix^{-1}, the resolution $R = 45,000$, and the SNR 38 pix^{-1}. Additional information on both of these spectra may also be found in Lawton et al. (2008).

Chapter 3

Diffuse Interstellar Bands in Damped Lyman-α Systems

3.1 Overview

I will begin with an overview of the known characteristics of the DLAs, both individually and collectively (§3.2). Following this in §3.3 I will provide DIB equivalent widths and detection limits. I will then discuss several aspects of the DIBs in DLAs, including the relative DIB strengths (§3.3.2), the relationship between DIB strength and N(H I) (§3.3.3), the relationship between DIB strength and reddening (§3.4), and the use of DIB strength to derive gas-to-dust ratios (§3.5).

3.2 The DLA Sample

The first phase of the search for DIBs involved examining seven DLAs towards six QSOs, as shown in Tables 2.5, 2.6, and 2.13. The observational characteristics of the DLAs are shown in Table 3.1. The absorption redshifts range from $z = 0.091$ to $z = 0.525$, so that in all cases both the Ly α transition and the Zn II metal lines (considered the best description of metallicity in DLAs due to its close tracking of Fe II and its low dust depletion rate, e.g. Pettini et al. 1990, §II in particular, and

see §1.3.1) are still in the UV, and thus inaccessible to ground-based observations.[1] All of the targets have existing UV measurements of N(H I), and some also have measurements of Zn II and/or Fe II. The physical characteristics of the absorbers are shown in Table 3.2. The characteristics of the DLAs will be discussed in order from low to high redshift.

Table 3.1: DLA Observational Characteristics

QSO	m_V (mag)	z_{em}	z_{abs}	N(H I)/10^{20} (cm^{-2})	Refs
AO 0235+164	18.0[1]	0.940	0.524	50 ± 10	1, 2, 3
Q 0738+313	16.1	0.631	0.091	15 ± 2	4, 5
			0.221	7.9 ± 1.4	4, 5
B2 0827+243	17.3	0.940	0.518	2.0 ± 0.2	5, 6
PKS 0952+179	17.2	1.472	0.239	21 ± 3	5, 6
PKS 1127−145	16.9	1.184	0.313	51 ± 9	5, 7
Q 1229−020	16.8	1.043	0.395	5.6 ± 1.0	5, 8

[1] AO 0235+164 is extremely variable, and magnitudes as bright as $m_V = 16$ have been observed. Raiteri et al. (2007) has R-band data corresponding to our observation period.

NOTE m_V is the apparent V-band magnitude of the QSO, z_{em} the redshift of the QSO, z_{abs} the redshift of the DLA, and N(H I) the H I column density of the DLA. REFERENCES 1. Junkkarinen et al. (2004); 2. Odell et al. (1978); 3. Hagen-Thorn et al. (2008); 4. Rao & Turnshek (1998) 5. Rao et al. (2006); 6. Rao & Turnshek (2000); 7. Turnshek et al. (2003); 8. Boissé et al. (1998)

Since only 10% of QSOs are radio-loud, and only a small fraction of the DLAs towards radio-loud quasars have detected 21-cm absorption, it is remarkable (and remarkably fortunate) that 21-cm absorption has been detected in all of the DLAs which make up our sample. The H I 21-cm line is caused by the spin-flip transition of neutral hydrogen, and the ability of H I to absorb at 21-cm depends on its spin temperature (the relative population in the upper energy state), which in turn depends on its kinetic temperature, with low-temperature clouds having stronger absorption. In particular, the 21-cm optical depth (τ_{21}) of an optically thin cloud of neutral hy-

[1]While the DLA towards AO 0235+164 is at sufficiently high redshift that the Zn II lines at $\lambda\lambda$ 2026,2062 Å might be accessible from ground-based telescopes, the combination of atmospheric extinction and the faint target make such observations impractical.

drogen is related to the column density N(H I) and the spin temperature T_s by the equation (e.g. Rohlfs & Wilson 2006)

$$\mathrm{N(H\ I)} = \frac{1.823 \times 10^{18} T_s}{f} \int \tau_{21} \mathrm{d}V, \tag{3.1}$$

where f is the covering factor of the absorber, and represents the fraction of the background radio source actually covered by the absorbing H I cloud,[2] and dV represents the velocity width over which the absorption is integrated. If the cloud contains multiple phases of H I at different temperatures, T_s measures the column-density weighted harmonic mean of the temperatures of the individual phases (see e.g. Kanekar & Chengalur 2003 for a discussion of the use of spin temperature in DLA systems). A two-phase interstellar medium, with a cold dense phase [the cold neutral medium (CNM), with $T \sim 100$ K] and a warm phase [the warm neutral medium (WNM), with $T \sim 8000$ K] is stable over a range of temperatures and pressures (Wolfire et al. 1995). This two-phase medium has been observed not only locally, but also in dwarf galaxies (e.g. Young & Lo 1997) and DLAs (e.g. Lane et al. 2000, Kanekar et al. 2001). Using the above temperatures, the spin temperature of a given line of sight may be interpreted as

$$T_s = (\frac{f_{cold}}{T_{cold}} + \frac{f_{warm}}{T_{warm}})^{-1}, \tag{3.2}$$

with f_{cold} and f_{warm} the fractions of the total N(H I) in the cold and warm phases respectively. Kanekar & Chengalur (2003) examined the spin temperatures of DLAs associated with galaxies of known morphology, and determined that low T_s values were associated with spiral galaxies, while high T_s values were associated with dwarf

[2]Because the radio source in a quasar is likely much larger than the associated optical source, the gas cloud which provides the Lyα absorption may not completely cover the background radio source. The covering factor may be estimated by observing the QSO at high resolution (using an interferometer array), and then again at low resolution (at the same frequency). The ratio of the high-resolution core flux to the low-resolution total flux then provides an estimate of the covering factor. In the case of the DLAs used for the DIB search, covering factors were taken from Kanekar & Chengalur (2003).

and low surface brightness (LSB) galaxies, suggesting that spiral galaxies have much more of their N(H I) in the CNM phase than dwarf and LSB galaxies. The DLAs in our sample exemplify the T_s–morphology relationship, as shown in Table 3.2, and in the following paragraphs where each DLA is described in more detail.

Table 3.2: DLA Physical Characteristics

QSO	Host	N(H I)/10^{20} (cm^{-2})	[Zn/H]	[Fe/H]	T_s K	Refs.
AO 0235+164	Spiral	50 ± 10	—[1]	—[1]	210	1,2,3
Q 0738+313	LSB	15 ± 2	< -1.14	$-1.63^{+0.13}_{-0.18}$	825 ± 120	4,5,6,7
	Dwarf	7.9 ± 1.4	≤ -0.70	—	890 ± 165	4,5,6,8
B2 0827+243	Spiral	2.0 ± 0.2	< 0.30	-1.02 ± 0.05	330 ± 70	1,3,6,9,15
PKS 0952+179	Dwarf	21 ± 3	< -1.02	—	2055 ± 330	1,6,9,10
PKS 1127−145	Dwarf LSB	51 ± 9	—	> -2	910 ± 160	1,3,11,12
Q 1229−020	Spiral	5.6 ± 1.0	-0.47	< -1.32	170 ± 15	3,13,14

NOTE Host refers to the morphology of the DLA host galaxy, N(H I) to the DLA H I column density, [Zn/H] and [Fe/H] to the detected abundance of Zn and Fe relative to solar abundance, and T_s to the spin temperature of the absorber.

[1] $Z = 0.24 \pm 0.06 Z_\odot$ (Turnshek et al. 2003) or $Z = 0.72 \pm 0.28 Z_\odot$ (Junkkarinen et al. 2004).

REFERENCES 1. Rao et al. (2003); 2. Junkkarinen et al. (2004); 3. Kanekar & Chengalur (2003); 4. Turnshek et al. (2001); 5. Rao & Turnshek (1998), 6. Kulkarni et al. (2005); 7. Lane et al. (2000); 8. Kanekar et al. (2001); 9. Rao & Turnshek (2000); 10. Kanekar & Chengalur (2001); 11. Turnshek et al. (2003); 12. Lawton et al. (2008); 13. Steidel et al. (1994); 14. Boissé et al. (1998); 15. Khare et al. (2004)

Uncertainties are 1 σ, while upper limits are 3 σ.

Q0738+313, z=0.091 This DLA was identified by Turnshek et al. (2001) as associated with a low surface brightness (LSB) galaxy, with a measured impact parameter[3] of $< 3.5 h_{70}^{-1}$ kpc.[4] The DLA has a relatively high column density of $1.5 \pm 2 \times 10^{21}$ cm^{-2} (Rao & Turnshek 1998), and 21-cm absorption corresponding to a spin temperature $T_s = 825 \pm 120$ K (Kanekar & Chengalur 2003). Lane et al. (2000) found that the 21-cm absorption required a three-component fit, with a broad component ($T_s = 5050 \pm 950$ K) and two narrow components ($T_s = 297 \pm 3$ K and $T_s = 103 \pm 10$ K), with 70–80% of the H I in the warm component, a situation which resembles the ISM of local dwarf galaxies (Young & Lo 1997). Kulkarni et al. (2005)

[3] The impact parameter (b) measures the physical separation corresponding to a given redshift (i.e. cosmological distance) and angular separation.

[4] The associated galaxy is $< 2\farcs0$ from the QSO, making a precise measurement of the impact parameter difficult (Turnshek et al. 2001).

used HST observations to derive an upper limit of [Zn/H] < -1.63 based on the Zn II lines at 2026 and 2062 Å, and [Fe/H] $= -1.63^{+0.13}_{-0.18}$ based on the Fe II line at 2600 Å.

Q0738+313, z=0.221 This DLA has an N(H I) of $7.9 \pm 1.4 \times 10^{20}$ cm^{-2} (Rao & Turnshek 1998), and a T_s of 890 ± 165 K (Kanekar et al. 2001), with a warm neutral medium (WNM) fraction of 70–80%. Kanekar et al. (2001) find that the ISM here is best fit by three components, with the WNM component at $T_k = 7600 \pm 1250$ K, and CNM components with $T_k = 308 \pm 24$ K and $T_k = 180 \pm 30$ K.[5] Kulkarni et al. (2005) placed an upper limit on this system's metallicity of [Zn/H] ≤ -0.70. Turnshek et al. (2001) identified this DLA as being associated with with a dwarf spiral galaxy with an impact parameter of $20.5h_{70}^{-1}$ kpc.

PKS 0952+179 This DLA has N(H I) $= 2.1 \pm 0.3 \times 10^{21}$ cm^{-2} (Rao & Turnshek 2000), and the highest spin temperature in the sample at $T_s = 2055 \pm 330$ K (Kanekar & Chengalur 2001). Rao et al. (2003) found two possible absorbing galaxies, both with impact parameters $< 4.6h_{70}^{-1}$, and both of which appear to be edge-on dwarf galaxies. Kanekar & Chengalur (2001) derived a covering factor $f \geq 0.25$ from VLBA observations at 2.3 GHz, which found that the radio source consisted of three components in a $0\farcs4$ central region which when combined accounted for $\sim 25\%$ of the total flux. Assuming $f = 0.25$, the spin temperature is then $T_s = 330$ K, which suggests a system dominated by the WNM. T_s would only increase if the true covering factor were higher. The metallicity value [Zn/H] < -1.02 was derived based on the non-detection of Zn II in Kulkarni et al. (2005).

PKS1127−145 This $z = 0.313$ DLA has the highest measured N(H I) in our sample, at $5.1 \pm 0.9 \times 10^{21}$ cm^{-2} (Turnshek et al. 2003), but a relatively high T_s at 910 ± 160 K (Kanekar & Chengalur 2003). The absorbing galaxy has been identified as a tidally disturbed dwarf LSB galaxy which extends into the point spread function (PSF) of the quasar, limiting the accuracy of the impact parameter $b = 6.9h_{70}^{-1}$ kpc

[5] T_k values from Kanekar et al. (2001) show the kinetic temperatures of the components of the multi-component model used to fit the detected 21-cm absorption.

Table 3.3: DLA Detections and Limits, calculated based on SNR

QSO	z_{abs}	DIB	Wavelength (Å)	SNR	Rest EW (mÅ)
AO 0235+164	0.524	4428	6752	—	742 ± 26[1]
		5705	8697	150	63.2 ± 8.7
		5780	8812	155	216 ± 9
		5797	8837	58	< 155
		6284	9580	44	< 214
		6613	10082	61	< 158
Q 0738+313	0.091	4428	4833	235	< 56
		5780	6308	34	< 199
		5797	6326	99	< 68
		6284	6858	350	< 19
		6613	7218	42	< 161
Q 0738+313	0.221	4428	5409	55	< 264
		5780	7060	200	< 30
		5797	7080	75	< 81
		6284	7675	20	< 302
B2 0827+243	0.525	4428	6756	30	< 95
		5780	8818	30	< 39
		5797	8843	30	< 27
PKS 0952+179	0.239	4428	5489	300	< 67
		5780	7164	400	< 27
		5797	7184	92	< 117
		6284	7788	300	< 37
		6613	8197	65	< 177
PKS 1127−145	0.313	5780	7592	62	< 500[2]
		5797	7613	58	< 500[2]
		6284	8253	50	< 352
		6613	8686	29	< 623
Q 1229−020	0.395	5780	8066	145	< 65
		5797	8089	125	< 75
		6284	8769	150	< 65
		6613	9228	69	< 146

Limits are 5 σ, while errors are 1 σ

[1] Junkkarinen et al. (2004)

[2] Limits established by simulation due to presence of telluric absorption, see §3.3.1 for details.

to the radius of the circle that includes all residuals left over from subtracting the quasar PSF (Rao et al. 2003). The metallicity value [Fe/H] > -2[6] was obtained by

[6]Because the available Fe II lines were saturated, only a lower limit to the metallicity could be derived.

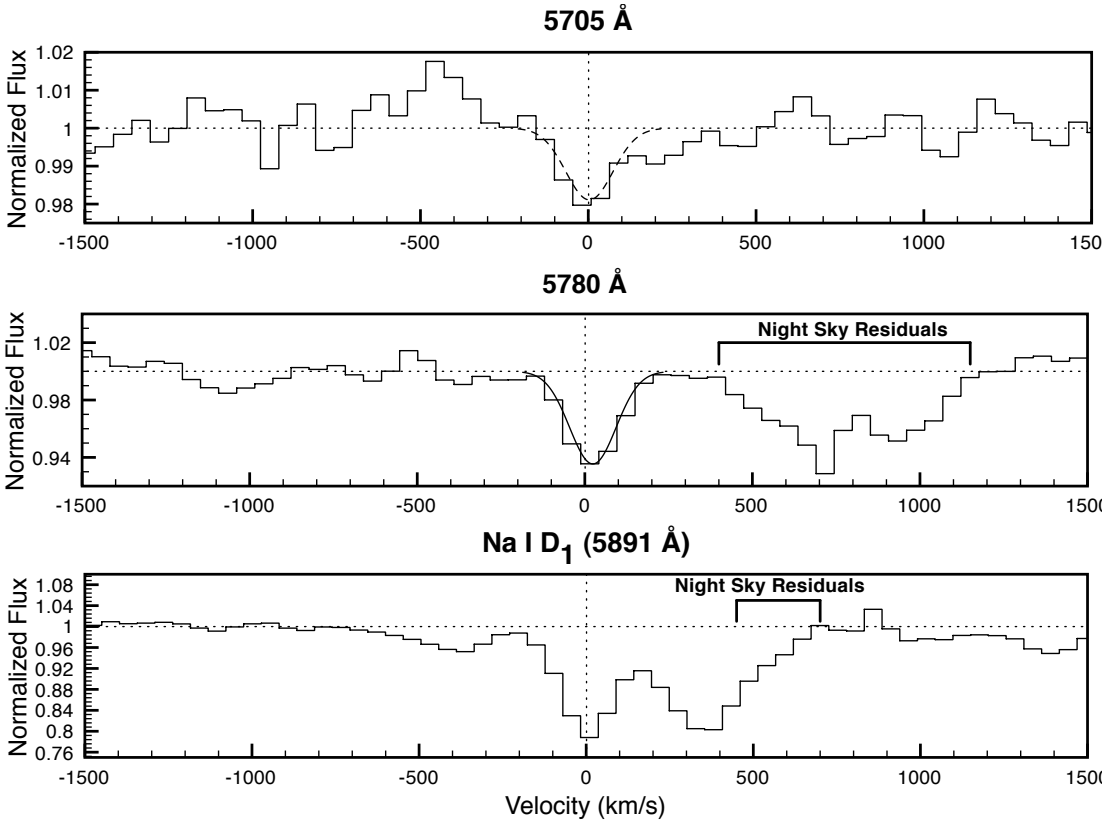

Figure 3.1: The 5705 and 5780 Å DIBs towards AO 0235+164, along with the Na I D_1 line. These features have been converted into velocity space relative to $z = 0.5238$. The histograms show the absorption lines, the vertical dotted lines 0 km s^{-1} relative velocity, and the dashed curves gaussian profiles with equivalent widths the same as the DIB EW.

Lawton et al. (2008) using a VLT/UVES spectrum obtained by Dr. M. Murphy.

Q 1229−020 This $z = 0.395$ DLA has N(H I) $= 5.6 \pm 1.0 \times 10^{20}$ (Boissé et al. 1998), and a low measured spin temperature $T_s = 170 \pm 15$ K (Brown & Spencer 1979), based on a measured covering factor of 0.5 (Kanekar & Chengalur 2003). Steidel et al. (1994) find that the associated galaxy at an impact parameter of $8.2h_{70}^{-1}$ kpc has colours consistent with a spiral, while Le Brun et al. (1997) suggest that the object is fainter than would be expected for a spiral, and instead suggest an LSB galaxy. Le Brun et al. (1997) note that the WFPC2 detector they employed is not very sensitive to LSB emission, raising the possibility that the brightness found with

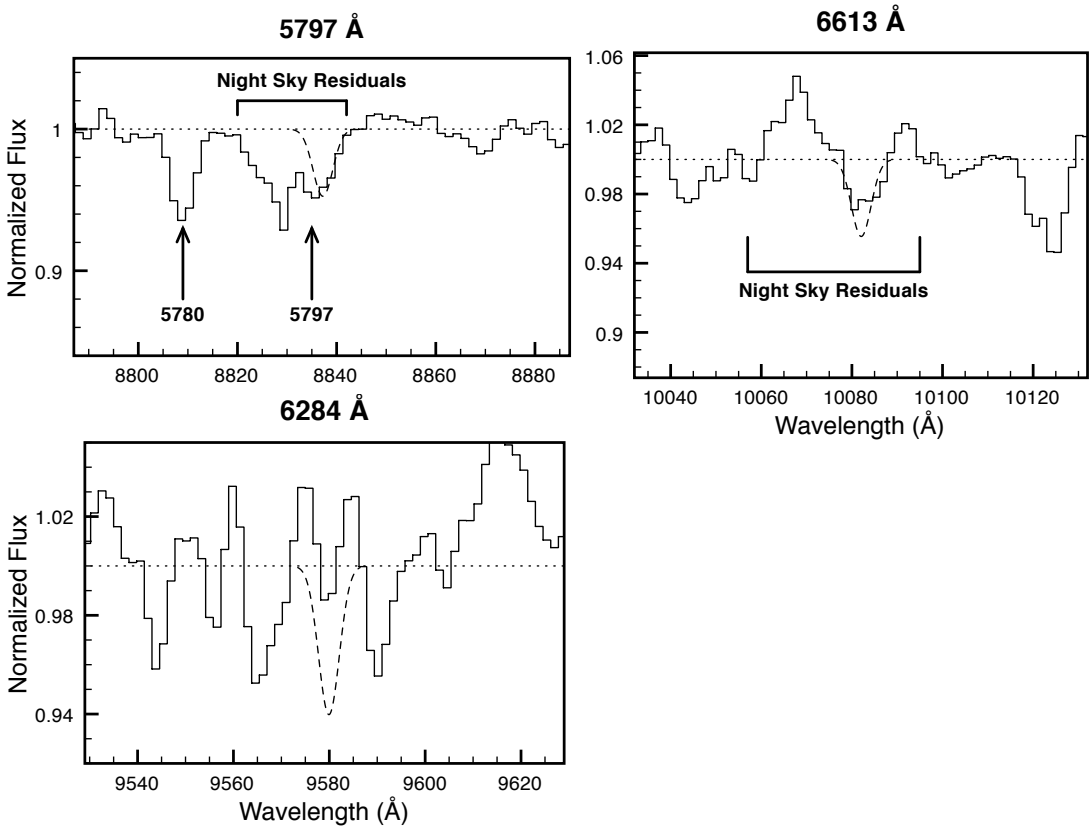

Figure 3.2: Upper limits on DIB strength towards AO 0235+164. In all cases, the histogram is the normalized spectrum, while the dashed lines are the 5-σ limits.

the CFHT, $m_R = 22.1$, is more accurate than the $m_{702} = 23.1$ from WFPC2. The measured metallicity of [Zn/H] $= -0.47$ (Boissé et al. 1998) is quite high for a DLA, commensurate with the low T_s and possibility of a spiral galaxy.

AO 0235+164 The $z = 0.524$ DLA towards the BL Lac object AO 0235+164 is unique in our sample for a variety of reasons. It is the only DLA in our sample with a previous diffuse interstellar band detection (the 4428 Å DIB was detected by Junkkarinen et al. 2004), it has an extinction value $E(B-V) = 0.23$, and it has a measured dust extinction curve which includes the 2200 Å bump also found in the Milky Way extinction curve (Junkkarinen et al. 2004). The $E(B-V)$ was obtained by Junkkarinen et al. (2004) through modelling the underlying QSO spectrum as a power

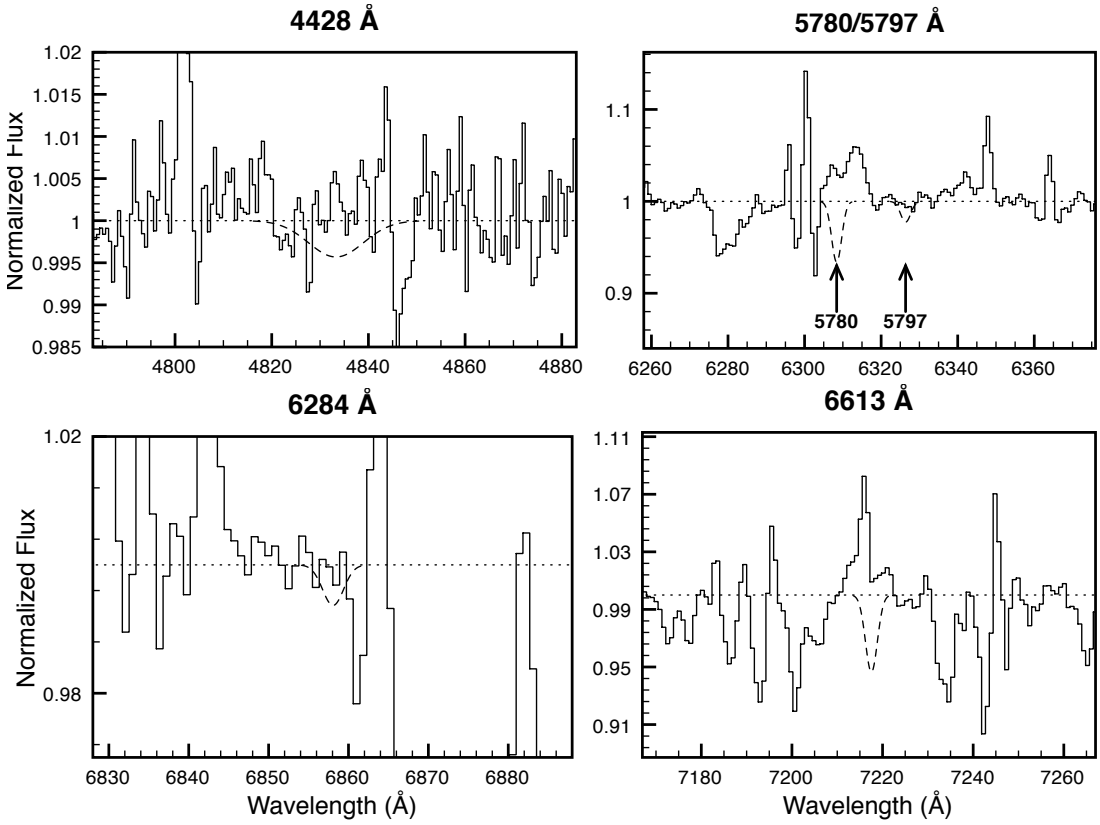

Figure 3.3: Upper limits on DIB strength in the $z = 0.091$ DLA towards Q 0738+313. In all cases, the histogram is the normalized spectrum, and the dashed lines are 5-σ limits.

law, and then fitting a Galactic extinction curve to the measured QSO spectrum. The measured spin temperature is quite low at $T_s = 210$ K, with four primary absorption components, all variable (Wolfe et al. 1982). The field surrounding the QSO, imaged by Burbidge et al. (1996), revealed multiple galaxies near the absorption site. Rao et al. (2003) note that the closest galaxy, with impact parameter $6.7h_{70}^{-1}$, is a late-type spiral. Chen & Lanzetta (2003), however, note that there are at least three galaxies within $62h_{70}^{-1}$ kpc of the QSO, all of which are at the proper redshift for the absorption. This result, combined with the multi-component 21-cm absorption, suggests that the DLA absorption may be due to the combination of multiple absorbing objects. No optical metallicity measurements have been made of the DLA, but two groups have

taken X-ray observations, with Chandra (Turnshek et al. 2003), as well as ASCA and ROSAT (Junkkarinen et al. 2004). Turnshek et al. (2003) derived a metallicity $Z = 0.24 \pm 0.06 Z_{\odot}$, while Junkkarinen et al. (2004) found $Z = 0.72 \pm 0.28 Z_{\odot}$, both assuming solar abundance ratios and solar metallicity for the foreground Galactic absorption. Junkkarinen et al. (2004) state that the difference in the results may be due to different noise realizations, as well as the intrinsic variability of the QSO. A metallicity of $0.26 Z_{\odot}$ corresponds to [X/H] $= -0.61$, while $0.72 Z_{\odot}$ corresponds to [X/H] $= -0.14$, making this system potentially the most metal-rich DLA in the sample.

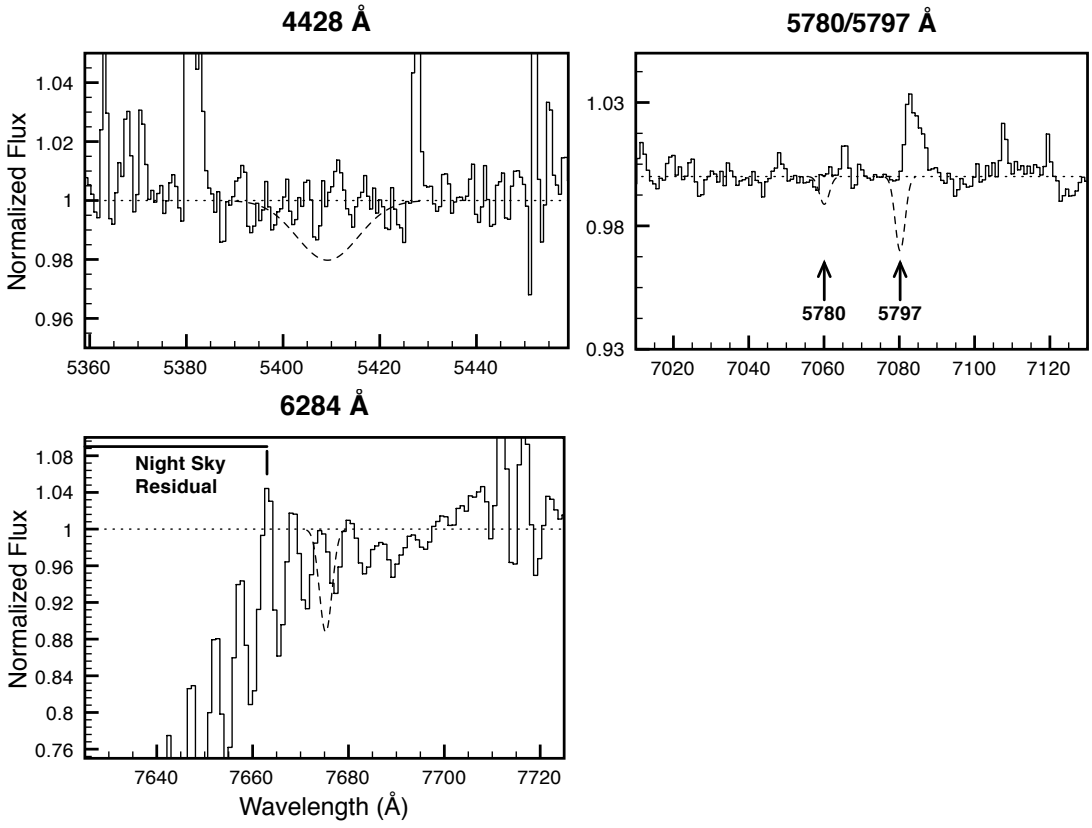

Figure 3.4: Upper limits on DIB strength in the $z = 0.221$ DLA towards Q 0738+313. In all cases, the histogram is the normalized spectrum, and the dashed lines are 5-σ limits.

B2 0827+243 The DLA found at $z = 0.525$ towards B2 0827+243 has a relatively

low N(H I) value [N(H I) = $2.0 \pm 0.2 \times 10^{20}$ cm^{-2}, Rao & Turnshek 2000] and a low spin temperature of $T_s = 330 \pm 70$ K (Kanekar & Chengalur 2003). The metallicity [Zn/H] < 0.30 is from Kulkarni et al. (2005), whilst [Fe/H] $= -1.02 \pm 0.05$ is from Khare et al. (2004). Rao et al. (2003) suggests that the host galaxy is a disturbed spiral with impact parameter $38.2 h_{70}^{-1}$ kpc, with the absorption originating in extended gas.

3.3 Results

I will begin by describing the DIBs that were detected and the limits that were established in §3.3.1, including a discussion of the removal of telluric absorption in the spectrum of PKS 1127−145, and how the detection limits were derived in that case. I will discuss the relative strengths of the various DIBs in §3.3.2, and compare these results to those obtained along sightlines in the Milky Way and the Magellanic Clouds. DIB strengths are known to vary along different sightlines in the Milky Way (see e.g. Cami et al. 1997) and these variations are attributed to differences in the physical conditions along these sightlines. §3.3.3 combines the DIB strengths with the N(H I) values of the DLAs to determine whether the DLAs fall on the Galactic relationship between H I column density and EW_{5780} (Herbig 1993).

The DIB strengths shown in §3.3.1 may also be used to derive information about the host DLAs. The diffuse bands are known to correlate with $E(B-V)$ (Herbig 1993), so the strength of the diffuse bands can therefore be used to constrain the $E(B-V)$ of the DLAs, as shown in §3.4. In addition, the reddening values may be used to constrain the gas-to-dust ratios of the DLAs, as is shown in §3.5.

3.3.1 DIB Detections and Limits

Only two DIBs were detected in our sample, both in the DLA towards AO 0235+164. The 5780 Å DIB was detected with an equivalent width of 216 ± 9 mÅ and the 5705 Å DIB was detected with an equivalent width of 63.2 ± 8.7 mÅ (York et al. 2006). Only

upper limits are available for the other DIBs and DLAs. Table 3.3 shows the limits derived from the signal-to-noise ratios of the spectra in the region of the DIBs [see Equation (2.2)], and converted to the rest limit. Lawton et al. (2008) also provides limits for these DLAs, calculated by an independent method. In general, Lawton et al. (2008) derives slightly more conservative limits for the same lines, although the values are usually very close. For a graphical representation of the limits in Table 3.3 compared to the normalized spectra, see Figures 3.2 to 3.9.

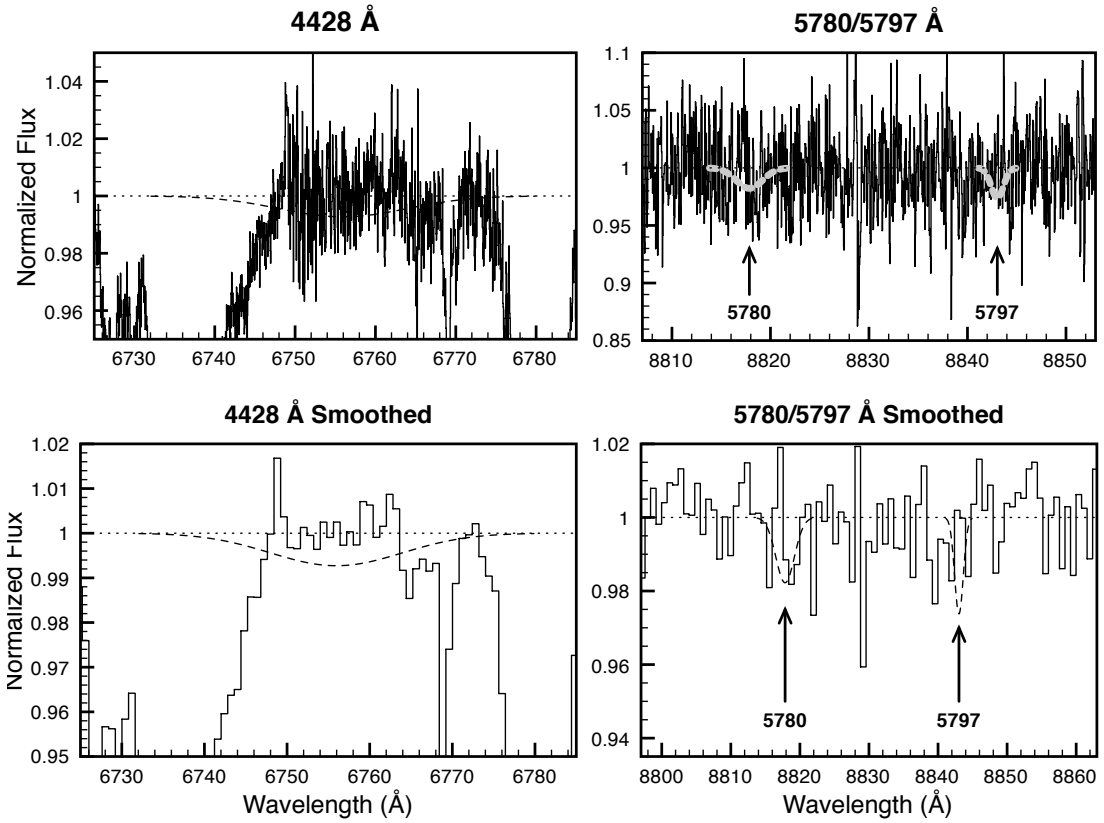

Figure 3.5: Upper limits on DIB strength in B2 0827+243. The top panels show the original Keck HIRES spectra, while in the bottom panels the spectra have been smoothed to 0.8 Å pix^{-1} in order to show the DIB detection limits more clearly. In all cases, the histogram is the normalized spectrum, and the dashed lines are 5-σ limits.

Telluric Corrections for PKS 1127−145

No diffuse bands were detected in the spectrum of PKS 1127−145 even after telluric removal, but the possibility existed that DIBs had been present, but were removed (along with the telluric absorption) by IRAF's `telluric` package (see §2.3.3 for a description of how telluric removal was performed). In order to quantify how strong a DIB would have to be before it would be apparent even after telluric removal, a series of simulations were performed. Simulated absorbers representing the 5780 Å DIB were constructed with various strengths (EW_{5780} = 100, 200, 300, 400, 500, 1000, 10000 mÅ), convolved to the resolution of GMOS-South, and then added to the spectrum of PKS 1127−145 before the telluric removal was performed. The additions were performed through combining optical depth (τ), where $I/I_0 = e^{-\tau}$, and $\tau_{final} = \tau_1 + \tau_2$.

After the simulated absorber was added to the QSO spectrum, the `telluric` package was used to remove the telluric absorption, both using the same parameters as were used for the unmodified spectrum, and varying the parameters in order to produce the minimum residual telluric absorption. The resulting spectrum was then normalized and searched for absorption lines. Table 3.4 shows the resulting measured absorption for EW_{5780} values ranging from 0 to 500 mÅ. The measured absorption tended to be greater than the added absorber's EW by $\sim$ 20 mÅ, except that, for the 500 mÅ simulated absorber, the minimum-residual method resulted in a large overestimate. Figure 3.6 shows the final absorption caused by the 100, 300, and 500 mÅ simulated absorbers. By 500 mÅ, the absorber, even after telluric removal, was as strong as the already-present absorption line around 7680 Å, indicating that this is a conservative upper limit.

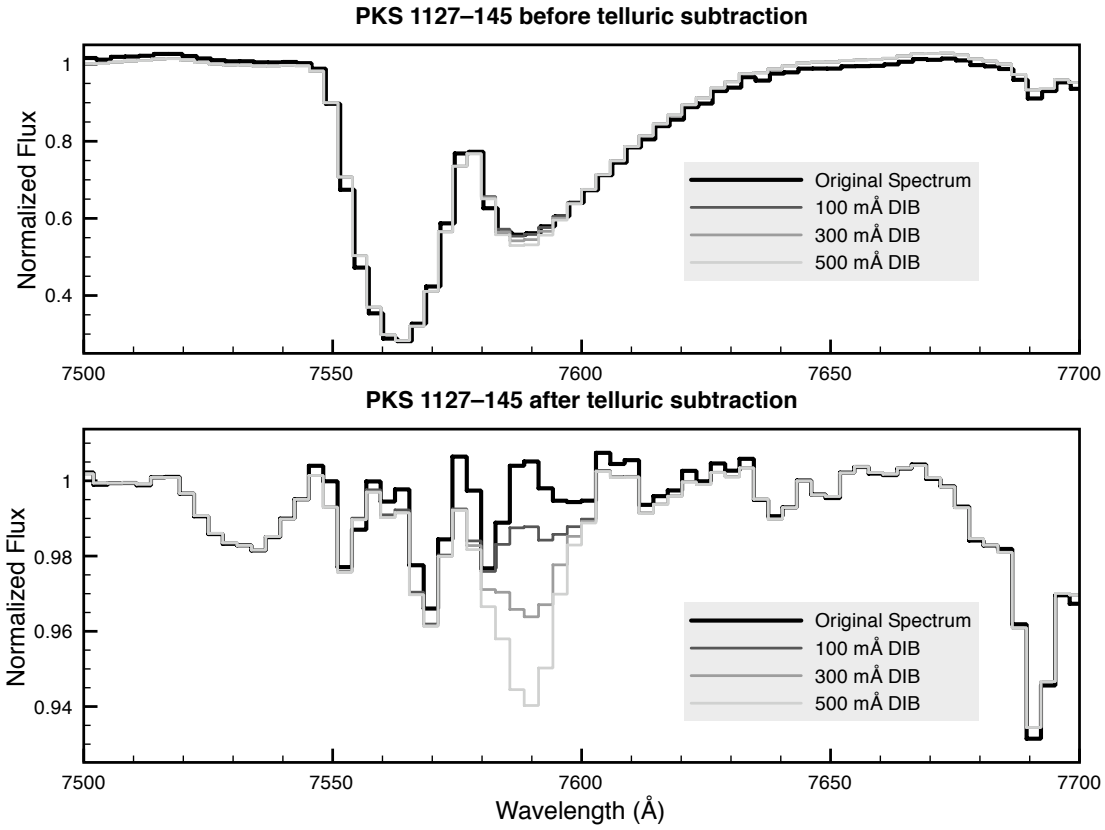

Figure 3.6: The spectrum of PKS 1127−145 showing the region affected by the telluric line. The top panel shows both the original spectrum and the original spectrum after simulated DIB absorption has been added, while the bottom panel shows the spectrum after telluric removal, again both with and without the simulated DIB absorption added. Table 3.4 shows both the measured and simulated absorption.

Table 3.4: Measured vs. Simulated DIB strength after telluric removal

Simulated EW (mÅ)	With Optimal Removal (mÅ)	With Minimum-Residual Removal (mÅ)
0	0	0
100	0	0
200	387	422
300	492	529
400	604	613
500	694	927
1000	1182	1102

3.3.2 Relative DIB Strengths

On Galactic sightlines, the relative strengths of the diffuse bands may be used to derive information about the environmental conditions along the sightline. Cami

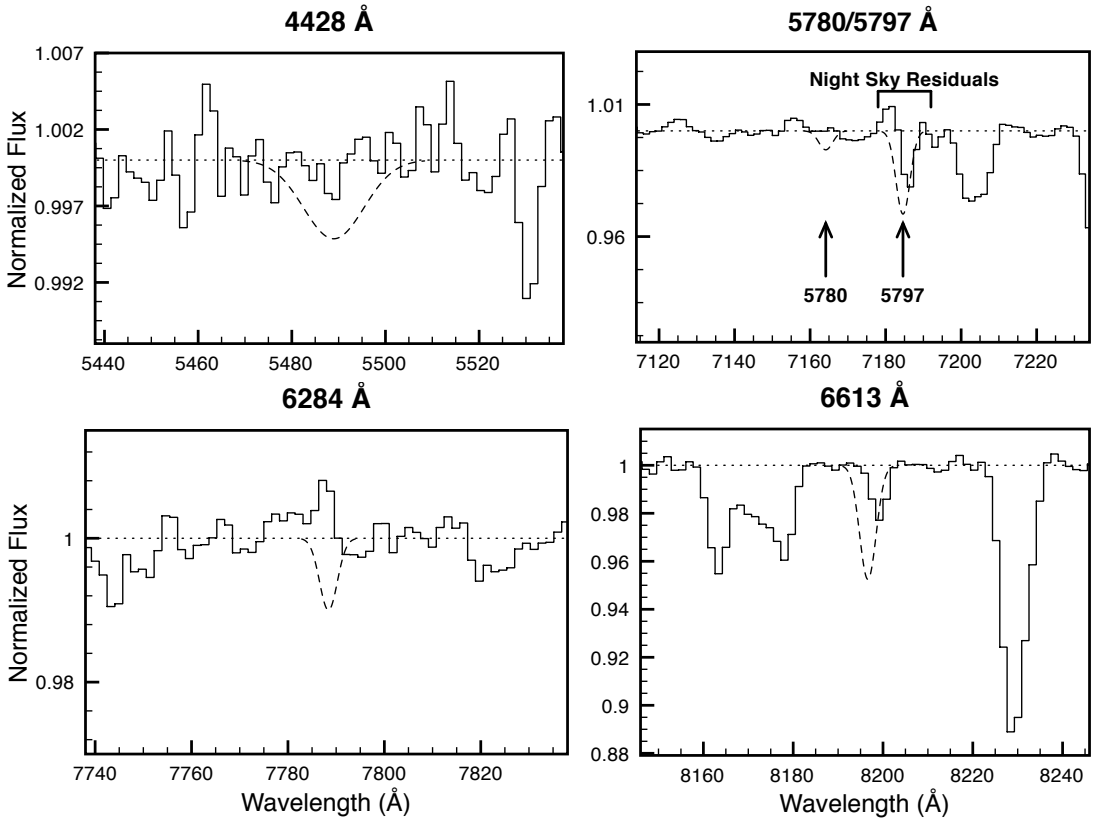

Figure 3.7: Upper limits on DIB strength in PKS 0952+179. In all cases, the histogram is the normalized spectrum, and the dashed lines are 5-σ limits.

et al. (1997) find that the relative strength of the 5780 and 5797 Å DIBs varies with the UV field, with the 5797 Å DIB being stronger along sightlines with a low UV field and the 5780 Å DIB growing stronger (and the 5797 Å DIB growing weaker) as the UV field increases. Although there are no tight correlations amongst the strong DIBs at 5780, 5797, 6284, and 6613 Å, there are general trends which are observed almost universally. The 6284 Å DIB, for example, is at least twice as strong as the 5780 Å DIB when both are detected (Herbig 1995), and this trend extends to the Magellanic Clouds (with the exception of a single sightline) (Welty et al. 2006) and to local starburst galaxies (Heckman & Lehnert 2000). Figure 3.10 shows the relative strengths of the DIBs in the sightline towards AO 0235+164 along with a sample of

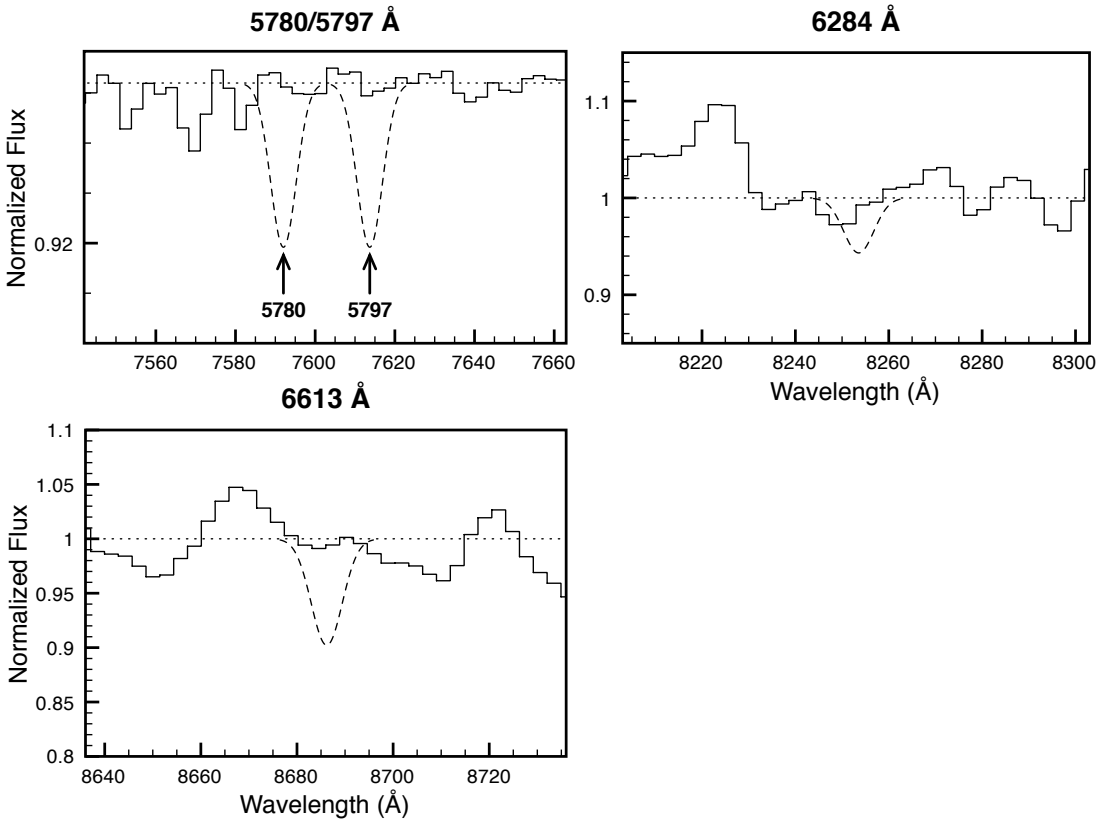

Figure 3.8: Upper limits on DIB strength in PKS 1127−145. In all cases, the histogram is the normalized spectrum, and the dashed lines are 5-σ limits.

Galactic and extra-galactic sightlines.

As is shown in Figure 3.10, the relative ratios of the 5780 and 6284 Å DIBs in the sightline towards AO 0235+164 are inconsistent with every sightline shown except that towards Sk 143 in the SMC. Note that the Sk 143 sightline is not typical even of the SMC, as the AV 476 sightline shows. Ehrenfreund et al. (2002) note that the sightline towards Sk 143 is part of the SMC wing, and offers a more protected environment than other SMC sightlines. The sightline also shows traces of the 2175 Å bump in its extinction curve, whereas other SMC sightlines show no trace of the bump, and LMC sightlines show a much smaller bump than sightlines in the Milky Way (Pei 1992). The 2175 Å feature is also rare amongst DLAs, although Junkkarinen

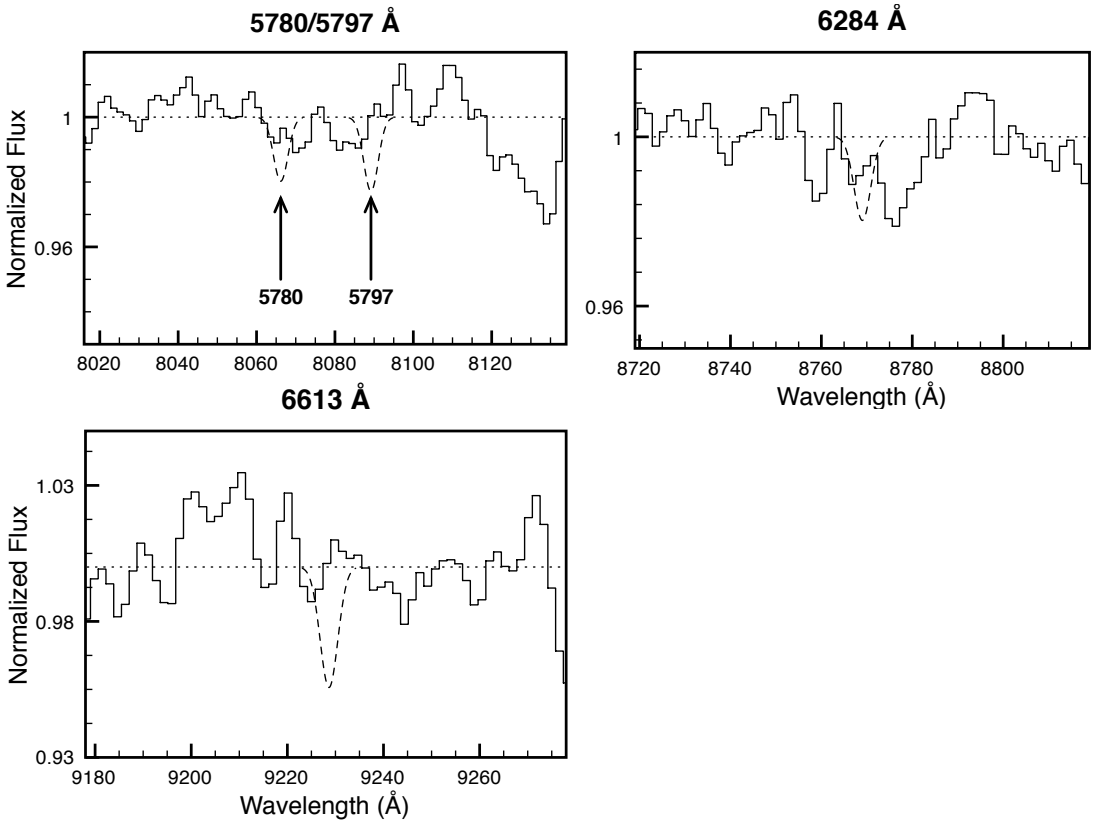

Figure 3.9: Upper limits on DIB strength in PKS 1229-020. In all cases, the histogram is the normalized spectrum, and the dashed lines are 5-σ limits.

et al. (2004) detected it in the DLA towards AO 0235+164. Note however that linking the 2175 Å feature to the *presence* of DIBs is likely a red herring, as strong DIBs have been detected towards starburst galaxies in which the 2175 Å feature is definitely absent (Heckman & Lehnert 2000).

Cox et al. (2006) note that the 6284 Å DIB is weak in the LMC compared to its Galactic value (see the two leftmost panels in Figure 3.10), and suggest that this may be due to a softer UV field with a high far-UV rise suppressing the formation of the ionized carrier. Cami et al. (1997) further find that the EW_{5797}/EW_{5780} ratio depends on the strength of the UV background, with the 5797 Å DIB becoming weaker as the UV background becomes stronger. Towards AO 0235+164, $EW_{5797}/EW_{5780} \leq 0.71$,

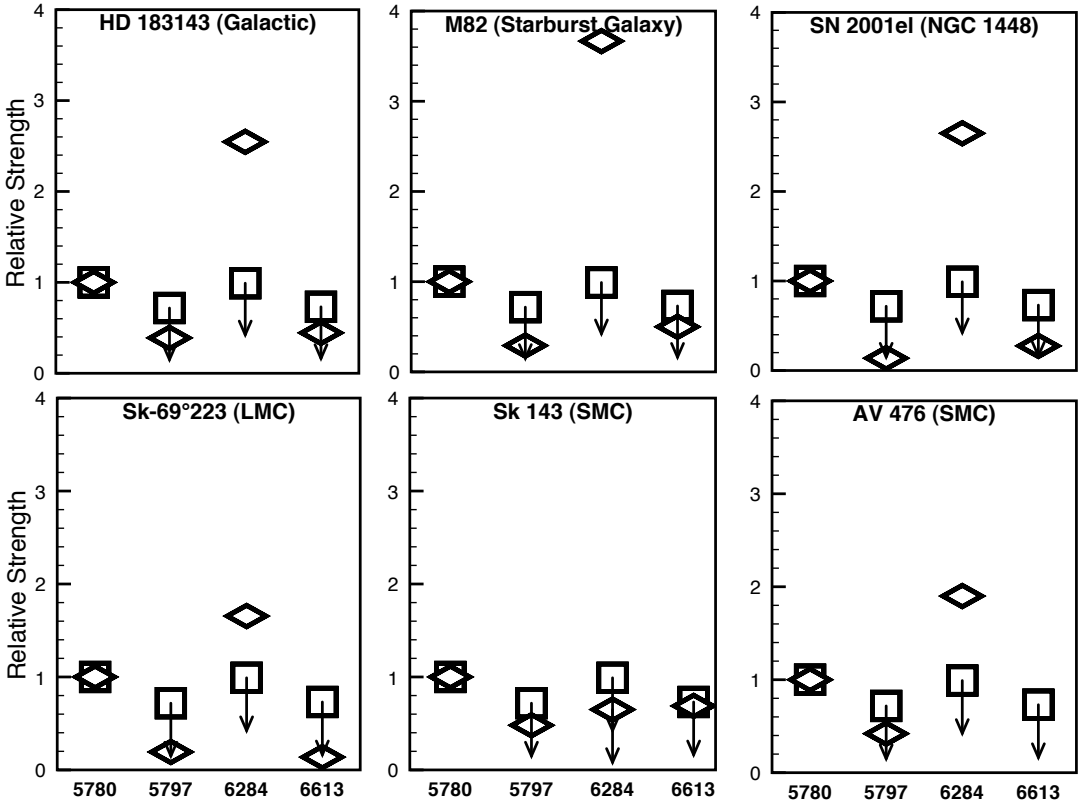

Figure 3.10: Relative strengths of the DIBs at 5780, 5797, 6284, and 6613 Å along a variety of sightlines, normalized to the strength of the 5780 Å DIB. In all cases the squares show the results from AO 0235+164, whilst the diamonds show the results from the other system. See Tables B.1 and B.2 for DIB equivalent widths on these sightlines.

while $EW_{6284}/EW_{5780} \leq 0.99$, indicating that the 5797 Å DIB is suppressed relative to the 5780 Å DIB when compared to ζ-type clouds (see §1.2.2 for a description of the cloud types), and the 6284 Å DIB suppressed relative to the 5780 Å DIB when compared to all Galactic and almost all extragalactic sightlines. The combined evidence thus points to a sightline where the UV background is both strong and soft. This would be consistent with the sightline towards Sk 143, which also has $EW_{6284}/EW_{5780} < 1$, where Ehrenfreund et al. (2002) find a more protected, softer UV background than is typical of the SMC.

In addition to the 5780 Å DIB, the 5705 Å DIB was also detected in the absorber

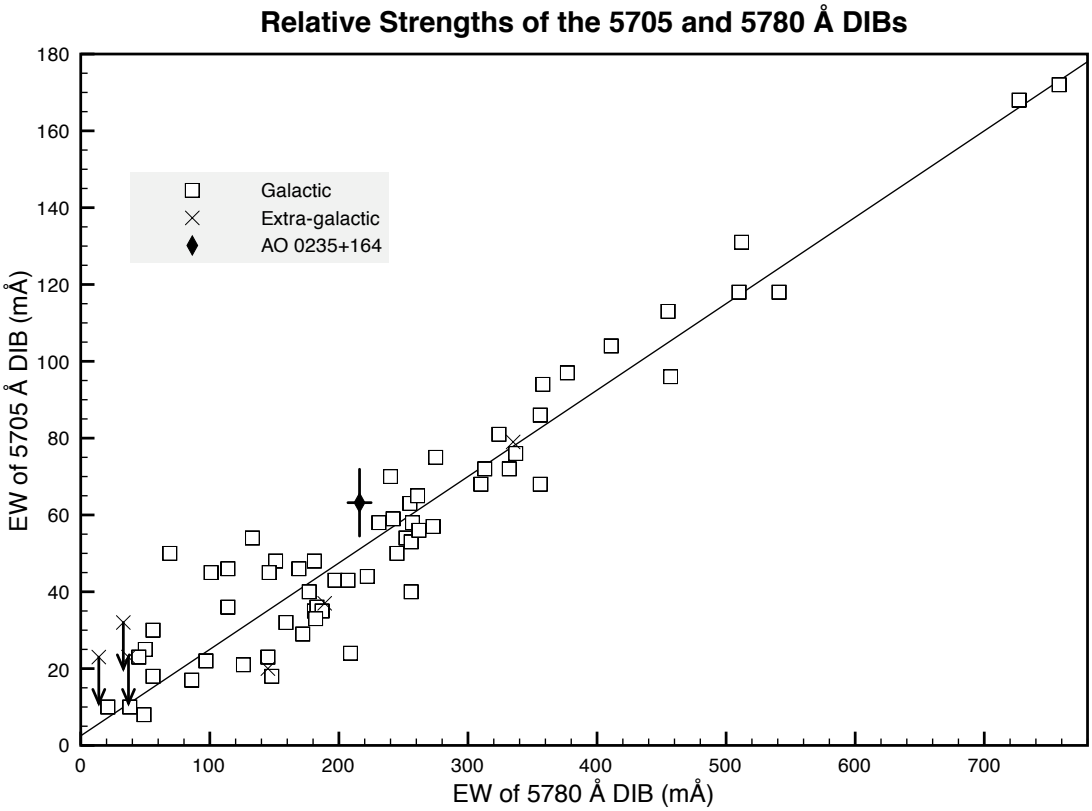

Figure 3.11: Relative strengths of the 5705 and 5780 Å DIBs. Galactic data taken from Table B.2, and extragalactic data from Table B.1.

towards AO 0235+164. Thorburn et al. (2003) noted that these two DIBs are correlated in the Galaxy, and the 5705 Å DIB towards AO 0235+164 is within 10 mÅ of the predicted width, consistent with its 1-σ error bars plus the small additional scatter in the relation (see Figure 3.11). That these two DIBs are correlated in the DLA as well as the Galaxy strongly suggests that the carriers of these DIBs are either closely related or react similarly to changes in their environment. In addition to its relationship with the 5705 Å DIB, the 5780 Å DIB is also correlated with other features of Galactic sightlines, and these relationships will be examined below.

3.3.3 Relationship between DIB strength and N(H I)

In addition to correlations between the diffuse bands, the DIBs correlate with a number of other elements. The relationship between the 5780 Å DIB EW and the neutral hydrogen column density is one of the tightest correlations known between the diffuse bands and gas-phase atoms. The initial relationship was shown in Herbig (1993), and has been confirmed and extended with additional data (D. York, private communication). While the relationship has a low scatter over several orders of magnitude in the Milky Way, Welty et al. (2006) found that both the Large and Small Magellanic Clouds had weaker DIBs than would be predicted by the relationship (see Figure 3.12). Our sole detection of the 5780 Å DIB, towards AO 0235+164, is similarly weaker than would be predicted from the N(H I) towards AO 0235+164. In addition, four of the DLAs in our sample (towards PKS 1127−145, PKS 0952+179, and both DLAs towards Q 0738+313) have upper limits for the strength of the 5780 Å DIB that are inconsistent with their N(H I) values according to the relationship. Whilst the DLAs towards Q 0738+313 [N(H I) = 1.5×10^{21},7.9×10^{20} cm^{-2}] would be within the scatter of the Galactic relationship if the upper limit on the DIB strength were treated as a detection, the DLA towards PKS 0952+179 [N(H I) = 2.1×10^{21} cm^{-2}] is clearly beyond the Galactic scatter, with the 5780 Å DIB weaker than Galactic by a factor of 17, and the DLA towards PKS 1127−145 (N(H I) = 5.1×10^{21} cm^{-2}) is at a higher N(H I) than any of the Galactic points, making a determination of the offset highly uncertain.

This same trend is even more obvious when the 6284 Å DIB is plotted against N(H I), as shown in Figure 3.13, a result consistent with the weakness of the 5780 Å DIB relative to N(H I) in the DLAs observed, and with the weakness of the 6284 Å DIB relative to the 5780 Å DIB towards AO 0235+164 (see §3.3.2). Here, five of the six DLAs are inconsistent with the Galactic relationship (B2 0827+243 does not have a limit for the 6284 Å DIB), and three of the DLAs are inconsistent with the

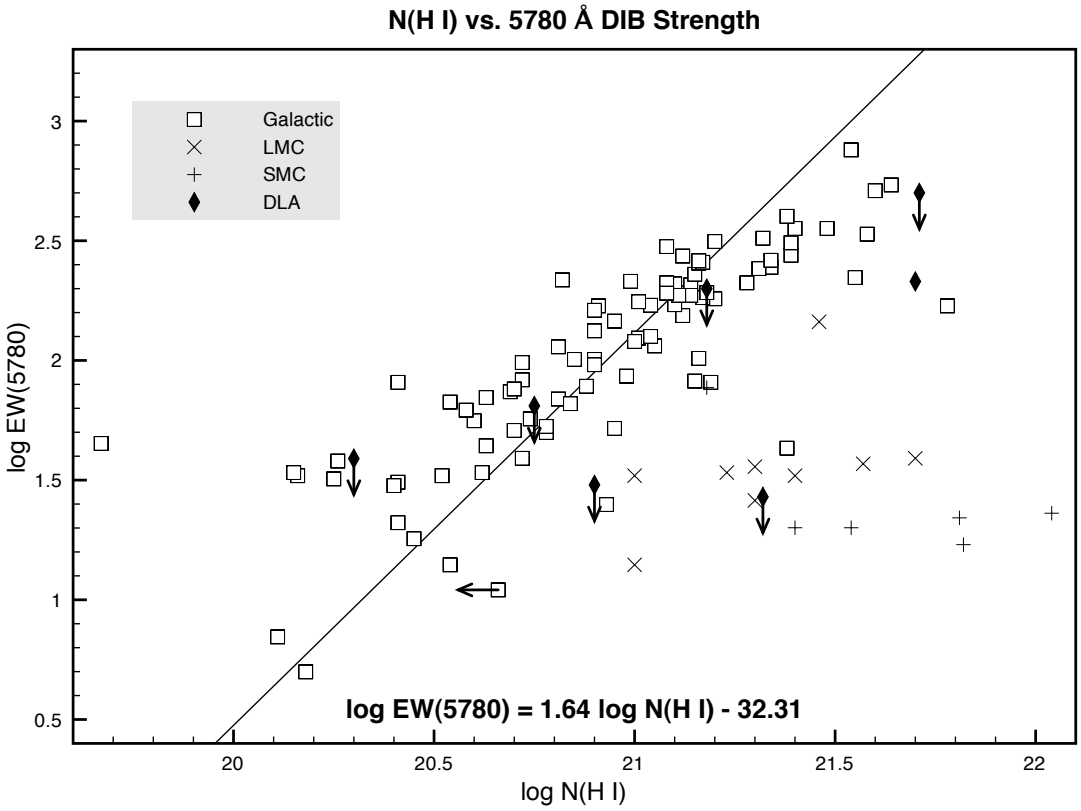

Figure 3.12: The relationship between N(H I) and the 5780 Å DIB. The best fit line was calculated based only on Galactic points, as presented in Ellison et al. (2008). Galactic data from Table B.2, and LMC and SMC data from Table B.1.

LMC values. This is a clear demonstration that the 5780 and 6284 ÅDIBs in DLAs are inconsistent with the Galactic relationship with N(H I).

3.4 DIB Strength and Reddening

In addition to the relationship between N(H I) and the 5780 Å DIB, there is a relationship between $E(B-V)$ and the 5780 Å DIB. Herbig (1993) shows the relationship in the Milky Way, and Welty et al. (2006) demonstrates that DIBs detected in the Magellanic Clouds still match the Galactic relationship quite well. Of the DLAs in our sample, only AO 0235+164 has a known $E(B-V)$ value, with $E(B-V) = 0.23$ (Junkkarinen et al. 2004). As shown in Figure 3.14, this value falls on the same

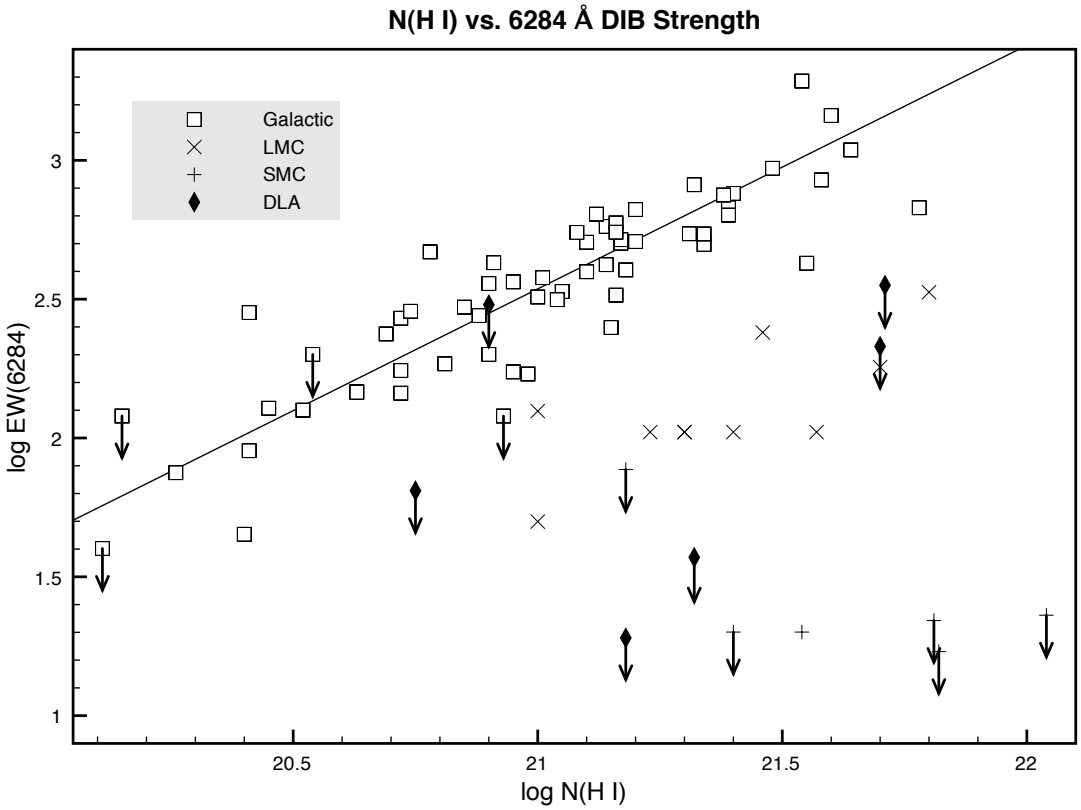

Figure 3.13: The relationship between N(H I) and the 6284 Å DIB. The best fit line was taken from Welty et al. (2006), Galactic data points from Table B.2, and extragalactic data points from Table B.1.

relationship as known Galactic and local extra-galactic DIBs.

While none of the other DLAs in this sample have measured values for $E(B-V)$, if we assume that the Galactic relationship applies (as indeed it seems to based on the existing Galactic, extra-galactic and DLA data points) we may then derive upper limits on $E(B-V)$ for the remaining DLAs based on the relationship. These limits are shown in Table 3.5, derived separately for the 5780 Å DIB (as shown in Figure 3.14) and the 6284 Å DIB (as shown in Figure 3.15). Typical limits are $E(B-V) < 0.1$, with some as sensitive as $E(B-V) < 0.01$. Ellison et al. (2005a) found that DLAs in the redshift range $1.9 \leq z \leq 3.5$ on sightlines towards radio-selected QSOs had

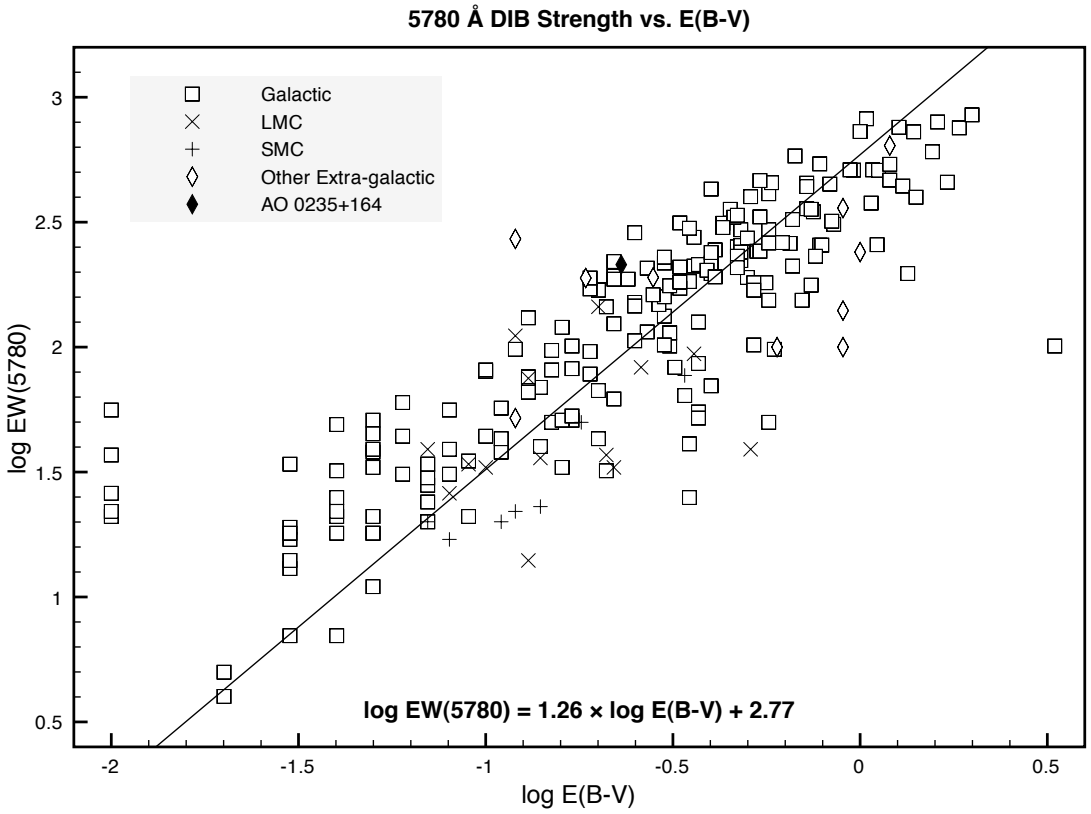

Figure 3.14: The relationship between $E(B-V)$ and the 5780 Å DIB. The best fit line was presented in Ellison et al. (2008), and includes all data points, both Galactic and extragalactic. Extragalactic data are taken from Table B.1, and Galactic data points from Table B.2.

an average $E(B-V) < 0.04$ assuming an SMC-like extinction curve.[7] Murphy & Liske (2004), examining 70 DLAs from the Sloan Digital Sky Survey (SDSS) found $E(B-V) < 0.02$ at $z \sim 3$ (see also Vladilo et al. 2008). The limits which I derive for $E(B-V)_{5780}$ are less sensitive than the limits discussed above, whilst those derived for $E(B-V)_{6284}$ are more sensitive (except in the case of the $z = 0.221$ DLA towards Q 0738+313), with three of the DLAs having limits below the limit established by Ellison et al. (2005a), and two below the limit established by Murphy & Liske (2004).

However, the use of upper limits on EW_{6284} in deriving upper limits for $E(B-V)$

[7]Selecting the QSOs at radio wavelengths ensured that any DLAs sufficiently dusty to conceal the background QSO from an optical survey would still be detected and measured.

Table 3.5: Upper limits on DLA reddening

QSO	z_{abs}	EW_{5780} (mÅ)	$E(B-V)_{5780}$
Q 0738+313	0.091	< 199	< 0.42
	0.221	< 30	< 0.09
B2 0827+243	0.518	< 39	< 0.12
PKS 0952+179	0.239	< 27	< 0.09
PKS 1127−145	0.313	< 500	< 0.88
Q 1229−020	0.395	< 65	< 0.17

depends on the same relationship existing between EW_{6284} in the Milky Way and in extragalactic sightlines including DLAs. As can be seen from Figure 3.15, the extragalactic data points, whilst still within the scatter of the Galactic relationship, are *systematically* weak compared to $E(B-V)$. In order to quantify this apparent systematic offset, a 2-dimensional Kolmogorov-Smirnov (K-S) test was conducted to compare galactic and extra-galactic points. The K-S test determined that the extragalactic points are not drawn from the same distribution as the Galactic points ($P < 0.001$) at the 99.9% confidence level. As such, the limits on reddening derived from the upper limits on EW_{6284} will not be used further.

3.5 Gas to Dust Ratios

With the limits derived for $E(B-V)$ in §3.4, it now becomes possible to derive lower limits for the gas-to-dust ratio (N(H I)/$E(B-V)$) in our sampled DLAs, see Table 3.5. Figure 3.16 shows the limits I have derived, along with reference lines indicating typical values for the Milky Way (Cox et al. 2006), the LMC (Cox et al. 2006), and the SMC (averaging the lower and upper values from Bouchet et al. 1985).

Figure 3.16 shows that three of the DLAs (towards Q 0738+313 ($z = 0.091$), B2 0827+243, and Q 1229−020) are potentially consistent with the Galactic gas-to-dust ratio, two more (towards Q 0738+313 ($z = 0.221$) and PKS 1127−145) are inconsistent with the Milky Way but potentially consistent with the LMC, whilst the DLA towards AO 0235+164 is consistent with the SMC, and the DLA towards

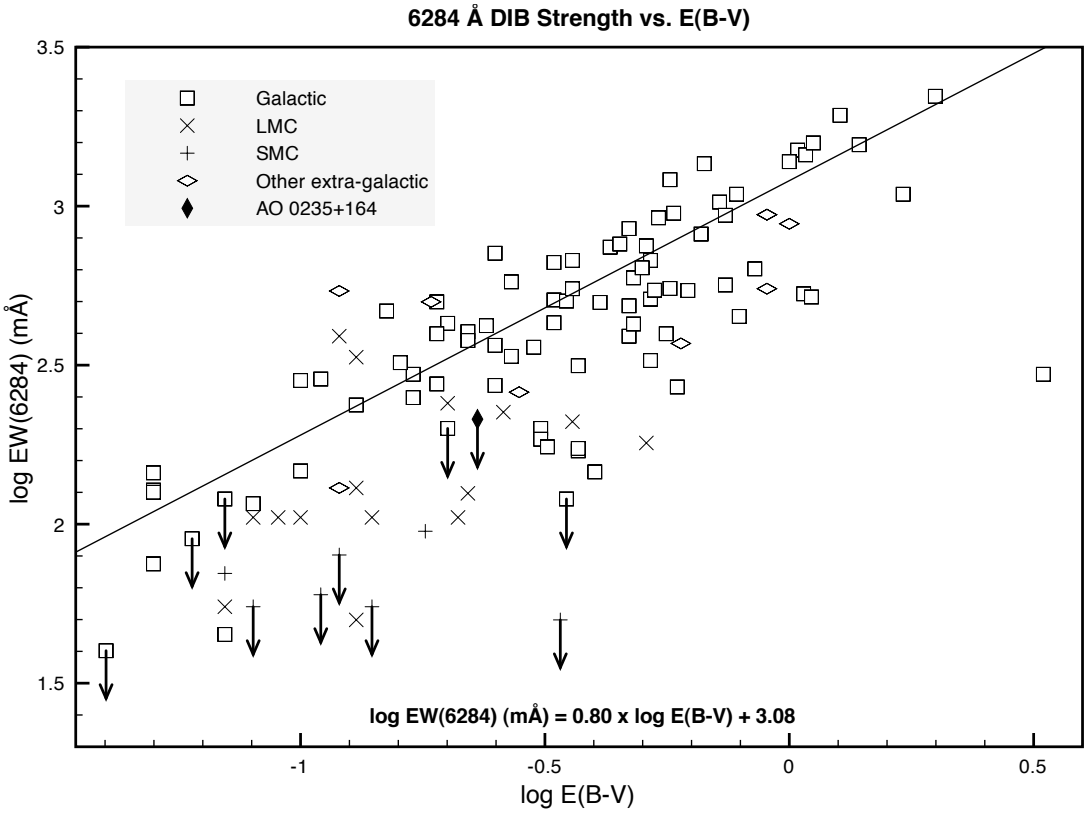

Figure 3.15: The relationship between $E(B-V)$ and the 6284 Å DIB. The best fit line was presented in Welty et al. (2006), and includes all data points, both Galactic and extra-galactic. Data points are from Table B.1 (extragalactic) and Table B.2 (Galactic).

Table 3.6: Gas to Dust ratios for DLAs

QSO	z_{abs}	Morphology	[Zn/H]	[Fe/H]	b (kpc/h_{70})	$GDR/10^{21}$ (cm^{-2} mag^{-1})
AO 0235+164	0.524	Spiral	—	—	6.7	22
Q 0738+313	0.091	LSB	< -1.14	-1.63	< 3.5	> 3.6
	0.221	Dwarf	≤ -0.70	—	20.5	> 8.8
B2 0827+243	0.518	Spiral	< 0.30	-1.02	38.2	> 1.7
PKS 0952+179	0.239	Dwarf	< -1.02	—	< 4.6	> 23
PKS 1127−145	0.313	Dwarf LSB	—	> -2	6.9	> 5.8
Q 1229−020	0.395	Spiral	-0.47	< -1.32	8.2	> 3.3

PKS 0952+179 is potentially consistent with the SMC. These results are consistent with the DLAs studied by Ellison et al. (2005a) at $1.8 < z < 3.5$, which also had higher gas-to-dust ratios than the Milky Way. Table 3.6 shows the minimum gas-to-dust ratios derived for the DLAs here, along with the other characteristics of the

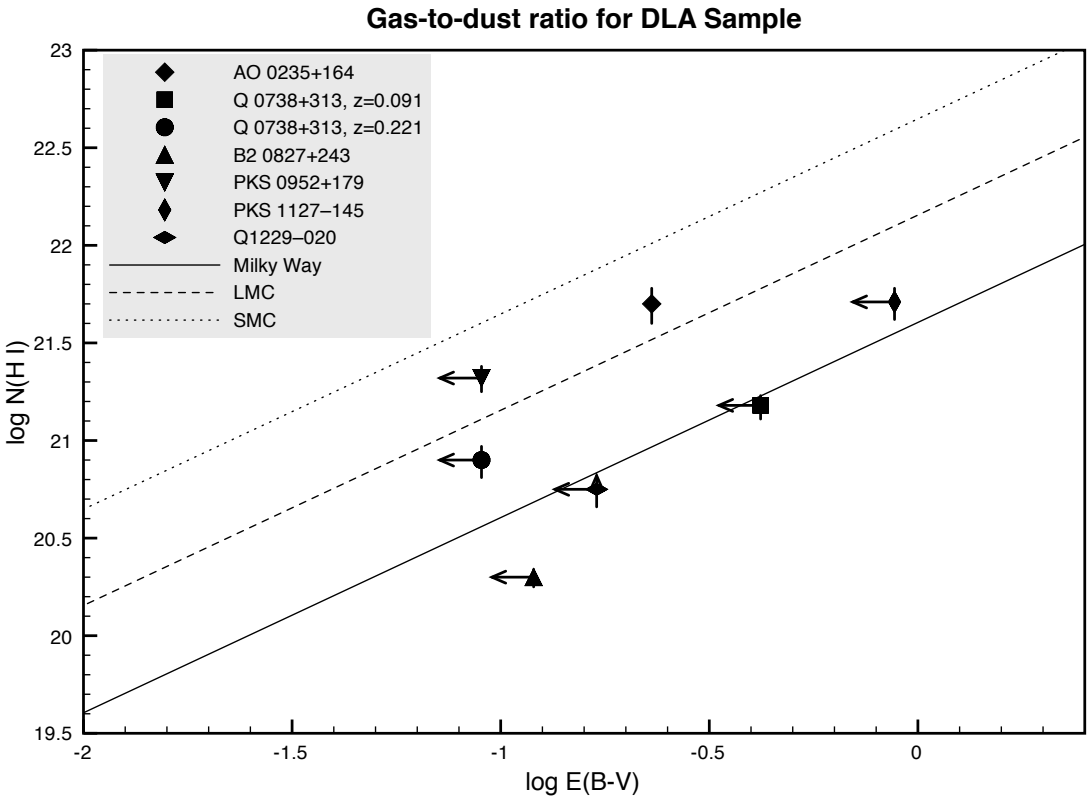

Figure 3.16: Minimum gas-to-dust ratios for DLAs. The diagonal lines represent median gas-to-dust ratios for the Milky Way (solid) (Cox et al. 2006), the Large Magellanic Cloud (dashed) (Cox et al. 2006), and the Small Magellanic Cloud (dotted) (average of lower and upper values from Bouchet et al. 1985), while filled squares represent the DLAs in our sample.

DLA host galaxies, and the DLA–galaxy impact parameters.

Chapter 4

Diffuse Interstellar Bands in Ca II Systems

4.1 Overview

I will begin with an overview of the known characteristics of the Ca II systems in my sample, individually and collectively (§4.2). Following this in §4.3 I will provide DIB equivalent widths and detection limits. I will then discuss the relative DIB strengths (§4.3.2), what conclusions may be drawn about the N(H I) of the Ca II systems from the DIB strengths (§4.3.3), and the relationship between DIB strength and reddening (§4.3.4).

4.2 The Ca II Systems

The second phase of the search for DIBs in QSOAL systems involved examining nine Ca II systems, as shown in Table 2.6. The observational characteristics of these Ca II systems are shown in Table 4.1. Ca II systems were selected for the second phase of the search because, not only are they likely to be DLAs (Wild et al. 2006), but their average reddening [$E(B-V) = 0.06$ Wild & Hewett 2005] is considerably higher than the average reddening for DLAs [$E(B-V) \leq 0.02$ Murphy & Liske 2004]. Furthermore, Ca II systems with $EW_{Ca\ II,3934} > 0.5$ Å, the typical value for my sample, had average $E(B-V) = 0.1$ (Wild et al. 2006). Because EW_{5780} appears to correlate well with $E(B-V)$ in both galactic and extra-galactic sightlines (see

Chapter 3), a higher reddening should offer a better chance to detect the diffuse bands.

Table 4.1: Ca II System Observational Characteristics

QSO	m_r (mag)	z_{em}	z_{abs}	Ca II K λ3934 (Å)	Na I D_1 λ5891 (Å)
SDSS J001342.44−002412.6	18.6	1.644	0.1556	1.09 ± 0.18 (S)	1.12 ± 0.02
SDSS J100943.55+052953.8	16.9	0.942	0.3862	0.51 ± 0.05 (S)	—
SDSS J104029.94+070528.3	18.6	1.532	0.2063	0.61 ± 0.12 (S)	< 0.17
SDSS J113702.03+013622.1	18.6	1.641	0.4492	0.35 ± 0.04 (F)	< 0.15
SDSS J121911.23−004345.5	18.0	2.293	0.4485	0.40 ± 0.02 (F)	0.09 ± 0.02
SDSS J122608.02−000602.2	18.4	1.125	0.5179	0.67 ± 0.02 (F)	—
SDSS J143701.20−010418.0	19.1	0.286	0.0725	1.07 ± 0.20 (S)	1.31 ± 0.02
SDSS J213502.45+103823.5	18.8	1.511	0.0984	0.90 ± 0.19 (S)	—
SDSS J225913.74−084419.6	18.4	1.290	0.5293	0.38 ± 0.02 (F)	—

NOTE (F) indicates $EW_{Ca\ II}$ measured from the FORS2 spectrum, and (S) $EW_{Ca\ II}$ measured from the SDSS spectrum. Errors are 1-σ whilst limits are 5-σ. Data from Ellison et al. (2008).

Table 4.1 shows the Ca II and Na I equivalent widths for the Ca II systems examined here. The host galaxies of two of the Ca II systems in this sample have been studied in detail [the system towards J0013−0024 (B. Zych, private communication), and the system towards J1219−0043 (Zych et al. 2007)]. The remainder of this section provides information on the individual Ca II systems in the sample.

J0013−0024 The sightline of the QSO J0013−0024 passes directly through the disk host galaxy of the Ca II system with an impact parameter < 1 kpc.[1] As such, both the QSO and the absorbing galaxy are within the radius of the SDSS spectral fibre, leading to significant contamination of the QSO spectrum with light from the host galaxy (see Figure 4.1). It is therefore conceivable that the Ca II H and K absorption lines detected in the SDSS spectrum are due to photospheric absorption from the stars in the absorbing galaxy (B. Zych, private communication). While there may well be a contribution to the H and K line absorption from the ISM [indeed a QSO sightline through the Milky Way at this impact parameter would likely be a Ca II absorber, and see Bowen (1991) for Ca II absorption in both the Milky Way

[1]The impact parameter is stated here as an upper limit due to residuals from the QSO PSF subtraction.

and quasar absorption systems], it is impossible to determine what that contribution is. The system is almost certain to be a DLA, however, given its impact parameter.

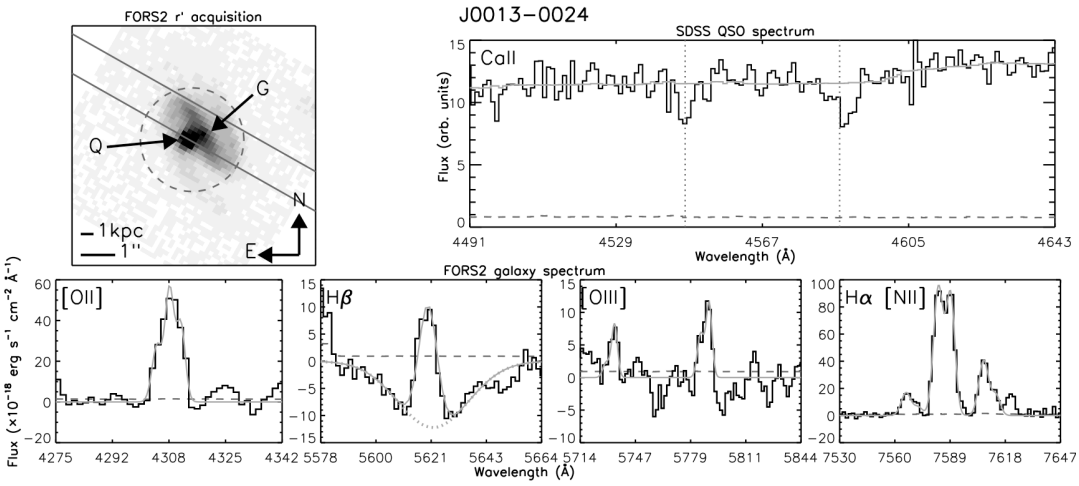

Figure 4.1: Spectrum and image of J0013−0024. The top left panel shows an SDSS image of the system, with the QSO (marked Q) and the absorbing galaxy (marked G). The dashed circle represents the SDSS fibre aperture, whilst the solid lines represent the slit of the VLT FORS2 spectrometer. The top right spectrum shows the Ca II lines from the SDSS spectrum of J0013−0024, whilst the bottom panels show emission lines from the spectrum of the associated galaxy. In all cases the histograms show the actual spectrum and the dashed line shows the zero level. In the SDSS spectrum the solid line shows the continuum level whilst the vertical dotted lines show the position of the Ca II absorption. In the FORS2 spectra, the solid lines show the spectral fit whilst the dotted lines show the fitted continuum level. Image courtesy of B. Zych.

The absorbing galaxy is an Sb spiral with a B_j luminosity of $L = (1.22 \pm 0.02)\ L^*$.[2] The nebular emission line metallicity was derived from the O3N2 method (Pettini & Pagel 2004) and calculated to be $\log(\mathrm{O/H}) + 12 = 8.68 \pm 0.02$; from the R23 method (Pagel et al. 1979) (see e.g. Kobulnicky et al. 1999 for more a recent calibration) $\log(\mathrm{O/H}) + 12 = 8.71 \pm 0.03$ on the upper branch, while from the N2 method (Pettini & Pagel 2004) $\log(\mathrm{O/H}) + 12 = 8.59 \pm 0.01$ (B. Zych, private communication). All of the nebular emission line metallicities have systematic uncertainties of 0.3 dex (B. Zych, private communication). The solar value for $\log(\mathrm{O/H}) + 12 = 8.69 \pm 0.05$

[2] L^* here is as in Zych et al. (2007), with $M^*_{B_j} = -20.43$ mag (Norberg et al. 2002), and $M^*_{B_j}(z) = M^*_{B_j}(z) - z$ (Ilbert et al. 2005).

(Lodders 2003), and therefore the overall result for the nebular emission metallicity of roughly solar. Note, however, that the abundances determined here are based on emission lines, whereas QSOALS abundances are based on absorption, and it is unclear whether the two are equivalent. Ellison et al. (2005b) obtained emission-line abundances for $z < 0.5$ galaxies associated with Mg II systems, finding that if the galaxies lie on the upper branch of R23 their abundances are approximately solar (and thus inconsistent with absorber abundances), whereas if they lie on the lower branch their abundances, while consistent with absorber abundances at that redshift, are inconsistent with the metallicity-luminosity relationship. Bowen et al. (2005) and Schulte-Ladbeck et al. (2005), examining single galaxies, find consistent emission and absorption metallicities, but both of these comparisons are made at low impact parameters, whereas absorbers frequently intersect with their host galaxies at impact parameters of tens of kiloparsecs (e.g. Ellison et al. 2005b). Thus, the relationship of the emission and absorption-line metallicities has not been conclusively determined. The star formation rate was measured to be (4.5 ± 0.3) $M_\odot$ yr^{-1} based on [O II] (see e.g. Kewley et al. 2004), and (4.4 ± 0.3) $M_\odot$ yr^{-1} from Hα (see e.g. Kennicutt 1998), with systematic errors of up to 10% in both cases (values and systematics from B. Zych, private communication). The star formation rates were corrected for extinction and geometry. Finally, the $E(B-V)$ value was determined to be 0.66 ± 0.02 mag based on the Balmer decrement, with Galactic $E(B-V)$ for this sightline of 0.030 ± 0.001.

J1009+0529 This Ca II system has a redshift $z_{abs} = 0.3862$. In addition to the Ca II doublet, several other absorption lines were detected. The Mg II $\lambda\lambda$ 2796,2803 doublet was detected with $EW_{2796} = 1.877$ Å, and $EW_{2803} = 1.867$ Å, as was the Mg I λ 2852 absorption line with $EW_{2852} = 0.654$ Å. In addition, Ti II λ 3242 was detected at the 4-σ level, with $EW_{3242} = 0.260$ Å. Figure 4.2 shows an SDSS image and spectrum of J1009+0529.

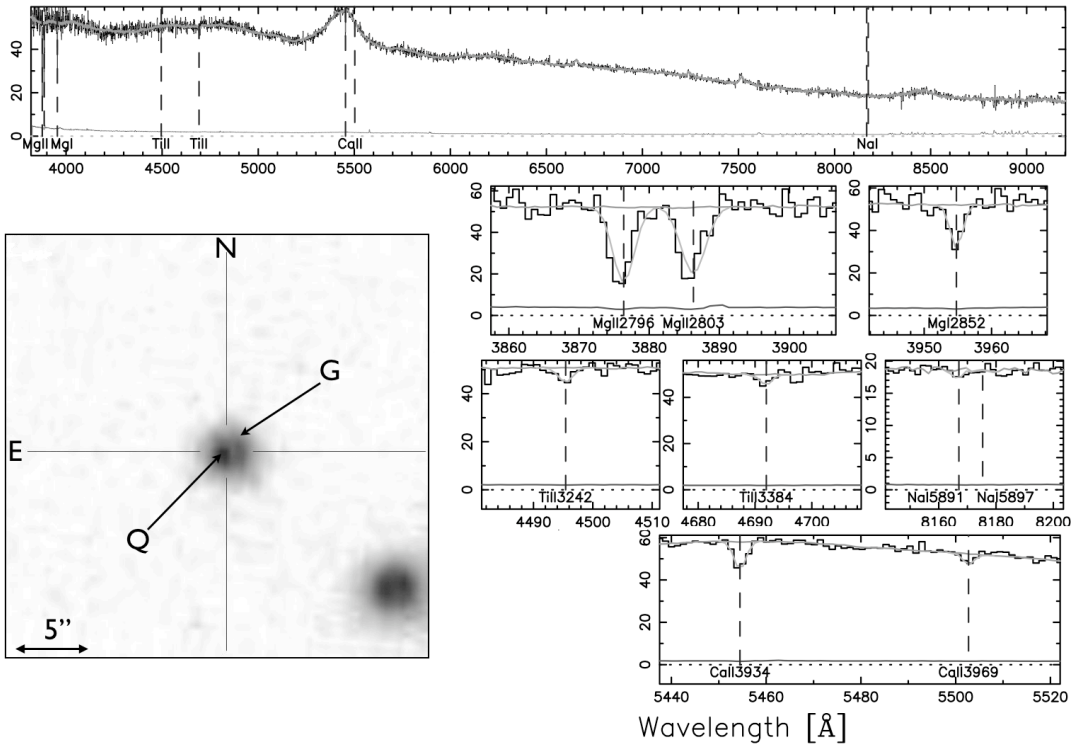

Figure 4.2: Spectrum and image of J1009+0529. The top panel shows the full SDSS spectrum whilst the bottom panels show individual metal lines. The histogram shows the actual data, the vertical dashed lines the position of metal absorption lines, the solid lines the continuum fit (does not follow the absorption profile), line fits (follows the absorption profile) and SDSS errors (near zero flux). The image is a multiband SDSS image of the field, with the quasar labelled Q and the galaxy G. Image courtesy of Dr. M. Murphy.

J1040+0705 This Ca II system is at redshift $z_{abs} = 0.2063$. The SDSS image does not show any galaxies within 30.″0 of the QSO ($71h^{-1}$ kpc). The closest visible galaxy-like object has a separation of $\sim 60.''0$ ($143h^{-1}$ kpc). No additional absorption lines are detected, although limits on Na I $\lambda\lambda$ 5891,5897 are shown in Table 4.1. Figure 4.3 shows an SDSS image and spectrum of J1040+0705.

J1137+0136 The absorber is at $z_{abs} = 0.4492$. The closest galaxy lies 5.″58 away (impact parameter of $23h^{-1}$ kpc). In addition to the Ca II doublet, the Mg II $\lambda\lambda$ 2796,2803 doublet was detected with $EW_{2796} = 1.402$ Å, and $EW_{2803} = 1.108$ Å, as was the Mg I λ 2852 absorption line with $EW_{2852} = 0.563$ Å. Figure 4.4 shows an

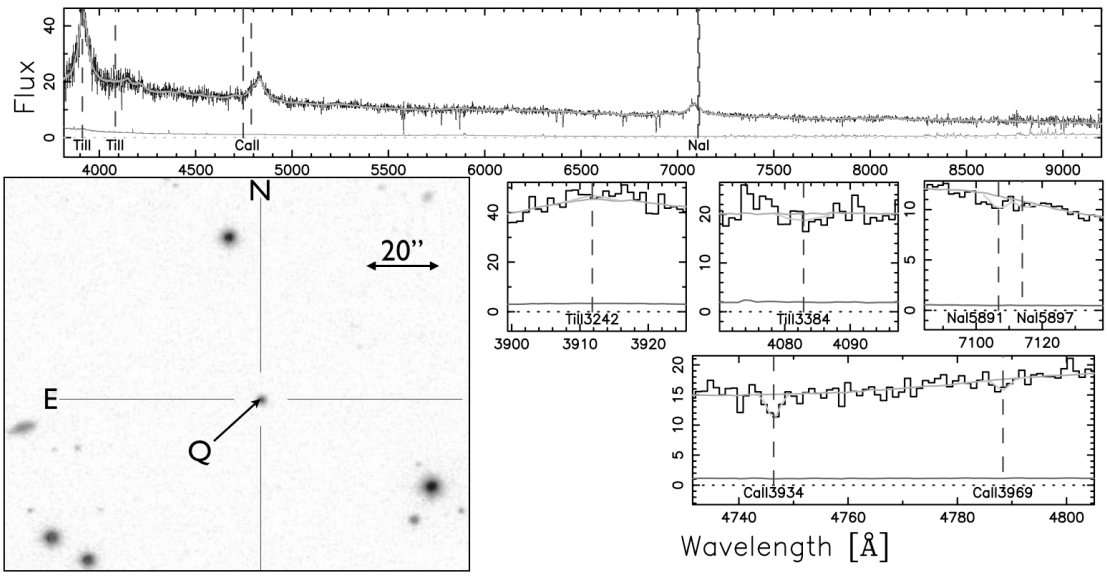

Figure 4.3: Spectrum and image of J1040+0705. The top panel shows the full SDSS spectrum whilst the bottom panels show individual metal lines. The histogram shows the actual data, the vertical dashed lines the position of metal absorption lines, the solid lines the continuum fit (does not follow the absorption profile), line fits (follows the absorption profile) and SDSS errors (near zero flux). The image is a multiband SDSS image of the field, with the quasar labelled Q. Image courtesy of Dr. M. Murphy.

SDSS image and spectrum of J1137+0136.

J1219−0043 The Ca II system towards J1219−0043 is associated with an Sbc spiral at a redshift of $z = 0.448$ with a B_j luminosity of $0.68 \pm 0.07 L^*$ and an impact parameter of (7 ± 1) kpc from the QSO (Zych et al. 2007). The nebular emission line metallicity from the O3N2 method $\log(\mathrm{O/H}) + 12 = 8.84 \pm 0.06$, compared to $\log(\mathrm{O/H}) + 12 = 9.01 \pm 0.02$ from the upper branch of R23. Based on the O3N2 metallicity, this galaxy has a slightly super solar metallicity with $[\mathrm{O/H}] = 0.15$. The star formation rate was measured to be (0.54 ± 0.04) $\mathrm{M}_\odot$ yr^{-1} based on [O II], and (1.19 ± 0.03) $\mathrm{M}_\odot$ yr^{-1} based on Hα (Zych et al. 2007). This star formation rate is comparable to the median SFR for local galaxies of 0.5 $\mathrm{M}_\odot$ yr^{-1} based on the NFGS (Kewley et al. 2002). In addition to the Ca II doublet, the Mg I λ 2852 line was detected with $EW_{2852} = 0.762$ Å. Figure 4.5 shows an SDSS image and spectrum of

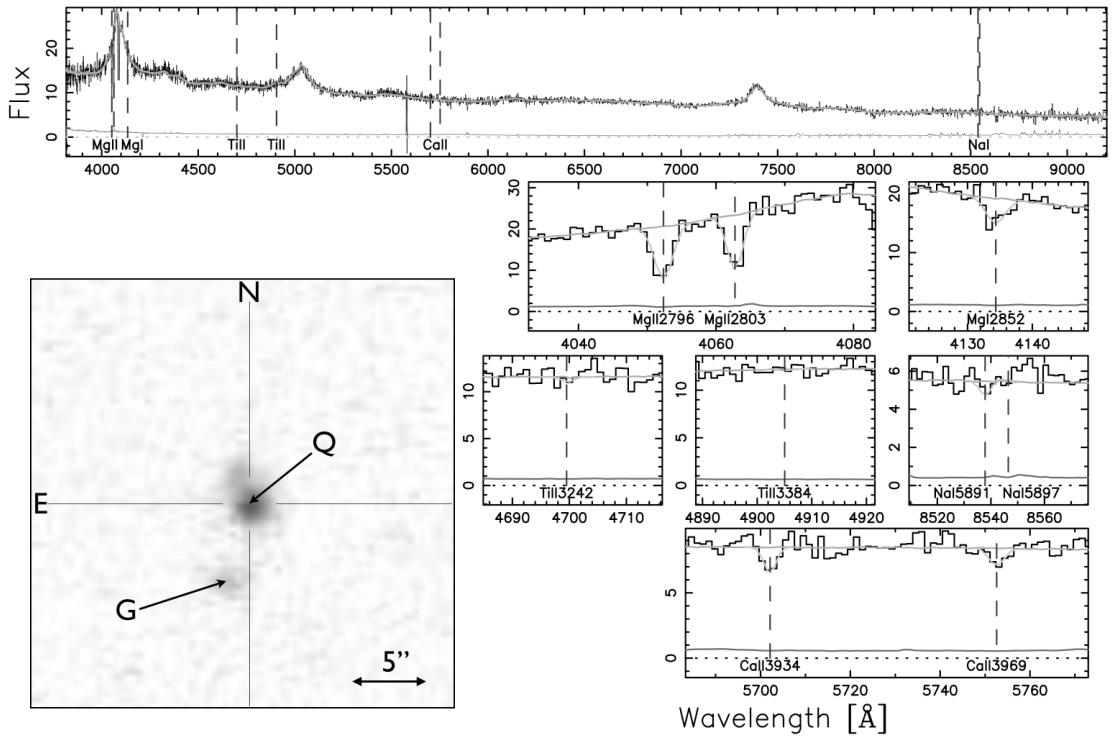

Figure 4.4: Spectrum and image of J1137+0136. The top panel shows the full SDSS spectrum whilst the bottom panels show individual metal lines. The histogram shows the actual data, the vertical dashed lines the position of metal absorption lines, the solid lines the continuum fit (does not follow the absorption profile), line fits (follows the absorption profile) and SDSS errors (near zero flux). The image is a multiband SDSS image of the field, with the quasar labelled Q and the galaxy G. Image courtesy of Dr. M. Murphy.

J1219−0043 and the associated absorbing galaxy.

J1226−0006 This Ca II system, with $z_{abs} = 0.51793$, is 17.″0 from the closest galaxy identified by SDSS, for an impact parameter of $74h^{-1}$ kpc. In addition to the Ca II doublet, the Mg II $\lambda\lambda$ 2796,2803 doublet was detected with $EW_{2796} = 2.406$ Å, and $EW_{2803} = 2.685$ Å. The Fe II absorption line at 2587 Å was detected at the 4-σ level ($EW_{2587} = 1.132$ Å), and the line at 2600 Å was detected at the 5.8-σ level ($EW_{2600} = 1.576$ Å). Figure 4.6 shows an SDSS image and spectrum of J1226−0006 and the associated absorbing galaxy.

J1437−0104 The Ca II system towards J1437−0104 is at $z_{abs} = 0.07254$. The ab-

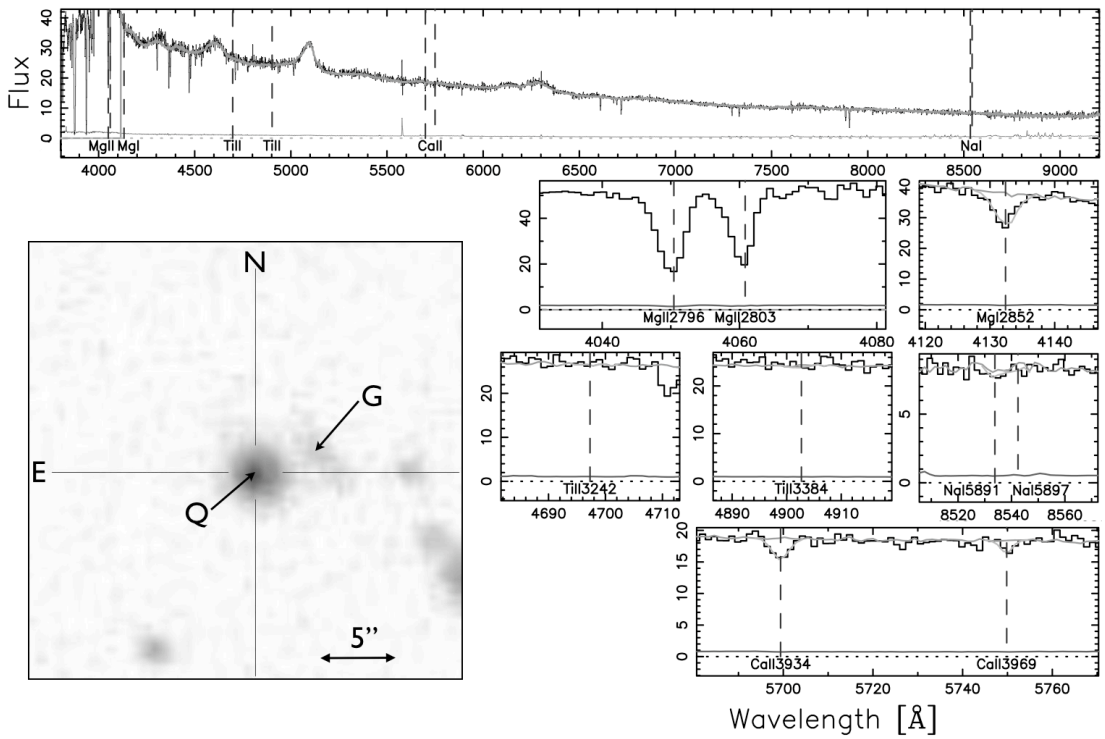

Figure 4.5: Spectrum and image of J1219−0043. The top panel shows the full SDSS spectrum whilst the bottom panels show individual metal lines. The histogram shows the actual data, the vertical dashed lines the position of metal absorption lines, the solid lines the continuum fit (does not follow the absorption profile), line fits (follows the absorption profile) and SDSS errors (near zero flux). The image is a multiband SDSS image of the field, with the quasar labelled Q and the galaxy G. Image courtesy of Dr. M. Murphy.

sorbing galaxy overlaps the PSF of the quasar, with an impact parameter $4.6h^{-1}$ kpc ($4\farcs7$) based on the SDSS image and calculating from the apparent centre of the galaxy. In addition to the Ca II doublet, the Na I $\lambda\lambda$ 5891,5897 doublet was detected with $EW_{5891} = 1.31$ Å, and $EW_{5897} = 0.85$ Å. Figure 4.7 shows an SDSS image and spectrum of J1437−0104 and the associated absorbing galaxy.

J2135+1038 This Ca II system, at $z_{abs} = 0.09839$, has a faint galaxy $5\farcs7$ away, with an impact parameter $7.3h^{-1}$ kpc (the bright object immediately to the Southeast of the galaxy in Figure 4.8 is a star rather than a galaxy). No other galaxies within $30\farcs0$ are significantly brighter than this galaxy. No absorption lines other than the

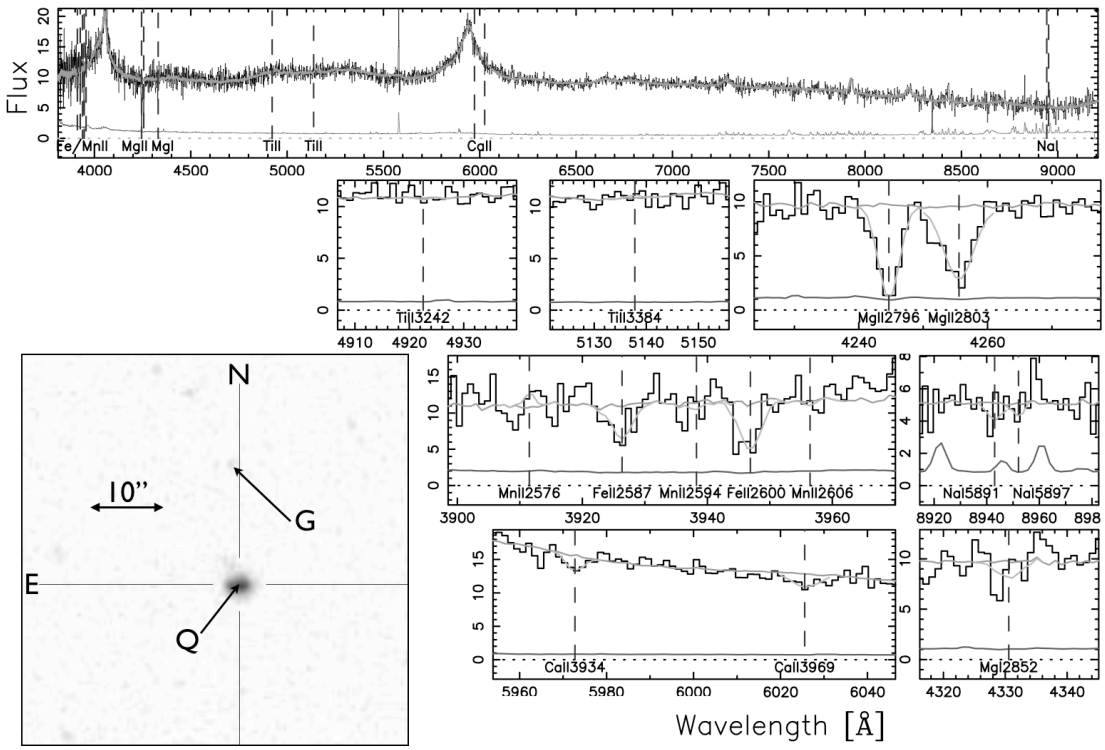

Figure 4.6: Spectrum and image of J1226−0006. The top panel shows the full SDSS spectrum whilst the bottom panels show individual metal lines. The histogram shows the actual data, the vertical dashed lines the position of metal absorption lines, the solid lines the continuum fit (does not follow the absorption profile), line fits (follows the absorption profile) and SDSS errors (near zero flux). The image is a multiband SDSS image of the field, with the quasar labelled Q and the galaxy G. Image courtesy of Dr. M. Murphy.

Ca II doublet were confirmed in the SDSS spectrum of this absorber, although the Na I $\lambda\lambda$ 5891,5897 doublet was detected at low significance in the SDSS spectrum (2-σ detection). Figure 4.8 shows an SDSS image and spectrum of J2135+1038 and the associated absorbing galaxy.

J2259−0844 The Ca II system towards J2259−0844 has a redshift $z_{abs} = 0.5293$. The closest visible galaxy (marked as such on the SDSS image in Figure 4.9) is 12.″1 away from the QSO, which corresponds to an impact parameter of $53.9h^{-1}$ kpc, so whilst this might be the absorbing galaxy, there may well also be a closer galaxy not visible on the SDSS image. Many metal lines beyond the Ca II doublet were detected

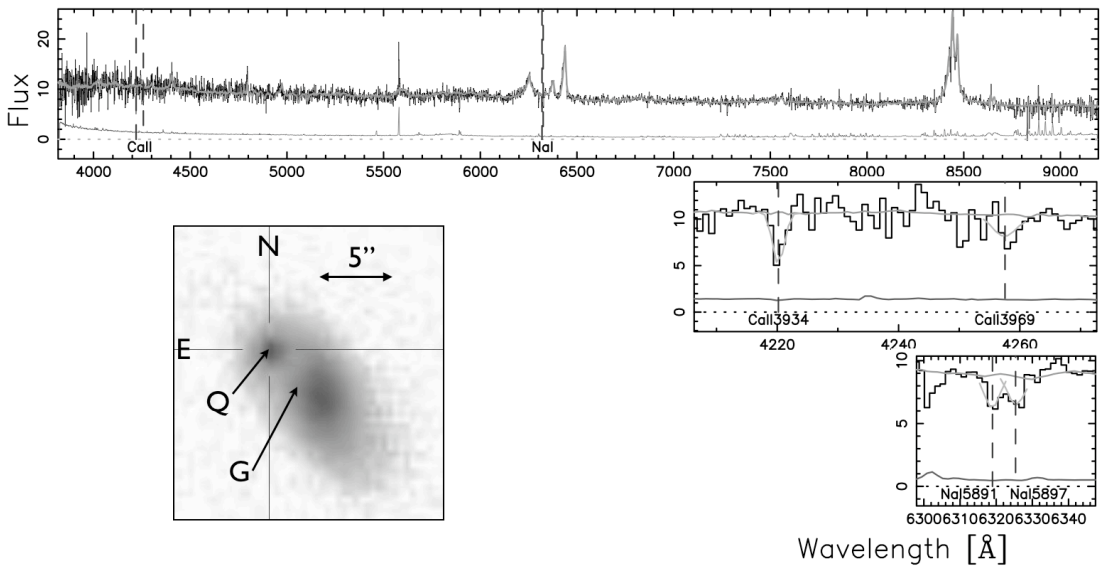

Figure 4.7: Spectrum and image of J1437−0104. The top panel shows the full SDSS spectrum whilst the bottom panels show individual metal lines. The histogram shows the actual data, the vertical dashed lines the position of metal absorption lines, the solid lines the continuum fit (does not follow the absorption profile), line fits (follows the absorption profile) and SDSS errors (near zero flux). The image is a multiband SDSS image of the field, with the quasar labelled Q and the galaxy G. Image courtesy of Dr. M. Murphy.

in this spectrum, including the Mg II doublet at $\lambda\lambda$ 2796,2803, with $EW_{2796} = 2.73$ Å, and $EW_{2803} = 2.20$ Å. The Mg I line at 2852 Å was also detected, with $EW_{2852} = 0.542$ Å, as well as the Fe II lines at 2587 Å ($EW_{2587} = 1.408$ Å) and 2600 Å ($EW_{2600} = 2.035$ Å). Figure 4.9 shows an SDSS image and spectrum of J2259−0844 and the associated absorbing galaxy.

4.3 Results

I will begin by describing the single diffuse band detected, and the upper limits established for the remaining diffuse bands in §4.3.1. I will then discuss the relative strengths of the various diffuse bands in §4.3.2, comparing the diffuse bands in Ca II systems with the Milky Way, the local galaxies, and the damped Lyman-α systems (see §3.3.2 for further discussion of diffuse band strength in DLAs). In §4.3.3, I will discuss whether the DIB strengths and limits in the Ca II systems allows any

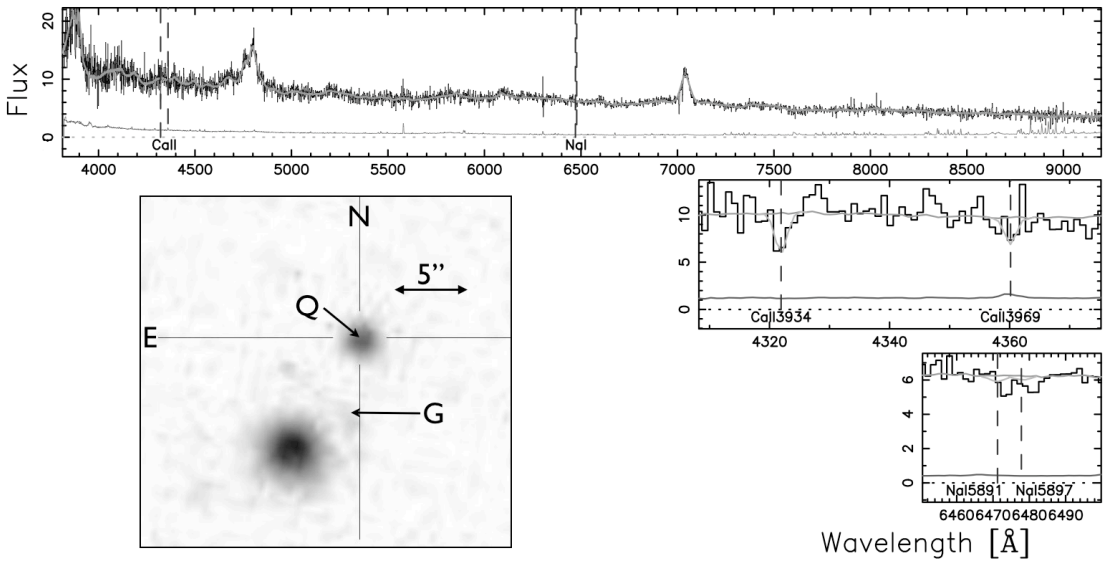

Figure 4.8: Spectrum and image of J2135+1038. The top panel shows the full SDSS spectrum whilst the bottom panels show individual metal lines. The histogram shows the actual data, the vertical dashed lines the position of metal absorption lines, the solid lines the continuum fit (does not follow the absorption profile), line fits (follows the absorption profile) and SDSS errors (near zero flux). The image is a multiband SDSS image of the field, with the quasar labelled Q and the galaxy G. Image courtesy of Dr. M. Murphy.

determination as to the H I column density in Ca II systems, based on the relationship defined in Herbig (1993) and the results obtained from DLAs in §3.3.3. Finally, in §4.3.4 I will use the DIB strengths and limits to constrain the reddening of the Ca II systems in this sample, and to compare $E(B-V)$ values from Ca II systems with those derived for DLAs in §3.4.

4.3.1 DIB Detections and Limits

Only one diffuse band was detected in the Ca II systems in this sample. The 5780 Å DIB was detected in the Ca II system towards J0013−0024 with rest $EW_{5780} = 94 \pm 16$ mÅ(see Figure 4.10). The redshift of this DIB is in excellent agreement with the Na I $\lambda\lambda$ 5891,5897 doublet also present in the FORS spectrum, as well as with the Ca II $\lambda\lambda$ 3934,3969 doublet in the SDSS spectrum, with the velocity offsets always < 50 km s^{-1} (i.e. less than 0.5 resolution elements), and < 20 km s^{-1} in the majority

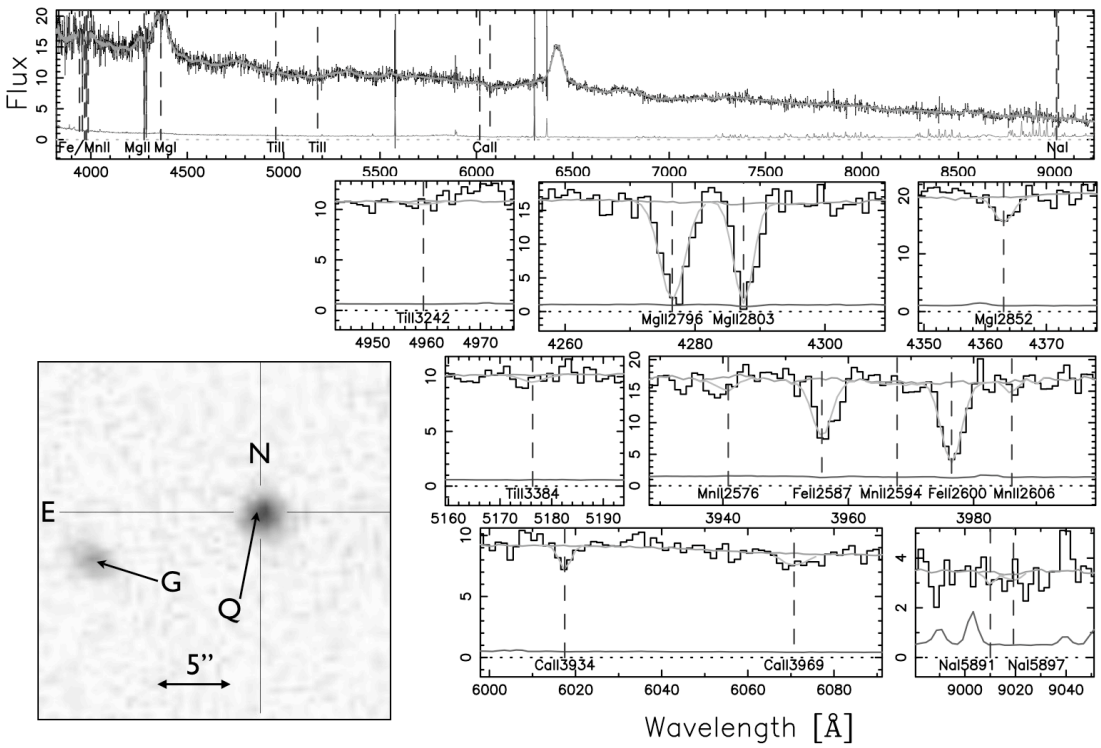

Figure 4.9: Spectrum and image of J2259−0844. The top panel shows the full SDSS spectrum whilst the bottom panels show individual metal lines. The histogram shows the actual data, the vertical dashed lines the position of metal absorption lines, the solid lines the continuum fit (does not follow the absorption profile), line fits (follows the absorption profile) and SDSS errors (near zero flux). The image is a multiband SDSS image of the field, with the quasar labelled Q and the galaxy G. Image courtesy of Dr. M. Murphy.

of cases (see Figure 4.10 for the an example of several relative velocities). Another absorption line is also present ~ 130 km s^{-1} to the red of the 5780 Å DIB. This line does not correspond to any known feature at $z = 0.1556$, so it is likely due to the presence of gas at a different redshift.

A complete list of the DIB strengths and upper limits is presented in Table 4.2. With the exception of the 5780 Å DIB detection described above, no other diffuse bands were detected, although upper limits have been derived for the remaining DIBs. The 5-σ limits are presented in Figures 4.11 to 4.19. Note that these spectra were taken with several different grisms, which results in different upper limits for the same

Table 4.2: Ca II System Detections and Limits

QSO	z_{abs}	DIB	Wavelength Observed (Å)	SNR	Rest EW (mÅ)
SDSS J0013−0024	0.1556	5705	6595	72	< 103
		5780	6682	74	94 ± 16
		5797	6701	74	< 75
		6284	7264	65	< 130
SDSS J1009+0529	0.3862	4428	6141	155	< 207
		5705	7911	200	< 47
		5780	8015	150	< 70
		5797	8038	150	< 70
		6284	8714	87	< 97
SDSS J1040+0705	0.2063	5780	6975	45	< 212
		5797	6995	45	< 212
		6284	7583	43	< 258
		6613	7980	39	< 243
SDSS J1137+0136	0.4492	4428	6420	77	< 293
		5705	8270	75	< 135
		5780	8380	74	< 137
		5797	8403	74	< 82
SDSS J1219−0043	0.4485	4428	6417	113	< 200
		5705	8266	55	< 165
		5780	8376	100	< 100
		5797	8399	100	< 100
SDSS J1226−0006	0.5179	4428	6724	116	< 190
SDSS J1437−0104	0.0725	5780	6201	70	< 88
		5797	6219	60	< 102
		6613	7095	72	< 85
SDSS J2135+1038	0.0984	4428	4866	81	< 307
		5705	6268	74	< 165
		5780	6351	72	< 170
SDSS J2259−0844	0.5293	4428	6775	97	< 227

Limits are 5 σ, while errors are 1 σ

diffuse band, even with the same SNR. For example, the spectrum of J1437−0104 used the 1200R grism whilst the spectrum of J2135+1038 used the 600B grism, which accounts for the factor of two difference in their detection limits for the 5780 Å DIB ($<$ 88 mÅ compared to $<$ 170 mÅ), despite these two systems having the same redshift, and the spectra in the vicinity of these two DIBs having the same signal-to-noise ratio.

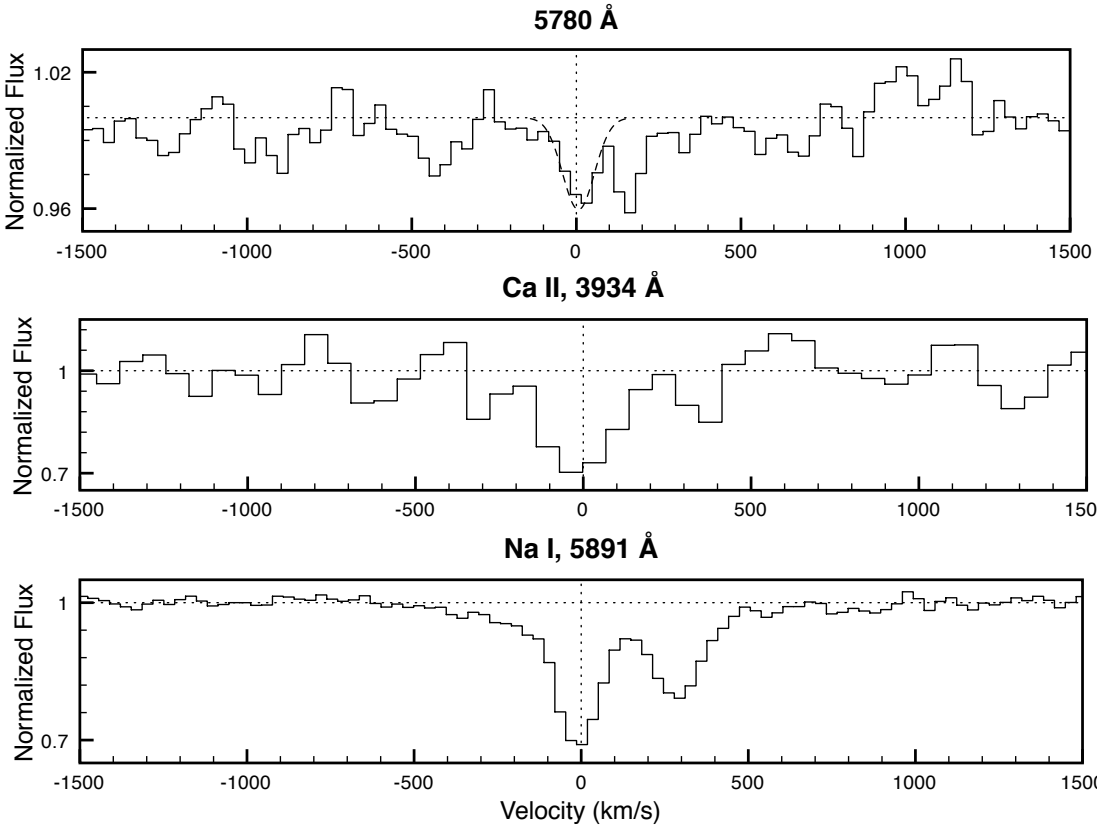

Figure 4.10: The 5780 Å DIB towards J0013−0024, along with the Ca II K line and the Na I D_1 line. These features have been converted into velocity space relative to $z = 0.1556$. The histograms show the absorption lines, the vertical dotted lines 0 km s^{-1} relative velocity, and the dashed curves gaussian profiles with equivalent widths the same as the DIB *EW*.

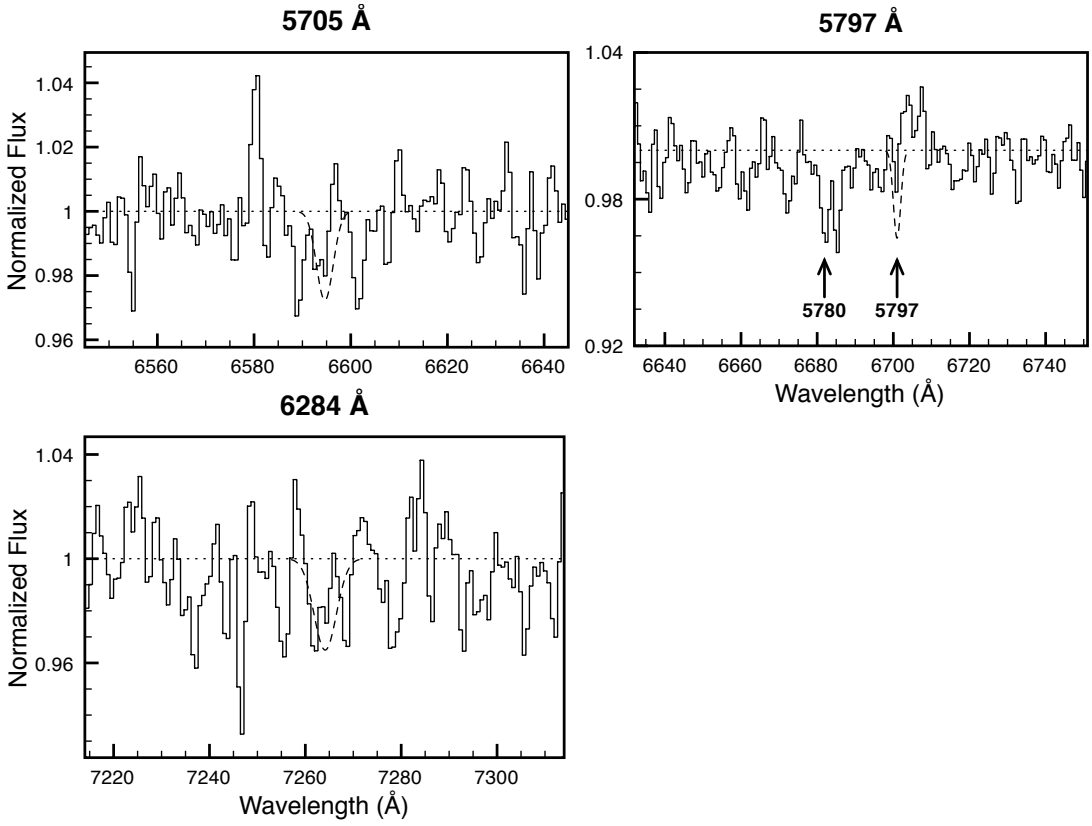

Figure 4.11: DIB upper limits in the Ca II system towards J0013−0024. In all cases, the histogram is the normalized spectrum, and the dashed lines are 5-σ limits.

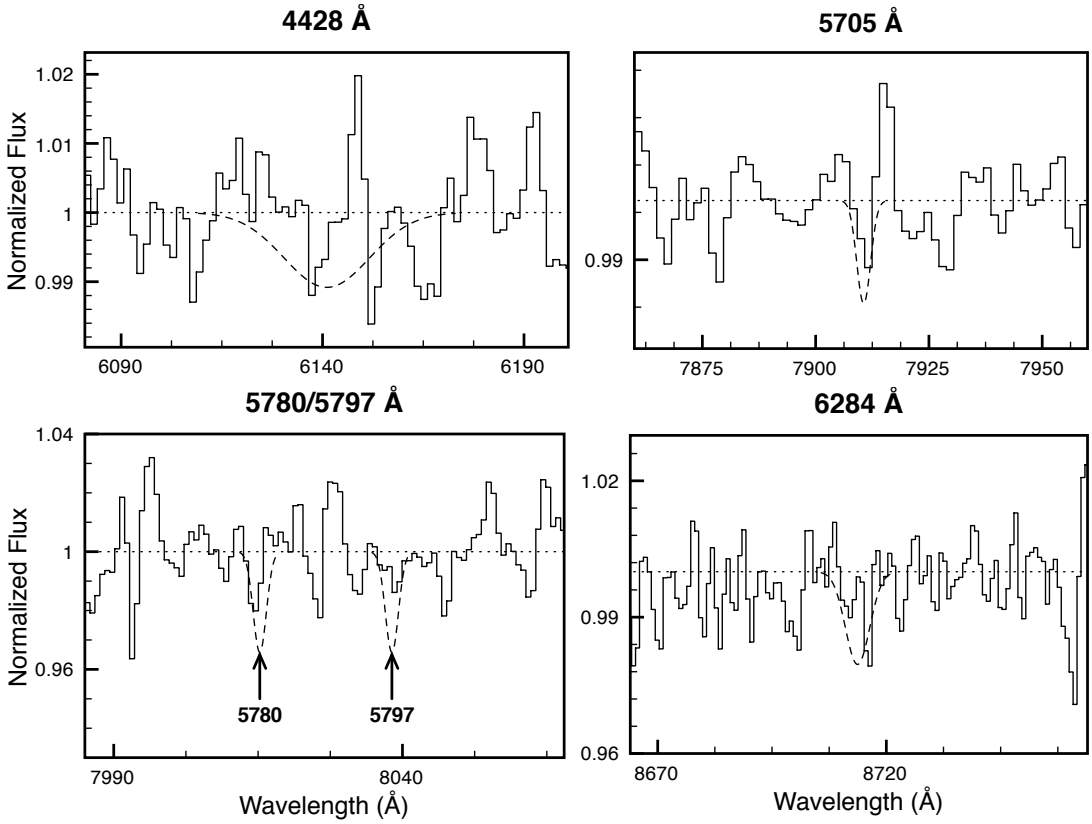

Figure 4.12: DIB upper limits in the Ca II system towards J1009+0529. In all cases, the histogram is the normalized spectrum, and the dashed lines are 5-σ limits.

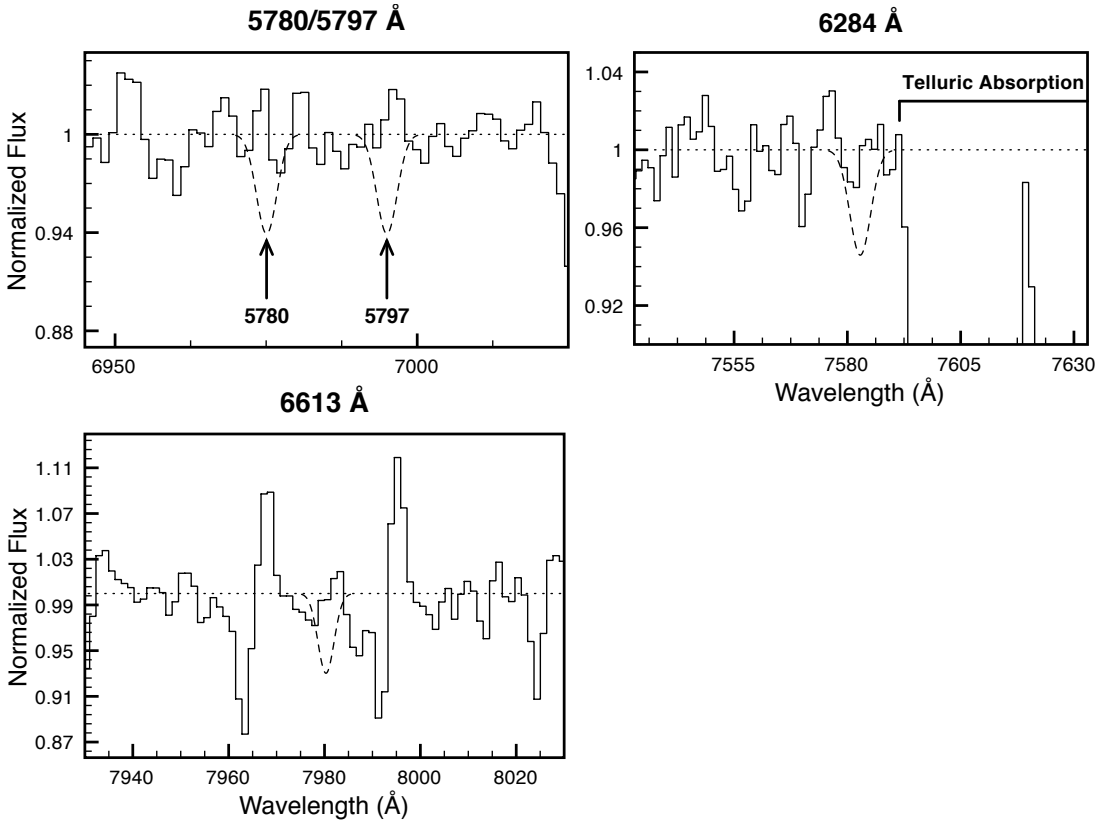

Figure 4.13: DIB upper limits in the Ca II system towards J1040+0705. In all cases, the histogram is the normalized spectrum, and the dashed lines are 5-σ limits.

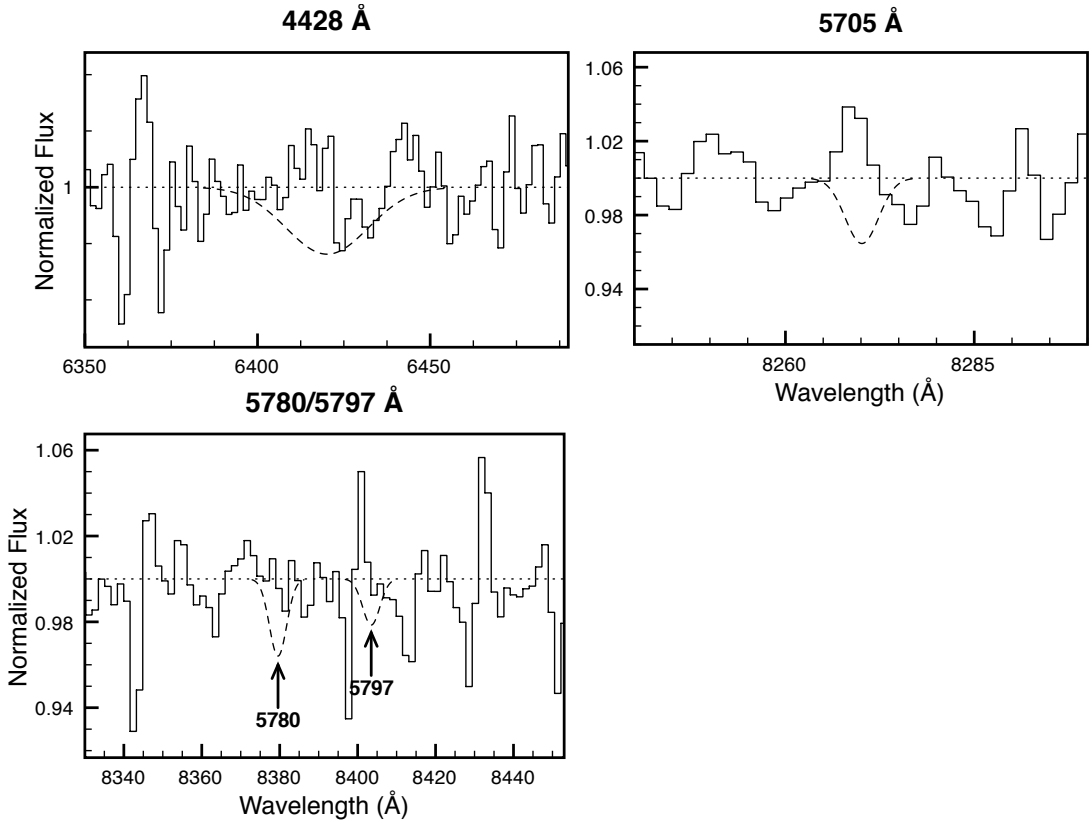

Figure 4.14: DIB upper limits in the Ca II system towards J1137+0136. In all cases, the histogram is the normalized spectrum, and the dashed lines are 5-σ limits.

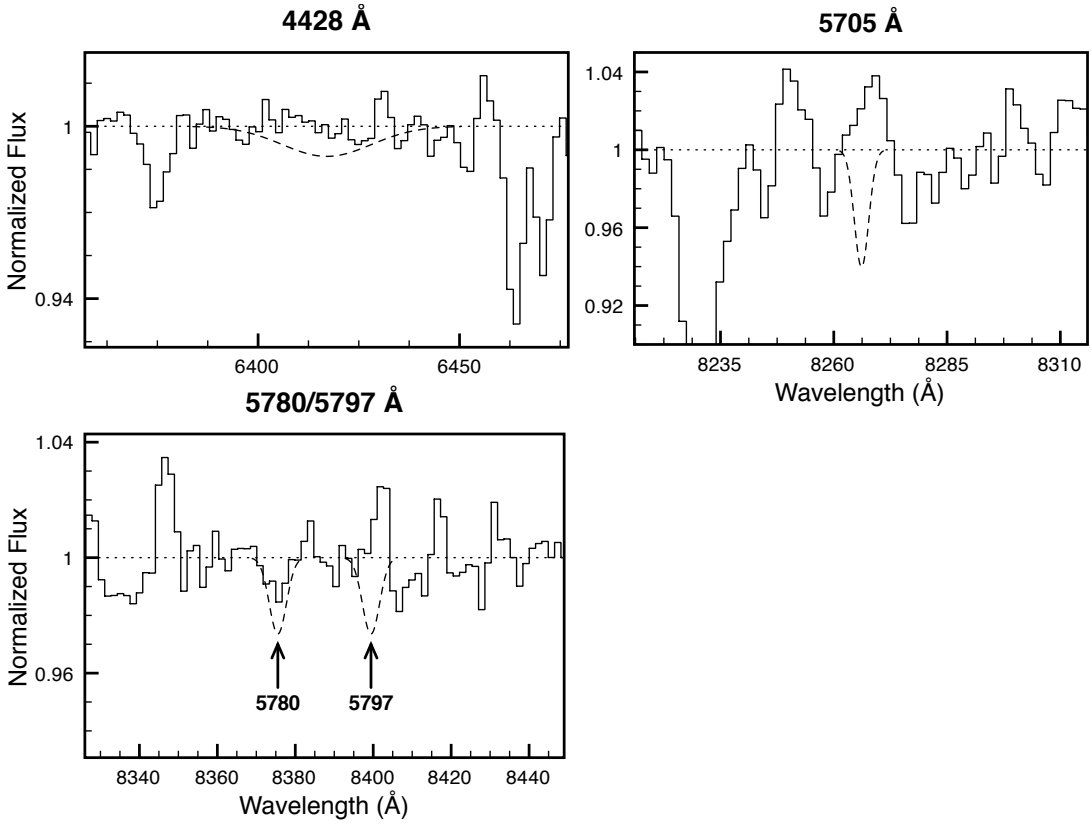

Figure 4.15: DIB upper limits in the Ca II system towards J1219−0043. In all cases, the histogram is the normalized spectrum, and the dashed lines are 5-σ limits.

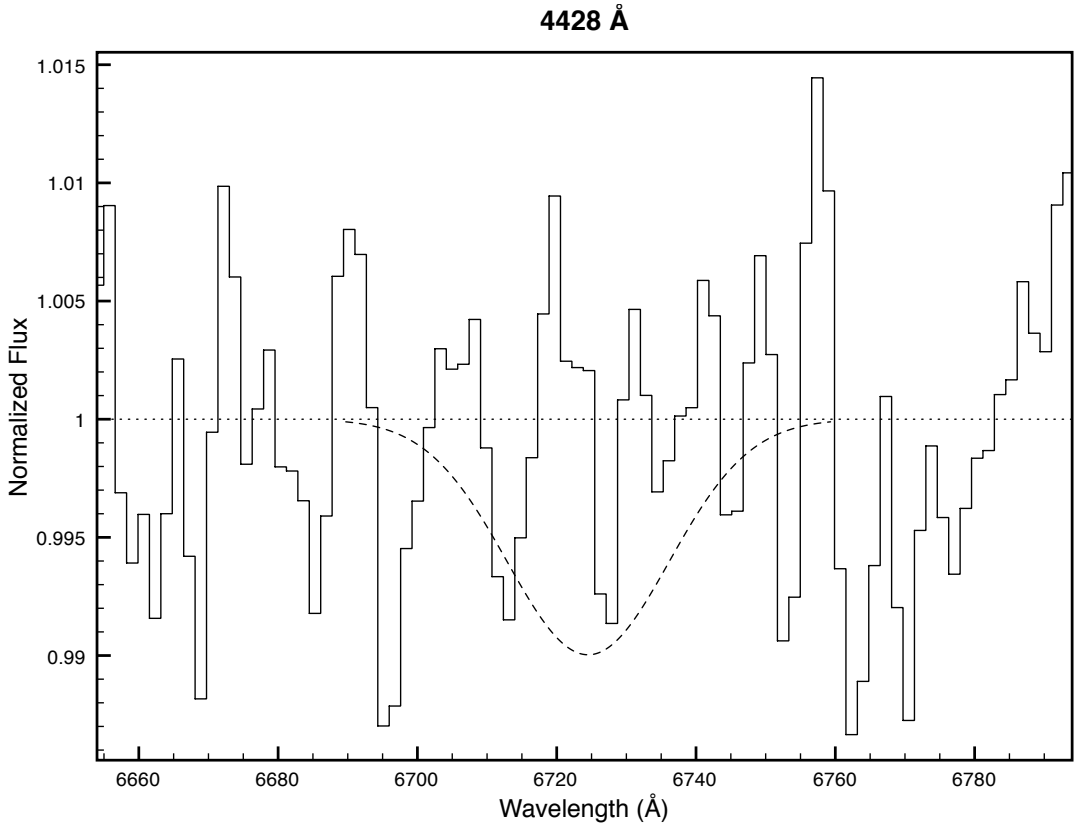

Figure 4.16: DIB upper limit in the Ca II system towards J1226−0006. The histogram is the normalized spectrum, and the dashed line is the 5-σ limit.

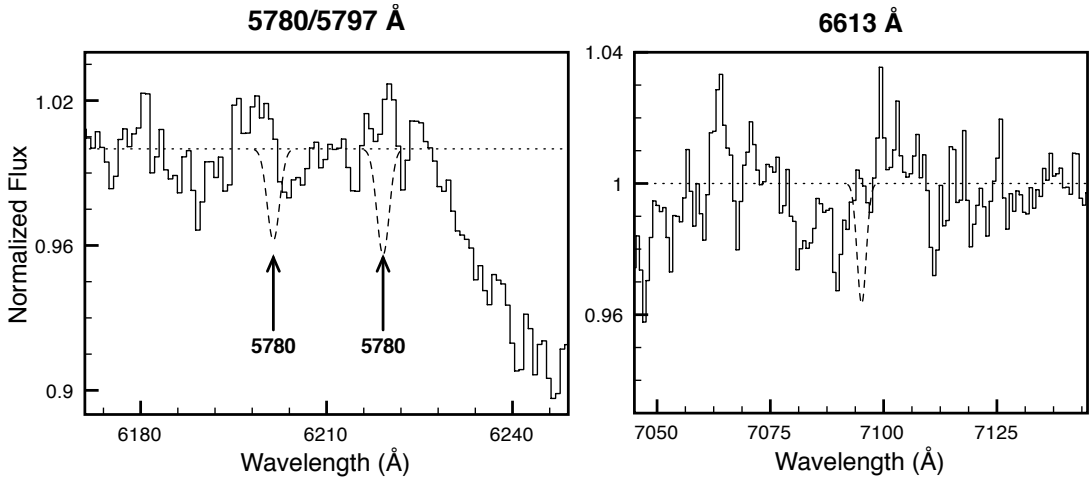

Figure 4.17: DIB upper limits in the Ca II system towards J1437−0104. In all cases, the histogram is the normalized spectrum, and the dashed lines are 5-σ limits.

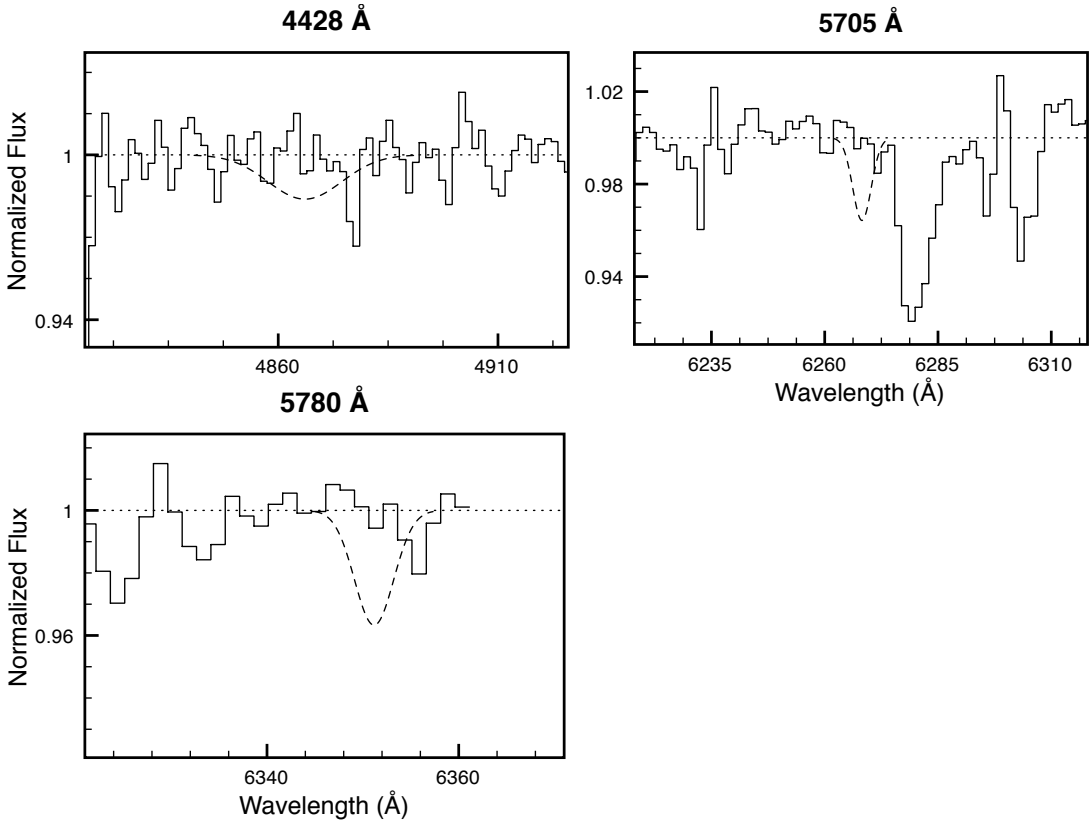

Figure 4.18: DIB upper limits in the Ca II system towards J2135+1038. In all cases, the histogram is the normalized spectrum, and the dashed lines are 5-σ limits.

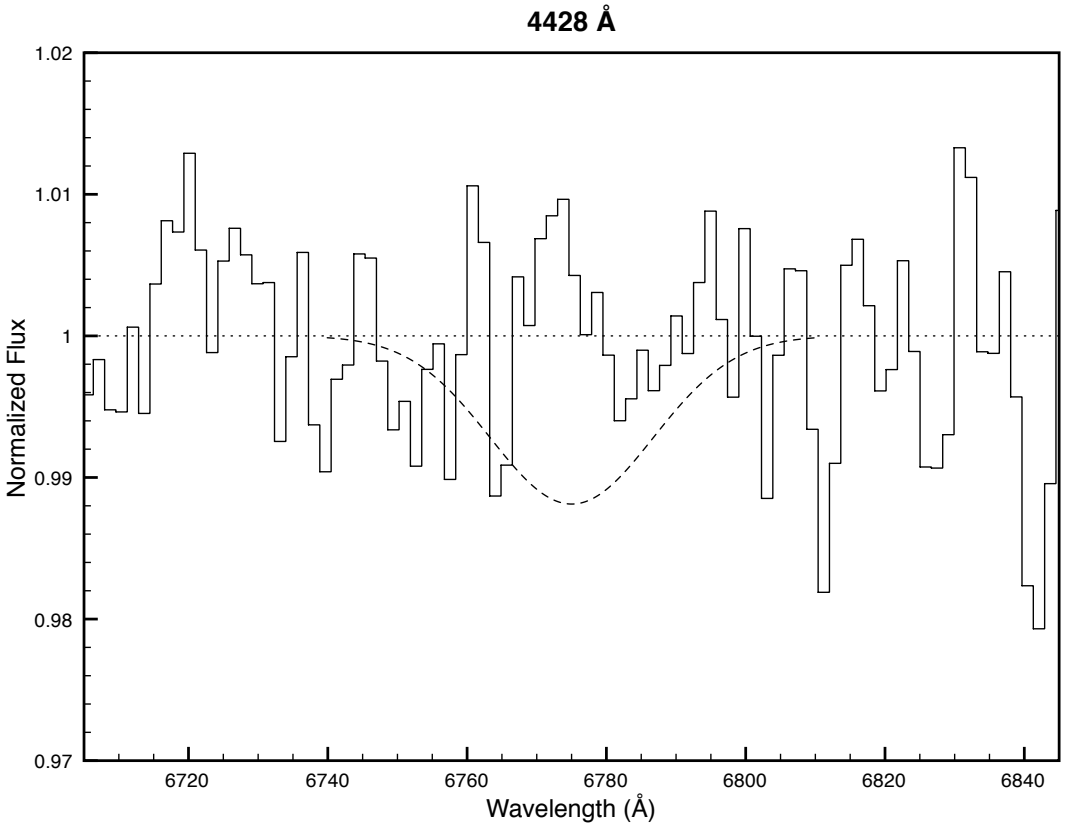

Figure 4.19: DIB upper limit in the Ca II system towards J2259−0844. The histogram is the normalized spectrum, and the dashed line is the 5-σ limit.

4.3.2 Relative DIB Strengths

I previously showed (in §3.3.2) that the 6284 Å DIB, which is two–three times stronger than the 5780 Å DIB in local sight-lines, including in the Milky Way (e.g. Herbig 1995), Magellanic Cloud (e.g. Welty et al. 2006), and local starburst galaxies (e.g. Heckman & Lehnert 2000), is instead weaker than the 5780 Å DIB in the DLA towards AO 0235+164. While the 6284 Å DIB is not constrained to be *weaker* than the 5780 Å DIB in the Ca II system towards J0013−0024 ($EW_{6284}/EW_{5780} \leq 1.38$ based on 5-σ limits)[3], this is still a lower ratio than *any* $z = 0$ sightline with the exception of the sightline towards Sk 143 in the SMC (Ehrenfreund et al. 2002). Figure 4.20 shows the DIB relative strengths towards J0013−0024 (normalized to EW_{5780}) compared to the $z = 0.524$ DLA towards AO 0235+164 and to two sightlines at $z = 0$.

Another ratio which may be compared is EW_{5705}/EW_{5780}. In the DLA towards AO 0235+164, this ratio is consistent with a correlation described by Thorburn et al. (2003) (and see Figure 3.11). Although the 5705 Å DIB is not detected in any of the Ca II systems here, the upper limit on EW_{5705} towards J0013−0024 is consistent with the strength of the 5780 Å DIB in that system, based on the Thorburn relation. If EW_{5705}/EW_{5780} towards J0013−0024 does follow the relationship detailed by Thorburn et al. (2003), then the 5705 Å DIB would have $EW_{5705} = 24$ mÅ, compared to our current limit of $EW_{5705} < 103$ mÅ. See Figure 4.21 for a plot of the 5705–5780 relationship from Thorburn et al. (2003) with both AO 0235+164 and J0013−0024 plotted.

Ca II systems are thought to be selected from the most dusty and metal rich of quasar absorption systems (Wild et al. 2006), including DLAs, and it is extremely likely that the system towards J0013−0024 is a DLA, if only because of its low impact parameter (see §4.2, and see §4.3.3 for additional evidence that the Ca II system towards J0013−0024 is a DLA). If the Ca II system towards J0013−0024 *is* a

[3]Ellison et al. (2008) constrains $EW_{6284}/EW_{5780} \leq 1$ based on 3-σ limits

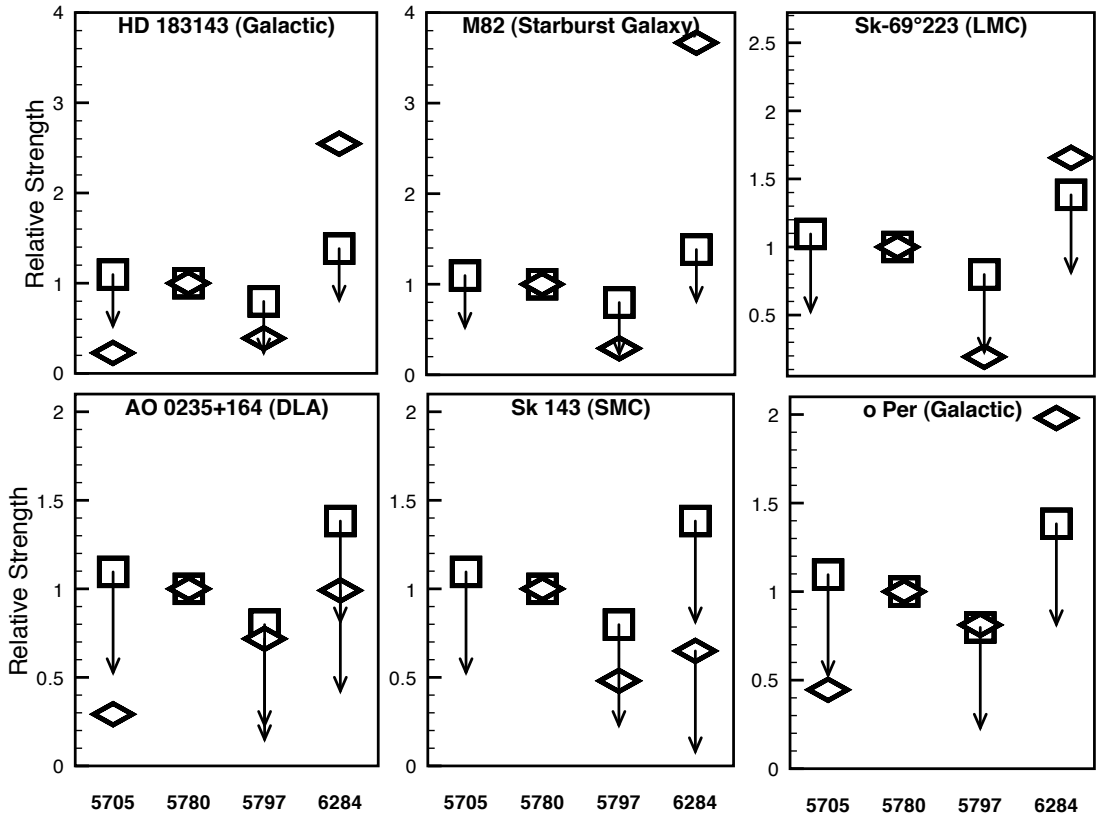

Figure 4.20: Relative strengths of the DIBs at 5705, 5780, 5797, and 6284 Å along a variety of sightlines, normalized to the strength of the 5780 Å DIB. In all cases the squares show the results from J0013−0024, whilst the diamonds show the results from the other systems. See Tables B.1 and B.2 for DIB equivalent widths on these sightlines.

DLA, its DIB ratios may then be compared to those of the $z = 0.524$ DLA towards AO 0235+164 (see Figure 4.20 for a comparison). Thus far these two systems are consistent in having $EW_{6284}/EW_{5780} \leq 1.38$ and $EW_{5797}/EW_{5780} < 0.8$, and it is possible that the two systems also have consistent EW_{5705}/EW_{5780} ratios. While this is at most a sample size of two, it still suggests the intriguing possibility that DLA sightlines may have a consistent set of relative DIB strengths.

4.3.3 Can DIB strength be used to determine N(H I) in Ca II Systems?

Based on the Galactic relationship between EW_{5780} and N(H I) (Herbig 1993), the detection of the 5780 Å DIB should allow the N(H I) of a Ca II system to be de-

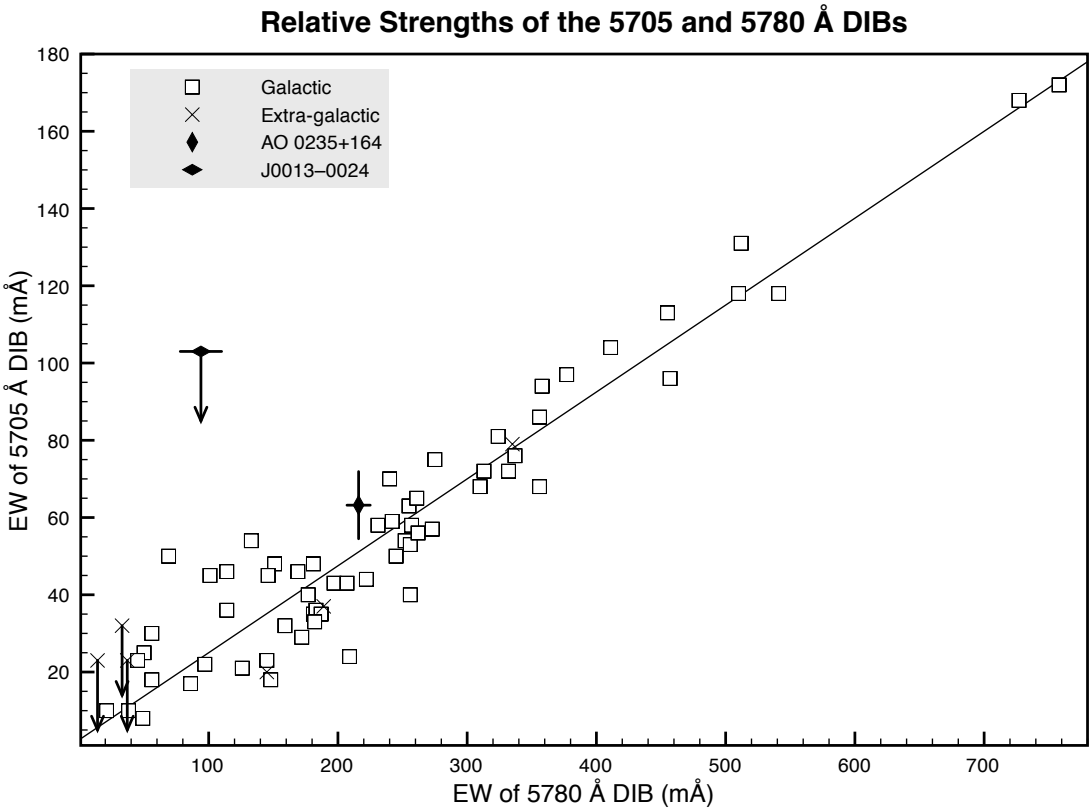

Figure 4.21: Relative strengths of the 5705 and 5780 Å DIBs. Galactic data taken from Table B.2 and extragalactic data from Table B.1.

termined, while an upper limit would in turn allow an upper limit on N(H I) to be derived. As §3.3.3 shows, however, the 5780 Å DIB is weaker relative to N(H I) in DLAs (and in the Magellanic Clouds) than the relationship obtained by Herbig (1993) would predict (see Figure 3.12). The presence of the 5780 Å DIB in the Ca II system towards J0013−0024 then may be regarded as placing a lower limit N(H I) $\geq 5.9 \times 10^{20}$ cm^{-2} for that system. This value is considerably higher than the threshold for DLAs, N(H I) $\geq 2.0 \times 10^{20}$ cm^{-2}, thus providing further evidence that the Ca II system towards J0013−0024 is a DLA. Indeed, given that the extragalactic data shown in Figure 4.22 give N(H I) $\geq 2.0 \times 10^{20}$ cm^{-2} for $EW_{5780} = 9.27$ mÅ, any system in which the 5780 Å DIB is detected at a moderate SNR is likely to be a DLA.

Figure 4.22 shows the EW_{5780}–N(H I) relationship, and equivalent width strengths and limits obtained for the Ca II systems in this sample.

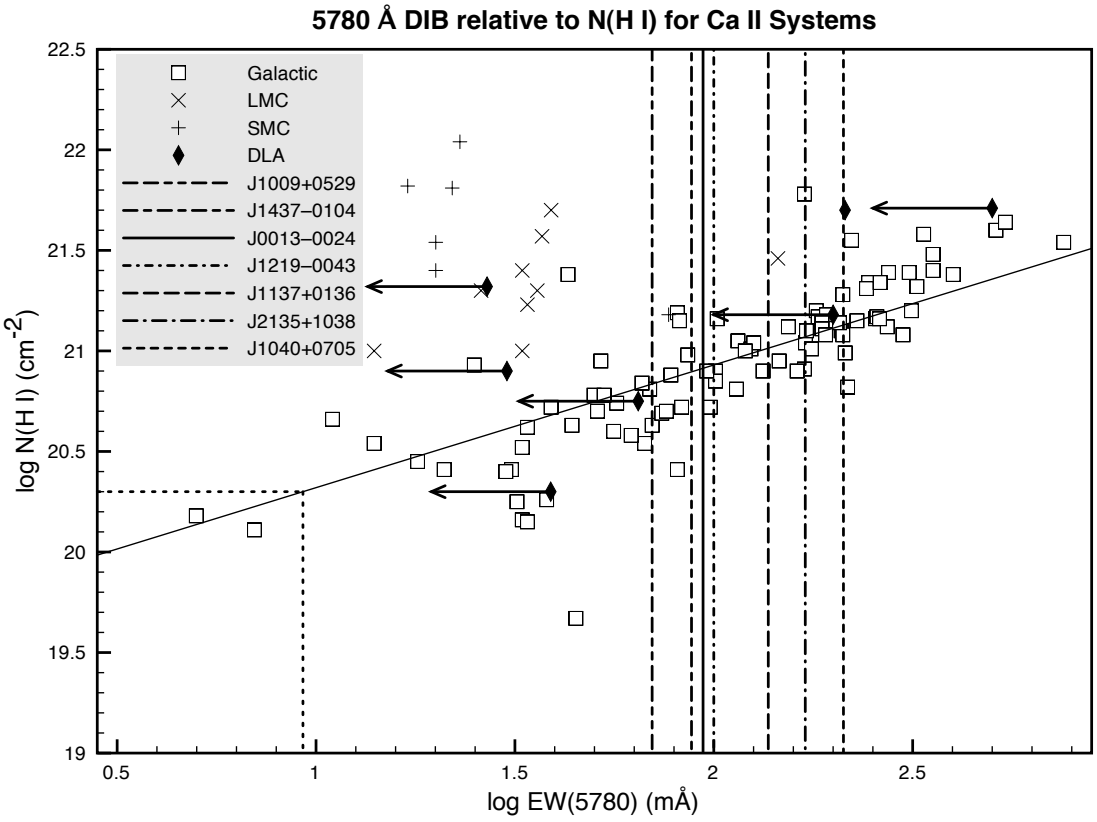

Figure 4.22: The relationship between N(H I) and the 5780 Å DIB. The vertical lines represent the detection (for J0013−0024) and upper limits to EW_{5780} obtained for the Ca II systems presented here. The vertical and horizontal dotted lines in the lower left quadrant show N(H I) = 2.0×10^{20} cm^{-2}, the threshold for a system to be considered a DLA, and EW_{5780} = 9.27 mÅ, the strength of the 5780 Å DIB corresponding to that N(H I). Data from Tables B.1 and Table B.2.

4.3.4 DIB Strength and Reddening

As shown in §3.4, the Galactic relationship between $E(B-V)$ and EW_{5780} appears to hold for DLAs as well, at least in the case of AO 0235+164 (see Figure 3.14). Indeed it was this discovery, combined with the discovery by Wild & Hewett (2005) that Ca II systems appeared to have a higher $E(B-V)$ than typical DLAs that suggested Ca II systems as a potential target for DIB detection. The detection of the 5780 Å

Table 4.3: Upper limits on N(H I) derived from EW_{5780}

QSO	z_{abs}	EW_{5780} (mÅ)	N(H I)/10^{20} (cm^{-2})
J1009+0529	0.3862	< 70	< 4.4
J1040+0705	0.2063	< 212	< 13
J1137+0136	0.4492	< 137	< 8.6
J1219−0043	0.4485	< 100	< 6.3
J1437−0104	0.0725	< 88	< 5.6
J2135+1038	0.0984	< 170	< 11

DIB towards J0013−0024 allows this relationship to be tested. The galaxy associated with the Ca II absorber has $E(B-V) = 0.66$ derived from the Balmer decrement (B. Zych, private communication), but the reddening along the line of sight towards the quasar is unknown. The existing relationship between EW_{5780} and $E(B-V)$ implies that the reddening of the Ca II system towards J0013−0024 is $E(B-V) = 0.23$. Even if the reddening is substantially higher, approaching the value derived from the associated galaxy [$E(B-V) = 0.66$], the value would still be within the scatter of the relationship (see Figure 4.23). In any case, it appears that the reddening of J0013−0024 is considerably above the average value $E(B-V) = 0.09$ obtained for Ca II systems with $EW_{Ca\ II,3934} > 0.7$ Å obtained by Wild & Hewett (2005), and also higher than the limits on $E(B-V)$ obtained for the DLAs in §3.4 from the 5780 Å DIB (with the exception of the limits for the $z = 0.091$ DLA towards Q 0738+313, and for the DLA towards PKS 1127−145). Thus, the detection of DIBs with $EW_{5780} \sim 100$ mÅ appears to select the host absorbers with large values of $E(B-V)$.

The upper limits on EW_{5780} (see §3.4 for an explanation of why limits on EW_{6284} are not used here to derive limits on $E(B-V)$) derived for the remaining Ca II systems allow the reddening of these systems to be determined from the Galactic relationship (e.g. see Figure 4.23). The upper limits on $E(B-V)$ are shown in Table 4.4. While the limits derived on reddening are not as sensitive as the average

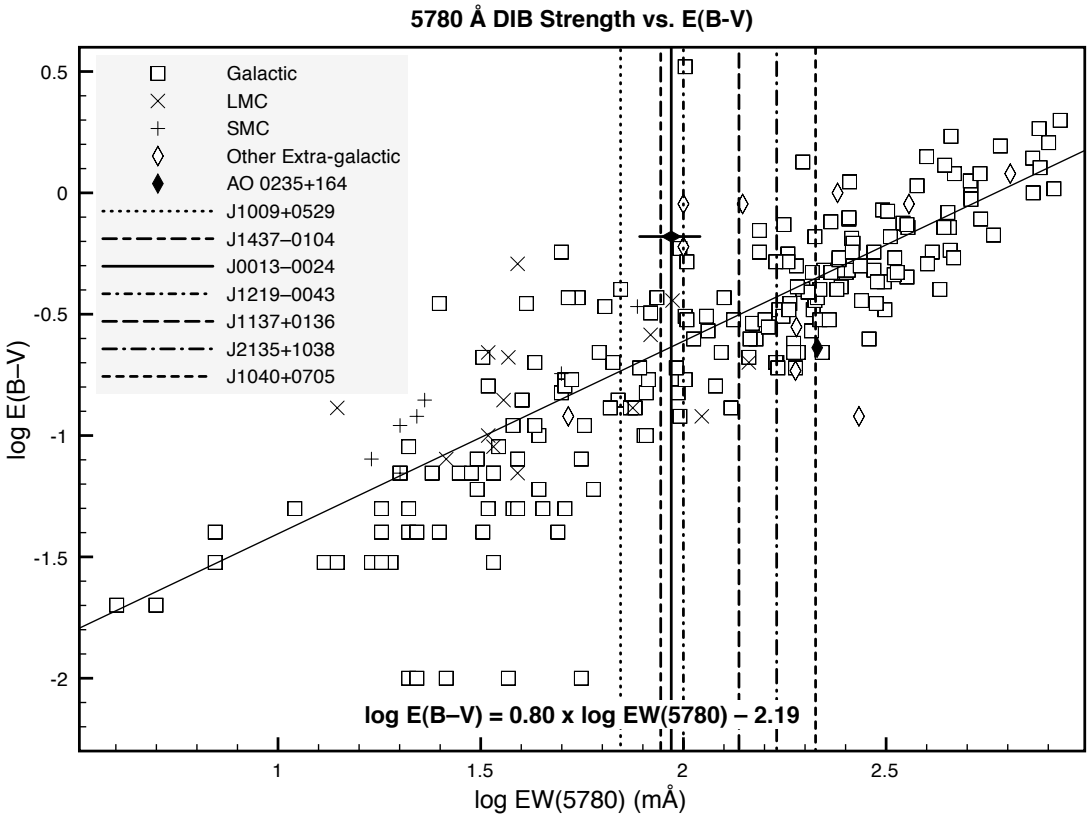

Figure 4.23: The relationship between $E(B-V)$ and the 5780 Å DIB. All points are as described in Figure 3.14, except for the vertical lines which represent the limits on $E(B-V)$ derived for the Ca II systems as well as the value of $E(B-V)$ derived for the Ca II system towards J0013−0024. The horizontal diamond represents the $E(B-V) = 0.66$ value derived for J0013−0024 through the Balmer decrement, and the horizontal error bar shows the error in W_{5780}. Data from Tables B.1 and B.2.

Table 4.4: Upper limits on Ca II system reddening

QSO	z_{abs}	EW_{5780} (mÅ)	$E(B-V)_{5780}$
J0013−0024	0.1556	94 ± 16	0.23 ± 0.03
J1009+0529	0.3862	< 70	< 0.18
J1040+0705	0.2063	< 212	< 0.44
J1137+0136	0.4492	< 137	< 0.31
J1219−0043	0.4485	< 100	< 0.24
J1437−0104	0.0725	< 88	< 0.22
J2135+1038	0.0984	< 170	< 0.37

reddening $E(B-V) = 0.06$ derived for Ca II systems by Wild & Hewett (2005), or even the average reddening $E(B-V) = 0.1$ derived by Wild et al. (2006) for Ca II systems with $EW_{Ca\ II,3934} > 0.5$ Å, these limits do allow the reddening of individual absorbers to be constrained *without* any assumptions as to the underlying extinction curve. Thus, whilst the detection of the 5780 Å DIB at the sensitivity limits of this search serves to select gas- and dust-rich absorbers, more sensitive limits will be required to constrain the dust content of Ca II systems directly.

Chapter 5

Summary and Future Prospects

5.1 Summary

A total of 16 quasar absorption systems with $0.091 \leq z \leq 0.525$ were searched for the diffuse interstellar bands at 5705, 5780, 5797, 6284, and 6613 Å, with the 5780 Å diffuse band being detected in two of the systems (at $z = 0.524$ towards AO 0235+164 and at $z = 0.1556$ towards J0013−0024), and the 5705 Å diffuse band detected in the system towards AO 0235+164. This marks the first detections of any narrow DIB at $z > 0$, and the first detection of any diffuse bands in a Ca II absorber. Upper limits were derived for those DIBs which were not detected.

5.1.1 Diffuse Bands in DLAs

Seven of the quasar absorbers studied were damped Lyman α systems, including the absorber towards AO 0235+164. In that DLA, the 6284 Å DIB was constrained to be weaker than the 5780 Å DIB, a result inconsistent with every sightline along which these two DIBs have been detected at $z = 0$ except for a single SMC sightline towards Sk 143. The ratio of the 5705 and 5780 Å DIBs, however, was consistent with the Galactic relationship derived by Thorburn et al. (2003). The DLA towards AO 0235+164 thus appears to have an environment unfavourable to the formation of the 6284 Å DIB carrier, but favourable to the the possibly related DIBs at 5705

and 5780 Å.

In general, the upper limits on both the 5780 and 6284 Å DIBs were found to be underabundant relative to Galactic sightlines compared to N(H I) in the DLAs. Five of the seven DLAs have 5780 Å DIB equivalent widths inconsistent with the Galactic EW_{5780}–N(H I) relationship, and six of the seven DLAs were inconsistent with the Galactic EW_{6284}–N(H I) relationship (see Figure 3.12, and 3.13). When these DIB strengths were compared with $E(B-V)$, the strength of the 5780 Å DIB towards AO 0235+164 was found to be consistent with the Galactic relationship, whilst the 6284 Å DIB had an upper limit within the scatter of its relationship with $E(B-V)$, so the consistency of that relationship could not be tested. The low DIB strengths relative to N(H I) mean that N(H I) is not a good method of selecting likely DIB-bearing DLAs. Based on the results of this study, however, $E(B-V)$, does appear to be a good method of pre-selecting DLAs in which DIBs are likely to be detected. Based on the DIB upper limits, I derive limits on $E(B-V)$ in the DLAs as shown in Table 3.5. These are consistent with previous statistical determinations of reddening in DLAs, and have the two-fold advantage of being independent of assumptions of the extinction curve and yield $E(B-V)$ values on a case by case basis.

5.1.2 Diffuse Bands in Ca II Systems

Nine of the absorbers searched were low-redshift Ca II systems, which Wild & Hewett (2005) have argued form a dust-rich subset of the DLA population. The 5780 Å DIB was detected in the $z = 0.1556$ Ca II system towards J0013−0024 ($EW_{5780} = 94 \pm 16$ mÅ), and limits were derived for the 5705, 5780, 5797, 6284, and 6613 Å DIBs for the remaining systems. Based on the strength of the 5780 Å DIB towards J0013−0024, and the Galactic EW_{5780}–N(H I) relation, it is confirmed that the absorber is very likely to be a DLA. Assuming that, like DLAs, Ca II absorbers have low DIB EWs for a given N(H I), a lower limit N(H I) $\geq 7.9 \times 10^{20}$ cm^{-2} is derived for J0013−0024. The limit N(H I) $< 2.0 \times 10^{20}$ cm^{-2} would correspond to

$EW_{5780} < 9.3$ mÅ given the Galactic relationship.

Whilst the $E(B-V)$ of the Ca II system towards J0013−0024 is not known for the absorption spectrum, it has been derived in emission from the Balmer decrement to be $E(B-V) = 0.66$. Although this value is not necessarily the value which would be measured in absorption, it still falls within the Galactic relationship when compared with EW_{5780}, indicating that this same relationship still holds [based on the EW_{5780}–$E(B-V)$ relationship, the Ca II system would have an absorption-derived $E(B-V) = 0.21$]. Further, the 6284 Å DIB is constrained to be the same strength as or weaker than the 5780 Å DIB, indicating that EW_{6284}/EW_{5780} is weaker here than almost all other sightlines, just as in the DLA towards AO 0235+164.

Although Ca II systems may well be a dust-rich subset of the DLA population, detecting diffuse bands in these systems does not appear to be notably easier than detecting them towards DLAs. This result, however, is unsurprising given the limits on $E(B-V)$ established in Table 4.4. Thus, whilst Ca II systems may be more likely targets for future DIB searches than DLAs, more sensitive limits will be required to test whether this is the case.

5.1.3 Diffuse Band Characteristics

The 5705 and 5780 Å DIBs detected towards AO 0235+164 have strengths which are consistent with the correlation described by Thorburn et al. (2003). While the 5705 Å DIB was not detected towards J0013−0024, its upper limit is consistent with the relationship given the strength of the 5780 Å DIB towards J0013−0024. That this correlation is found in the only QSO absorber in which it can be tested is intriguing (albeit tentative) evidence that either the carriers of the 5705 and 5780 Å DIBs share a similar environmental dependence (and are found in similar abundances in quasar absorbers as in the Milky Way) or that the carriers are related to each other in some way.

With only upper limits available for the other strong DIBs, there are no other

correlations which can be tested directly. The upper limit on the 6284 Å DIB towards AO 0235+164, however, constrains $EW_{6284}/EW_{5780} < 1$, whilst towards J0013−0024 $EW_{6284}/EW_{5780} < 1.4$. This ratio is $\gtrsim 2$ in Galactic and LMC sightlines, and is > 1.5 in SMC sightlines except for the sightline towards Sk 143, in which $EW_{6284}/EW_{5780} < 0.7$. Ehrenfreund et al. (2002) note that this sightline is located in the SMC wing, and thus likely more protected against UV radiation than the rest of the SMC, which may explain its unusual DIB ratios. Another possible explanation for the low EW_{6284}/EW_{5780} ratios in the QSO absorbers is that the carrier for the 6284 Å DIB may be significantly less abundant in these systems, possibly because the ISM environment in QSOAL systems is less favourable for its formation.

With the detection of only three DIBs on two sightlines, including only the 5705 and 5780 Å DIBs, there is as yet no way to constrain DIB strengths with respect to elemental abundances in quasar absorbers, especially since both absorbers in which DIBs are detected appear to be more metal rich than typical absorbers. With respect to the UV background and DIB ionization potentials, $EW_{5797}/EW_{5780} < 0.8$ for both absorbers, but this likely provides more information about the absorber sightlines than about the UV background (see §5.1.4). More DIBs will need to be detected along a single sightline in order to use their relative strengths to constrain either DIB composition or the UV background.

5.1.4 Diffuse Interstellar Bands and QSO Absorber Characteristics

Cami et al. (1997) note that the EW_{5797}/EW_{5780} ratio provides some indication as to environmental conditions along a sightline in which DIBs are detected. Sightlines dominated by the innermost regions of clouds (ζ-type) have almost equal 5780 and 5797 Å strengths, while less protected sightlines with a higher UV background have weaker 5797 Å DIB strengths. $EW_{5797}/EW_{5780} < 0.8$ for both AO 0235+164 and J0013−0024, which is inconsistent with ζ-type sightlines. The absorber sightline, however, is averaged through the entire galaxy and likely includes multiple different

clouds. The low EW_{5797}/EW_{5780} ratios towards these absorbers then could also indicate that such protected areas provide only a low fraction of the DLA sightline. If true, this would be consistent with the low f_{H_2} detected towards most DLAs.

The detection of DIBs in QSO absorbers confirms that complex organic molecules are present in QSO absorbers even at $z \sim 0.5$. However, the DLA towards AO 0235+164 and the Ca II system towards J0013−0024 are both atypical absorbers. The DLA has a high reddening $E(B-V) = 0.23$ and a high metallicity ($Z \sim 0.3$–$0.8 Z_{\odot}$) (Junkkarinen et al. 2004), neither of which are typical for QSO absorbers, which tend to have $Z \leq 0.1 Z_{\odot}$ (Pettini 2004) and $E(B-V) \leq 0.02$ (Murphy & Liske 2004). The Ca II system towards J0013−0024 also appears to be an unusual absorber in that its host galaxy is an L* spiral with near-solar metallicity, a star formation rate of ~ 4.5 $M_{\odot}$ yr^{-1} (compared to a local median rate of 0.5 $M_{\odot}$ yr^{-1} from the Near Field Galaxy Survey Kewley et al. 2002), and a reddening $E(B-V) = 0.66$ (B. Zych, private communication). The presence of strong diffuse bands, then, appears to single out unusually dust- and metal-rich absorbers as a subset of the overall population. Any future search for diffuse bands in quasar absorbers then, should concentrate on systems likely to be part of this subset.

5.2 Future Prospects

The future prospects for the diffuse band search may be divided into three main categories. Serendipitous observations focus on the detection of diffuse bands in spectra taken for other purposes, targeted observations on organized searches for diffuse bands in absorbers, and deep observations on studying systems where DIBs have been detected in great detail in order to learn more about relative DIB strengths in these systems.

5.2.1 Serendipitous Observations: individual spectra

Serendipitous observations focus on checking existing spectra of known absorbers for possible diffuse bands. Such spectra will need relative high signal-to-noise ratios (SNR $\geq$ 100, see e.g. Table 2.3 for the target signal-to-noise ratios for the DLA search) and with red spectral coverage (the 5780 Å DIB is redshifted to 1 μm by $z = 0.73$). As is shown by our moderate-resolution observations, spectral resolution need not be high in order to successfully detect the diffuse bands. Indeed, in a search for the broad DIBs (e.g. 4428 Å) a high spectral resolution is likely to make detections more difficult, because any broad shallow DIB absorption may be lost in normalization (e.g. see Figure 3.5).

The primary advantage of serendipitous observations is that no additional observing time is required, because the spectra have already been taken. A disadvantage is that the number of suitable spectra is likely to be low, because the wavelengths of the strong diffuse bands (between $\sim$ 4428 and 6613 Å) are removed considerably from the metal lines most often sought in QSO absorbers (e.g. C IV at $\lambda\lambda$ 1548.1,1550.7 Å, Mg II at $\lambda\lambda$ 2796.3,2803.5 Å, Si II at λ 1526.7 and λ 1808.0 Å, Zn II at $\lambda\lambda$ 2026.1,2062.7 Å). Only the Ca II doublet at $\lambda\lambda$ 3934.8,3969.6 Å and the Na I doublet at $\lambda\lambda$ 5891.6,5897.6 Å are close to the DIB wavelengths. Serendipitous observations are likely to be most useful in the case of background sources where the redshift of foreground absorbers is not previously known, and so a large spectral range is observed.

5.2.2 Serendipitous Observations: stacked spectra

Stacked observations are obtained by stacking together large numbers of existing spectra of different objects in order to produce a composite spectrum with considerably higher signal to noise than the original spectra. Stacked observations requires a source of spectra with known absorbers which can then be stacked. Data Release

6 (DR6) of the SDSS, for example, includes more than 100,000 QSO spectra with wavelength coverage from 3800–9200 Å (Adelman-McCarthy et al. 2008). In order to use the SDSS as a source for stacked observations, QSO spectra must be identified which contain absorbers at redshifts where diffuse bands may be observed. The 6613 Å DIB, for example, may be detected at $z \leq 0.39$, the 6284 Å DIB at $z \leq 0.46$, and the 5780 Å DIB at $z \leq 0.59$. Low-redshift quasar absorbers are best detected through metal line absorption, with potential lines including the Mg II doublet at $\lambda\lambda$ 2796,2803 Å, the Ca II doublet at $\lambda\lambda$ 3934,3969 Å, and the Na I doublet at $\lambda\lambda$ 5891,5897 Å. Table 5.1 shows the redshift ranges over which both the metal lines and all four strong DIBs could be detected. In this table the absorption wavelengths are the wavelengths of the absorption doublet of the specified ion, z_{min} indicates the lowest redshift at which the metal lines indicated can be detected in SDSS spectra, $z_{max,X}$ the maximum redshift at which the provided DIB (and any DIBs with shorter wavelengths) can be detected, and Δz_X the redshift path ($\Delta z_X = z_{max,X} - z_{min}$) over which appropriate absorbers might be found.

Table 5.1: Possible Metal Lines for SDSS DIB Search

Element	Absorption Wavelengths (Å)	z_{min}	$z_{max,6613}$	Δz_{6613}	$z_{max,6284}$	Δz_{6284}
Mg II	2796.35,2803.53	0.36	0.39	0.03	0.46	0.10
Ca II	3934.78,3969.59	0	0.39	0.39	0.46	0.46
Na I	5891.58,5897.56	0	0.39	0.39	0.46	0.46

As Table 5.1 shows, Mg II offers only a short redshift range for any DIB search, whilst both Ca II and Na I have the same redshift range available as the DIBs themselves do. Dr. M. Murphy has already conducted a search for low-redshift Ca II absorbers using SDSS DR3, which found 28 systems with $z \leq 0.39$ from amongst the $\sim 50,000$ QSO spectra in DR3 (Abazajian et al. 2005). Another search, conducted on the new systems included in DR6, would thus likely double the number of suitable systems. Given an average $SNR = 17.5$ for the existing 28 systems (B. Zych, private

communication), the the 5780 Å DIB should be detected at 5-σ down to a strength of 93 mÅ, which would allow detection given an average $E(B-V) = 0.23$ in these systems. If another 28 such systems were found through including SDSS data up to DR6, and these systems had the same average SNR, the detection limit would be 65 mÅ, which would allow detection given an average $E(B-V) = 0.17$.

The great advantage of stacked observations from the SDSS (or another survey) is that no additional observing time is required. Stacking also has the potential to achieve extremely high signal-to-noise ratios, and to build up a synthetic spectrum showing the average pattern of DIB strengths in QSO absorbers. A set of stacked spectra may also be split according to chosen criteria, which has the potential to determine what factors have the greatest influence on DIB strength in QSO absorbers. The effects of night sky interference can be mitigated with a large sample size, and even weak bands might be detected if enough spectra are available. The disadvantages of such a search include the low redshift range over which observations are possible (the SDSS, for example, extends only to 9200 Å, limiting observations to $z \leq 0.39$), and the inability to plan observations in order to optimize the target selection and methods of observation. The role of stacked observations may be both to investigate which factors affect DIB strength, and to suggest systems for further targeted or deep observations.

5.2.3 Targeted Observations

Targeted observations consist of searching for absorber candidates in which diffuse bands would be expected. Based on the results of the DIB search in DLAs and Ca II systems, the best candidates would be dust-rich systems. Further observations of Ca II systems might be expected to detect more diffuse bands as long as observations with high signal-to-noise are obtained. Ménard et al. (2008) have found that, for quasar absorbers with high $EW_{Mg\ II}$, the $E(B-V)$ is correlated with $EW_{Mg\ II}$, in

the form

$$\langle E(B-V)\rangle = (0.8 \pm 0.1) \times 10^{-2} \left(\frac{EW_{Mg\ II}}{1\text{Å}} \right)^{1.88\pm0.17} \tag{5.1}$$

so systems with $EW_{Mg\ II} = 7$ Å would have $\langle E(B-V)\rangle = 0.31$, which corresponds to $EW_{5780} = 135$ mÅ, considerably higher than the value derived for Ca II systems, and well within the average detection limits of the two surveys conducted thus far.

The main advantage of a targeted search for diffuse bands is that observations may be planned in advance to include the the appropriate wavelengths, and to avoid night sky interference (either through selecting targets by redshift, or using a technique such as nod-and-shuffle to reduce night sky interference). The primary disadvantage is, of course, the need to secure sufficient observing time to conduct the search. The role of targeted searches for diffuse bands is likely to be primarily in order to discover any variations in diffuse band strength (or relative strength) in the population of quasar absorbers. If stacked observations can identify a population of QSOAL systems with strong diffuse bands, then targeted observations may be used to examine individual systems in that population in greater detail.

5.2.4 Deep Observations

Deep observations involve additional exposure time being allocated to systems in which diffuse bands are known to be present, currently either the DLA towards AO 0235+164 or the Ca II system towards J0013−0024. More observing time on these targets has the potential to detect the remaining strong DIBs (e.g. at 5797, 6284, and 6613 Å), and even potentially some weak DIBs. For example, if the relationship noted by Thorburn et al. (2003) between EW_{5705} and EW_{5780} holds for for the Ca II system towards J0013−0024, the 5705 Å DIB would be expected to have a strength of 24 mÅ. The ESO exposure time calculator shows that 5 hours of observation with the 1200R Grism would be sufficient to detect the 5705 Å DIB at 5-σ given a 24 m$\mathring{A}$ equivalent width. When the 5280 s already taken during the Ca II system diffuse

band search are considered, the remaining time required would be ~ 3.6 hours.

Deep observations have the potential to allow even weaker DIBs to be detected in systems where diffuse bands are known to exist (discovered either through stacked or targeted observations). Because the targets are already known to have diffuse bands, the chance of detecting additional DIBs is much greater. Deep observations also share the advantage of targeted observations in that the targets may be chosen to minimize disruption from night sky lines, and that techniques such as nod-and-shuffle may be used to improve the sky subtraction. The primary disadvantage of deep observations is the observing time required. Observations of weak diffuse bands in the Milky Way have generally required signal-to-noise ratios of several hundred per pixel (e.g. Hobbs et al. 2008, with $SNR = 750$ pix^{-1}). Such high SNRs would be difficult to obtain for QSO absorbers, which tend to be much fainter systems than Galactic O and B stars, the primary local sightlines used for DIB searches.

5.3 Concluding Remarks

In this thesis, I have presented the search for diffuse interstellar bands in quasar absorption systems, including seven DLAs and nine Ca II absorbers. The 5705 and 5780 Å DIBs were detected in the $z_{abs} = 0.524$ DLA towards AO 0235+164, and the 5780 Å DIB in the $z_{abs} = 0.1556$ Ca II system towards J0013−0024, marking the first, and so far the only, detection of narrow diffuse bands at $z > 0$. These detections, combined with the upper limits derived for the other diffuse bands and other absorbers, show an intriguing picture of the diffuse bands in quasar absorbers. The 6284 Å DIB appears underabundant compared to nearly all local sightlines, whilst the close relationship between EW_{5705} and EW_{5780} appears to exist even in these systems. Whilst the 5780 and 6284 Å DIBs are weaker relative to N(H I) in the QSOAL systems than in the Milky Way, the 5780 Å DIB appears to have the same correlation with $E(B-V)$ in the absorbers as it does at $z = 0$. This connection

between DIB strength and reddening suggests that future searches in highly reddened absorbers are likely to yield more detections.

Bibliography

Abazajian, K., et al. (2005), The Third Data Release of the Sloan Digital Sky Survey, *Astron. J.*, *129*, 1755–1759, doi:10.1086/427544.

Adelman-McCarthy, J. K., et al. (2008), The Sixth Data Release of the Sloan Digital Sky Survey, *Astrophys. J. Suppl.*, *175*, 297–313, doi:10.1086/524984.

Akerman, C. J., S. L. Ellison, M. Pettini, & C. C. Steidel (2005), Zn and Cr abundances in damped Lyman alpha systems from the CORALS survey, *Astron. & Astrophys.*, *440*, 499–509, doi:10.1051/0004-6361:20052947.

Bada, J. L., & A. Lazcano (2002), Origin Of Life: Some Like It Hot, But Not the First Biomolecules, *Science*, *14*, 1982–1983, doi:10.1126/science.1069487.

Bahcall, J. N., B. A. Peterson, & M. Schmidt (1966), On the Absorption Spectrum of 1116+12, *Astrophys. J.*, *145*, 369–372, doi:10.1086/148778.

Blades, J. C., & B. F. Madore (1979), The interstellar lambda 4428 feature in the Large Magellanic Cloud, *Astron. & Astrophys.*, *71*, 359–361.

Blades, J. C., R. W. Hunstead, & H. S. Murdoch (1981), Detection of CA II absorption in the spectrum of the QSO 0446-208 due to an intervening galaxy, *Mon. Notic. Royal Astron. Soc.*, *194*, 669–678.

Boissé, P., V. Le Brun, J. Bergeron, & J.-M. Deharveng (1998), A HST spectroscopic study of QSOs with intermediate redshift damped Lyalpha systems, *Astron. & Astrophys.*, *333*, 841–863.

Boksenberg, A., & W. L. W. Sargent (1978), The existence of CA II absorption lines in the spectrum of the quasar 3C 232 due to the Galaxy NGC 3067, *Astrophys. J.*, *220*, 42–46, doi:10.1086/155880.

Bouchet, P., J. Lequeux, E. Maurice, L. Prevot, & M. L. Prevot-Burnichon (1985), The visible and infrared extinction law and the gas-to-dust ratio in the Small Magellanic Cloud, *Astron. & Astrophys.*, *149*, 330–336.

Bowen, D. V. (1991), Interstellar CA II in the galactic halo and in QSO absorption systems, *Mon. Notic. Royal Astron. Soc.*, *251*, 649–663.

Bowen, D. V., E. B. Jenkins, M. Pettini, & T. M. Tripp (2005), A Comparison of Absorption- and Emission-Line Abundances in the Nearby Damped Lyα Galaxy SBS 1543+593, *Astrophys. J.*, *635*, 880–893, doi:10.1086/497617.

Brown, R. L., & R. E. Spencer (1979), 21 centimeter absorption at z=0.395 in the quasar 1229-021, *Astrophys. J.*, *230*, L1–L4, doi:10.1086/182950.

Burbidge, E. M., E. A. Beaver, R. D. Cohen, V. T. Junkkarinen, & R. W. Lyons (1996), AO 0235 + 164 and Surrounding Field: Surprising HST Results, *Astron. J.*, *112*, 2533–2540, doi:10.1086/118199.

Cami, J., P. Sonnentrucker, P. Ehrenfreund, & B. H. Foing (1997), Diffuse Interstellar Bands in single clouds: new families and constraints on the carriers., *Astron. & Astrophys.*, *326*, 822–830.

Cardelli, J. A., G. C. Clayton, & J. S. Mathis (1989), The relationship between infrared, optical, and ultraviolet extinction, *Astrophys. J.*, *345*, 245–256, doi:10.1086/167900.

Centurión, M., P. Molaro, G. Vladilo, C. Péroux, S. A. Levshakov, & V. D'Odorico (2003), Early stages of nitrogen enrichment in galaxies: Clues from measurements

in damped Lyman alpha systems, *Astron. & Astrophys.*, *403*, 55–72, doi:10.1051/0004-6361:20030273.

Chen, H.-W., & K. M. Lanzetta (2003), The Nature of Damped Lyα Absorbing Galaxies at z $\leq$ 1: A Photometric Redshift Survey of Damped Lyα Absorbers, *Astrophys. J.*, *597*, 706–729, doi:10.1086/378635.

Chen, H.-W., R. C. Kennicutt, Jr., & M. Rauch (2005), Abundance Profiles and Kinematics of Damped Lyα Absorbing Galaxies at z $<$ 0.651,, *Astrophys. J.*, *620*, 703–722, doi:10.1086/427088.

Chen, Y. Q., P. E. Nissen, G. Zhao, & M. Asplund (2002), Sulphur abundances in disk stars: A correlation with silicon, *Astron. & Astrophys.*, *390*, 225–233, doi:10.1051/0004-6361:20020735.

Christensen, L., L. Wisotzki, M. M. Roth, S. F. Sánchez, A. Kelz, & K. Jahnke (2007), An integral field spectroscopic survey for high redshift damped Lyman-α galaxies, *Astron. & Astrophys.*, *468*, 587–601, doi:10.1051/0004-6361:20066410.

Cordiner, M. A., N. L. J. Cox, C. Trundle, C. J. Evans, I. Hunter, N. Przybilla, F. Bresolin, & F. Salama (2008), Detection of diffuse interstellar bands in M 31, *Astron. & Astrophys.*, *480*, L13–L16, doi:10.1051/0004-6361:20079309.

Cox, N. L. J., & F. Patat (2008), Interstellar atoms, molecules and diffuse bands toward SN2006X in M 100, *Astron. & Astrophys.*, *485*, L9–L12, doi:10.1051/0004-6361:200809785.

Cox, N. L. J., & M. Spaans (2006), The effects of metallicity, radiation field and dust extinction on the charge state of PAHs in diffuse clouds: implications for the DIB carrier, *Astron. & Astrophys.*, *451*, 973–980, doi:10.1051/0004-6361:20054484.

Cox, N. L. J., M. A. Cordiner, J. Cami, B. H. Foing, P. J. Sarre, L. Kaper, & P. Ehrenfreund (2006), The Large Magellanic Cloud: diffuse interstellar bands, atomic lines and the local environmental conditions, *Astron. & Astrophys.*, *447*, 991–1009, doi:10.1051/0004-6361:20053367.

Cox, N. L. J., N. Boudin, B. H. Foing, R. S. Schnerr, L. Kaper, C. Neiner, H. Henrichs, J.-F. Donati, & P. Ehrenfreund (2007), Linear and circular polarisation of diffuse interstellar bands, *Astron. & Astrophys.*, *465*, 899–906, doi:10.1051/0004-6361:20065278.

Crawford, M. K., A. G. G. M. Tielens, & L. J. Allamandola (1985), Ionized polycyclic aromatic hydrocarbons and the diffuse interstellar bands, *Astrophys. J.*, *293*, L45–L48, doi:10.1086/184488.

Curran, S., J. Webb, M. Murphy, & Y. Pihlström (2004), Atomic and Molecular Absorption at High Redshift, in *The Neutral ISM in Starburst Galaxies*, *Astronomical Society of the Pacific Conference Series*, vol. 320, edited by S. Aalto, S. Huttemeister, & A. Pedlar, pp. 342–345.

Curran, S. J., M. T. Whiting, M. T. Murphy, J. K. Webb, S. N. Longmore, Y. M. Pihlström, R. Athreya, & C. Blake (2006), A survey for redshifted molecular and atomic absorption lines - I. The Parkes half-Jansky flat-spectrum red quasar sample, *Mon. Notic. Royal Astron. Soc.*, *371*, 431–443, doi:10.1111/j.1365-2966.2006.10677.x.

Dessauges-Zavadsky, M., C. Péroux, T.-S. Kim, S. D'Odorico, & R. G. McMahon (2003), A homogeneous sample of sub-damped Lyman α systems - I. Construction of the sample and chemical abundance measurements, *Mon. Notic. Royal Astron. Soc.*, *345*, 447–479, doi:10.1046/j.1365-8711.2003.06949.x.

Dessauges-Zavadsky, M., J. X. Prochaska, S. D'Odorico, F. Calura, & F. Matteucci (2006), A new comprehensive set of elemental abundances in DLAs. II. Data analysis and chemical variation studies, *Astron. & Astrophys.*, *445*, 93–113, doi:10.1051/0004-6361:20053200.

Dessauges-Zavadsky, M., F. Calura, J. X. Prochaska, S. D'Odorico, & F. Matteucci (2007), A new comprehensive set of elemental abundances in DLAs. III. Star formation histories, *Astron. & Astrophys.*, *470*, 431–448, doi:10.1051/0004-6361:20077050.

Destree, J. D., T. P. Snow, & K. Eriksson (2007), The Presence of Diffuse Interstellar Bands in the Spectra of Cool Stars, *Astrophys. J.*, *664*, 909–914, doi:10.1086/519069.

D'Odorico, S., S. di Serego Alighieri, M. Pettini, P. Magain, P. E. Nissen, & N. Panagia (1989), A study of the interstellar medium in line to NGC 5128 from high resolution observations of the supernova 1986G, *Astron. & Astrophys.*, *215*, 21–32.

Duley, W. (1995), DIB Carriers on Grain Surfaces, in *The Diffuse Interstellar Bands*, *Astrophysics and Space Science Library*, vol. 202, edited by A. G. G. M. Tielens & T. P. Snow, pp. 359–362.

Duley, W. W., & W. R. M. Graham (1969), Possible Identification of the Diffuse Interstellar Absorption Band at 4430 Angstrom, *Nature*, *224*, 785–787.

Edvardsson, B., J. Andersen, B. Gustafsson, D. L. Lambert, P. E. Nissen, & J. Tomkin (1993), The Chemical Evolution of the Galactic Disk - Part One - Analysis and Results, *Astron. & Astrophys.*, *275*, 101–152.

Ehrenfreund, P., J. Cami, E. Dartois, & B. H. Foing (1997), Diffuse Interstellar Bands towards BD+63 1964. A new reference target., *Astron. & Astrophys.*, *318*, L28–L31.

Ehrenfreund, P., et al. (2002), Detection of Diffuse Interstellar Bands in the Magellanic Clouds, *Astrophys. J.*, *576*, L117–L120, doi:10.1086/343731.

Ellison, S. L., L. Yan, I. M. Hook, M. Pettini, J. V. Wall, & P. Shaver (2001), The CORALS survey I: New estimates of the number density and gas content of damped Lyman alpha systems free from dust bias , *Astron. & Astrophys.*, *379*, 393–406, doi:10.1051/0004-6361:20011281.

Ellison, S. L., P. B. Hall, & P. Lira (2005a), The Optical-Infrared Colors of CORALS QSOs: Searching for Dust Reddening Associated with High-Redshift Damped Lyα Systems, *Astron. J.*, *130*, 1345–1357, doi:10.1086/444537.

Ellison, S. L., L. J. Kewley, & G. Mallén-Ornelas (2005b), Emission-line abundances of absorption-selected galaxies at z $<$ 0.5, *Mon. Notic. Royal Astron. Soc.*, *357*, 354–360, doi:10.1111/j.1365-2966.2005.08674.x.

Ellison, S. L., B. A. York, M. T. Murphy, B. J. Zych, A. M. Smith, & P. J. Sarre (2008), Diffuse interstellar bands in z $<$ 0.6 CaII absorbers, *Mon. Notic. Royal Astron. Soc.*, *383*, L30–L34, doi:10.1111/j.1745-3933.2007.00404.x.

Fall, S. M., & Y. C. Pei (1993), Obscuration of quasars by dust in damped Lyman-alpha systems, *Astrophys. J.*, *402*, 479–492, doi:10.1086/172151.

Federman, S. R., P. A. Vanden Bout, & C. K. Kumar (1984), Observations of narrow diffuse interstellar bands toward stars with low reddening, *Astrophys. J.*, *282*, 485–490, doi:10.1086/162226.

Galazutdinov, G. A., J. Krełowski, F. A. Musaev, P. Ehrenfreund, & B. H. Foing (2000), On the identification of the C_{60}^{+} interstellar features, *Mon. Notic. Royal Astron. Soc.*, *317*, 750–758.

Galazutdinov, G. A., G. Manicò, V. Pirronello, & J. Krełowski (2004), Correlations between diffuse interstellar bands and atomic lines, *Mon. Notic. Royal Astron. Soc.*, *355*, 169–177, doi:10.1111/j.1365-2966.2004.08314.x.

García-Lario, P., R. Luna, & M. A. Satorre (2005), The Use of Planetary Nebulae Precursors in the Study of Diffuse Interstellar Bands, in *Planetary Nebulae as Astronomical Tools*, *American Institute of Physics Conference Series*, vol. 804, edited by R. Szczerba, G. Stasińska, & S. K. Gorny, pp. 222–228, doi:10.1063/1.2146281.

Geers, V. C., E. F. van Dishoeck, R. Visser, K. M. Pontoppidan, J.-C. Augereau, E. Habart, & A. M. Lagrange (2007), Spatially extended polycyclic aromatic hydrocarbons in circumstellar disks around T Tauri and Herbig Ae stars, *Astron. & Astrophys.*, *476*, 279–289, doi:10.1051/0004-6361:20078466.

Glownia, J. H., & P. P. Sorokin (1994), L(alpha)-induced two-photon absorption of visible light emitted from an O-type star by H2(+) ions located near the surface of the Stromgren sphere surrounding the star: A possible explanation for the diffuse interstellar absorption bands (DIDs), in *The Diffuse Interstellar Bands*, edited by A. G. G. M. Tielens, pp. 99–104.

Hagen-Thorn, V. A., V. M. Larionov, S. G. Jorstad, A. A. Arkharov, E. I. Hagen-Thorn, N. V. Efimova, L. V. Larionova, & A. P. Marscher (2008), The Outburst of the Blazar AO 0235+164 in 2006 December: Shock-in-Jet Interpretation, *Astrophys. J.*, *672*, 40–47, doi:10.1086/523841.

Hartmann, J. (1904), Investigations on the spectrum and orbit of delta Orionis., *Astrophys. J.*, *19*, 268–286, doi:10.1086/141112.

Hazard, C., M. B. Mackey, & A. J. Shimmins (1963), Investigation of the Radio Source 3C273 by the method of Lunar Occultations, *Nature*, *197*, 1037–1039.

Heckman, T. M., & M. D. Lehnert (2000), The Detection of the Diffuse Interstellar Bands in Dusty Starburst Galaxies, *Astrophys. J.*, *537*, 690–696, doi: 10.1086/309086.

Heger, M. L. (1922), The spectra of certain class B stars in the regions 5630A-6680A and 3280A-3380A., *Lick Observatory Bulletin*, *10*, 146–147.

Heisler, J., & J. P. Ostriker (1988), Models of the quasar population. II - The effects of dust obscuration, *Astrophys. J.*, *332*, 543–574, doi:10.1086/166677.

Henroteau, F. (1921), The Interstellar Clouds of Metallic Gasses, *J. Royal Astron. Soc. Canada*, *15*, 62–70,109–119.

Henry, R. B. C., & J. X. Prochaska (2007), The Chemical Evolution of High-z Galaxies from the Relative Abundances of N, Si, S, and Fe in Damped Lyα Systems, *Publ. Astron. Soc. Pacific*, *119*, 962–979, doi:10.1086/522038.

Henry, R. B. C., M. G. Edmunds, & J. Köppen (2000), On the Cosmic Origins of Carbon and Nitrogen, *Astrophys. J.*, *541*, 660–674, doi:10.1086/309471.

Herbig, G. H. (1963), The Diffuse Interstellar Bands. I. a Possible Identification of λ 4430., *Astrophys. J.*, *137*, 200–212.

Herbig, G. H. (1993), The diffuse interstellar bands. IX - Constraints on the identification, *Astrophys. J.*, *407*, 142–156, doi:10.1086/172500.

Herbig, G. H. (1995), The Diffuse Interstellar Bands, *Ann. Rev. Astron. Astrophys.*, *33*, 19–74, doi:10.1146/annurev.aa.33.090195.000315.

Hobbs, L. M., et al. (2008), A Catalog of Diffuse Interstellar Bands in the Spectrum of HD 204827, *Astrophys. J.*, *680*, 1256–1270, doi:10.1086/587930.

Hollenbach, D., & E. E. Salpeter (1971), Surface Recombination of Hydrogen Molecules, *Astrophys. J.*, *163*, 155–164.

Holmlid, L. (2008), The diffuse interstellar band carriers in interstellar space: all intense bands calculated from He doubly excited states embedded in Rydberg Matter, *Mon. Notic. Royal Astron. Soc.*, *384*, 764–774, doi:10.1111/j.1365-2966.2007.12753.x.

Hudgins, D. M., C. W. Bauschlicher, Jr., & L. J. Allamandola (2005), Variations in the Peak Position of the 6.2 μm Interstellar Emission Feature: A Tracer of N in the Interstellar Polycyclic Aromatic Hydrocarbon Population, *Astrophys. J.*, *632*, 316–332, doi:10.1086/432495.

Hutchings, J. B. (1966), 4430Å Band absorption in the Magellanic Clouds, *Mon. Notic. Royal Astron. Soc.*, *131*, 299–305.

Ilbert, O., et al. (2005), The VIMOS-VLT deep survey. Evolution of the galaxy luminosity function up to z = 2 in first epoch data, *Astron. & Astrophys.*, *439*, 863–876, doi:10.1051/0004-6361:20041961.

Izotov, Y. I., & T. X. Thuan (1999), Heavy-Element Abundances in Blue Compact Galaxies, *Astrophys. J.*, *511*, 639–659, doi:10.1086/306708.

Jenniskens, P., P. Ehrenfreund, & B. Foing (1994), Diffuse interstellar bands in Orion: The environment dependence of DIB strength, *Astron. & Astrophys.*, *281*, 517–525.

Johnson, F. (1995), Porphyrins Within Interstellar Grains, in *The Diffuse Interstellar Bands*, *Astrophysics and Space Science Library*, vol. 202, edited by A. G. G. M. Tielens & T. P. Snow, pp. 341–348.

Josafatsson, K., & T. P. Snow (1987), CCD observations of diffuse interstellar bands in reflection nebulae, *Astrophys. J.*, *319*, 436–445, doi:10.1086/165468.

Junkkarinen, V. T., R. D. Cohen, E. A. Beaver, E. M. Burbidge, R. W. Lyons, & G. Madejski (2004), Dust and Diffuse Interstellar Bands in the $z_a = 0.524$

Absorption System toward AO 0235+164, *Astrophys. J.*, *614*, 658–670, doi: 10.1086/423777.

Kanekar, N., & J. N. Chengalur (2001), HI 21 cm absorption in low vec z damped Lyman-alpha systems, *Astron. & Astrophys.*, *369*, 42–48, doi:10.1051/0004-6361: 20010096.

Kanekar, N., & J. N. Chengalur (2003), A deep search for 21-cm absorption in high redshift damped Lyman-alpha systems, *Astron. & Astrophys.*, *399*, 857–868, doi: 10.1051/0004-6361:20021922.

Kanekar, N., T. Ghosh, & J. N. Chengalur (2001), Detection of a multi-phase ISM at {vec z=} 0.2212, *Astron. & Astrophys.*, *373*, 394–401, doi:10.1051/0004-6361: 20010545.

Kennicutt, R. C., Jr. (1998), Star Formation in Galaxies Along the Hubble Sequence, *Ann. Rev. Astron. Astrophys.*, *36*, 189–232, doi:10.1146/annurev.astro.36.1.189.

Kewley, L. J., M. J. Geller, R. A. Jansen, & M. A. Dopita (2002), The Hα and Infrared Star Formation Rates for the Nearby Field Galaxy Survey, *Astron. J.*, *124*, 3135–3143, doi:10.1086/344487.

Kewley, L. J., M. J. Geller, & R. A. Jansen (2004), [O II] as a Star Formation Rate Indicator, *Astron. J.*, *127*, 2002–2030, doi:10.1086/382723.

Khare, P., V. P. Kulkarni, J. T. Lauroesch, D. G. York, A. P. S. Crotts, & O. Nakamura (2004), Metals and Dust in Intermediate-Redshift Damped Lyα Galaxies, *Astrophys. J.*, *616*, 86–109, doi:10.1086/424893.

Khare, P., V. P. Kulkarni, C. Péroux, D. G. York, J. T. Lauroesch, & J. D. Meiring (2007), The nature of damped Lyman α and sub-damped Lyman α absorbers, *Astron. & Astrophys.*, *464*, 487–493, doi:10.1051/0004-6361:20066186.

Khare, P., et al. (2005), Evidence for the presence of dust in intervening QSO absorbers from the Sloan Digital Sky Survey, in *IAU Colloq. 199: Probing Galaxies through Quasar Absorption Lines*, edited by P. Williams, C.-G. Shu, & B. Menard, pp. 427–429, doi:10.1017/S1743921305002978.

Kobulnicky, H. A., & E. D. Skillman (1996), Elemental Abundance Variations and Chemical Enrichment from Massive Stars in Starbursts. I. NGC 4214, *Astrophys. J.*, *471*, 211–+, doi:10.1086/177964.

Kobulnicky, H. A., R. C. Kennicutt, Jr., & J. L. Pizagno (1999), On Measuring Nebular Chemical Abundances in Distant Galaxies Using Global Emission-Line Spectra, *Astrophys. J.*, *514*, 544–557, doi:10.1086/306987.

Krełowski, J., & C. Sneden (1995), Diffuse Interstellar Bands in Individual Sightlines, in *The Diffuse Interstellar Bands*, *Astrophysics and Space Science Library*, vol. 202, edited by A. G. G. M. Tielens & T. P. Snow, pp. 13–24.

Krelowski, J., & G. A. H. Walker (1987), Three families of diffuse interstellar bands?, *Astrophys. J.*, *312*, 860–867, doi:10.1086/164932.

Krełowski, J., P. Ehrenfreund, B. H. Foing, T. P. Snow, T. Weselak, S. Ó. Tuairisg, G. A. Galazutdinov, & F. A. Musaev (1999), On the relation between diffuse interstellar bands and simple molecular species, *Astron. & Astrophys.*, *347*, 235–242.

Kulkarni, V. P., S. M. Fall, J. T. Lauroesch, D. G. York, D. E. Welty, P. Khare, & J. W. Truran (2005), Hubble Space Telescope Observations of Element Abundances in Low-Redshift Damped Lyα Galaxies and Implications for the Global Metallicity-Redshift Relation, *Astrophys. J.*, *618*, 68–90, doi:10.1086/425956.

Kulkarni, V. P., D. G. York, G. Vladilo, & D. E. Welty (2007), 9.7 μm Silicate Absorption in a Damped Lyα Absorber at z = 0.52, *Astrophys. J.*, *663*, L81–L84, doi:10.1086/520048.

Lane, W. M., F. H. Briggs, & A. Smette (2000), Detection of Warm and Cold Phases of the Neutral ISM in a Damped Lyα Absorber, *Astrophys. J.*, *532*, 146–151, doi:10.1086/308578.

Lawton, B., C. W. Churchill, B. A. York, S. L. Ellison, T. P. Snow, R. A. Johnson, S. G. Ryan, & C. R. Benn (2008), Limits on Reddening and Gas-To Ratios for Seven Intermediate Redshift Damped Lyα Absorbers from Diffuse Interstellar Bands, *Astron. J.*, *136*, 994–1012, doi:10.1088/0004-6256/136/3/994.

Le Brun, V., J. Bergeron, P. Boissé, & J. M. Deharveng (1997), The nature of intermediate-redshift damped Lyα absorbers., *Astron. & Astrophys.*, *321*, 733–748.

Le Page, V., T. P. Snow, & V. M. Bierbaum (2001), Hydrogenation and Charge States of PAHS in Diffuse Clouds. I. Development of a Model, *Astrophys. J. Suppl.*, *132*, 233–251, doi:10.1086/318952.

Le Page, V., T. P. Snow, & V. M. Bierbaum (2003), Hydrogenation and Charge States of Polycyclic Aromatic Hydrocarbons in Diffuse Clouds. II. Results, *Astrophys. J.*, *584*, 316–330, doi:10.1086/345595.

Leger, A., & L. d'Hendecourt (1985), Are polycyclic aromatic hydrocarbons the carriers of the diffuse interstellar bands in the visible?, *Astron. & Astrophys.*, *146*, 81–85.

Leger, A., & J. L. Puget (1984), Identification of the 'unidentified' IR emission features of interstellar dust?, *Astron. & Astrophys.*, *137*, L5–L8.

Lodders, K. (2003), Solar System Abundances and Condensation Temperatures of the Elements, *Astrophys. J.*, *591*, 1220–1247, doi:10.1086/375492.

Luna, R., N. L. J. Cox, M. A. Satorre, D. A. García Hernández, O. Suárez, & P. García Lario (2008), A search for diffuse bands in the circumstellar envelopes of post-AGB stars, *Astron. & Astrophys.*, *480*, 133–148, doi:10.1051/0004-6361:20065282.

Maier, J. P., G. A. H. Walker, & D. A. Bohlender (2004), On the Possible Role of Carbon Chains as Carriers of Diffuse Interstellar Bands, *Astrophys. J.*, *602*, 286–290, doi:10.1086/381027.

Maier, J. P., A. E. Boguslavskiy, H. Ding, G. A. H. Walker, & D. A. Bohlender (2006), The Gas Phase Spectrum of Cyclic C_{18} and the Diffuse Interstellar Bands, *Astrophys. J.*, *640*, 369–372, doi:10.1086/500110.

Malville, J. M. (1964), Abundance of Metastable Hydrogen Molecules in the Interstellar Medium., *Astrophys. J.*, *139*, 198–207.

McCall, B. J., J. Thorburn, L. M. Hobbs, T. Oka, & D. G. York (2001), Rejection of the C_7^- Diffuse Interstellar Band Hypothesis, *Astrophys. J.*, *559*, L49–L53, doi:10.1086/323669.

McKellar, A., H. L. Welsh, & F. C. Stephenson (1955), The spectrum of solid oxygen a few degrees above absolute zero., *Astron. J.*, *60*, 170–171, doi:10.1086/107155.

Megier, A., J. Krełowski, & T. Weselak (2005), Correlation patterns between 11 diffuse interstellar bands and ultraviolet extinction, *Mon. Notic. Royal Astron. Soc.*, *358*, 563–571, doi:10.1111/j.1365-2966.2005.08802.x.

Meiring, J. D., V. P. Kulkarni, P. Khare, J. Bechtold, D. G. York, J. Cui, J. T. Lauroesch, A. P. S. Crotts, & O. Nakamura (2006), Elemental abundance mea-

surements in low-redshift damped Lyman α absorbers, *Mon. Notic. Royal Astron. Soc.*, *370*, 43–62, doi:10.1111/j.1365-2966.2006.10500.x.

Ménard, B., D. Nestor, D. Turnshek, A. Quider, G. Richards, D. Chelouche, & S. Rao (2008), Lensing, reddening and extinction effects of MgII absorbers from z = 0.4 to 2, *Mon. Notic. Royal Astron. Soc.*, *385*, 1053–1066, doi:10.1111/j.1365-2966.2008.12909.x.

Merrill, P. W. (1934), Unidentified Interstellar Lines, *Publ. Astron. Soc. Pacific*, *46*, 206–207.

Møller, P., S. J. Warren, S. M. Fall, J. U. Fynbo, & P. Jakobsen (2002), Are High-Redshift Damped Lyα Galaxies Lyman Break Galaxies?, *Astrophys. J.*, *574*, 51–58, doi:10.1086/340934.

Moutou, C., J. Krełowski, L. D'Hendecourt, & J. Jamroszczak (1999), On correlations between diffuse interstellar bands, *Astron. & Astrophys.*, *351*, 680–688.

Murphy, M. T., & J. Liske (2004), Dust-reddening and gravitational lensing of SDSS QSOs due to foreground damped Lyman α systems, *Mon. Notic. Royal Astron. Soc.*, *354*, L31–L36, doi:10.1111/j.1365-2966.2004.08374.x.

Narayanan, A., T. Misawa, J. C. Charlton, & T.-S. Kim (2007), A Survey of Weak Mg II Absorbers at $0.4 < z < 2.4$, *Astrophys. J.*, *660*, 1093–1105, doi:10.1086/512852.

Nissen, P. E., Y. Q. Chen, M. Asplund, & M. Pettini (2004), Sulphur and zinc abundances in Galactic stars and damped Lyα systems, *Astron. & Astrophys.*, *415*, 993–1007, doi:10.1051/0004-6361:20034063.

Nissen, P. E., C. Akerman, M. Asplund, D. Fabbian, F. Kerber, H. U. Kaufl, & M. Pettini (2007), Sulphur and zinc abundances in Galactic halo stars revisited, *Astron. & Astrophys.*, *469*, 319–330, doi:10.1051/0004-6361:20077344.

Norberg, P., et al. (2002), The 2dF Galaxy Redshift Survey: the b_J-band galaxy luminosity function and survey selection function, *Mon. Notic. Royal Astron. Soc.*, *336*, 907–931, doi:10.1046/j.1365-8711.2002.05831.x.

Noterdaeme, P., C. Ledoux, P. Petitjean, & R. Srianand (2008), Molecular hydrogen in high-redshift damped Lyman-α systems: the VLT/UVES database, *Astron. & Astrophys.*, *481*, 327–336, doi:10.1051/0004-6361:20078780.

Odell, S. L., J. J. Puschell, W. A. Stein, F. Owen, R. W. Porcas, S. Mufson, T. J. Moffett, & M.-H. Ulrich (1978), Coordinated photometric and spectroscopic observations of strong extragalactic 90 GHz sources, *Astrophys. J.*, *224*, 22–31, doi:10.1086/156345.

Oke, J. B. (1963), Absolute Energy Distribution in the Optical Spectrum of 3C273, *Nature*, *197*, 1040–1041.

Pagel, B. E. J., M. G. Edmunds, D. E. Blackwell, M. S. Chun, & G. Smith (1979), On the composition of H II regions in southern galaxies. I - NGC 300 and 1365, *Mon. Notic. Royal Astron. Soc.*, *189*, 95–113.

Pei, Y. C. (1992), Interstellar dust from the Milky Way to the Magellanic Clouds, *Astrophys. J.*, *395*, 130–139, doi:10.1086/171637.

Pei, Y. C., S. M. Fall, & J. Bechtold (1991), Confirmation of dust in damped Lyman-alpha systems, *Astrophys. J.*, *378*, 6–16, doi:10.1086/170401.

Perets, H. B., O. Biham, G. Manicó, V. Pirronello, J. Roser, S. Swords, & G. Vidali (2005), Molecular Hydrogen Formation on Ice Under Interstellar Conditions, *Astrophys. J.*, *627*, 850–860, doi:10.1086/430435.

Pettini, M. (2004), Element abundances through the cosmic ages, in *Cosmochemistry. The melting pot of the elements*, edited by C. Esteban, R. García López, A. Herrero, & F. Sánchez, pp. 257–298.

Pettini, M., & S. Dodorico (1986), A search for million degree gas in the Galactic halo and the Large Magellanic Cloud through forbidden Fe X 6375 A absorption, *Astrophys. J.*, *310*, 700–709, doi:10.1086/164721.

Pettini, M., & B. E. J. Pagel (2004), [OIII]/[NII] as an abundance indicator at high redshift, *Mon. Notic. Royal Astron. Soc.*, *348*, L59–L63, doi:10.1111/j.1365-2966.2004.07591.x.

Pettini, M., A. Boksenberg, & R. W. Hunstead (1990), Metal enrichment, dust, and star formation in galaxies at high redshifts. I - The Z = 2.3091 absorber toward PHL 957, *Astrophys. J.*, *348*, 48–56, doi:10.1086/168212.

Pettini, M., S. L. Ellison, J. Bergeron, & P. Petitjean (2002), The abundances of nitrogen and oxygen in damped Lyman alpha systems, *Astron. & Astrophys.*, *391*, 21–34, doi:10.1051/0004-6361:20020809.

Prochaska, J. X., E. Gawiser, A. M. Wolfe, S. Castro, & S. G. Djorgovski (2003), The Age-Metallicity Relation of the Universe in Neutral Gas: The First 100 Damped Lyα Systems, *Astrophys. J.*, *595*, L9–L12, doi:10.1086/378945.

Prochaska, J. X., A. M. Wolfe, J. C. Howk, E. Gawiser, S. M. Burles, & J. Cooke (2007), The UCSD/Keck Damped Lyα Abundance Database: A Decade of High-Resolution Spectroscopy, *Astrophys. J. Suppl.*, *171*, 29–60, doi:10.1086/513714.

Prochter, G. E., J. X. Prochaska, & S. M. Burles (2006), On the Incidence and Kinematics of Strong Mg II Absorbers, *Astrophys. J.*, *639*, 766–780, doi:10.1086/499341.

Raiteri, C. M., M. Villata, A. Capetti, J. Heidt, M. Arnaboldi, & A. Magazzù (2007), Spectroscopic monitoring of the BL Lac object AO 0235+164, *Astron. & Astrophys.*, *464*, 871–878, doi:10.1051/0004-6361:20066599.

Rao, S. M., & D. A. Turnshek (1998), Discovery of z = 0.0912 and z = 0.2212 Damped Ly alpha Absorption-Line Systems toward the Quasar OI 363: Limits on the Nature of Damped LY alpha Galaxies, *Astrophys. J.*, *500*, L115–L119, doi:10.1086/311411.

Rao, S. M., & D. A. Turnshek (2000), Discovery of DampedLyα Systems at Redshifts Less than 1.65 and Results on Their Incidence and Cosmological Mass Density, *Astrophys. J. Suppl.*, *130*, 1–35, doi:10.1086/317344.

Rao, S. M., D. B. Nestor, D. A. Turnshek, W. M. Lane, E. M. Monier, & J. Bergeron (2003), Low-Redshift Damped Lyα Galaxies toward the Quasars B2 0827+243, PKS 0952+179, PKS 1127-145, and PKS 1629+120, *Astrophys. J.*, *595*, 94–108, doi:10.1086/377331.

Rao, S. M., D. A. Turnshek, & D. B. Nestor (2006), Damped Lyα Systems at z $<$ 1.65: The Expanded Sloan Digital Sky Survey Hubble Space Telescope Sample, *Astrophys. J.*, *636*, 610–630, doi:10.1086/498132.

Rohlfs, C., & T. L. Wilson (2006), *Tools of Radio Astronomy*, Astronomy and Astrophysics Library, 4 ed., Springer.

Ruiterkamp, R., N. L. J. Cox, M. Spaans, L. Kaper, B. H. Foing, F. Salama, & P. Ehrenfreund (2005), PAH charge state distribution and DIB carriers: Implications from the line of sight toward HD 147889, *Astron. & Astrophys.*, *432*, 515–529, doi:10.1051/0004-6361:20040331.

Sargent, W. L. W., A. Boksenberg, & C. C. Steidel (1988), C IV absorption in a new sample of 55 QSOs - Evolution and clustering of the heavy-element absorption redshifts, *Astrophys. J. Suppl.*, *68*, 539–641, doi:10.1086/191300.

Sarre, P. J. (1991), Diffuse bands in emission, *Nature*, *351*, 356, doi:10.1038/351356a0.

Sarre, P. J. (2006), The diffuse interstellar bands: A major problem in astronomical spectroscopy, *Journal of Molecular Spectroscopy*, *238*, 1–10, doi:10.1016/j.jms.2006.03.009.

Savage, B. D., R. C. Bohlin, J. F. Drake, & W. Budich (1977), A survey of interstellar molecular hydrogen. I, *Astrophys. J.*, *216*, 291–307.

Scarrott, S. M., S. Watkin, J. R. Miles, & P. J. Sarre (1992), Evidence for a link between the more prominent optical emission bands in the Red Rectangle and some of the diffuse instellar absorption, *Mon. Notic. Royal Astron. Soc.*, *255*, 11P–16P.

Schmidt, M. (1963), 3C 273 : A Star-Like Object with Large Red-Shift, *Nature*, *197*, 1040, doi:10.1038/1971040a0.

Schmidt, T. W., & R. G. Sharp (2005), The Optical Spectroscopy of Extraterrestrial Molecules, *Australian Journal of Chemistry*, *58*, 69–81.

Schulte-Ladbeck, R. E., B. König, C. J. Miller, A. M. Hopkins, I. O. Drozdovsky, D. A. Turnshek, & U. Hopp (2005), Emission-Line Spectroscopy of Damped Lyα Systems: The Case of SBS 1543+593/HS 1543+5921, *Astrophys. J.*, *625*, L79–L82, doi:10.1086/431324.

Shapiro, P. R., & K. A. Holcomb (1986), On the dust grain hypothesis for the diffuse interstellar bands, *Astrophys. J.*, *310*, 872–888, doi:10.1086/164740.

Snow, T. (1995a), Observational Constraints on the Carriers of the Diffuse Bands, in *The Diffuse Interstellar Bands*, *Astrophysics and Space Science Library*, vol. 202, edited by A. G. G. M. Tielens & T. P. Snow, pp. 325–340.

Snow, T. (1995b), A Critique of Suggested Diffuse Band Carriers, in *The Diffuse Interstellar Bands*, *Astrophysics and Space Science Library*, vol. 202, edited by A. G. G. M. Tielens & T. P. Snow, pp. 379–393.

Snow, T. (2001a), The Diffuse Interstellar Bands in External Galaxies, in *Gaseous Matter in Galaxies and Intergalactic Space*, *IAP Colloquium Series*, vol. 17, edited by R. Ferlet, M. Lemoine, J. M. Desért, & P. Raban, pp. 63–68.

Snow, T. P. (2001b), The unidentified diffuse interstellar bands as evidence for large organic molecules in the interstellar medium, *Spectrochimica Acta*, *57*, 615–626.

Snow, T. P., & C. G. Seab (1989), A search for interstellar and circumstellar C60, *Astron. & Astrophys.*, *213*, 291–294.

Snow, T. P., E. L. O. Bakes, R. H. Buss, Jr., & C. G. Seab (1995), The weakness of diffuse bands in nebular environments. Possible impact on the PAH^+ hypothesis., *Astron. & Astrophys.*, *296*, L37–L40.

Snow, T. P., Jr., & G. Wallerstein (1973), A Search for Diffuse Interstellar Features in Stars with Circumstellar Dust Shells (presented by T. P. Snow, JR.), in *Interstellar Dust and Related Topics*, *IAU Symposium*, vol. 52, edited by J. M. Greenberg & H. C. van de Hulst, pp. 65–70.

Sollerman, J., N. Cox, S. Mattila, P. Ehrenfreund, L. Kaper, B. Leibundgut, & P. Lundqvist (2005), Diffuse Interstellar Bands in NGC 1448, *Astron. & Astrophys.*, *429*, 559–567, doi:10.1051/0004-6361:20041465.

Sonnentrucker, P., J. Cami, P. Ehrenfreund, & B. H. Foing (1997), The diffuse interstellar bands at 5797, 6379 and 6613 Angstroms. Ionization properties of the carriers, *Astron. & Astrophys.*, *327*, 1215–1221.

Srianand, R., P. Noterdaeme, C. Ledoux, & P. Petitjean (2008), First detection of CO in a high-redshift damped Lyman-α system, *Astron. & Astrophys.*, *482*, L39–L42, doi:10.1051/0004-6361:200809727.

Steidel, C. C., & W. L. W. Sargent (1992), MG II absorption in the spectra of 103 QSOs - Implications for the evolution of gas in high-redshift galaxies, *Astrophys. J. Suppl.*, *80*, 1–108, doi:10.1086/191660.

Steidel, C. C., M. Pettini, M. Dickinson, & S. E. Persson (1994), Imaging of two damped Lyman Alpha absorbers at intermediate redshifts, *Astron. J.*, *108*, 2046–2053, doi:10.1086/117217.

Storrie-Lombardi, L. J., & A. M. Wolfe (2000), Surveys for $z > 3$ Damped Lyα Absorption Systems: The Evolution of Neutral Gas, *Astrophys. J.*, *543*, 552–576, doi:10.1086/317138.

Teplitz, H. I., et al. (2007), Measuring PAH Emission in Ultradeep Spitzer IRS Spectroscopy of High-Redshift IR-Luminous Galaxies, *Astrophys. J.*, *659*, 941–949, doi:10.1086/512802.

Thorburn, J. A., L. M. Hobbs, B. J. McCall, T. Oka, D. E. Welty, S. D. Friedman, T. P. Snow, P. Sonnentrucker, & D. G. York (2003), Some Diffuse Interstellar Bands Related to Interstellar C_2 Molecules, *Astrophys. J.*, *584*, 339–356, doi:10.1086/345665.

Tielens, A. (1995), Summary, in *The Diffuse Interstellar Bands*, *Astrophysics and Space Science Library*, vol. 202, edited by A. G. G. M. Tielens & T. P. Snow, pp. 395–404.

Tielens, A. G. G. M., S. Hony, C. van Kerckhoven, & E. Peeters (1999), Interstellar and circumstellar PAHs, in *The Universe as Seen by ISO*, *ESA Special Publication*, vol. 427, edited by P. Cox & M. Kessler, pp. 579–587.

Tulej, M., D. A. Kirkwood, M. Pachkov, & J. P. Maier (1998), Gas-Phase Electronic Transitions of Carbon Chain Anions Coinciding with Diffuse Interstellar Bands, *Astrophys. J.*, *506*, L69–L73, doi:10.1086/311637.

Tumlinson, J., et al. (2002), A Far Ultraviolet Spectroscopic Explorer Survey of Interstellar Molecular Hydrogen in the Small and Large Magellanic Clouds, *Astrophys. J.*, *566*, 857–879, doi:10.1086/338112.

Turnshek, D. A., S. Rao, D. Nestor, W. Lane, E. Monier, J. Bergeron, & A. Smette (2001), The z=0.0912 and z=0.2212 Damped Lyα Galaxies along the Sight Line toward the Quasar OI 363, *Astrophys. J.*, *553*, 288–298, doi:10.1086/320660.

Turnshek, D. A., S. M. Rao, A. F. Ptak, R. E. Griffiths, & E. M. Monier (2003), Chandra ACIS-S Observations of Three Quasars with Low-Redshift Damped Lyα Absorption: Constraints on the Cosmic Neutral Gas-Phase Metallicity at Redshift z$\sim$0.4, *Astrophys. J.*, *590*, 730–739, doi:10.1086/375019.

van der Zwet, G. P., & L. J. Allamandola (1985), Polycyclic aromatic hydrocarbons and the diffuse interstellar bands, *Astron. & Astrophys.*, *146*, 76–80.

van Dokkum, P. G. (2001), Cosmic-Ray Rejection by Laplacian Edge Detection, *Publ. Astron. Soc. Pacific*, *113*, 1420–1427.

van Zee, L., M. P. Haynes, J. J. Salzer, & A. H. Broeils (1996), Evolutionary Studies of the Low Metallicity Dwarf Irregular Galaxy UGCA 20, *Astron. J.*, *112*, 129–145, doi:10.1086/117994.

van Zee, L., M. P. Haynes, & J. J. Salzer (1997), Element Enrichment and Stellar Populations of Gas-Rich Low Surface Brightness Dwarf Galaxies, *Astron. J.*, *114*, 2497–2504, doi:10.1086/118662.

Vidal-Madjar, A., P. Andreani, S. Cristiani, R. Ferlet, T. Lanz, & G. Vladilo (1987), The interstellar spectrum toward SN 1987A, *Astron. & Astrophys.*, *177*, L17–L20.

Vladilo, G., L. Crivellari, P. Molaro, & J. E. Beckman (1987), Detections of diffuse interstellar bands toward the SN 1987A in the Large Magellanic Cloud, *Astron. & Astrophys.*, *182*, L59–L62.

Vladilo, G., J. X. Prochaska, & A. M. Wolfe (2008), The color excess of quasars with intervening DLA systems. Analysis of the SDSS data release five, *Astron. & Astrophys.*, *478*, 701–715, doi:10.1051/0004-6361:20078480.

Welty, D. E., S. R. Federman, R. Gredel, J. A. Thorburn, & D. L. Lambert (2006), VLT UVES Observations of Interstellar Molecules and Diffuse Bands in the Magellanic Clouds, *Astrophys. J. Suppl.*, *165*, 138–172, doi:10.1086/504153.

Wickramasinghe, N. C., J. G. Ireland, K. Nandy, H. Seddon, & R. D. Wolstencroft (1968), Origin of the Diffuse Interstellar Bands, *Nature*, *217*, 412–415.

Wild, V., & P. C. Hewett (2005), Evidence for dust reddening in damped Lyα absorbers identified through CaII (H&K) absorption, *Mon. Notic. Royal Astron. Soc.*, *361*, L30–L34, doi:10.1111/j.1745-3933.2005.00058.x.

Wild, V., P. C. Hewett, & M. Pettini (2006), Selecting damped Lyman α systems through CaII absorption - I. Dust depletions and reddening at z$\sim$1, *Mon. Notic. Royal Astron. Soc.*, *367*, 211–230, doi:10.1111/j.1365-2966.2005.09935.x.

Wolfe, A. M., F. H. Briggs, & M. M. Davis (1982), Time variations in the high-redshift 21 centimeter absorption spectrum of the BL Lacertae object AO 0235+164, *Astrophys. J.*, *259*, 495–521, doi:10.1086/160187.

Wolfe, A. M., E. Gawiser, & J. X. Prochaska (2005), Damped Ly α Systems, *Ann. Rev. Astron. Astrophys.*, *43*, 861–918.

Wolfire, M. G., D. Hollenbach, C. F. McKee, A. G. G. M. Tielens, & E. L. O. Bakes (1995), The neutral atomic phases of the interstellar medium, *Astrophys. J.*, *443*, 152–168, doi:10.1086/175510.

Wszołek, B., & W. Godłowski (2003), Toward an adequate method to isolate spectroscopic families of diffuse interstellar bands, *Mon. Notic. Royal Astron. Soc.*, *338*, 990–998, doi:10.1046/j.1365-8711.2003.06143.x.

Wszołek, B., & M. Wszołek (2003), Diffuse interstellar bands, *Astronomical and Astrophysical Transactions*, *22*, 821–825.

York, B. A., S. L. Ellison, B. Lawton, C. W. Churchill, T. P. Snow, R. A. Johnson, & S. G. Ryan (2006), Detection of Diffuse Interstellar Bands in the z=0.5 Damped Lyα System toward AO 0235+164, *Astrophys. J.*, *647*, L29–L32, doi:10.1086/505907.

Young, L. M., & K. Y. Lo (1997), The Neutral Interstellar Medium in Nearby Dwarf Galaxies. III. Sagittarius DIG, LGS 3, and PHOENIX, *Astrophys. J.*, *490*, 710–728, doi:10.1086/304909.

Young, P., W. L. W. Sargent, & A. Boksenberg (1982), C IV absorption in an unbiased sample of 33 QSOs - Evidence for the intervening galaxy hypothesis, *Astrophys. J. Suppl.*, *48*, 455–505, doi:10.1086/190786.

Young, R. K. (1920), The Calcium Lines H and K in Early Type Stars, *J. Royal Astron. Soc. Canada*, *14*, 219–231.

Zhou, Z., M. Y. Sfeir, L. Zhang, M. S. Hybertsen, M. Steigerwald, & L. Brus (2006), Graphite, Tubular PAHs, and the Diffuse Interstellar Bands, *Astrophys. J.*, *638*, L105–L108, doi:10.1086/501006.

Zych, B. J., M. T. Murphy, M. Pettini, P. C. Hewett, E. V. Ryan-Weber, & S. L. Ellison (2007), The host galaxies of strong CaII quasar absorption systems at z < 0.5, *Mon. Notic. Royal Astron. Soc.*, *379*, 1409–1422, doi:10.1111/j.1365-2966.2007.12015.x.

Appendix A

Observing Conditions

This appendix contains a complete journal of the observing conditions for all observations. Date gives the UT date of the observations, System the QSO observed, Telescope the telescope used for the observations, Seeing the average seeing (or range of seeing) during the observations (in arcseconds), Clouds the cloud cover (if any), Wind the average wind speed, and Moon the phase of the moon.

Table A.1: Journal of Observations

Date (UT)	System	Telescope	Seeing (")	Clouds	Wind (m/s)	Moon
2004 May 20	PKS 0952+179	WHT	1.3–1.5	cirrus	light	Dark
2004 May 20	Q 1229−020		1.3–1.5	heavy cirrus	light	Dark
2004 Jun 19	PKS 1127−145	Gemini South	observable	light	light	Dark
2005 Apr 04	PKS 0952+179	VLT	0.5–0.7	clear	~ 10	Grey
2005 Apr 07			0.55	clear	5–10	Dark
2005 Apr 09	Q 1229−020		0.9–1.1	clear	< 5	Dark
2005 Apr 13			1.0	light	~ 9	Grey
2005 Jul 20	AO 0235+164		0.78–1.0	moderate	8–12	Bright
2005 Sep 06			0.6–0.8	clear	< 5	Dark
2005 Oct 01			1.0–1.2	clear	~ 20	Dark

Continued on next page

Table A.1 – Continued

Date (UT)	System	Telescope	Seeing (")	Clouds	Wind (m/s)	Moon
2006 Apr 02	J1009+0529	VLT	0.8–1.2	clear	~ 5	Grey
2006 Apr 02	J1219−0043	VLT	0.8–1.2	clear	~ 5	Grey
	J1437−0104					
2006 Apr 03	J1009+0529		0.7–1.3	clear	~ 5	Grey
2006 Apr 04	J1137+0136		0.5	clear	5–10	Grey
2006 Apr 06	J1137+0136		1.0–1.2	clear	10–15	Grey
	J1226−0006					
2006 May 17	J1226−0006		0.5	clear	< 5	Bright
2006 May 22	J1040+0705		0.5–1.0	cirrus	~ 8	Grey
2006 May 28	J2135+1038		1.2–1.5	clear	~ 10	Dark
2006 Jun 22	J2135+1038		0.7–1.3	clear	~ 5	Dark
2006 Jul 10	J2259−0844		1.0	light cirrus	< 5	Dark
2006 Aug 06	J0013−0024		0.5–1.0	clear	5–10	Bright
2006 Sep 02	J0013−0024		1.2	clear	< 5	Grey

Appendix B

Diffuse Band Strengths

This appendix contains a list of extragalactic DIB strengths from the literature (Table B.1), as well as a list of Galactic DIB strengths (Table B.2) for those sightlines used in the figures and tables presented here. In addition to the strengths of the 4428, 5705, 5780, 5797, 6284, and 6613 Å DIBs, the tables also include log N(H I) and $E(B-V)$ values where available, as well as references.

Table B.1: Extragalactic DIBs

Source	Location	log N(H I) (cm^{-2})	$E(B-V)$	EW_{4428} (mÅ)	EW_{5705} (mÅ)	EW_{5780} (mÅ)	EW_{5797} (mÅ)	EW_{6284} (mÅ)	EW_{6613} (mÅ)	Refs
AO 0235+164	DLA	21.70 ± 0.09	0.23	742 ± 26	63.2 ± 8.7	216 ± 9	< 155	< 214	< 158	1
Q 0738+313a[1]	DLA	21.18 ± 0.05	...	< 56	...	< 199	< 68	< 19	< 161	2
Q 0738+313b[2]	DLA	20.90 ± 0.07	...	< 264	...	< 30	< 81	< 302	...	2
B2 0827+243	DLA	20.3 ± 0.04	...	< 95	...	< 39	< 27	...	...	3
PKS 0952+179	DLA	21.32 ± 0.06	...	< 67	...	< 27	< 117	< 37	< 177	3
PKS 1127−145	DLA	21.71 ± 0.07	...	...	...	< 500	< 500	< 352	< 623	4
Q 1229−020	DLA	20.75 ± 0.07	...	...	...	< 65	< 75	< 65	< 146	5
J0013−0024	Ca II	...	0.66	...	< 103	94 ± 16	< 75	< 130	< 207	14
J1009+0529	Ca II	...	...	< 207	< 47	< 70	< 70	< 97	...	...
J1040+0705	Ca II	...	...	...	...	< 212	< 212	< 258	< 243	...
J1137+0136	Ca II	...	...	< 293	< 135	< 137	< 82	...	...	...
J1219−0043	Ca II	...	...	< 200	< 165	< 100	< 100	...	...	...
J1226−0006	Ca II	...	...	< 190	...	...	...	...	...	...
J1437−0104	Ca II	...	...	...	...	< 88	< 102	...	< 85	...
J2135+1038	Ca II	...	...	< 307	< 165	< 170	...	...	...	...
J12259−0844	Ca II	...	...	< 227	...	...	...	...	...	...

Continued on next page

Table B.1 – Continued

Source	Location	log N(H I) (cm^{-2})	$E(B-V)$	EW_{4428} (mÅ)	EW_{5705} (mÅ)	EW_{5780} (mÅ)	EW_{5797} (mÅ)	EW_{6284} (mÅ)	EW_{6613}	Refs
BI 237	LMC	...	0.12	...	...	111 ± 16	...	390 ± 35	...	7
BI 253	LMC	...	0.13	...	...	75 ± 16	< 18	130 ± 35	...	7
LH 10−3061	LMC	...	0.26	...	...	83 ± 20	23 ± 7	225 ± 35	...	7
Melnick 42	LMC	...	0.36	...	...	94 ± 17	12 ± 4	210 ± 35	...	1
Sk−67^o2	LMC	21.00	0.22	< 247	< 32	33 ± 5	23 ± 3	125 ± 20	13 ± 8	6,7
Sk−67^o5	LMC	21.00	0.13	< 200	< 23	14 ± 5	10 ± 3	50 ± 20	< 13	6,7
Sk−68^o52	LMC	21.23	0.09	...	...	34 ± 5	8 ± 2	105 ± 20	...	7
Sk−68^o73	LMC	21.70	0.51	...	...	39 ± 4	14 ± 2	180 ± 20	...	7
Sk−68^o135	LMC	21.57	0.21	< 200	< 23	37 ± 4	18 ± 2	105 ± 20	5 ± 3	6,7
Sk−69^o202	LMC	21.40	0.10	...	...	33	7	105	...	7
Sk−69^o223	LMC	21.46	0.20	< 180	20 ± 9 145 ± 2	28 ± 6	240 ± 21	20 ± 8	1	
Sk−69^o243	LMC	21.80	0.13	150	25 ± 21	...	...	335 ± 47	50 ± 14	6,7
Sk−69^o246	LMC	21.30	0.08	...	...	26 ± 4	11 ± 2	105 ± 20	...	7
Sk−70^o115	LMC	21.30	0.14	...	...	36 ± 5	10 ± 2	105 ± 20	...	7
SN 1987a	LMC	...	0.07	...	...	39	10.5	55	...	8,9
AV 80	SMC	21.81	0.12	...	...	22 ± 14	< 21	< 80	...	7

Continued on next page

Table B.1 – Continued

Source	Location	log N(H I) (cm^{-2})	$E(B-V)$	EW_{4428} (mÅ)	EW_{5705} (mÅ)	EW_{5780} (mÅ)	EW_{5797} (mÅ)	EW_{6284} (mÅ)	EW_{6613}	Refs
AV 476	SMC	...	0.18	...	...	50 ± 11	21 ± 5	95 ± 25	...	7
Sk 13	SMC	22.04	0.14	...	...	23 ± 5	8 ± 2	< 55	...	7
Sk 18	SMC	21.82	0.08	...	...	17 ± 7	4 ± 2	< 55	...	7
Sk 40	SMC	21.54	0.07	...	...	20 ± 8	< 12	70 ± 25	...	7
Sk 143	SMC	21.18	0.34	...	...	77 ± 10	37 ± 4	< 50	53 ± 4	7,10
Sk 155	SMC	21.40	0.11	...	...	20 ± 6	< 8	< 60	...	7
SNe 2001el	NGC 1448	...	0.185	...	37 ± 5	189 ± 3	26 ± 2	500 ± 80	52 ± 3	11
SN 2003hn	NGC 1448	...	0.12	...	...	52 ± 7	...	130 ± 11	...	11
SN 1986g	NGC 5128	...	...	...	79 ± 5	335 ± 5	151 ± 5	...	...	12
M82	Starburst	...	1.0	...	...	240	70	880 ± 30	120	13
NGC 1614	Starburst	...	0.9	...	...	100	...	940 ± 40	...	13
NGC 1808	Starburst	...	0.9	...	...	140	...	550 ± 40	...	13
NGC 2146	Starburst	...	0.9	...	...	360	100	940 ± 30	120	13
NGC 3256	Starburst	...	0.6	...	...	100	...	370 ± 40	...	13
NGC 6240 (8)	Starburst	...	1.2	...	...	640 ± 70	...	...	...	13
MAG 63885	M31	...	0.28	...	...	190^{+26}_{-16}	44^{+8}_{-5}	260 ± 11	63^{+7}_{-8}	14

Continued on next page

Table B.1 – Continued

Source	Location	log N(H I) (cm^{-2})	$E(B-V)$	EW_{4428} (mÅ)	EW_{5705} (mÅ)	EW_{5780} (mÅ)	EW_{5797} (mÅ)	EW_{6284} (mÅ)	EW_{6613}	Refs
MAG 70817	M31	...	0.12	...	...	271^{+17}_{-26}	58^{+32}_{-16}	541 ± 21	74^{+11}_{-12}	14
SN 2006X	M100	...	1.4	...	...	...	...	177 ± 25	$\lesssim 18$	16

[1] $z_{abs} = 0.091$

[2] $z_{abs} = 0.221$

REFERENCES 1. Junkkarinen et al. (2004); 2. Rao & Turnshek (1998); 3. Rao & Turnshek (2000); 4. Turnshek et al. (2003); 5. Boissé et al. (1998); 6. Cox et al. (2006); 7. Welty et al. (2006); 8. Vladilo et al. (1987); 9. Vidal-Madjar et al. (1987); 10. Ehrenfreund et al. (2002); 11. Sollerman et al. (2005); 12. D'Odorico et al. (1989); 13. Heckman & Lehnert (2000); 14. Zych et al. (2007); 15. Cordiner et al. (2008); 16. Cox & Patat (2008)

Table B.2: Galactic DIBs

Name	HD	log N(H I) (cm^{-2})	$E(B-V)$	EW_{4428} (mÅ)	EW_{5705} (mÅ)	EW_{5780} (mÅ)	EW_{5797} (mÅ)	EW_{6284} (mÅ)	EW_{6613} (mÅ)	Refs
κ Cas	HD 2905	21.20	0.33	...	...	314 ± 5	74	665 ± 65	...	1,6
ζ Cas	HD 3360	...	0.04	...	...	18	< 3	...	...	1
γ Cas	HD 5394	20.16	0.16	...	< 5	33	16	...	...	1,6,7
ϕ Per	HD 10516	20.54	0.2	...	...	67 ± 4	23 ± 4	< 200	...	1
...	HD 14818	...	0.48	...	...	295	65	...	...	8
...	HD 15570	...	0.96	...	...	511	146	...	...	8
...	HD 15629	...	0.72	...	...	453	99	...	...	8
...	HD 16219	...	0.04	...	< 5	32	10	...	...	7
...	HD 20041	...	0.72	...	...	439 ± 8	161 ± 6	1030 ± 60	...	1
...	HD 21278	...	0.10	...	...	80	26	...	...	1
...	HD 21279	...	0.12	...	...	98	28	...	...	1
...	HD 21291	...	0.40	...	43	197	78	...	...	1,7
...	HD 21379	...	0.01	...	...	26	5	...	...	1
...	HD 21389	...	0.57	...	104 ± 7	411 ± 8	160 ± 7	1211 ± 80	161 ± 4	2
...	HD 21483	...	0.56	...	35 ± 10	181 ± 7	96 ± 6	397 ± 45	89 ± 4	2
...	HD 21856	21.04	0.20	...	...	170	49	...	...	1,6

Continued on next page

Table B.2 – Continued

Name	HD	log N(H I) (cm^{-2})	$E(B-V)$	EW_{4428} (mÅ)	EW_{5705} (mÅ)	EW_{5780} (mÅ)	EW_{5797} (mÅ)	EW_{6284} (mÅ)	EW_{6613}	Refs
40 Per	HD 22951	21.05	0.27	...	...	115 ± 5	52 ± 6	337 ± 40	...	1,6
o Per	HD 23180	20.90	0.31	...	45 ± 6	101 ± 7	82 ± 6	200 ± 60	51 ± 3	2,6
16 Tau	HD 23288	...	0.09	...	...	21	6	...	...	1
17 Tau	HD 23302	...	0.04	...	10	21	3	...	...	1,7
18 Tau	HD 23324	...	0.04	...	...	25	3	...	...	1
19 Tau	HD 23338	...	0.04	...	...	22	4	...	...	1
20 Tau	HD 23408	...	0.04	...	8	49	13	...	...	1,7
21 Tau	HD 23432	...	0.07	...	...	24	4	...	...	1
23 Tau	HD 23480	...	0.08	...	< 5	31 ± 5	4	116 ± 30	...	1,7
η Tau	HD 23630	...	0.03	...	< 5	19	2	...	...	1,7
...	HD 23850	...	0.03	...	< 5	34	7	...	...	7
...	HD 23862	...	0.03	...	< 5	17	10	...	...	7
ζ Per	HD 24398	20.81	0.31	...	36 ± 10	114 ± 7	77 ± 5	185 ± 50	66 ± 5	2,6
...	HD 24432	...	0.75	...	...	348	117	...	...	1
X Per	HD 24534	20.72	0.59	...	< 30	98 ± 8	68 ± 4	270 ± 60	72 ± 5	2
ϵ Per	HD 24764	20.41	0.10	...	...	81 ± 5	22 ± 4	283 ± 40	...	1

Continued on next page

Table B.2 – Continued

Name	HD	log N(H I) (cm^{-2})	$E(B-V)$	EW_{4428} (mÅ)	EW_{5705} (mÅ)	EW_{5780} (mÅ)	EW_{5797} (mÅ)	EW_{6284} (mÅ)	EW_{6613}	Refs
ξ Per	HD 24912	21.10	0.33	...	24 ± 7	209 ± 7	46 ± 7	507 ± 60	79 ± 3	2
...	HD 25137	...	0.13	...	...	131	45	...	...	1
...	HD 25638	...	0.65	...	...	260	117	...	...	8
...	HD 26571	...	0.25	...	48 ± 7	151 ± 7	82.6 ± 10	273 ± 40	83 ± 3	2
...	HD 27311	...	0.50	...	...	190	74	...	...	8
62 Tau	HD 27778	20.98	0.37	...	17 ± 3	86 ± 4	39 ± 2	170 ± 50	44 ± 2	2
α Cam	HD 30614	20.90	0.3	...	54 ± 10	133 ± 5	56 ± 3	360 ± 60	71.5 ± 5	2
π4 Ori	HD 30836	20.60	0.08	...	18	56	10	...	...	7
π5 Ori	HD 31237	20.41	0.05	...	< 5	21	7	...	...	7
AE Aur	HD 34078	21.20	0.52	...	48 ± 3	181 ± 5	56 ± 3	510 ± 80	61 ± 2	2
β Ori	HD 34085	...	0.01	...	< 5	21	< 3	...	...	1,7
...	HD 34748	...	0.14	...	< 6	40	19	...	...	7
λ Lep	HD 34816	20.18	0.02	...	< 5	5	4	...	...	7
23 Ori	HD 35149	20.74	0.11	...	< 12	57 ± 3	15.7 ± 3	286 ± 45	21.7 ± 2	2
...	HD 36351	...	0.07	...	< 5	28	6	...	...	7
χ Aur	HD 36371	...	0.43	...	72 ± 5	313 ± 7	127 ± 7	743 ± 60	145 ± 4	2

Continued on next page

Table B.2 – Continued

Name	HD	log N(H I) (cm^{-2})	$E(B-V)$	EW_{4428} (mÅ)	EW_{5705} (mÅ)	EW_{5780} (mÅ)	EW_{5797} (mÅ)	EW_{6284} (mÅ)	EW_{6613}	Refs
ϕ Ori	HD 36822	20.81	0.14	...	50	69	40	...	...	1,7
λ Ori	HD 36861	20.78	0.15	...	...	50 ± 5	26 ± 4	468 ± 70	...	1
...	HD 36959	...	0.03	...	...	7	< 3	...	...	1
...	HD 36960	...	0.03	...	...	13	...	...	...	1
...	HD 37016	...	0.07	...	...	20	4	...	...	1
42 Ori	HD 37018	...	0.07	...	...	20	5	...	...	1
θ1 Ori A	HD 37020	...	0.35	...	...	41	19	...	...	1
θ1 Ori C	HD 37022	< 17.2	0.34	...	...	64	3	...	...	1,6
θ1 Ori D	HD 37023	...	0.37	...	...	55	16	...	...	1
θ2 Ori A	HD 37041	21.38	0.20	...	...	43	6	...	...	1,6
ι Ori	HD 37043	20.15	0.07	...	...	34 ± 6	< 3	< 120	...	1
νOri	HD 37061	21.78	0.52	...	46 ± 5	169 ± 7	35 ± 5	675 ± 55	34.4 ± 3.0	2
ϵ Ori	HD 37128	20.45	0.05	...	...	18 ± 3	< 5	128 ± 40	...	1
...	HD 37140	...	0.15	...	22	97	33	...	...	7
...	HD 37367	...	0.40	...	...	429	108	...	...	1
...	HD 37490	...	0.06	...	< 5	60	14	...	...	7

Continued on next page

Table B.2 – Continued

Name	HD	log N(H I) (cm^{-2})	$E(B-V)$	EW_{4428} (mÅ)	EW_{5705} (mÅ)	EW_{5780} (mÅ)	EW_{5797} (mÅ)	EW_{6284} (mÅ)	EW_{6613}	Refs
ζ Ori	HD 37742	20.41	0.06	...	...	31 ± 4	< 6	< 90	...	1
...	HD 37903	21.17	0.35	...	36 ± 5	183 ± 10	33 ± 5	503 ± 70	36 ± 4	2
...	HD 38087	...	0.29	...	18	148	34	...	...	1,7
...	HD 38563A	...	0.78	...	40	256	80	...	...	7
...	HD 38563B	...	1.34	...	100	197	75	...	...	7
...	HD 38681	...	0.06	...	...	44	18	...	...	8
κ Ori	HD 38771	20.52	0.05	...	...	33 ± 5	15 ± 4	126 ± 35	...	1
139 Tau	HD 40111	20.91	0.2	...	...	169 ± 6	44 ± 5	428 ± 50	...	1
χ2 Ori	HD 41117	21.40	0.45	...	86 ± 5	356 ± 10	148 ± 8	760 ± 100	154 ± 3	2
3 Gem	HD 42087	21.39	0.36	...	75 ± 6	275 ± 7	99 ± 2	675 ± 70	115 ± 3	2
9 Gem	HD 43384	...	0.58	...	113 ± 4	455 ± 7	155 ± 5	950 ± 50	194 ± 3	2
...	HD 46056	21.38	0.51	...	...	400 ± 40	135 ± 15	750 ± 100	...	1
...	HD 46150	...	0.46	...	...	331	102	...	...	1
...	HD 46202	21.58	0.47	...	76 ± 10	337 ± 8	145 ± 9	850 ± 100	135 ± 4	2
...	HD 46300	...	0.01	...	30	56	12	...	...	7
...	HD 46711	...	1.04	...	173 ± 15	820 ± 10	269 ± 8	1500 ± 150	363 ± 5	2

Continued on next page

Table B.2 – Continued

Name	HD	log N(H I) (cm^{-2})	$E(B-V)$	EW_{4428} (mÅ)	EW_{5705} (mÅ)	EW_{5780} (mÅ)	EW_{5797} (mÅ)	EW_{6284} (mÅ)	EW_{6613}	Refs
...	HD 47129	21.08	0.36	...	...	211 ± 5	89 ± 4	550 ± 50	...	1
S Mon A	HD 47839	20.40	0.07	...	...	30 ± 3	7 ± 2	45 ± 15	...	1
...	HD 48099	21.14	0.27	...	43 ± 5	207 ± 7	58 ± 5	578 ± 50	76.3 ± 2	2
...	HD 53367	...	0.74	...	40 ± 6	177 ± 9	82 ± 8	565 ± 70	81 ± 5	2
...	HD 53974	...	0.31	...	46	114	22	...	...	7
29 CMa	HD 57060	20.70	0.17	...	...	51	12	...	...	1,6
τ CMa	HD 57061	20.70	0.16	...	...	51	6	...	...	1,6
...	HD 62542	20.93	0.35	...	...	25 ± 6	10 ± 2	< 120	...	1
...	HD 73882	21.12	0.7	...	...	154 ± 9	32 ± 3	...	...	1
...	HD 87015	...	0.03	...	< 5	18	9	...	...	7
ρ Leo	HD 91316	20.26	0.05	...	10	38 ± 3	14 ± 2	75 ± 20	...	7
...	HD 93521	20.11	0.04	...	< 5	7	2	< 40	...	7
...	HD 97991	20.54	0.03	...	< 5	14	7	...	...	7
...	HD 129956	...	0.05	...	< 5	18	3	...	...	7
...	HD 138764	...	0.05	...	< 5	51	< 3	...	...	7
1 Sco	HD 141637	21.19	0.15	...	...	81	16	...	...	1

Continued on next page

Table B.2 – Continued

Name	HD	log N(H I) (cm^{-2})	$E(B-V)$	EW_{4428} (mÅ)	EW_{5705} (mÅ)	EW_{5780} (mÅ)	EW_{5797} (mÅ)	EW_{6284} (mÅ)	EW_{6613}	Refs
π Sco	HD 143018	20.72	0.05	...	< 5	39 ± 4	7 ± 2	145 ± 40	...	1,7
δ Sco	HD 143275	21.15	0.17	...	...	82 ± 5	25 ± 4	250 ± 25	...	1
...	HD 143992	...	0.09	...	...	35	...	...	...	1
β1 Sco	HD 144217	21.10	0.19	...	...	171 ± 5	34 ± 4	397 ± 75	40	5
ω1 Sco	HD 144470	21.18	0.22	...	...	192 ± 5	40 ± 4	403 ± 40	...	1
ν Sco	HD 145502	21.14	0.24	...	35	187 ± 5	49 ± 5	421 ± 40	...	1,7
...	HD 147009	...	0.30	...	< 14	102	54	...	...	7
...	HD 147010	...	0.22	...	< 10	220	70	...	...	7
σ Sco	HD 147165	21.34	0.41	...	50	245 ± 5	54 ± 3	498 ± 50	...	1,7
ρ Oph D	HD 147888	...	0.47	...	54 ± 4	252 ± 12	60 ± 5	390 ± 60	82 ± 2	2
...	HD 147889	...	1.07	...	97 ± 4	377 ± 8	163 ± 5	530 ± 50	180 ± 5	2
ρ Oph A	HD 147933	21.55	0.48	...	44 ± 8	222 ± 10	71 ± 6	426 ± 80	68 ± 5	2
χ Oph	HD 148184	21.16	0.52	...	...	102 ± 5	64 ± 4	327 ± 45	...	1
22 Sco	HD 148605	20.95	0.37	...	...	52 ± 4	12 ± 4	173 ± 45	...	1
μ Nor	HD 149038	20.99	0.37	...	...	214	43	...	...	8
ζ Oph	HD 149757	20.72	0.32	...	< 18	83 ± 7	38 ± 4	175 ± 35	41 ± 3	2

Continued on next page

Table B.2 – Continued

Name	HD	log N(H I) (cm^{-2})	$E(B-V)$	EW_{4428} (mÅ)	EW_{5705} (mÅ)	EW_{5780} (mÅ)	EW_{5797} (mÅ)	EW_{6284} (mÅ)	EW_{6613}	Refs
...	HD 149881	20.63	0.10	...	...	44 ± 4	12 ± 3	147 ± 40	...	1
...	HD 151804	20.82	0.40	...	...	217	42	...	...	1
...	HD 152408	...	0.43	...	...	301	43	...	...	8
...	HD 154445	...	0.39	...	...	203	60	...	...	8
μ Oph	HD 159975	...	0.19	...	...	189 ± 5	72 ± 4	500 ± 50	...	1
...	HD 163472	...	0.30	...	...	217 ± 2	85 ± 1	...	...	8
67 Oph	HD 164353	21.01	0.22	...	...	124 ± 4	38 ± 4	378 ± 45	...	1
...	HD 164402	21.11	0.22	...	...	187	52	...	...	1
...	HD 166734	...	1.39	...	168 ± 9	727 ± 8	322 ± 15	1560 ± 200	401 ± 5	2
μ Sgr	HD 166937	...	0.25	...	...	287 ± 4	105 ± 4	711 ± 75	...	1
16 Sgr	HD 167263	21.08	0.35	...	...	299	79	...	...	1,6
15 Sgr	HD 167264	21.15	0.30	...	...	229	85	...	...	1
...	HD 167838	...	0.54	...	...	464	130	...	...	1
...	HD 167971	21.60	1.08	...	131 ± 5	512 ± 9	208 ± 6	1450 ± 200	219 ± 5	2
...	HD 168076	21.64	0.78	...	118 ± 12	541 ± 10	250 ± 8	1090 ± 150	221 ± 6	2
...	HD 169454	...	1.12	...	118 ± 5	510 ± 7	213 ± 5	1580 ± 170	205 ± 5	2

Continued on next page

Table B.2 – Continued

Name	HD	log N(H I) (cm^{-2})	$E(B-V)$	EW_{4428} (mÅ)	EW_{5705} (mÅ)	EW_{5780} (mÅ)	EW_{5797} (mÅ)	EW_{6284} (mÅ)	EW_{6613}	Refs
...	HD 170740	21.16	0.48	...	63 ± 5	255 ± 7	92 ± 5	595 ± 60	125 ± 4	2
...	HD 172028	...	0.79	...	53 ± 5	256 ± 8	217 ± 5	450 ± 60	137 ± 3	2
...	HD 176437	...	0.01	...	...	22 ± 3	< 10	...	...	1
20 Aql	HD 179406	...	0.33	...	29 ± 6	172 ± 5	217 ± 5	430 ± 60	98 ± 2	2
...	HD 182918	...	0.30	...	32	159	49	...	...	7
...	HD 183143	21.54	1.27	...	172 ± 7	758 ± 8	295 ± 10	1930 ± 150	337 ± 4	2
κ Aql	HD 184915	20.90	0.28	...	...	162	24		...	8
...	HD 185418	21.12	0.5	...	57 ± 3	273 ± 5	105 ± 5	640 ± 50	164 ± 4	2
...	HD 185859	...	0.57	...	...	295	193	...	...	8
...	HD 186745	...	0.94	...	...	512	264	...	...	8
...	HD 186994	20.85	0.17	...	< 30	101 ± 5	23 ± 4	296 ± 40	17 ± 3	2
...	HD 187459	...	0.40	...	...	239	86	...	...	8
...	HD 188209	20.90	0.19	...	...	96	16	...	...	1
...	HD 188439	20.78	0.17	...	...	53	27	...	...	1
...	HD 190603	...	0.72	...	94	358	112	...	...	7
...	HD 192639	21.32	0.66	...	81 ± 5	324 ± 5	79 ± 7	817 ± 50	150 ± 3	2

Continued on next page

Table B.2 – Continued

Name	HD	log N(H I) (cm^{-2})	$E(B-V)$	EW_{4428} (mÅ)	EW_{5705} (mÅ)	EW_{5780} (mÅ)	EW_{5797} (mÅ)	EW_{6284} (mÅ)	EW_{6613}	Refs
ρ Cyg	HD 193237	21.28	0.66	...	...	211	71	...	...	1
...	HD 193322A	21.08	0.41	...	...	191	72	...	...	1
...	HD 194279	...	1.20	...	...	466 ± 3	142 ± 3	...	...	8
...	HD 194839	...	1.20	...	...	539	116	...	...	8
55 Cyg	HD 198478	...	0.54	...	72 ± 4	332 ± 5	112 ± 4	919 ± 60	139 ± 3	2
...	HD 199478	...	0.48	...	70	240	92	...	...	7
...	HD 199579	21.04	0.37	...	21 ± 3	126 ± 3	54 ± 4	315 ± 50	63 ± 2	2
59 Cyg	HD 200120	20.25	0.21	...	...	32	6	...	...	1,6
...	HD 200775	...	0.57	...	25	50	21	...	...	7
68 Cyg	HD 203064	21.01	0.31	...	...	176	48	...	...	1
...	HD 203938	21.48	0.74	...	68 ± 4	356 ± 5	152 ± 5	936 ± 60	146 ± 3	2
69 Cyg	HD 204172	21.00	0.16	...	...	120 ± 4	32 ± 3	322 ± 60	...	1
...	HD 204827	21.17	1.11	...	58 ± 3	257 ± 4	199 ± 3	518 ± 60	171 ± 3	2,3
9 Cep	HD 206165	...	0.47	...	58 ± 5	231 ± 7	105 ± 5	486 ± 60	111 ± 3	2
...	HD 206267A	21.31	0.53	...	59 ± 4	242 ± 7	102 ± 5	544 ± 45	126 ± 3	2
...	HD 207198	21.34	0.62	...	56 ± 5	262 ± 6	144 ± 3	543 ± 40	125 ± 3	2

Continued on next page

Table B.2 – Continued

Name	HD	log N(H I) (cm^{-2})	$E(B-V)$	EW_{4428} (mÅ)	EW_{5705} (mÅ)	EW_{5780} (mÅ)	EW_{5797} (mÅ)	EW_{6284} (mÅ)	EW_{6613}	Refs
...	HD 208501	...	0.76	...	...	231 ± 4	98 ± 1	...	...	8
18 Peg	HD 209008	...	0.08	...	...	39	9	...	...	1
...	HD 209744	...	0.47	...	...	208	84	...	...	8
...	HD 210072	...	0.54	...	...	242	58	...	...	1
...	HD 210121	20.63	0.40	...	< 20	70 ± 7	46 ± 9	146 ± 50	25 ± 2	2,3
35 Aqr	HD 210191	< 20.66	0.05	...	...	11	< 3	...	...	1
λ Cep	HD 210839	21.16	0.57	...	65 ± 5	261 ± 5	72 ± 6	551 ± 45	150 ± 3	2
31 Peg	HD 212076	...	0.11	...	...	38	13	...	...	1
π Aqr	HD 212571	20.58	0.22	...	...	62	13	...	...	1
...	HD 214080	20.62	0.07	...	...	34	17	...	...	1
10 Lac	HD 214680	20.69	0.13	...	< 5	74 ± 5	25 ± 3	237 ± 50	...	1,6,7
...	HD 214930	...	0.11	...	...	43	16	...	...	1
...	HD 215733	20.70	0.13	...	...	76	19	...	...	1
...	HD 216200	...	0.25	...	...	106 ± 4	48 ± 2	...	...	8
o And	HD 217675	19.67	0.05	...	23	45	14	...	...	7
1 Cas	HD 218376	20.95	0.25	...	45 ± 5	146 ± 8	61.7 ± 6	365 ± 45	68 ± 3	2

Continued on next page

Table B.2 – Continued

Name	HD	log N(H I) (cm^{-2})	$E(B-V)$	EW_{4428} (mÅ)	EW_{5705} (mÅ)	EW_{5780} (mÅ)	EW_{5797} (mÅ)	EW_{6284} (mÅ)	EW_{6613}	Refs
58 Peg	HD 218700	...	0.01	...	...	37	7	...	...	1
...	HD 219188	20.84	0.13	...	...	66	18	...	...	1,6
ψ2 Aqr	HD 219688	...	0.02	...	...	4	...	...	...	1
6 Cas	HD 223385	...	0.67	...	...	582 ± 6	167 ± 6	1360 ± 70	...	1
...	HD 224055	...	0.83	...	...	449	144	...	...	8
σ Cas	HD 224572	20.88	0.19	...	...	78 ± 4	31 ± 4	276 ± 40	...	1
...	HD 228712	...	1.30	...	...	441	126	...	...	8
...	HD 229059	...	1.71	...	96 ± 5	457 ± 7	163 ± 3	1090 ± 150	249 ± 5	2
B+31D643	HD 281159	21.39	0.85	...	68 ± 10	310 ± 10	120 ± 15	635 ± 80	151 ± 5	2
$+66^o1675$	...	...	1.41	...	...	398	223	...	...	1
-14^o5037	...	...	1.56	...	...	605	265	...	...	1
$BD+30^o549$	...	...	0.57	...	< 11	154	68	...	...	7
BD+40	...	...	1.84	...	...	754	213	...	...	8
$BD+41^o3737$	...	...	0.33	...	33	182	54	...	...	7
$BD+63^o1964$	...	...	1.00	...	211 ± 20	729 ± 10	419 ± 12	1380 ± 200	330 ± 6	2
$BD+69^o1232$	...	...	0.21	...	23	145	58	...	...	7

Continued on next page

Table B.2 – Continued

Name	HD	log N(H I) (cm^{-2})	$E(B-V)$	EW_{4428} (mÅ)	EW_{5705} (mÅ)	EW_{5780} (mÅ)	EW_{5797} (mÅ)	EW_{6284} (mÅ)	EW_{6613}	Refs
CygOB2 5	...	...	1.99	...	...	850 ± 20	381 ± 15	2215 ± 200	...	1
CygOB2 8A	...	...	1.61	...	...	796	205	...	...	8
CygOB2 12	...	...	3.31	...	< 30	101 ± 5	23 ± 4	296 ± 40	17 ± 3	2
IC348 12	...	...	0.84	...	...	319	87	...	...	8

REFERENCES 1. Herbig (1993); 2. Thorburn et al. (2003); 3. Welty et al. (2006); 4. Cox et al. (2006); 5. Sollerman et al. (2005); 6. Savage et al. (1977); 7. Josafatsson & Snow (1987); 8. Krełowski et al. (1999)